

AD-A265 995



172

The Pennsylvania State University
APPLIED RESEARCH LABORATORY
P.O. Box 30
State College, PA 16804

DTIC
ELECTE
JUN 21 1993
S c D

**SUPPRESSION OF THE NEAR WALL BURST PROCESS
OF A FULLY DEVELOPED TURBULENT PIPE FLOW**

by

A. A. Fontaine
S. Deutsch

Technical Report No. TR 93-06
May 1993

Supported by:
Office of Naval Research

L.R. Hettche, Director
Applied Research Laboratory

Approved for public release; distribution unlimited

93 6 18 004

93-13798



REPORT DOCUMENTATION PAGE

Form Approved
OARF No. 0704-0188

Public reporting burden for this collection of information is estimated to average 1 hour per response, including the time for reviewing instructions, searching existing data sources, gathering and maintaining the data needed, and completing and reviewing the collection of information. Send comments regarding this burden estimate or any other aspect of this collection of information, including suggestions for reducing this burden, to Washington Headquarters Services, Directorate for Information Operations and Reports, 1215 Jefferson Davis Highway, Suite 1204, Arlington, VA 22202-4302, and to the Office of Management and Budget, Paperwork Reduction Project (0704-0188), Washington, DC 20503.

1. AGENCY USE ONLY (Leave blank)		2. REPORT DATE May 1993		3. REPORT TYPE AND DATES COVERED	
4. TITLE AND SUBTITLE Suppression of the Near Wall Burst Process of a Fully Developed Turbulent Pipe Flow				5. FUNDING NUMBERS N00014-91-J-1064 N00014-91-J-1608	
6. AUTHOR(S) A. A. Fontaine, S. Deutsch					
7. PERFORMING ORGANIZATION NAME(S) AND ADDRESS(ES) The Pennsylvania State University Applied Research Laboratory P.O. Box 30 State College, PA 16804				8. PERFORMING ORGANIZATION REPORT NUMBER TR#93-06	
9. SPONSORING / MONITORING AGENCY NAME(S) AND ADDRESS(ES) Office of Naval Research 800 North Quincy Street Arlington, VA 22217				10. SPONSORING / MONITORING AGENCY REPORT NUMBER	
11. SUPPLEMENTARY NOTES					
12a. DISTRIBUTION / AVAILABILITY STATEMENT Unlimited Distribution				12b. DISTRIBUTION CODE	
13. ABSTRACT (Maximum 200 words) <p>A local suppression of the near wall region burst process is achieved by modifying the buffer region and sublayer ($Y^+ < 30$) of a fully developed turbulent pipe flow with a 16.4 wall unit high, wall-mounted bump. A downstream converging flow field is produced by the divergence of the approaching mean flow around the bump. In addition, a pair of counter-rotating vortices are generated by the bump and convected downstream. The vortices have a circulation which produces a common wall directed flow between them, which also contributes to the flow convergence. These vortices are 10 to 15 wall units in diameter and persist for more than 174 wall units downstream. The investigation is conducted in the ARL/PSU glycerin tunnel at a Reynolds number, based on pipe diameter, of approximately 10,000. The momentum thickness Reynolds number is 730. Multi-component, multi-point, time resolved laser Doppler velocimetry measurements are made in both the undisturbed and modified boundary layers. The measurements include single-point three-component velocity profiles, two-point multi-component velocity correlations and velocity spectral estimates.</p>					
14. SUBJECT TERMS turbulent pipe flow, burst process, buffer region, sublayer, fully developed, vortices, glycerine tunnel, velocity profile, velocity correlation, velocity spectrum				15. NUMBER OF PAGES 210	
				16. PRICE CODE	
17. SECURITY CLASSIFICATION OF REPORT UNCLASSIFIED	18. SECURITY CLASSIFICATION OF THIS PAGE UNCLASSIFIED	19. SECURITY CLASSIFICATION OF ABSTRACT	20. LIMITATION OF ABSTRACT		

ABSTRACT

A local suppression of the near wall region burst process is achieved by modifying the buffer region and sublayer ($Y^+ < 30$) of a fully developed turbulent pipe flow with a 16.4 wall unit high, wall-mounted bump. A downstream converging flow field is produced by the divergence of the approaching mean flow around the bump. In addition, a pair of counter-rotating vortices are generated by the bump and convected downstream. The vortices have a circulation which produces a common wall directed flow between them, which also contributes to the flow convergence. These vortices are 10 to 15 wall units in diameter and persist for more than 174 wall units downstream. The investigation is conducted in the ARL/PSU glycerin tunnel at a Reynolds number, based on pipe diameter, of approximately 10,000. The momentum thickness Reynolds number is 730. Multi-component, multi-point, time resolved laser Doppler velocimetry measurements are made in both the undisturbed and modified boundary layers. The measurements include single-point three-component velocity profiles, two-point multi-component velocity correlations and velocity spectral estimates.

The wall directed flow convergence occurs over a region 15 wall units high and more than 100 wall units long. Locally, turbulent velocity fluctuations, in the form of ejections and sweeps, are retarded within this region. This yields a reduction in the near wall uv Reynolds stress and burst rate. A reduction in the local wall shear stress is observed over significant region, which results in mean velocity profiles similar to those observed in polymer drag reduced boundary layers. Velocity statistics indicate that the vortices increase the rate of the turbulent diffusion of energy.

Velocity measurements in the undisturbed turbulent pipe flow are in excellent agreement with and validate recent direct numerical simulations of a fully developed turbulent

channel flow at a momentum thickness Reynolds number of about 700. In addition, the high resolution three component velocity measurements in both the undisturbed and modified flow fields provide an excellent data base to be used for validation of turbulent boundary layer computational codes.

TABLE OF CONTENTS

	<u>Page</u>
LIST OF TABLES	vii
LIST OF FIGURES	viii
NOMENCLATURE	xv
ACKNOWLEDGEMENTS	xix
 <u>Chapter</u>	
1. INTRODUCTION	1
1.1 Background	1
1.2 Focus of the Present Research	12
2. EXPERIMENTAL APPARATUS AND INSTRUMENTATION	17
2.1 Facility	17
2.2 The Laser Doppler Velocimeter	24
2.3 LDV Signal Processing	32
3. DATA ACQUISITION AND REDUCTION	35
3.1 Data Acquisition	35
3.1.1 TSI Coincident Mode	35
3.1.2 External Digitization	38
3.2 Data Reduction	43
3.3 Post Processing	44
3.3.1 Velocity Statistics	44
3.3.2 Wall Shear Stress Estimates	45
3.3.3 Time Between Bursts Estimates	45
3.3.4 Relative Quadrant Analysis of the uv Reynolds Stress	49
3.3.5 Turbulent Velocity Spectra	49
4. GLYCERIN TUNNEL TURBULENT PIPE FLOW CHARACTERIZATION	52
4.1 Introduction	52
4.2 Axial Pressure Surveys	52
4.3 Velocity Profile Statistics	54
4.4 Post Processed Results	59
4.5 Summary	70

5.	THE MODIFIED WALL REGION: SINGLE-POINT MEASUREMENTS	75
5.1	The Global Flow Field	75
5.1.1	Introduction	75
5.1.2	Summary of the Characteristics of the Global Flow Field	76
5.2	Local Velocity Measurements Around the Bump	78
5.2.1	Confirmation of the Junction Vortex	78
5.2.2	Confirmation of a Downstream Separation zone	80
5.3	Measurements in the Development and Recovery Region $58 \leq x^+ \leq 350$	81
5.3.1	Mean Velocity Results	81
5.3.2	Turbulent Velocity Fluctuation Statistics	87
5.3.2.1	Turbulent Velocity Hodographs	87
5.3.2.2	RMS Velocity Measurements	92
5.3.2.3	Reynolds Stress Data	99
5.3.2.4	Velocity Skewness and Kurtosis	110
5.4	Summary of the Single-Point Statistics	115
6.	TURBULENT KINETIC ENERGY BALANCE AND SPECTRA	118
6.1	Turbulent Kinetic Energy Balance	118
6.2	Velocity Spectra	139
6.3	Summary	153
7.	STOCHASTIC ESTIMATION	158
7.1	Introduction	158
7.2	Two-Point Correlation Measurements	158
7.3	Linear Stochastic Estimation	177
8.	SUMMARY AND RECOMMENDATIONS FOR FURTHER STUDY	193
8.1	Summary	193
8.2	Major Significance of the Present Results	198
8.3	Recommendations for Further Study	200
	REFERENCES	202
	Appendix A. LDV VELOCITY MEASUREMENT ERROR DUE TO REFRACTION EFFECTS	207
	Appendix B. VELOCITY CORRECTIONS FOR OFF-CENTER MEASUREMENTS	209

LIST OF TABLES

<u>Tables</u>	<u>Page</u>
2.1 Glycerin Properties and Tunnel Operating Conditions at 34.5° C	21

DTIC QUALITY INSPECTED 8

Accession For	
NTIS CRA&I	<input checked="" type="checkbox"/>
DTIC TAB	<input type="checkbox"/>
Unannounced	<input type="checkbox"/>
Justification	
By	
Distribution /	
Availability Codes	
Dist	Avail and/or Special
A-1	

LIST OF FIGURES

<u>Figures</u>	<u>Page</u>
1.1 Picture showing a model of the association of counter-rotating vortices and the lift-up of low speed streaks in the near wall region. Figure is taken from Blackwelder and Eckelmann (1979)	5
1.2 Illustration showing the formation and lift-up of sublayer low speed streaks and the regeneration of near wall vortices. The illustration is a modified figure from Robinson (1991)	11
1.3 Illustration of the proposed burst suppression scheme	15
2.1 Glycerin tunnel facility	18
2.2 Temperature dependence of glycerin kinematic viscosity	20
2.3 Illustration of the wall-mounted bump	23
2.4 Illustration of glycerin tunnel test section a) showing location of bump and measurement coordinate system and b) cross-sectional view a-a	25
2.5 Orientation of the LDV systems at the test section	28
2.6 Illustration of near wall refraction effects on the fiber-optic probe laser beams	33
3.1 Representative examples of the linear least squares fit to the velocity profiles in the viscous sublayer	46
3.2 Illustration of the determination of the ejection filter time used in the time between bursts estimates	48
3.3 Definitions of the four quadrants used in the uv quadrant analysis technique . . .	50
4.1 Measured axial pressure gradient along the test pipe of the glycerin tunnel	53
4.2 Typical streamwise mean velocity profile in the undisturbed glycerin tunnel turbulent boundary layer. The profile is plotted in wall variables	55
4.3 Measured rms velocities in the undisturbed glycerin tunnel turbulent boundary layer. Data are normalized by wall variables	56
4.4 Typical uv Reynolds stress profile measured in the undisturbed glycerin tunnel turbulent boundary layer. Data normalized by wall variables	58

4.5	Measured triple correlation profiles in the undisturbed glycerin tunnel turbulent boundary layer. Data normalized by wall variables. a) uuu , and vvv and b) uuv , and uvv	60
4.6	Typical profiles of the undisturbed glycerin tunnel turbulent boundary layer a) velocity fluctuation skewness levels and b) velocity fluctuation kurtosis levels	62
4.7	Relative quadrant analysis of the uv signal in the undisturbed glycerin tunnel turbulent boundary layer. TSI-1, TSI-2 and ext. dig. data represent three different LDV system configurations	65
4.8	Profiles of the components of the turbulent kinetic energy transport equation, Equation 4.3, in the undisturbed glycerin tunnel turbulent boundary layer	68
4.9	Typical auto-spectral estimates of the turbulent velocity fluctuations at $y^+ = 20$. Measured in the undisturbed glycerin tunnel turbulent boundary layer	69
4.10	Typical auto-spectral estimates of the streamwise velocity fluctuations at four locations in the undisturbed glycerin tunnel turbulent boundary layer	71
4.11	Typical auto-spectral estimates of the radial velocity fluctuations at four locations in the undisturbed glycerin tunnel turbulent boundary layer	72
4.12	Typical auto-spectral estimates of the circumferential velocity fluctuations at four locations in the undisturbed glycerin tunnel turbulent boundary layer	73
5.1	Illustration of global flow field around and downstream of the bump. Figure is not to scale	77
5.2	Two-component velocity vectors upstream of the bump, measured along the centerplane of the bump in the x - y plane	79
5.3	Development of the normalized wall shear stress downstream of the bump. The wall shear stress is normalized by the value obtained in the undisturbed glycerin tunnel boundary layer	82
5.4	Axial development of the streamwise mean velocity profiles downstream of the bump. The profiles are measured along the centerplane and are normalized by local friction velocity	83
5.5	Spanwise development of the radial mean velocity profile at $x^+ = 58$ Normalization with ref. u^*	84
5.6	Spanwise development of the circumferential mean velocity profile at $x^+ = 58$ Normalization with ref. u^*	85

5.7	Joint probability density contours shown in the two-component hodograph planes at $x^+ = 58$ and $z^+ = 0$. a) uw , b) uv , c) wv	88
5.8	Joint probability density contours shown in the two-component hodograph planes at $x^+ = 58$ and $z^+ = -5.5$. a) uw , b) uv , c) wv	89
5.9	Joint probability density contours shown in the two-component hodograph planes at $x^+ = 58$ and $z^+ = -11$. a) uw , b) uv , c) wv	90
5.10	Joint probability density contours shown in the two-component hodograph planes at $x^+ = 58$ and $z^+ = -17$. a) uw , b) uv , c) wv	91
5.11	Axial development of the streamwise rms velocity profiles along the centerplane. Normalization with ref. u^+	93
5.12	Spanwise development of the streamwise rms velocity profiles at $x^+ = 174$. Normalization with ref. u^+	94
5.13	Axial development of the radial rms velocity profiles along the centerplane. Normalization with ref. u^+	95
5.14	Axial development of the circumferential rms velocity profiles along the centerplane. Normalization with ref. u^+	96
5.15	Spanwise development of the circumferential rms velocity profiles at $x^+ = 58$. Normalization with ref. u^+	98
5.16	Axial development of the uv^+ Reynolds stress profiles along the centerplane. Normalization with ref. u^+	100
5.17	Profiles of the mean velocity strain rates at $x^+ = 58$ and $z^+ = 0$. Normalization with ref. u^+	102
5.18	Axial development of profiles of the time between bursts estimates along the centerplane. Normalization with ref. u^+	103
5.19	Axial development of profiles of the uv relative quadrant analysis results. The quadrant averages are normalized by the undisturbed total uv level and u^+ . a) quadrants 1 and 2 and b) quadrants 3 and 4	105
5.20	Spanwise development of the uw Reynolds stress component at $x^+ = 58$. Normalization with ref. u^+	108
5.21	Spanwise development of the wv Reynolds stress component at $x^+ = 58$. Normalization with ref. u^+	109
5.22	Axial development of profiles of the streamwise and radial velocity skewness levels. Normalization with ref. u^+	111

5.23	Spanwise development of profiles of the circumferential velocity skewness levels at $x^+ = 58$. Normalization with ref. u^+	113
5.24	Axial development of profiles of the circumferential velocity skewness levels at $z^+ = -11$. Normalization with ref. u^+	114
6.1	Axial development of profiles of the time averaged turbulent kinetic energy along the centerplane. Normalization with ref. u^+	119
6.2	Spanwise development of profiles of the time averaged turbulent kinetic energy at $x^+ = 58$. Normalization with ref. u^+	120
6.3	Profiles of the terms of the turbulent kinetic energy balance, Equation 4.2, at $x^+ = 58$ and $z^+ = 0$. Normalization with ref. u^+	122
6.4	Profiles of the components of the turbulent kinetic energy transport equation, Equation 4.3, in the undisturbed glycerin tunnel turbulent boundary layer. Normalization with ref. u^+	123
6.5	Contributions of the components of the rate of production of turbulent kinetic energy at $x^+ = 58$ and $z^+ = 0$. Normalization with ref. u^+	124
6.6	Profiles of the terms of the $u^2/2$ transport equation in the undisturbed glycerin tunnel turbulent boundary layer	128
6.7	Profiles of the terms of the $v^2/2$ transport equation in the undisturbed glycerin tunnel turbulent boundary layer	129
6.8	Profiles of the terms of the $w^2/2$ transport equation in the undisturbed glycerin tunnel turbulent boundary layer	130
6.9	Profiles of the terms of the $u^2/2$ transport equation at $x^+ = 58$ and $z^+ = 0$. Normalization with ref. u^+	132
6.10	Profiles of the terms of the $v^2/2$ transport equation at $x^+ = 58$ and $z^+ = 0$. Normalization with ref. u^+	133
6.11	Profiles of the terms of the $w^2/2$ transport equation at $x^+ = 58$ and $z^+ = 0$. Normalization with ref. u^+	134
6.12	Profiles of the terms of the turbulent kinetic energy balance, Equation 4.2, at $x^+ = 116$ and $z^+ = 0$. Normalization with ref. u^+	137
6.13	Profiles of the terms of the turbulent kinetic energy balance, Equation 4.2, at $x^+ = 58$ and $z^+ = -11$. Normalization with ref. u^+	138
6.14	Auto-spectral estimates of the streamwise velocity component at $y^+ = 5$. Lines are curve fits to the estimated auto-spectra	140

6.15	Auto-spectral estimates of the radial velocity component at $y^+ = 5$. Lines are curve fits to the estimated auto-spectra	141
6.16	Auto-spectral estimates of the circumferential velocity component at $y^+ = 5$. Lines are curve fits to the estimated auto-spectra	142
6.17	Auto-spectral estimates of the streamwise velocity component at $y^+ = 15$. Lines are curve fits to the estimated auto-spectra	146
6.18	Auto-spectral estimates of the radial velocity component at $y^+ = 15$. Lines are curve fits to the estimated auto-spectra	147
6.19	Auto-spectral estimates of the circumferential velocity component at $y^+ = 15$. Lines are curve fits to the estimated auto-spectra	148
6.20	Magnitude of the one-sided cross-spectral estimates of the u and v velocities at $y^+ = 5$	150
6.21	Magnitude of the one-sided cross-spectral estimates of the u and v velocities at $y^+ = 15$	151
6.22	Magnitude of the one-sided cross-spectral estimates of the u and v velocities at $y^+ = 20$	152
6.23	Magnitude of the one-sided cross-spectral estimates of the u and w velocities at $y^+ = 5$	154
6.24	Magnitude of the one-sided cross-spectral estimates of the w and v velocities at $y^+ = 5$	155
7.1	Two-point correlation contour map of the u-v velocity correlation at $y_1^+ = 2$. Measured in the undisturbed glycerin tunnel turbulent boundary layer. Symbols represent the locations of the moving probe measurements . . .	160
7.2	Two-point correlation contour map of the u-v velocity correlation at $y_1^+ = 12$. Measured in the undisturbed glycerin tunnel turbulent boundary layer. Symbols represent the locations of the moving probe measurements . . .	161
7.3	Locations of the moving probe velocity measurements for the two-point correlation measurements at $y_1^+ = 5$, $x^+ = 58$. Normalization with ref. u^* . . .	164
7.4	Locations of the moving probe velocity measurements for the two-point correlation measurements at $y_1^+ = 15$, $x^+ = 58$. Normalization with ref. u^* . .	165
7.5	Contour maps of the uu two-point correlation at $y_1^+ = 5$, $x^+ = 58$. Normalization with ref. u^*	166

7.6	Contour maps of the uu two-point correlation at $y_l^+ = 15$, $x^+ = 58$. Normalization with ref. u^+	167
7.7	Contour maps of the ww two-point correlation at $y_l^+ = 5$, $x^+ = 58$. Normalization with ref. u^+	169
7.8	Contour maps of the ww two-point correlation at $y_l^+ = 15$, $x^+ = 58$. Normalization with ref. u^+	170
7.9	Contour maps of the uv two-point correlation at $y_l^+ = 5$, $x^+ = 58$. Normalization with ref. u^+	171
7.10	Contour maps of the uv two-point correlation at $y_l^+ = 15$, $x^+ = 58$. Normalization with ref. u^+	172
7.11	Contour maps of the vu two-point correlation at $y_l^+ = 5$, $x^+ = 58$. Normalization with ref. u^+	174
7.12	Contour maps of the vu two-point correlation at $y_l^+ = 15$, $x^+ = 58$. Normalization with ref. u^+	175
7.13	Streamwise conditionally averaged velocity perturbation contours obtained from linear stochastic estimation for $y_l^+ = 5$. $u_c = 2.2$ m/s, $v_c = -0.27$ m/s and $w_c = -0.85$ m/s. Velocity contours are normalized by the magnitude of the velocity perturbation at $\Delta x = \Delta y = 0$, which is $u = 2.32$ m/s	182
7.14	Spanwise conditionally averaged velocity perturbation contours obtained from linear stochastic estimation for $y_l^+ = 5$. $u_c = 2.2$ m/s, $v_c = -0.27$ m/s and $w_c = -0.85$ m/s. Velocity contours are normalized by the magnitude of the velocity perturbation at $\Delta x = \Delta y = 0$, which is $w = -1.08$ m/s	183
7.15	Streamwise conditionally averaged velocity perturbation contours obtained from linear stochastic estimation for $y_l^+ = 5$. $u_c = -0.5$ m/s, $v_c = w_c = 0$ m/s. Velocity contours are normalized by the magnitude of the velocity perturbation at $\Delta x = \Delta y = 0$, which is $u = -0.54$ m/s	186
7.16	Streamwise conditionally averaged velocity perturbation contours obtained from linear stochastic estimation for $y_l^+ = 15$. $u_c = 2.35$ m/s, $v_c = -0.93$ m/s and $w_c = -1.46$ m/s. Velocity contours are normalized by the magnitude of the velocity perturbation at $\Delta x = \Delta y = 0$, which is $u = 2.2$ m/s	187
7.17	Spanwise conditionally averaged velocity perturbation contours obtained from linear stochastic estimation for $y_l^+ = 15$. $u_c = 2.35$ m/s, $v_c = -0.93$ m/s and $w_c = -1.46$ m/s. Velocity contours are normalized by the magnitude of the velocity perturbation at $\Delta x = \Delta y = 0$, which is $w = -1.2$ m/s	188

- 7.18 Streamwise conditionally averaged velocity perturbation contours obtained from linear stochastic estimation for $y_r^+ = 15$. $u_c = 2.35$ m/s, $v_c = 0.93$ m/s and $w_c = -1.46$ m/s. Velocity contours are normalized by the magnitude of the velocity perturbation at $\Delta x = \Delta y = 0$, which is $u = 2.2$ m/s 190

NOMENCLATURE

<u>Symbol</u>	<u>Definition</u>
A	- cross-sectional area enclosed by integration path for vortex circulation calculation
A_{ij}	- coefficient matrix for linear stochastic estimation
B_{ij}	- coefficient matrix for linear Stochastic estimation
C	- temperature in degrees Centigrade
$C_{uv,uv,vw}$	- cross-spectral estimate between the uv, uw or vw velocity fluctuations
D	- diameter of test pipe
d	- local diameter of the wall-mounted bump
dp/dx	- axial pressure gradient along the test pipe
E_i	- conditional vector for the linear stochastic estimation
f	- frequency
f_D	- Doppler frequency
Hz	- Hertz, frequency measurement defined as 1/second
k	- quadrant analysis threshold value
KW	- kilowatts
m	- meter, unit of measure in the metric system of measurement
MHz	- megahertz
mm	- millimeter, 1/1000 th meter
ms	- millisecond, 1/1000 th second
mv	- millivolt, 1/1000 th volt
N	- number of cycles, used for LDV Doppler signal validation
N_e	- number of ensembles used in the estimation of velocity spectra

nm	- nanometer, $1. \times 10^{-9}$ meters
ns	- nanosecond, $1. \times 10^{-9}$ seconds
Pa	- pascal, unit of measure for pressure
q	- turbulent kinetic energy, defined in equation 4.2
R	- test pipe radius
r	- radial displacement in the test section, measured from the center of the test section
R_{ij}	- velocity correlation coefficient
$Re_{D,d,\theta}$	- Reynolds number based on the length scale D, d or θ (θ is defined here as the momentum thickness which is estimated using the centerline velocity)
R_v	- vortex Reynolds defined by equation 5.1
$S_{u,v,w}$	- auto-spectral estimate of the u,v,w velocity fluctuations
T_b	- mean time between bursts
t	- time
t_b	- instantaneous time between bursts
t_e	- instantaneous time between ejections
U,V,W	- instantaneous streamwise, radial and circumferential velocity components
U_j	- velocity components U, V and W used in linear stochastic estimation, used in Chapter 7
\bar{U}'_i, \bar{u}'_i	- conditionally averaged total and fluctuating velocity from stochastic estimation, used in Chapter 7
u,v,w	- fluctuating streamwise, radial and circumferential velocity components
u',v',w'	- streamwise, radial and circumferential rms velocities
u^*	- friction velocity
uv_i	- uv Reynolds stress contribution to the i^{th} quadrant

x	- axial measurement coordinate along pipe axis
y	- radial measurement coordinate measured from the pipe wall towards the pipe center, $y = R - r$
y^*_{max}	- radial location of maximum uv Reynolds stress
z	- circumferential or spanwise measurement coordinate, $z = R\theta$
α	- preliminary angle estimation used in the estimation of rotation angle
β	- rotation angle of LDV system with off-center movement
Γ	- velocity circulation
Δ	- relative difference
γ_{ij}	- coherence function of the velocity cross-spectra
$\partial/\partial(n)$	- partial derivative with respect to variable n , n can be any variable x , y or z
θ	- circumferential coordinate in cylindrical coordinates
κ	- LDV half angle
λ	- wavelength of LDV laser beams, nano-meters
μm	- micrometer, $1. \times 10^{-6}$ meters
μs	- microsecond, $1. \times 10^{-6}$ meters
π	- Pi
ρ	- density of the glycerin
τ	- time delay in stochastic estimation
τ_e	- ejection filter time for the time between bursts estimations
τ_w	- wall shear stress
ν	- kinematic viscosity of the glycerin
ψ	- incident angle of laser beam with pipe wall

SUPERSCRIPTS

+ - denotes normalization by wall variables, u^* and ν

SUBSCRIPTS

a - actual in the tunnel values

c - denotes conditional event in stochastic estimation

f - denotes fixed probe in the two-point velocity correlation measurements

m - measured or estimated values

MISCELLANEOUS NOTATION

$|z|$ - absolute value of z

\bar{x} , \bar{X} - overbar represents ensemble average of variable x or X

ACKNOWLEDGEMENTS

This work was supported in part by Mr. James Fein under Grant No. N00014-91-J-1064 and in part by Dr. L. Patrick Purtell under Grant No. N00014-91J-1608.

Chapter 1

INTRODUCTION

1.1 Background

Turbulence has a significant effect on the drag, noise and heat transfer in wall bounded flows. For this reason, a considerable effort has been made both to understand the physics of turbulent boundary layers and to predict and control the characteristics associated with the turbulent flow. Sreenivasan (1990) and Robinson (1991) have recently provided thorough reviews of the turbulent boundary layer.

The structure of the near wall region of turbulent boundary layers plays a dominant role in the generation and maintenance of turbulence. Detailed flow visualization studies by Rundstadler et al. (1963) and Kline et al. (1967) have shown that the near wall region is composed of well organized, spatially intermittent streamwise streaky structures randomly occurring in space and time. These intermittent structures consisted of spanwise alternating elongated regions of high and low speed fluid originating in the viscous sublayer. These authors labeled the accumulation of the low speed fluid in the viscous sublayer as low speed streaks. Thorough reviews of the features of the sublayer streaky structure have recently been provided by Kline and Robinson (1990) and Robinson (1991).

According to Kline and Robinson (1990), low speed streaks originate as a collection of low speed fluid in the near wall region from $0 < y^+ \leq 7$. The low speed fluid has a typical streamwise velocity magnitude of approximately half the local mean streamwise velocity in canonical turbulent boundary layers. Experimental as well as direct numerical simulation results indicate that the low speed streaks have a spanwise scale of roughly 20 wall units and extend more than 1000 wall units in the streamwise direction. Robinson (1991)

indicates that the low speed streaks slowly move out from the wall as they convect downstream. They persist for a significant period of time until they eventually lose their coherence in the region outside the sublayer or are disturbed by another event.

The low speed streaks are observed to meander in the spanwise direction over a range of 30 to 50 wall units as they convect downstream. The streaks are also observed to occasionally lift from the sublayer region and extend a significant distance from the wall in the region of $y^+ < 40$. Robinson (1991) indicates that, in the low Reynolds number simulations, the lifted low speed streaks take on a mushroom shaped cross section as they are drawn up from the wall, with spanwise dimensions increasing with increasing y^+ . The width of the lifted streaks in the buffer region is on the order of 40 to 80 wall units. It is well established through both experiments and simulations that the low speed structures occur with a mean spanwise spacing of approximately 100 wall units. Smith and Metzler (1983) indicated that the mean spanwise spacing was Reynolds number independent and that the spanwise spacing slightly increased with increasing distance from the wall outside the sublayer. Spanwise meandering is also observed in the lifted streaks. These meandering and lifting characteristics of the low speed streaks indicate an inherent three-dimensionality to the dynamics of the near wall region.

Unlike the low speed streaks which are easily visualized experimentally, the associated high speed regions in the sublayer are more difficult to study. Through the direct numerical simulations of canonical turbulent boundary layer flows by Moin and Kim (1985) and Spalart (1988), the characteristics of the high speed regions have been clarified. These regions are less elongated than the low speed streaks and typically have streamwise extents on the order of 500 wall units. The high speed regions are typically two times wider than the

low speed streaks, and have velocity perturbations which are roughly 1.5 times the local mean velocity.

The importance of the formation and lift-up of the low speed streaks to the generation and maintenance of turbulence was illustrated in several landmark experiments. Kline et al. (1967) and Corino and Brodkey (1969) indicated that the lifting of the low speed regions of fluid dominantly contributes to the dynamics of the near wall region. These authors observed that the streamwise oriented low speed streaks undergo a process by which they lift up, stretch, oscillate and then breakup into fine scale turbulence. Kline referred to this process as bursting. Corino and Brodkey (1969), Blackwelder and Eckelmann (1979), Smith and Metzler (1983) and Bogard and Tiederman (1987) have shown, through independent investigations, that the bursting process correlates well with the generation of Reynolds stresses. Corino and Brodkey (1969) and Bogard and Tiederman (1987) estimated that the bursting process accounted for approximately 70% to 80% of the measured Reynolds stress. Bogard and Tiederman (1987) further defined the bursting process as a complex motion involving several ejections or lift-ups of a single low speed streak from the near wall region. In general, the first lift-up is the most energetic and is the major contributor to the Reynolds stress generation.

In addition to the strong correlation with the generation of Reynolds stress, the bursting process has also been connected to the production of turbulent kinetic energy. Laufer (1954) first showed that the production of turbulent kinetic energy peaks in the buffer region at $y^+ \approx 12$. Rundstadler et al. (1963) speculated that, in the near wall region, the bursting process played a dominant role in the production of turbulent kinetic energy. In a detailed study, Kim et al. (1971) confirmed this hypothesis by estimating, from measured instantaneous velocity profiles in a flat plate turbulent boundary layer, the instantaneous

turbulent production during bursting and non-bursting periods. These authors showed that essentially all the production of turbulent kinetic energy, below $y^+ = 100$, occurred during bursting. Furthermore, in the region $15 \leq y^+ \leq 30$, it was shown that the rate of production of turbulent kinetic energy during bursting periods was nearly an order of magnitude greater than the rate of production during non-bursting periods, and 2-3 times larger than the long time averaged levels.

A knowledge of the mechanisms governing the formation and dynamics of the lift-up of the low speed streaks is essential to a full understanding of the processes responsible for the generation of turbulence. Several investigators have speculated that vortices were responsible for the generation, lift-up and maintenance of the low speed streaks. In particular, streamwise oriented vortices generally in counter-rotating pairs, and/or horseshoe (hairpin) vortical structures were suggested as having velocity perturbation profiles necessary to accumulate and lift low speed fluid from the sublayer region. Significant experimental evidence has been accumulated over the past thirty years to support the existence of both types of structures in the turbulent boundary layer. The reader is referred to the extensive literature review and summary dealing with vortical structures compiled by Robinson (1991). A brief overview of selected works will be presented here to illustrate the evidence for both types of vortical structures.

Bakewell and Lumley (1967) and Herzog (1986) used Lumley's proper orthogonal decomposition to determine structural information from measured two-point correlations. Their results from the proper orthogonal decomposition suggested that, on average, a pair of streamwise oriented counter-rotating vortices are a dominant near wall structure. The average picture obtained from this sophisticated statistical procedure takes the form of a pair of counter-rotating vortices with a spanwise separation of approximately 65 wall units. The

vortices are centered at $y^+ \approx 35$ and are tilted 5° from the wall. The direction of rotation of the counter-rotating vortices is sufficient to collect and lift low speed fluid from the wall. It is important to note that, as Herzog (1986) states, these vortices are an average picture of a range of streamwise oriented vortices varying in size, position and strengths. Herzog also noted that when the mean velocity profile is superimposed on the velocity field generated by the vortices, the resulting vorticity lines resembled a stretched horse-shoe shaped structure when viewed from upstream.

Using conditionally sampled velocity data, Blackwelder and Eckelmann (1979) have also provided evidence for streamwise oriented vortical structures responsible for the lift-up of low speed streaks. Figure 1.1 is a picture provided by Blackwelder and Eckelmann (1979)

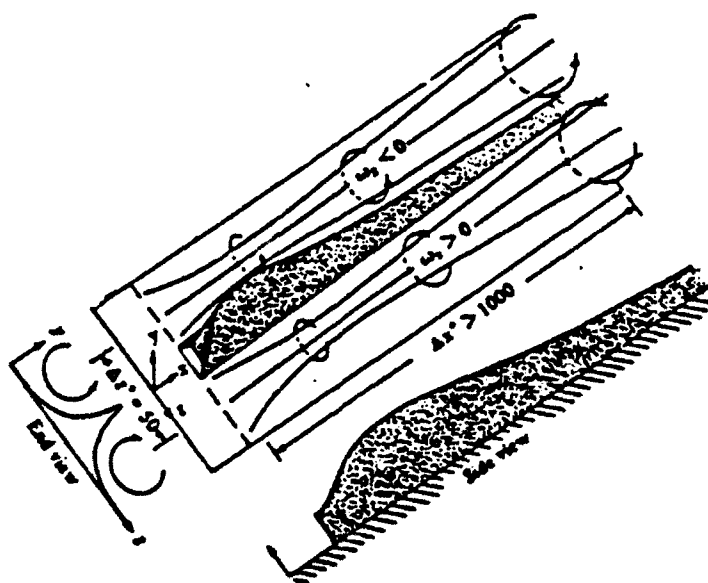


Figure 1.1 Picture showing a model of the association of counter-rotating vortices and the lift-up of low speed streaks in the near wall region. Figure is taken from Blackwelder and Eckelmann (1979)

illustrating their model of the near wall region process governing the formation and lift-up of the low speed streaks. These authors indicate that the vortex centers may lie at approximately $y^+ = 20$ to 30, with a typical diameter of 15 to 20 wall units. The streamwise extent of the vortices is estimated, based on two-point velocity correlations, at roughly 1000 wall units. These authors also caution that these estimates of position and size are average values of structures involved in a stochastic process. More than likely there is a distribution of sizes and positions associated with the model shown in Figure 1.1. Smith and Metzler (1983) and Nagib and Guezennec (1986) also discovered counter-rotating vortices using conditional sampling techniques on their extensive data bases. It must be noted that the symmetric structures obtained through these sophisticated statistical and conditional averaging procedures may be due to the symmetry conditions imposed on the data reduction procedure and from the averaging methods involved.

Flow visualization studies have also provided evidence for the existence of streamwise oriented vortices. Clark and Markland (1971) conducted hydrogen bubble wire flow visualization experiments in the near wall region of an open channel. They concluded that vortices played a major role in the formation of low speed streaks and in the bursting process. Both counter-rotating streamwise vortices and horseshoe type vortices were visually observed. The observed counter-rotating vortices appeared to originate around a $y^+ \approx 7$ and were tilted at a 3° to 7° angle with the wall. Kasagi et al. (1986) observed streamwise oriented vortical structures in their flow visualization experiments. Both single and counter-rotating vortex structures were observed. The structures had a mean diameter of approximately 40 wall units and were centered at approximately $25 \leq y^+ \leq 30$. The visualization techniques employed did not provide more detailed information about the vortices, such as their cross sectional shape, strength or whether the vortices were inclined at an angle. Kasagi modeled the near

wall region using velocity perturbations which were consistent with a pair of counter-rotating streamwise oriented vortices and were able to reproduce known velocity and Reynolds stress statistics.

Theodorsen (1952) first proposed that horseshoe vortices were a fundamental structure of the turbulent boundary layer. The most significant evidence for the existence of horseshoe vortices was obtained by Head and Bandyopadhyay (1981). These authors conducted detailed flow visualization experiments using smoke visualization and light sheet planes inclined at 45° to the flow direction. These visualization experiments were performed over a wide range of Reynolds numbers and clearly showed horseshoe or hairpin type structures throughout the turbulent boundary layer outside of the buffer region. Horseshoe vortices were common at low Reynolds numbers while hairpins appeared at higher Reynolds numbers. The hairpins were believed to be highly stretched horseshoe vortices. Head and Bandyopadhyay (1981) reported that their visualization results suggested that the observed horseshoe vortices appeared to originate in the near wall region, and are possibly associated with streamwise oriented vortices in the buffer region.

The experimental evidence supporting the existence of streamwise and horseshoe vortices, and their spatial relationship with the low speed streaks is significant. However, the evidence is inadequate in describing, in detail, the physics governing the formation and lift-up of the low speed streaks, and the exact relationship between vortices and the streaks. The significance of one form of vortex structure over the other governing the streak lift-up process is unclear. Furthermore, it may be asked if the streamwise oriented vortices in the buffer region are directly related to the horseshoe structures found outside of the buffer region. The recent low Reynolds number direct numerical simulations of canonical turbulent boundary layers are beginning to shed light on these issues.

A significant result of the numerical simulations was the importance of vortical structures in the turbulent transport process. The turbulent channel flow results of Moin and Kim (1985) and the flat plate turbulent boundary layer results of Spalart (1988) show that counter-rotating quasi-streamwise vortices, commonly believed to be the dominant near wall structure, occur very infrequently in the low Reynolds number simulations. The more commonly occurring near wall vortical structures were single quasi-streamwise vortices, which are considerably shorter in extent than the length of the low speed streaks. Typical quasi-streamwise vortices were found to extend only several hundred wall units in the streamwise direction. The prefix quasi- is used to denote a streamwise oriented vortex which is slightly askew of the streamwise direction; for instance, the vortex may be inclined upward at a small angle from this direction.

Robinson's (1991) detailed analysis of the kinematics of the low Reynolds number turbulent boundary layer simulation of Spalart (1988) shows that ejections played a dominant role in the production of turbulent energy below $y^+ = 80$. Furthermore, he observed a strong spatial correlation between vortical structures, ejections and sweeps, and the easily visualized near wall low speed streaks. According to Robinson (1991), the low speed streaks are the signature of quasi-streamwise vortices and/or near wall symmetric or asymmetric arch (horseshoe) vortices. In addition, these vortical structures are not only capable of collecting low momentum fluid near the wall, but can also pump it out into the higher momentum fluid in the buffer region.

The following description of the structure and dynamics of the near wall region can be inferred from Robinson's (1991) detailed study. While this description is based on the low Reynolds number turbulent boundary layer simulation of Spalart (1988), the general features are believed to hold for higher Reynolds number flows. Differences may arise in significance

of single as opposed to counter-rotating streamwise vortices, the intensities of the important vortices in the bursting process or whether horseshoe vortices are truly symmetric or asymmetric.

The buffer region of the low Reynolds number canonical turbulent boundary layer is dominated by single quasi-streamwise vortices. These near wall vortices are centered in the region from the wall of $10 \leq y^+ \leq 30$ and have diameters which range from 10 to 35 wall units. The streamwise oriented vortices are observed in the buffer region and lower log regions, and their diameters are observed to increase with increasing distance from the wall. The vortices have an observed mean upward tilt of 5° at $y^+ = 15$ which increases to 15° at $y^+ = 30$.

The quasi-streamwise vortices are formed when the leg of a mature (parent) arch (horseshoe) vortex descends into the low momentum fluid of the near wall region. As the parent vortex convects downstream, the leg is stretched into an elongated, tilted, quasi-streamwise vortex. The leg may break away from the parent vortex and then convect downstream as a single streamwise oriented vortex, or it may be continually stretched until dissipated. In either event, the spatial extent of the quasi-streamwise vortices is relatively short while the temporal persistence can be quite long. The stretching of the parent vortex leg produces streamwise vortices with significant circulation. Robinson (1991) found that, on average, the intensity of the observed near wall streamwise vortices are approximately double the intensity of the background spanwise vorticity due to the mean velocity gradient. Occasionally, vortices are observed with intensities up to ten times the background levels. Robinson (1991) indicates that vortices with an intensity greater than the background level should be sufficiently strong enough to accumulate and lift low speed fluid from the sublayer region.

As a quasi-streamwise vortex convects downstream through the buffer region, it collects or accumulates low speed fluid in the form of a long streamwise oriented streak. This formed streak is the signature of a convecting streamwise vortex. The initiating vortex has a long persistence time and thus convects downstream a great distance. This perpetuates the growth of the streaks, which are typically longer than the generating vortex. Eventually this vortex dissipates and leaves behind a well formed, long, low speed streak in the sublayer region. As the streak convects downstream it occasionally encounters other streamwise oriented vortices. Depending on the strength of this newly encountered vortex and its proximity to the streak, the new vortex may either continue to collect low momentum fluid and perpetuate the streak or it may lift the already formed streak out into the buffer region. In the event a strong closely flanked vortex lifts the streak into the buffer region, a significant generation of quadrant two (negative u and positive v) uv Reynolds stress is observed. A shear layer forms on the upstream edge of the lifted streak as the local high speed fluid impacts on the low momentum fluid. This creates a shear layer instability which in turn generates a new, infant transverse vortex atop the streak. Additional ejections or lift-ups of the same streak occur as the shear layer rolls up into the newly formed transverse vortex. This second ejection occurs immediately upstream of the vortex roll-up. The infant vortex grows and develops into an arch vortex as it convects downstream, and may itself generate new quasi-streamwise vortices downstream. Thus it appears as though the streak formation and lift-up process is a self generating process in the near wall region. This process is illustrated in Figure 1.2 which is a modified figure out of Robinson (1991).

Robinson (1991) observed that not all streaks are spatially associated with a streamwise oriented vortex; and likewise, not all streamwise oriented vortices flank low speed streaks. It was observed, however, that nearly all of the quadrant two uv Reynolds stress

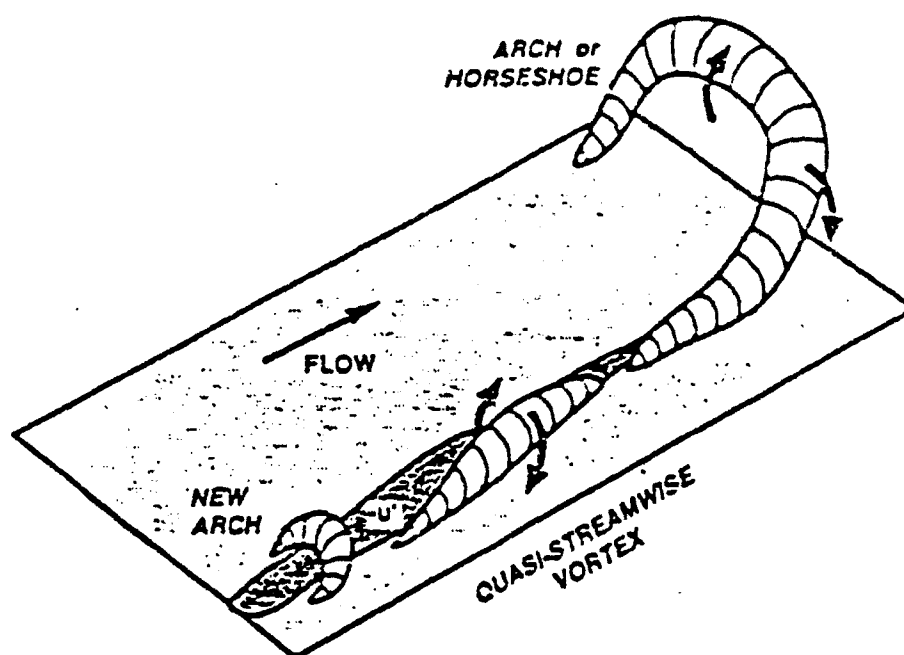


Figure 1.2 Illustration showing the formation and lift-up of sublayer low speed streaks and the regeneration of near wall vortices. The illustration is a modified figure from Robinson (1991)

generating events are spatially associated with the lift-up of a low speed streak by a quasi-streamwise vortex. In addition, these events are almost always flanked on one spanwise side by a quadrant four (positive u and negative v) uv Reynolds stress event. This event typically occurs below $y^+ \leq 12$, and is associated with a sweep type motion induced by the other side of the quasi-streamwise vortex. This process is consistent with the alternating high and low speed regions experimentally observed by Kline et al. (1967) and Corino and Brodkey (1969) in the near wall region.

The streak formation and lift-up process described above can also explain other experimentally observed phenomena. Because the streaks meander in the spanwise direction, it is possible that as a mature streak encounters a strong vortex it becomes skewed in the spanwise direction as it is being lifted from the wall. This would cause the resulting sweep motion to occur either slightly upstream or downstream of the ejection, and would appear, to

a fixed probe, as though the ejection either followed or preceded a sweep event. Both of these phenomena have been reported in the literature. Furthermore, the vortex regeneration mechanism may explain the multiple ejection per single burst phenomena described by Bogard and Tiederman (1987). The low Reynolds number simulation results described by Robinson (1991) show that upon rollup of a new vortex, the second quadrant two or ejection motion which occurs immediately upstream is considerably weaker than the initial ejection. The first ejection is the major Reynolds stress producing event and usually does not occur at the downstream edge of a streak, but at any arbitrary position along its length. This process agrees with the visually observed multiple ejection per burst process described by Bogard and Tiederman (1987).

In summary, the important process governing nearly all of the generation of turbulence in the near wall region is the lift-up of the low speed streaks by a streamwise oriented vortical structure. It appears that the low speed streaks are essentially a passive feature of the near wall region and the signature of convecting streamwise vortices. However, the spatial association of the quasi-streamwise vortices with mature streaks and the resulting dynamics (bursting phenomena) is a crucial element to the production of turbulence. It is this process which should be controlled or modified to achieve efficient control and reduction of the generation of turbulence.

1.2 Focus of the Present Research

A number of techniques have been developed to control the turbulent boundary layer on a global (as opposed to a small or local) scale. Merkle and Deutsch (1990) and Fontaine and Deutsch (1992) have shown that turbulent boundary layer skin friction can be considerably reduced by the injection of gas into water boundary layers. Long chain non-

Newtonian polymer solutions have been used by Walker and Tiederman (1990) and Fontaine et al. (1992) to reduce skin friction in both internal and external flows. However in both of these techniques, the near wall and logarithmic regions of the turbulent boundary layer are flooded with microbubbles or polymers. The injection of a large volume of polymer or bubbles, however, may in many ways be prohibitive.

One suspects intuitively that such global schemes cannot be optimum for the control of the spatially intermittent complex near wall turbulent boundary layer processes discussed in Section 1.1. A more efficient means of controlling the turbulent boundary layer may possibly be achieved by actively controlling the local wall structures. Active control processes should be directed towards the suppression of the bursting process. This may be accomplished in two ways. The first involves the control, inhibition or cancellation of the near wall quasi-streamwise vortices which are responsible for the streak lift-up. The second method would be aimed at the elimination of the low speed streaks by filling it in with high momentum fluid, or by directly suppressing the lift-up of a streak. It is the second method of control which is primarily investigated here.

Active control implies both the ability to detect the local production of turbulence, or the presence of a burst (lift-up of the low speed streak), and the ability to intervene physically to cancel or reduce it. Since the active control of the bursting process is of interest, the influence of local, control type disturbances on the bursting process must be established. As a first step in this process, the effects of possible control disturbances on the bursting process must be established when these disturbances are introduced in a non-active role.

Lumley (1988) suggested that streamwise vorticity might be introduced into the buffer region and sublayer in an active role to cancel or weaken the Reynolds stress producing events in the buffer region. By canceling or controlling the lift up of the near wall streaks, n

an active manner, turbulence production may be reduced. The generation of a pair of counter-rotating vortices will introduce a small scale disturbance which will also modify the counter-rotating vortex rolls produced by Lumley's proper orthogonal decomposition and the dynamical systems modeling approach of Aubry et al. (1988). Bloch and Marsden (1989) speculate that the dynamics of the near wall region can be favorably controlled by modifying the form of the mean flow eigenfunctions which directly feed into these turbulence models.

The objective of this investigation is to study, in detail, the effect of a controlled disturbance on the near wall region of a turbulent boundary layer, when it is introduced in a local, non-active manner. The control scheme investigated here involves the local generation of a pair of counter-rotating streamwise vortices into the near wall region, $y^+ < 20$, of a turbulent pipe flow. The vortices are created by a small wall-mounted bump and are generated to produce a rotation which induces a wall directed flux of fluid between them. In addition, the blockage of the near wall flow by the bump should produce a wall directed flow downstream as the near wall flow is forced around and over the bump. This induced motion towards the wall may act to either locally cancel a low speed sublayer streak or to prevent the lift-up of a low speed streak into the buffer region. In an active scheme, a lifting streak would be sensed and the vortices would be locally generated over a short instance of time to suppress the bursting event. Figure 1.3 illustrates the proposed control scheme.

Multi-component, one and two-point laser Doppler velocity measurements detailing the region downstream of the bump are presented. All measurements are made in the glycerin tunnel at the Applied Research Laboratory, The Pennsylvania State University. Because of the high viscosity of the glycerin, spatial and temporal scales are large affording excellent resolution. In addition, detailed three component velocity measurements will be made in the undisturbed glycerin tunnel. The unique glycerin tunnel facility together with the

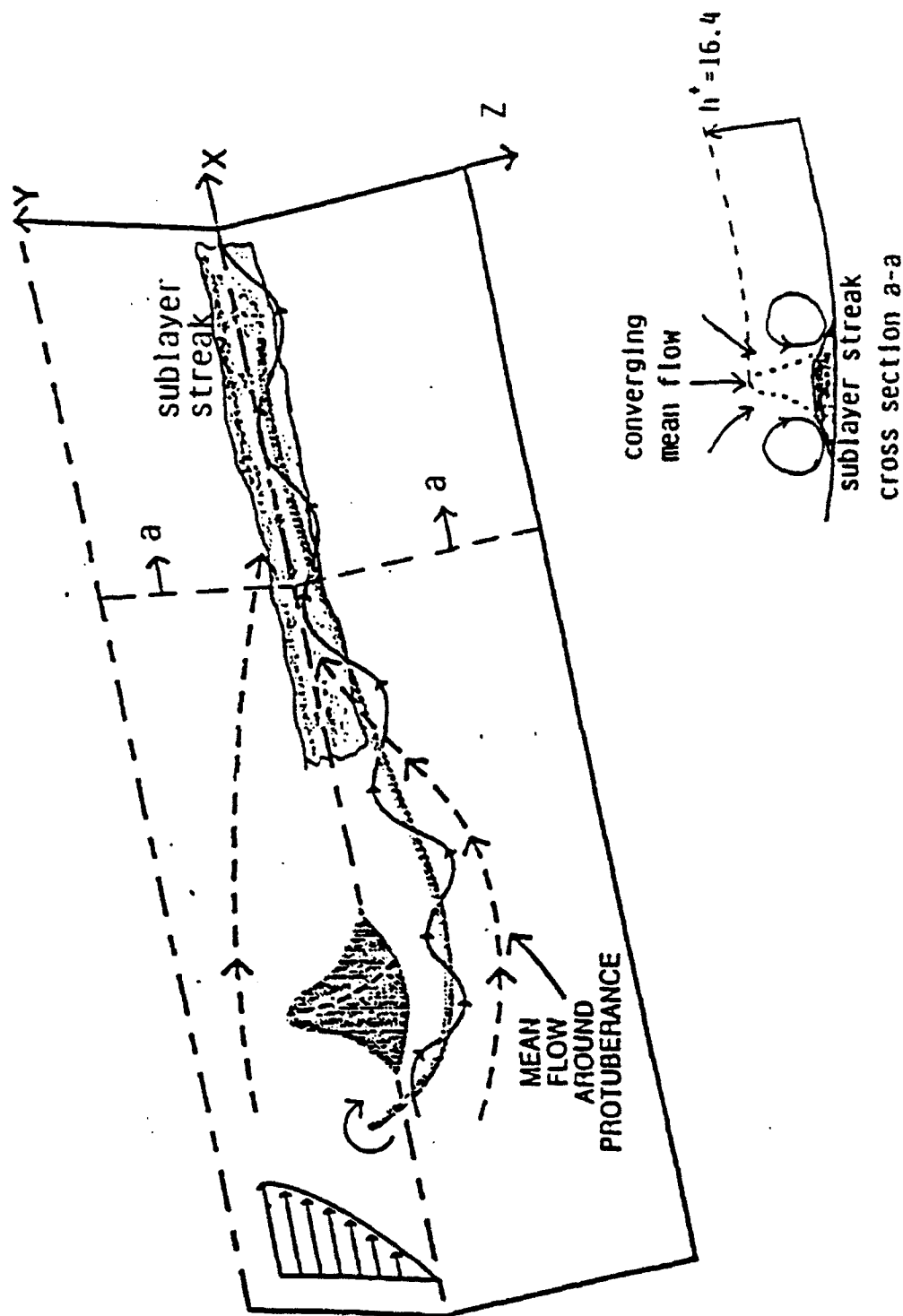


Figure 1.3 Illustration of the proposed burst suppression scheme

advanced measurement systems enables the compilation of an extensive velocity data base.

These detailed measurements combined with the measurements obtained in the modified boundary layer should provide an impressive and much needed velocity data base for use in validation of numerical turbulent boundary layer codes.

Chapter 2

EXPERIMENTAL APPARATUS AND INSTRUMENTATION

2.1 Facility

The experiments are conducted in the glycerin tunnel of the Applied Research Laboratory of The Pennsylvania State University. The tunnel, shown in Figure 2.1, is a closed loop pipe flow which uses a 96%/4% glycerin/water solution. The use of glycerin permits exceptional access to the near wall region of the turbulent pipe flow. The upper leg of the tunnel is a cylindrical pipe 285 mm in diameter and 7.6 m long. Turbulence management is achieved by a cylindrical settling chamber fitted with honeycomb and screens. A 16:1 contraction section couples the settling chamber with the test pipe. Boundary layer transition is fixed at the entrance to the test pipe by a 10 mm high serrated trip ring. The tunnel is operated by a 75 KW constant speed centrifugal pump, located in the bottom leg of the facility. A detailed description of the facility is provided by Bakewell (1966) and Chevrin (1988).

Midway through this investigation, the original honeycomb section was destroyed during an attempt to run the tunnel at laminar flow conditions. The original honeycomb section was not replaced with an identical section because its large size would make it prohibitively expensive. As a result, a new honeycomb section was installed upstream of the settling chamber. The new section is a 152.4 mm thick welded stainless steel honeycomb with a 9.5 mm cell size. The honeycomb is banded by a 1.6 mm thick by 203 mm wide stainless steel sheet, spot welded to the honeycomb cell walls. These dimensions were selected to match the pressure drop characteristics of the original honeycomb. Pressure drop measurements across the new honeycomb section confirm that an excellent match is obtained.

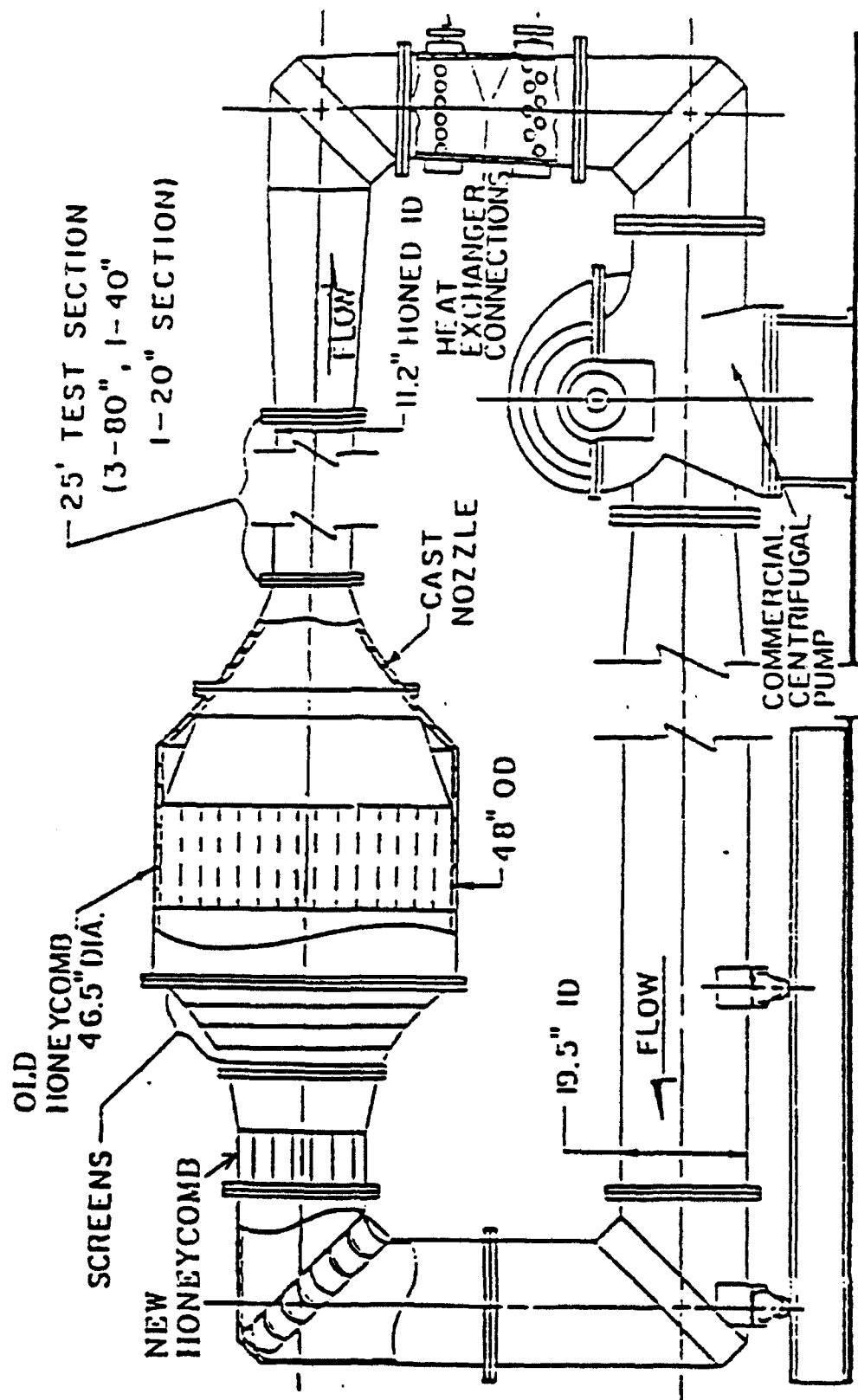


Figure 2.1 Glycerin tunnel facility

The location of the new honeycomb section is also shown in Figure 2.1.

The test section is an acrylic pipe 500 mm long located 7.1 m from the pipe entrance. The close match in the index of refraction of glycerin, 1.465, with that of acrylic, 1.49, is exploited to nearly eliminate the lens effects produced by the curved surfaces of the test section. This is accomplished by encasing the cylindrical test section in an acrylic box filled with glycerin. Excellent optical access is provided along the four sides of the test section.

As a result of the constant speed pump, the mean flow Reynolds number, Re_D , is adjusted by controlling the value of the strongly temperature dependent viscosity of the glycerin. The dependence of the glycerin viscosity on temperature is shown in Figure 2.2, as measured by the Cannon Instrument Company (Boalsburg, PA). The tunnel is fitted with a counter flow heat exchanger to maintain control of the tunnel temperature and thus the value of the glycerin viscosity. The temperature is adjusted by controlling the flow rate of cooling water through the unit. The cooling water is supplied by an outside water main connected to the University water supply. As a result, the temperature and pressure of the cooling water supply fluctuate with the changing outdoor conditions and supply needs of the University. This restricts the minimum operating temperature that can be set and maintained year round. The glycerin temperature is monitored by a thermistor approximately 0.6 m downstream of the test section.

All measurements are conducted at a glycerin temperature of 34.5°C which results in a fully developed pipe flow at an $Re_D = 10,110 \pm 500$ and a bulk velocity of approximately 6.6 m/s. This temperature assured good control year round and provided glycerin properties close to those used in the investigation of Chevrin (1988). Relevant properties of the glycerin as well as the tunnel operating conditions at 34.5°C are listed in Table 2.1. The uncertainty in Re_D is due to a 5% uncertainty in the value of the viscosity due to a temperature

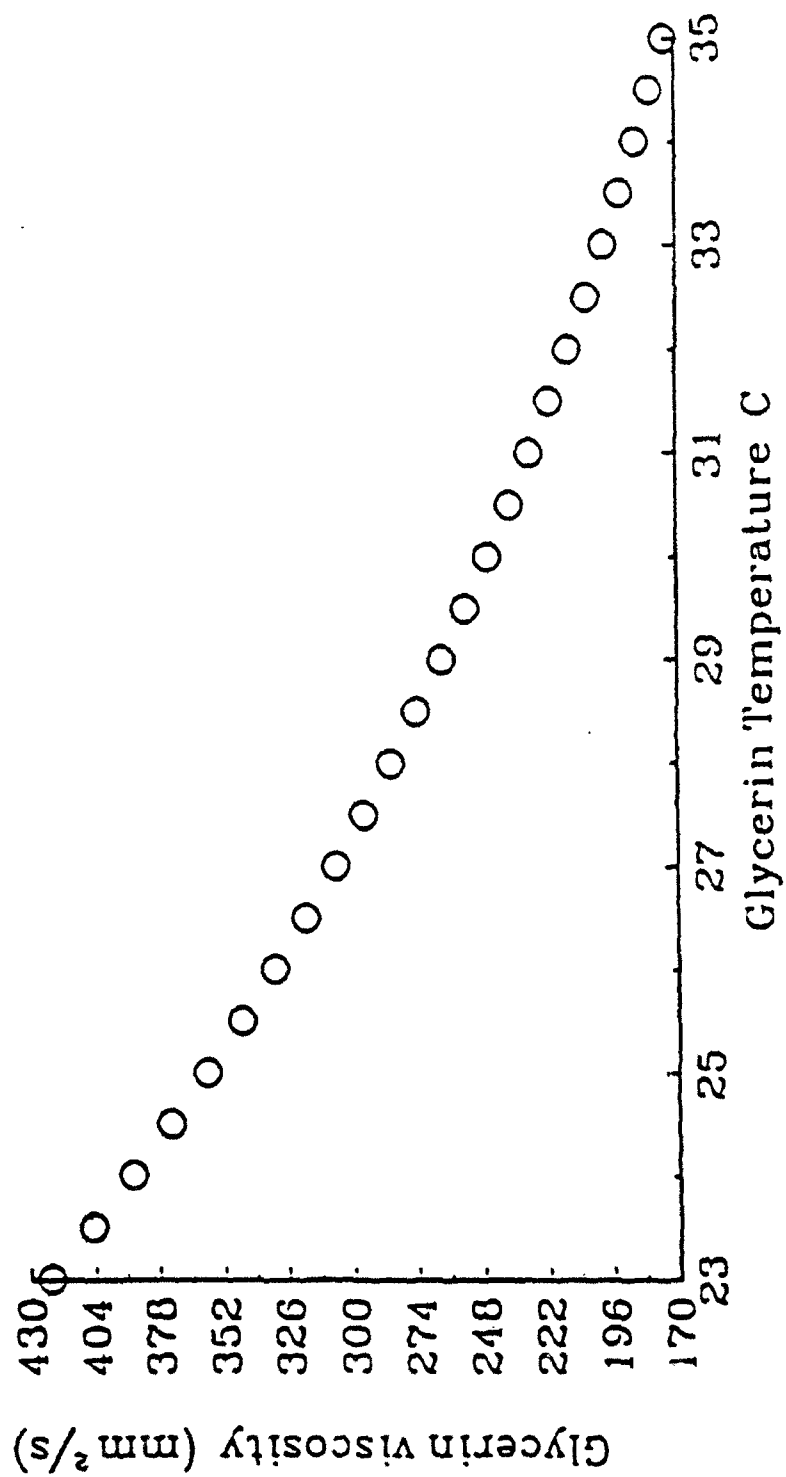


Figure 2.2 Temperature dependence of glycerin kinematic viscosity

Table 2.1 Glycerin Properties and Tunnel Operating Conditions at 34.5° C

$$\nu = 186 \text{ E-6 m}^2/\text{s}$$

$$n = 1.465$$

$$\rho = 1242 \text{ kg/m}^3$$

$$\text{Re}_D \approx 10110$$

$$\text{Re}_t \approx 730$$

$$\text{Re}_s \approx 613$$

$$U_b = 6.6 \text{ m/s}$$

$$U^* = 0.4 \text{ m/s}$$

$$1y^* \approx 0.465 \text{ mm}$$

$$1f^* \approx 860 \text{ Hz}$$

uncertainty. All uncertainties are estimated to 95% confidence levels by the methods presented in Coleman and Steele (1989) or by Student-T tests.

The high viscosity of glycerin, approximately 186 times that of water, provides a larger viscous sublayer than that found in conventional facilities using air or water. Viscous length and time scales are approximately 0.465 mm and 1.16 ms (860 Hz) respectively, which provides the opportunity for excellent spatial and temporal resolution.

The near wall region of the turbulent boundary layer is perturbed by a bump mounted on the wall of the test section. Throughout the remainder of the manuscript, the phrase turbulent boundary layer will be used interchangeably with turbulent pipe flow. The shape of the bump is given by the joint normal probability distribution:

$$y^+ = 16.43 \exp\left(-\frac{(x^+)^2 + (z^+)^2}{10.45}\right) \quad 2.1$$

The bump is 16.43 wall units high by 13 wall units wide at its base and is located 290 wall units (135 mm) from the upstream edge of the box enclosing the test section. Throughout the manuscript, the undisturbed pipe flow conditions are used to normalize in wall units unless otherwise noted. The bump shape is illustrated in Figure 2.3.

Lumley (1988) suggested a joint normal shape based on the premise that an elastic membrane would take a shape similar to this when deflected by a force applied at a point. He speculated that such bumps could be incorporated into a control scheme. The bump height is selected to produce a junction vortex approximately 15 wall units in diameter. To prevent Strouhal type shedding, the bump diameter must decrease with increasing distance from the wall so that the decreasing diameter maintains a local Reynolds number below a critical value for shedding. The local bump Reynolds number, Re_b , is based on the local bump diameter and local velocity. White (1974) indicates that the critical Re_b for Strouhal shedding is

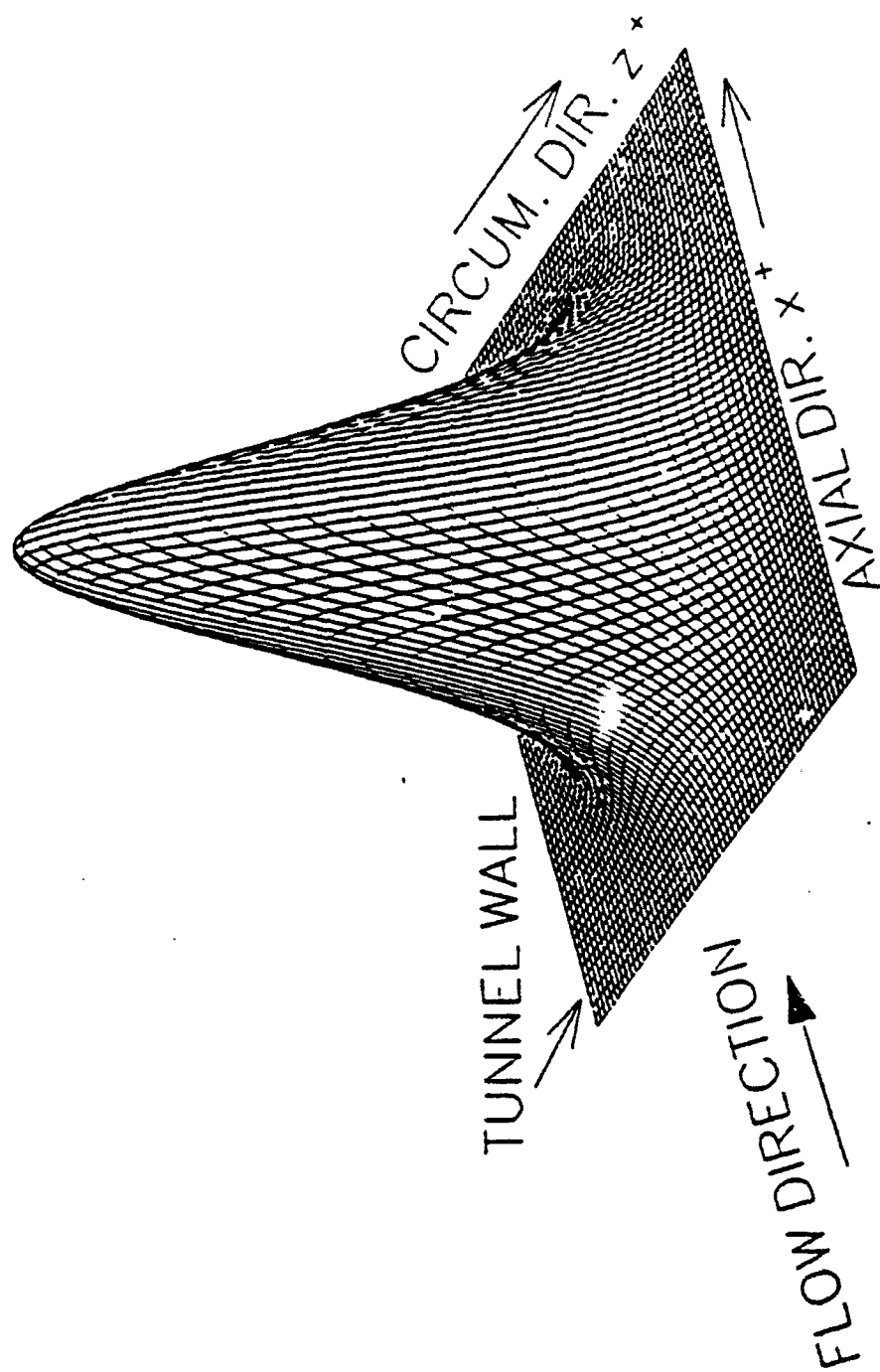


Figure 2.3 Illustration of the wall-mounted bump

approximately 50. At the operating conditions used during this investigation, the bump produces a maximum Reynolds number $Re_d \approx 36$ at $y^* \approx 8$. The value of Re_d decreases to approximately 20 near the top of the bump. Additionally, the top of the bump should be narrow to minimize shear layer growth and shedding along the top. The present shape satisfies these conditions.

A view of the test section and the location of the bump is provided in Figure 2.4a. The shaded cross sectional view a-a, appearing in Figure 2.4a, is shown in Figure 2.4b. The coordinate system used throughout the investigation is a cylindrical coordinate system. All measurements are referenced from a measurement coordinate system centered on the bump at the wall. The measurement coordinate axes and the origin are shown in Figure 2.4a and b. The following notation is adopted throughout the rest of the manuscript. The radial coordinate is denoted by y , where y is the radial displacement measured from the wall towards the pipe centerline. In this notation the radial coordinate y is defined by $y = R - r$. The circumferential coordinate is denoted as z , which is defined as the circumferential displacement along the pipe wall. This coordinate is defined by $z = R\theta$. The axial coordinate, x , is measured from the center of the bump along the pipe axis. The positive directions of all three coordinates are shown in Figure 2.4a and b.

2.2 The Laser Doppler Velocimeter

Fringe mode laser Doppler velocimetry (LDV) is used to probe the near wall velocity field in the glycerin tunnel. The measurements include single-point, three-component, coincident and two-point, three- or four-component, coincident velocity measurements. The multi-component LDV consists of a standard TSI two-component system and a TSI fiber-optic system. Both systems use a single five watt Spectra-Physics argon-ion laser. The two LDV

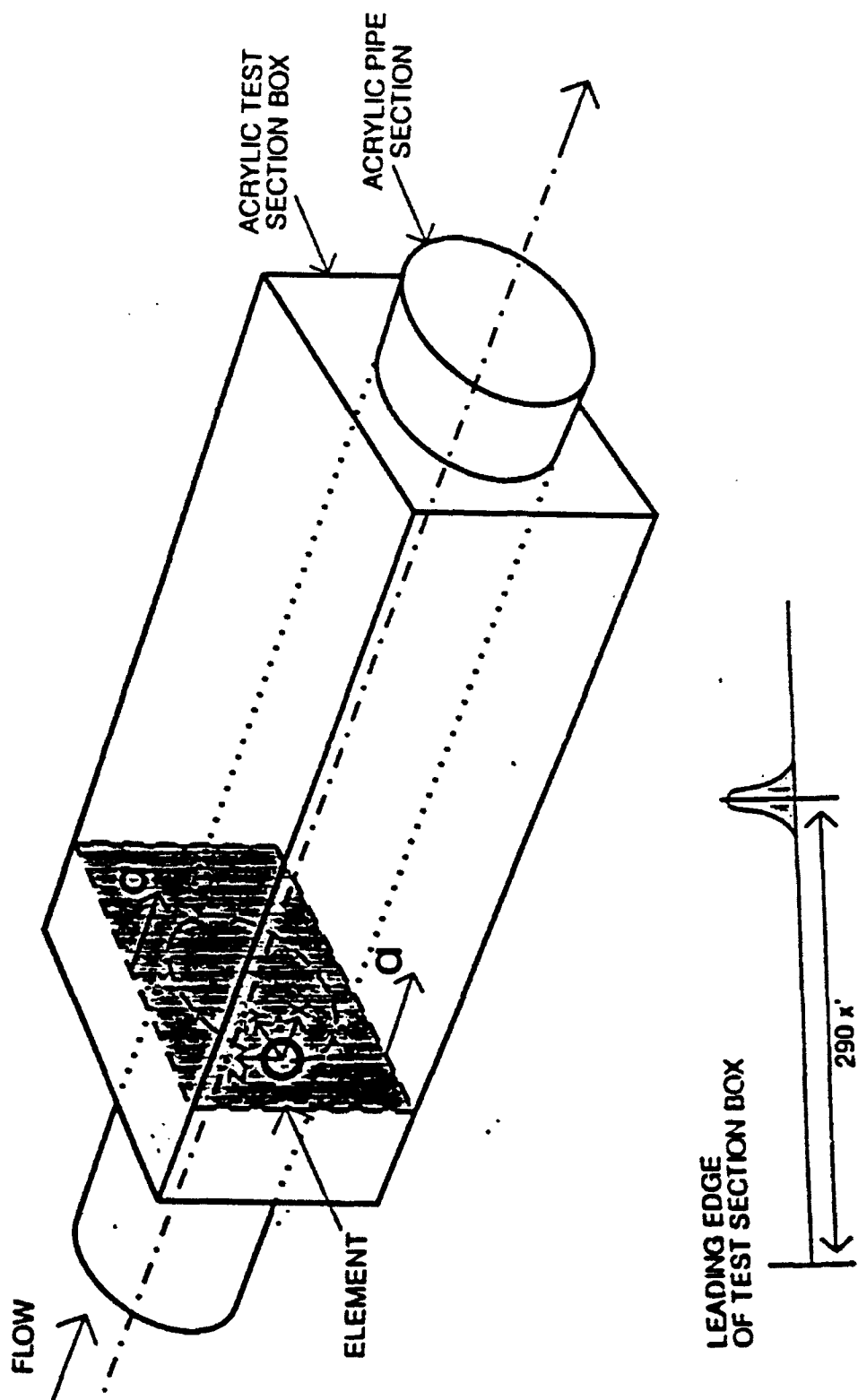


Figure 2.4 Illustration of glycerin tunnel test section a) showing location of bump and measurement coordinate system

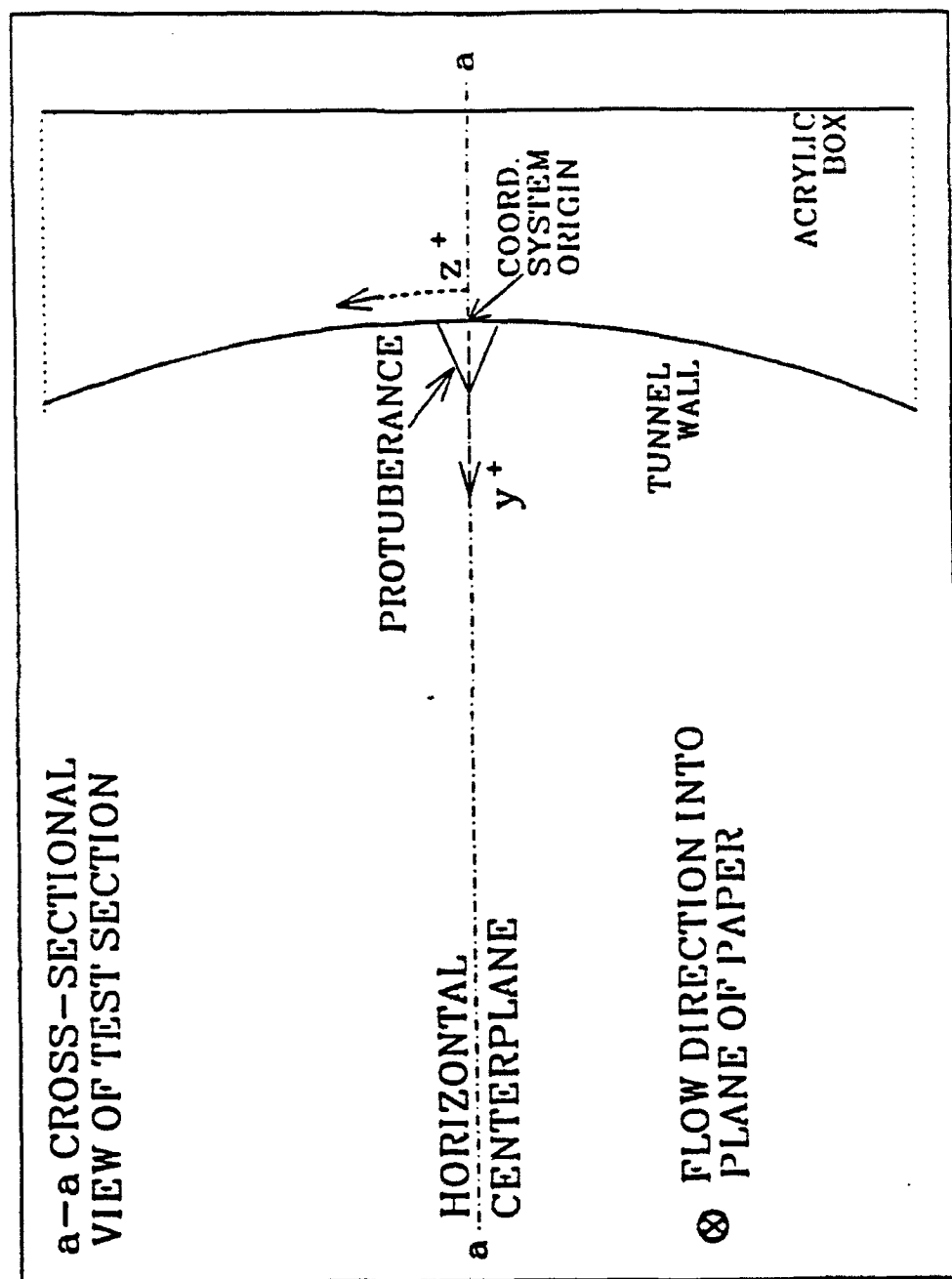


Figure 2.4(cont.) b) Cross-sectional view a-a

systems are operated in the forward scatter mode resulting in clean Doppler signals with an excellent signal to noise ratio.

The standard TSI two-component system, referred to hereafter as the primary LDV, is a three-color TSI Colorburst system capable of using the violet, blue and green lines (476.5 nm, 488 nm and 514.5 nm wavelengths respectively) of the five watt argon-ion laser. Throughout this investigation, the primary LDV used the blue 488 nm and green 514.5 nm wavelength lines. Conventional TSI two-component transmitting optics, including a 3.75x beam expander to improve spatial resolution, are used to transmit the two pairs of beams. A 459 mm focal length lens is used, resulting in a measured beam half angle of 7.93° for each pair of beams. This produces probe volume diameters and lengths in the glycerin of approximately $80\text{ }\mu\text{m}$ and $820\text{ }\mu\text{m}$, respectively, to the e^2 intensity level. These diameters and lengths are approximately 0.17 and 1.8 viscous units respectively.

The orientation of the LDV systems with the test section is illustrated in Figure 2.5. The 514.5 nm wavelength beams are aligned along the horizontal centerplane of the tunnel and measure the axial velocity component U. The 488 nm wavelength pair of beams are oriented in the vertical plane, perpendicular to the green beams, and measure the circumferential component of velocity W. One laser beam in each component is effectively frequency shifted at 2 MHz and 5 MHz for the 514.5 nm and the 488 nm wavelength beams respectively. Excellent spatial coincidence between the blue and green probe volumes is achieved with the beam alignment system of the Colorburst, and the quality windows of the test section.

The fiber-optic system uses a standard 25 mm diameter TSI two-component fiber-optic probe and coupler system. Only one component of the probe is used in the single-point three-component measurements while both components are used for the two-point,

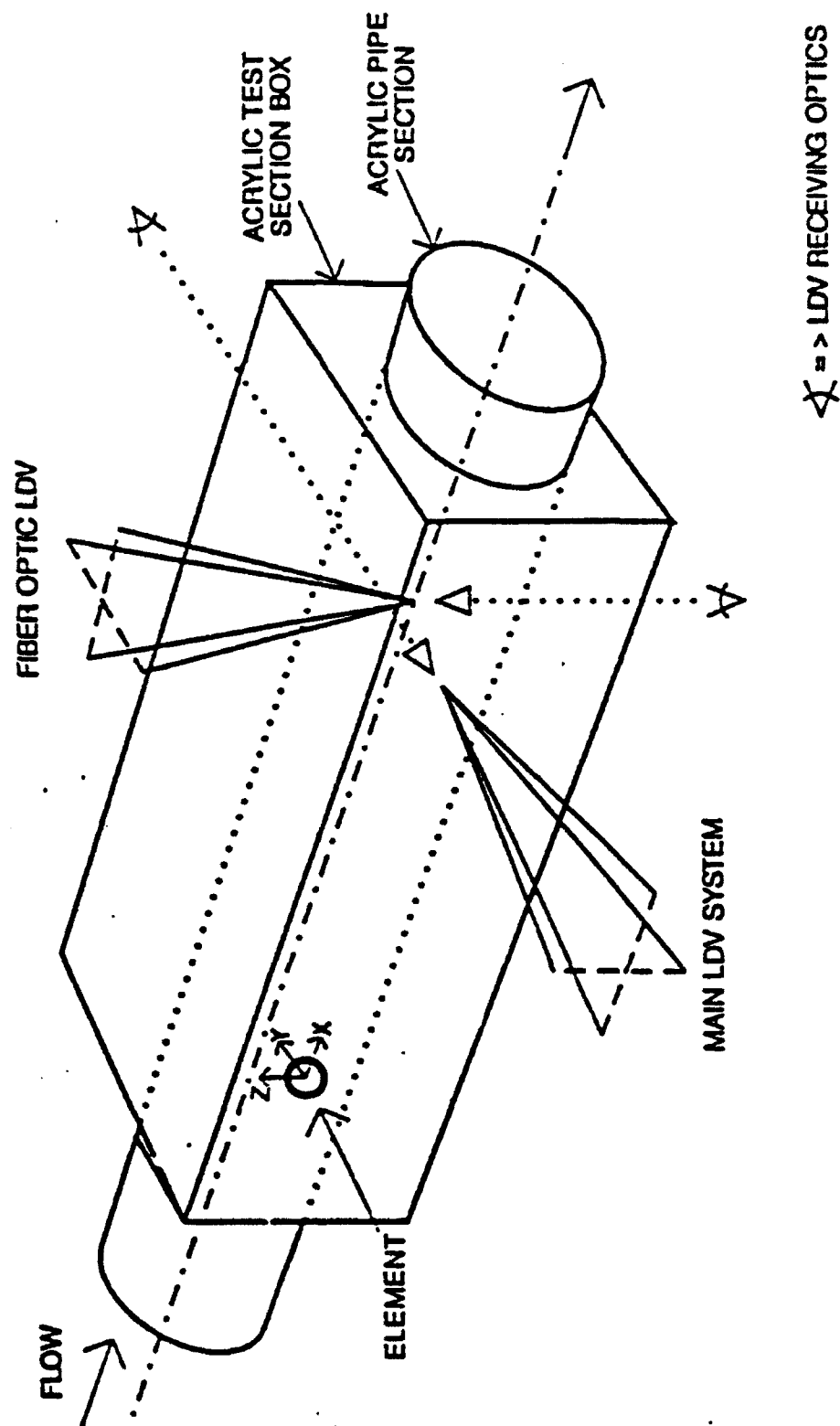


Figure 2.5 Orientation of the LDV systems at the test section

multi-component measurements. The fiber-optic probe is mounted such that its transmitting axis is perpendicular to the transmitting axis of the primary LDV. Thus the violet beams are aligned parallel with the radial (y) - circumferential (z) plane and measure the radial velocity component, V . An effective frequency shift of 5 MHz is applied to one of the violet beams. The probe comes with a 142 mm focal length lens which provides a 3° half angle. This produces a probe volume with a $95\text{ }\mu\text{m}$ diameter and a 2.7 mm length in the glycerin or approximately 0.2 and 6 wall units respectively.

The focusing optics for the two-component probe are factory set for the 488 nm and 514.5 nm wavelengths and this may lead to some eventual problems. The wavelength dependence is due to gradient index lenses which are needed to collimate the laser beams exiting the optical fibers. In the single-point measurements, the violet 476.5 nm wavelength beams exiting the Colorburst are coupled with the 488 nm component optical fibers of the fiber probe. Significant problems with beam collimation of the violet beams was not expected since the violet 476.5 nm and blue 488 nm wavelengths are reasonably close. In reality, it is almost impossible to obtain perfect collimation with any standard, readily available LDV system. Uncollimated laser beams cause an increase in velocity rms due to non-uniform fringe spacing along the probe volume length. This effect increases as the collimation of the laser beams becomes increasingly worse. However, the LDV signals and measured data appear remarkably clean in the current experiment. This indicates that the effect of imperfect collimation of the violet laser beams may not be a problem.

For the two-point measurements, a green 514.5 nm wavelength pair of beams are coupled to the second 514.5 nm component of the fiber-optic probe. The second pair of green beams are produced by splitting, using a 50/50 beam splitting cube, the multi-line laser beam exiting the laser before it enters the Colorburst. The split laser beam is transmitted

through a set of color separator optics to isolate the 514.5 nm wavelength line. Standard TSI transmitting optics are used to couple the green beams to the second component of the fiber-optic probe. The green pair of beams are aligned parallel to the streamwise (x) - circumferential (z) plane and measure the streamwise velocity component. An effective frequency shift of 2 MHz is applied to one of the green beams. The configuration of the radial component, discussed above, is unchanged.

Receiving optics modules are used to visually align the measurement volumes of both the primary and fiber-optic systems to approximately the same location. As a method of checking probe volume alignment between the primary and the fiber-optic systems, cross-correlation measurements of the streamwise velocity component are performed. Measured uu cross-correlations are typically greater than 98.7%, which confirms that excellent spatial coincidence between the LDV systems is obtained.

Johnson and Barlow (1989) indicate that to obtain accurate Reynolds stress measurements in densely seeded flows, LDV probe volume lengths should be less than 15 wall units. While the seeding density is not excessive in this investigation, the LDV probe volume dimensions in this facility more than meet this requirement in the undisturbed turbulent pipe flow. The seeding density will be discussed in Chapter 3. However, the length scales of the bump and the generated vortical structures in the near wall region of the modified boundary layer are the same order of magnitude as the length of the fiber-optic probe volume. As a result, some spatial averaging may occur in the fiber-optic velocity measurements. Methods are employed to attempt to reduce the effective LDV measuring volume length and thus reduce the effects of spatial averaging. These methods are discussed in Section 2.3.

The LDV transmitting and receiving optics for both systems are mounted on separate structurally sturdy bases. Each system can be traversed in three directions, independent of each other, with an uncertainty of ± 0.025 mm. In addition, the fiber-optic system can be rotated about its central axis if desired. Tilt in the x-z and y-z planes can also be achieved with the fiber system. The uncertainty in the location of the wall is approximately ± 0.22 mm, resulting in a ± 0.5 wall unit uncertainty. This estimate of the uncertainty is based on the physical dimensions of the probe volumes and is somewhat conservative. Typically, the location of wall can be determined within ± 0.15 mm. The fiber-optic traversing mechanism is limited to a 51 mm radial traverse. This results in radial velocity measurements limited to approximately $y^+ < 120$.

LDV seeding is provided by air bubbles entrapped in the glycerin. The bubble diameters were measured holographically by Chevrin (1988) and range in size from approximately 20 to 50 microns, which corresponds to 0.043 and 0.108 wall units respectively. Although the bubbles are considerably larger than the LDV fringe spacing, excellent Doppler signals are obtained. Adrian and Earley (1975) showed that good signal to noise ratios could be obtained with particles larger than the fringe spacing. Chevrin (1988) determined experimentally that the bubbles adequately follow the turbulent fluctuations because of the large viscosity of the glycerin.

The refractive index match between the acrylic pipe walls and the glycerin is sufficient to produce negligible refraction effects on the primary LDV laser beams at the curved pipe walls. This is a result of the limited measurement domain in the radial direction, the large pipe radius, and the small half angle of the primary LDV. A radial traverse of 50 mm results in a displacement error of the blue probe volume relative to the green probe volume of less than 0.2%. However, the fiber-optic system is more sensitive to the imperfect

refractive index match due to the orientation and position of the fiber-optic probe with respect to the tunnel wall. As the wall is approached, the fiber-optic laser beams pass through an increasing amount of acrylic at the cylindrical pipe wall as shown in Figure 2.6. In addition, the incidence angle ψ of each beam at the glycerin/acrylic interface and at the acrylic/glycerin interface increases. The incidence angle of each beam is different due to the curvature of the wall. This causes the laser beams to refract at different angles and effectively reduces the half angle κ between the beams in the glycerin tunnel. If the change is significant, an error in the radial velocity measurement can be introduced. It is shown in Appendix A that reducing the half angle inside the tunnel without compensating for it in the data reduction results in measured velocities which are lower than the actual velocity of the particle creating the Doppler burst. The refraction effect on the fiber-optic beams appears to be negligible for measurements above $y^+ \approx 5$.

2.3 LDV Signal Processing

Doppler signals are analyzed using TSI 1980 counter-type signal processors. The counter-processors are operated in the single measurement per burst mode, which allows one Doppler frequency measurement per validated Doppler burst. The Doppler signals are band-pass filtered to remove the signal pedestal and high and low frequency noise. An amplifier is used to amplify the incoming Doppler signal voltage into the range of the burst detector, which is ± 50 mv threshold. A Doppler burst is validated when the amplitude of the Doppler signal exceeds the threshold voltage for N consecutive zero crossings or cycles. The number of cycles, N , is a user selectable parameter, which can take one of the following values 2, 4, 8, 16, and 32. The Doppler signal must also pass a time comparator test for validation. The time comparator checks the ratio of the time to cross the first N cycles with the time to cross

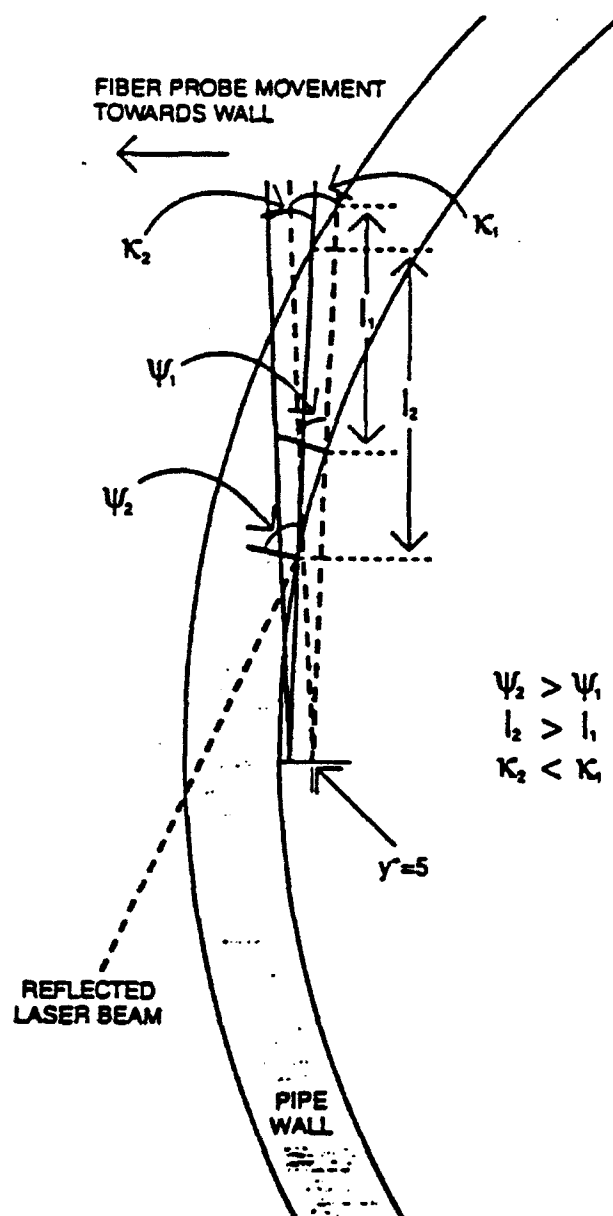


Figure 2.6 Illustration of near-wall refraction effects on the fiber-optic probe laser beams

the first $5/8 N$ cycles. The ratio must be equal to the ratio of the fringe crossings, $5/8$, within a user selected percent error for signal validation. The time comparator reduces background and phase noise.

The effective length of the LDV probe volume can be adjusted, to a certain degree, through judicious selection of the amplifier gain, the number of cycles and the percent error chosen for time comparison. In fringe mode LDV, the ellipsoidal probe volume consists of an alternating pattern of light and dark fringes aligned parallel with the long axis of the probe volume. The number of fringes peak at the center of the probe volume and decrease in number towards the ends of the probe volume. In addition, the intensity of the light fringes varies across the length of the probe volume in a Gaussian manner. The intensity is a maximum at the probe volume center and decreases towards each end of the probe volume. As a result, particles convected through the center of the probe volume cross more fringes and scatter light with a greater intensity than particles convected through the edges of the probe volume. Requiring a high number of cycles with both a low amplifier gain and a low comparator percent error effectively filters out Doppler signals from particles near the edges of the probe volume. However, operation of the counter-processor in this manner can significantly reduce data rate. A compromise is typically made between amplifier gain and number of cycles to produce low noise signals at reasonable data rates. The LDV measurements are obtained, in the current study, with the number of cycles set at 32 and the time comparator set to the lowest percentage of 1%.

Chapter 3

DATA ACQUISITION AND REDUCTION

3.1 Data Acquisition

Two methods of data acquisition of the processed LDV signal are used during this investigation. The first method, referred to as the TSI coincident mode, involves operating the LDV and counter-processors in the conventional random arrival and validation manner. The signal processor gains are restricted to maintain validated data rates for each velocity channel at approximately several thousand per second. The second method of data acquisition, referred to as the external digitization mode, involves operating the LDV and counter-processors in a saturated controlled state. This method yields significantly high data rates, on the order of ten thousand validated Doppler bursts per second. The external digitization mode provides excellent temporal resolution of the measured velocity signals.

3.1.1 TSI Coincident Mode

This method of data acquisition employs a TSI 1998a master interface module and several slave interface units. The master interface module transfers the validated Doppler frequencies in 12-bit digital form through direct memory access (DMA) to a PC-AT host computer. Slave interface units couple additional counter-processors to the master interface in multi-component systems. The master interface can accommodate up to three slave units. In addition to the Doppler frequency data, the time between coincident data points is transferred to the host computer. This information can be used to reconstruct the time velocity trace in the event of adequately high data rates.

The master interface is used in the coincident mode of operation. In this manner of operation, temporal coincidence between multiple LDV channels is required for the data to be validated and transferred to the host computer. Temporal coincidence is determined by requiring that the arrival times of validated Doppler bursts from all LDV channels fall within a specified time window, referred to as the coincidence window. The time window can be varied from 1 μs to 100 μs continuously.

The effect of coincidence window size on the processed velocity data is investigated by varying the window size from 1 μs to double the local mean velocity transit time. The results indicate that, within measurement uncertainty, there is no observable effect on the velocity statistics up to fourth order moments, including cross-correlations between velocity channels. This is a result of the excellent spatial and temporal resolution of the LDV system compared to the turbulent boundary layer viscous scales.

In general, the coincident data rate decreases as the width of the coincidence window decreases. Ideally a narrow coincidence window is desired to insure maximum coincidence between the LDV channels. However, the resulting coincident data rates would be unacceptably low in most situations. A compromise is usually made between time window width and acceptable data rates. The effect of coincidence window size on the coincident data rate intensifies as the number of LDV channels increases. The coincident data rate drops as additional channels are forced to be coincident in a fixed window.

Throughout this investigation, the size of the time window within which data are deemed coincident is set to approximately half the probe volume transit time of a particle traveling with the local mean velocity. The size of the time window is kept small to insure that the validated Doppler signals from the fiber probe come from approximately the center region of the length of the fiber optic probe volume, while maintaining reasonably high

three-component coincident data rates. Typically 10% to 20% of the data are validated as coincident for three components, compared to better than 50% for two components.

Three-component coincident data rates are typically maintained at several hundred samples per second except very close to the wall. The data rates continuously fall off as the wall is approached because of the low local velocities. Below $y^+ \approx 4$, the coincident data rates rarely exceed 100.

The maximum number of samples per channel that could be acquired is limited by the DMA transfer from the master interface to the host computer and the acquisition software. The maximum number of samples per channel is also dependent on the number of LDV channels. For three components, 6500 samples per channel are acquired and used to compute the velocity statistics. The total number of samples per channel could be increased to 9000 and 13,500 for two- and one-component data respectively.

Due to the random arrival of scattering particles in the LDV probe volume, this method of acquisition results in a random distribution of the sampling time between coincident data points. This is typically referred to as random sampling, and in the application of LDV, the times between validated samples are Poisson distributed. Short sampling times occur more frequently than long sampling times. This produces an inherent bias towards higher velocities measured by the LDV. More particles traveling at high velocities are convected through the LDV probe volume than particles traveling at low velocities over a finite acquisition time. Laser Doppler velocity bias and the effects of bias on the measured velocity statistics are addressed in detail by Edwards (1987).

3.1.2 External Digitization

The second method of data acquisition involves externally digitizing the transit time output from the TSI 1988 analog output modules. The analog output modules are 12-bit sample and hold D-A converters providing a 0 to 10 volt signal on the time output connector which is proportional to the transit time for N cycles. The output signals from the analog output devices are digitized at a constant sampling rate through an external 12-bit simultaneous transfer A-D converter. In this method of acquisition, the LDV and counter-processors are operated as a saturated controlled system and the resulting Doppler signal is treated as though it is a continuous signal similar to that of a hot-wire anemometer.

External digitization offers advantages over the conventional Poisson distributed, random sampling TSI coincident mode. Conventional, readily available data processing procedures can be used to process the acquired data. Time between data point information is no longer needed which frees up computer memory allowing the acquisition of additional samples per channel. In addition, Edwards (1987) indicates that constant rate sampling can eliminate velocity bias provided certain criteria are met. These criteria will be discussed in the following paragraphs.

A controlled LDV processor is a free running processor with restricted data transfer and acquisition. The arrival of valid Doppler bursts exceeds the rate at which the processed doppler signals are digitized and recorded. As a result, there is a new velocity measurement available every time the acquisition system is ready to record data, while several consecutive doppler bursts are validated but are not recorded during the acquisition dead time. A controlled processor acquires and records velocity data at constant sampling rates. The present system is referred to as a saturated controlled processor because the valid data rates on each counter-processor are nearly as high as the seeding density in the tunnel will allow.

The operation of the LDV and counter-processors in the saturated controlled mode involves increasing amplifier gains to obtain the highest valid data rate the seeding density allows without compromising the quality of the Doppler signal. The seeding density is the average number of scattering particles per unit volume. Typically, the higher the seeding density the higher the data rates. An ideal data rate would occur if at any instant of time only one particle is present in the LDV probe volume and as that particle exits the probe volume another particle enters. This corresponds to a burst density equal to one, which is defined as the average number of particles in the probe volume at any instant of time. For a fixed probe volume diameter, the measured data rates are proportional to the local velocity. The velocities measured in the glycerin tunnel range from about 0.5 m/s to about 8 m/s. This corresponds to a range of data rates from approximately 6000 to over 80,000 bursts per second. The maximum data rates that are obtained during this investigation, without compromising signal to noise ratio, range from approximately 2000 bursts per second at $y^+ \approx 3$ to greater than 10,000 bursts per second for $y^+ > 7$. These low data rates and the observed Doppler signal on an oscilloscope indicate that the burst density is less than one. Multiple particles in the probe volume increase signal noise; therefore, a low burst density is desirable.

Edwards (1987) indicates that unbiased velocity measurements can be obtained with the controlled processor as long as the data density is greater than five. He defines the data density as the ratio of the valid data rate processed by the counter to the data acquisition sample rate. Additionally, the inverse of the data acquisition sampling rate must be smaller than the Taylor time microscale of the flow. An estimate of the time microscale is obtained from a few measured auto-correlations of the streamwise velocity in the near wall region. The time microscale is approximately 8 to 10 ms. At the lowest data rates obtained,

approximately 2000, an acquisition rate of 400 Hz still satisfies the above constraints.

However, Winter et al. (1991) indicates the condition on the microscale is overly restrictive for sample and hold type of counter-processors, and that the integral time scale is a more appropriate time scale for governing the sample rate.

The data density defined above is based on the average valid data rate processed by the counters. This is somewhat misleading since the actual data rate randomly fluctuates around the mean with a higher probability for higher data rates, due to the random arrival of particles in the LDV probe volume. Significantly lower data rates than the mean data rate occasionally occur. As a result, LDV signal dropout can still occur even though the data density is high, that is greater than five. Dropout occurs when the time between the arrival of two consecutive valid Doppler bursts exceeds the sampling period. In this instance, data is acquired from the counters when no new data is present. Too many dropouts or dropouts which are too long can bias the calculated statistics. Adrian and Yao (1987) indicate that the effect of dropouts on velocity spectra consists of a white step noise and an effective low pass filtering of the velocity signals. The TSI analog output module sample and hold D-A converter holds the voltage output at the level of the last validated burst until a new burst is validated. In this case, a dropout appears as two or more consecutive velocity samples that are equal. Edwards and Jensen (1983) and Edwards (1987) indicate that the sample and hold operation of the D-A circuit will mitigate dropout effect to a certain degree, provided the dropout lengths are on the order of the sampling period.

The effects of varying data density on the number and length of dropouts and on the calculated velocity statistics are evaluated in the glycerin tunnel. Comparisons are made between three-component single-point measurements obtained from the TSI interfaces and the same data digitized from the analog output modules. The number and length of the dropouts

increases as the data density decreases. In the current experiment, the velocity statistics are unaffected when the dropout percentage compared to the total sample size is below 5%. Furthermore, the dropout percentage is less than 2% and more the 95% of the dropouts are of one sample period duration when counter data rates are approximately five times the A-D sample rate.

Based on these results, it is possible to obtain unbiased, temporally resolved velocity data by the external digitization method of data acquisition. Except very close to the wall, $y^+ < 7$, sufficiently high data rates are obtained on each counter-processor to allow data acquisition at sampling rates high enough to resolve the smallest time scales of the turbulent boundary layer. Data acquisition sampling rates are reduced below $y^+ \approx 7$ due to the reduced data rates on the counter-processors and the constraint on the data density, which must be greater than five.

A Metrabyte DAS-20 A-D converter and SSH-4 simultaneous transfer module are used to simultaneously sample up to four velocity channels. The Metrabyte A-D converter is a PC compatible plug-in computer card. The DAS-20 is a 12-bit, 8 channel differential or 16 channel single-ended input A-D converter. The software selectable input voltage range is variable from ± 50 mv to ± 10 volts bipolar and 0 - 100 mv to 0 - 10 volts unipolar. The A-D converter simultaneously samples all 4 channels with a skew time of less than 40 ns between consecutive channels. Streamer acquisition software, commercially available through Metrabyte, is used to control the A-D converter card.

The output signals from the analog output modules are filtered through anti-alias low-pass filters before digitization by the A-D converter. The anti-alias filters are fabricated in house to provide specific filter characteristics. The filters are four-pole Butterworth digital filters in series with a one-pole RC filter, resulting in an equivalent five-pole anti-aliasing

Butterworth filter. The filters have a measured DC offset of less than two microvolts and an amplifier gain of one. Precision electrical components are used to provide negligible temperature drift. A zero phase shift between the four filter channels is measured over a frequency range from 0 to 800 Hz. Due to time and cost constraints in the manufacture of the filters, a limited number of cut-off frequencies are available. The selectable cutoff frequencies are 250, 500, and 800 Hz.

All components (counters, filters, A-D converter and computer) are carefully grounded to prevent ground loops or ground voltage drift. Cables and filters are all electrically shielded to prevent spurious voltages. The careful attention to electronic setup, and the tight filter and A-D converter specifications are necessary to insure that the output voltage from the analog output devices is not contaminated by zero drift or amplifier gain.

The A-D converter is used in the differential mode with a unipolar input range of 0 to 10 volts. Built-in amplifier gains are set and calibrated to one and a negligible zero offset voltage is confirmed. The sampling rate is selected based on the maximum data rates that can be obtained on each LDV channel. This ranges from approximately 400 Hz to 1700 Hz depending on the position in the boundary layer. Typically, the digitization rate is 1700 Hz for $y^+ > 7$ and decreases proportionally as the wall is approached. Fifty-one thousand two-hundred samples per channel are acquired over a range of sampling times from 30.12 seconds at 1700 Hz to 128 seconds at 400 Hz. This corresponds to acquiring data over a period of approximately 800 to 3000 integral time scales respectively. Only the first 50,000 samples are used for data reduction.

Excellent temporal resolution and bias free velocity measurements are the major advantage of this method of LDV data acquisition. It also allows the acquisition of a large number of ensembles over many integral time scales. The major disadvantage is that larger

amplifier gains are required. As was discussed earlier, increasing the amplifier gains effectively increases the length of the LDV probe volumes. This is particularly important with the fiber-optic probe volume because the length is of the same order of magnitude as the perturbation scales in the disturbed near wall region. The higher gains amplify the Doppler signals from particles convected through the probe volume edges. These are particles which would have probably been rejected at lower gains. This results in a slight decrease in the spatial resolution of the fiber-optic probe. The effect on the measured velocity data is discussed in the results sections.

3.2 Data Reduction

Data reduction includes the estimation of long time-averaged velocity statistics up to fourth order including cross-correlations between velocity channels. All data reduction is performed on the host PC computer. The data reduction routines developed by Chevrin (1988) are used in this investigation with some minor modifications. The routines are modified to increase processing speed and sample size per channel, to compute additional triple correlations and to display the values of the principal stresses. The same processing routines are used for both the TSI coincident mode data and the external digitization mode data. Digital one-dimensional histogram and two-dimensional elliptical filtering are applied to the TSI coincident mode LDV data before computing the statistics. Baldwin (1990) provides a detailed discussion of the LDV post acquisition filtering techniques. Typically less than 0.2% of the sampled data are filtered. Digital filtering of the externally digitized LDV data is unnecessary as this data is remarkably clean of noise.

Because the LDV support table traverses in a rectangular coordinate system while the measurement coordinate system inside the pipe is cylindrical, a rotation of the V-W

measurement probe volumes about an axis parallel to the pipe axis occurs with spanwise displacement. As a result, the off-center plane V and W measurements must be corrected for the angular rotation. The axial, U, component of velocity is not affected. The corrections can only be applied to multi-component measurements involving both the V and W velocity components at a single point. The analysis and equations for these corrections are provided in Appendix B. The reduced data is then saved on storage media for later processing and plotting.

3.3 Post Processing

3.3.1 Velocity Statistics

Velocity statistics are computed immediately after the data is acquired. These include mean, variance, skewness, kurtosis and cross correlation estimates of the measured velocity data. The operator can examine these quantities on line, provide digital filtering and decide whether the sampled data are acceptable. The TSI interfaces occasionally transfer high frequency noise as data through the DMA. This noise typically resembles very high, physically unrealistic, velocity samples in the data record. This results in abnormally high skewness and kurtosis values. The operator can either filter this noise or decide to retake the data in the case of excessively large numbers of noise samples. As stated in chapter 2, the uncertainties in the calculated statistics are estimated to 95% confidence levels by the methods presented in Coleman and Steele (1989) or by Student-T tests. A velocity inverse correction for velocity bias, similar to that used by Petrie et al. (1988), is applied to the TSI coincidence mode LDV data before processing.

3.3.2 Wall Shear Stress Estimates

The local wall shear stress, τ_w , is estimated from the definition of the local friction velocity, $u^* = \tau_w / \rho$. The friction velocity is computed by least squares fitting the velocity data in the viscous sublayer to a straight line. On average, about ten velocity/position data pairs are used to compute the linear estimate. The uncertainty in estimating u^* is less than $\pm 3\%$. Figure 3.1 illustrates typical linear least squares best fit estimates to the velocity profile data in the viscous sublayer. Both undisturbed and modified boundary layer data are shown in Figure 3.1. The intercept from the least squares fit provides an estimate of the radial offset of the LDV probe volume from the wall. An offset occurs because the location of the wall, $y = 0$, cannot be determined exactly. Typically the offsets, obtained by the least squares estimate, are less than ± 0.15 mm or approximately 36% of the primary LDV probe volume length.

3.3.3 Time Between Bursts Estimates

Time between turbulent boundary layer bursts is calculated from the externally digitized velocity data using the ejection time filter technique developed by Luchik and Tiederman (1987). The time resolved velocity fluctuation data are conditionally filtered to isolate quadrant two, negative u and positive v fluctuations, using the quadrant technique of Lu and Willmarth (1973). In the quadrant technique, velocity data which also satisfy the threshold condition of

$$|uv| \geq k u' v' \quad 3.2$$

are grouped for later processing. An ejection is defined by Luchik and Tiederman (1987) as an event satisfying equation 3.2. The time between consecutive ejections, t_e , is determined and stored for later processing. The value of the threshold, k , is selected as one in the

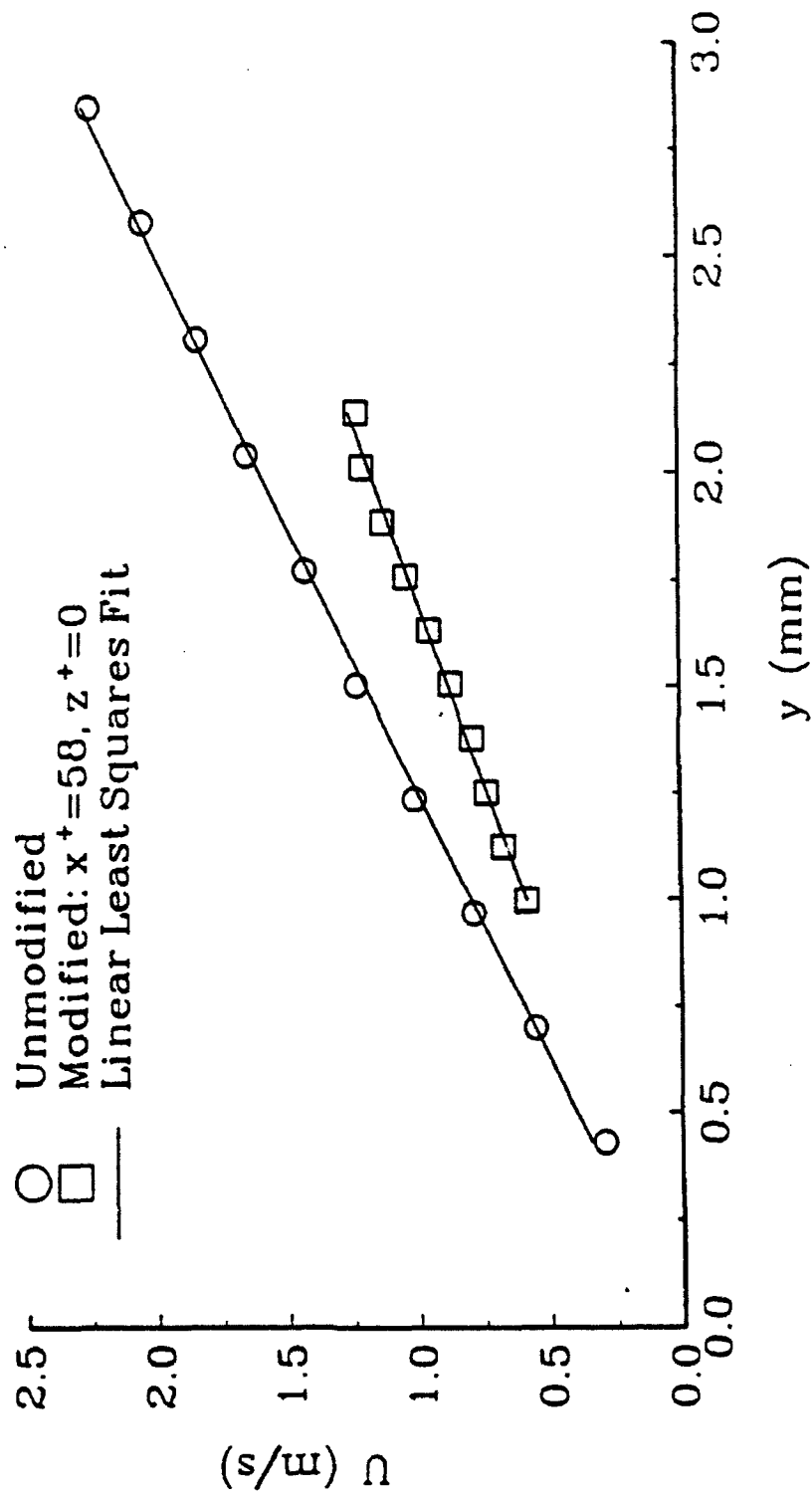


Figure 3.1 Representative examples of the linear least squares fit to the velocity profiles in the viscous sublayer

current investigation, as suggested by Comte-Bellot et al. (1978). The threshold, k , can have a significant effect on the estimated time between ejections and the bursting rate. A sensitivity study on the threshold parameter, similar to that suggested by Luchik and Tiederman (1987), indicates that for the current measurements the burst rate is independent of k for values ranging from 0.55 to 1.15.

Bogard and Tiederman (1987) have shown that the bursting process involves two to three ejections per burst on average. As a result, the average time between ejections obtained from the t_e ensembles is a low estimate of the mean time between bursts. It was observed by these authors that the probability histograms of t_e were nearly bimodal, and that in a semi-logarithmic plot the probability distribution $P(t_e > t)$ could be represented by two straight lines with an overlapping region. Each linear region corresponded to one of the modes in the bimodal histogram. Luchik and Tiederman (1987) showed that the linear region at short times corresponded to ejections from the same bursts while the distribution at longer times corresponded to ejections from two consecutive bursts. An ejection filtering time was obtained by selecting a time corresponding to the intersection of the two lines in the semi-logarithmic plot of $P(t_e > t)$. The reader is referred to Luchik and Tiederman (1987) for a more detailed discussion of the filtering time procedure. Figure 3.2 shows a typical plot of this probability distribution obtained from the present data. The time which corresponds to the intersection of the straight lines in figure 3.2 is the ejection filter time τ_e . The velocity is then conditionally filtered again with the constraint that the time between valid bursts, t_e , must be greater than τ_e . Consecutive events occurring with a shorter t_e compared to τ_e are considered ejections from the same burst and neglected. The ensemble average of the t_e estimates provides the mean time between bursts T_b .

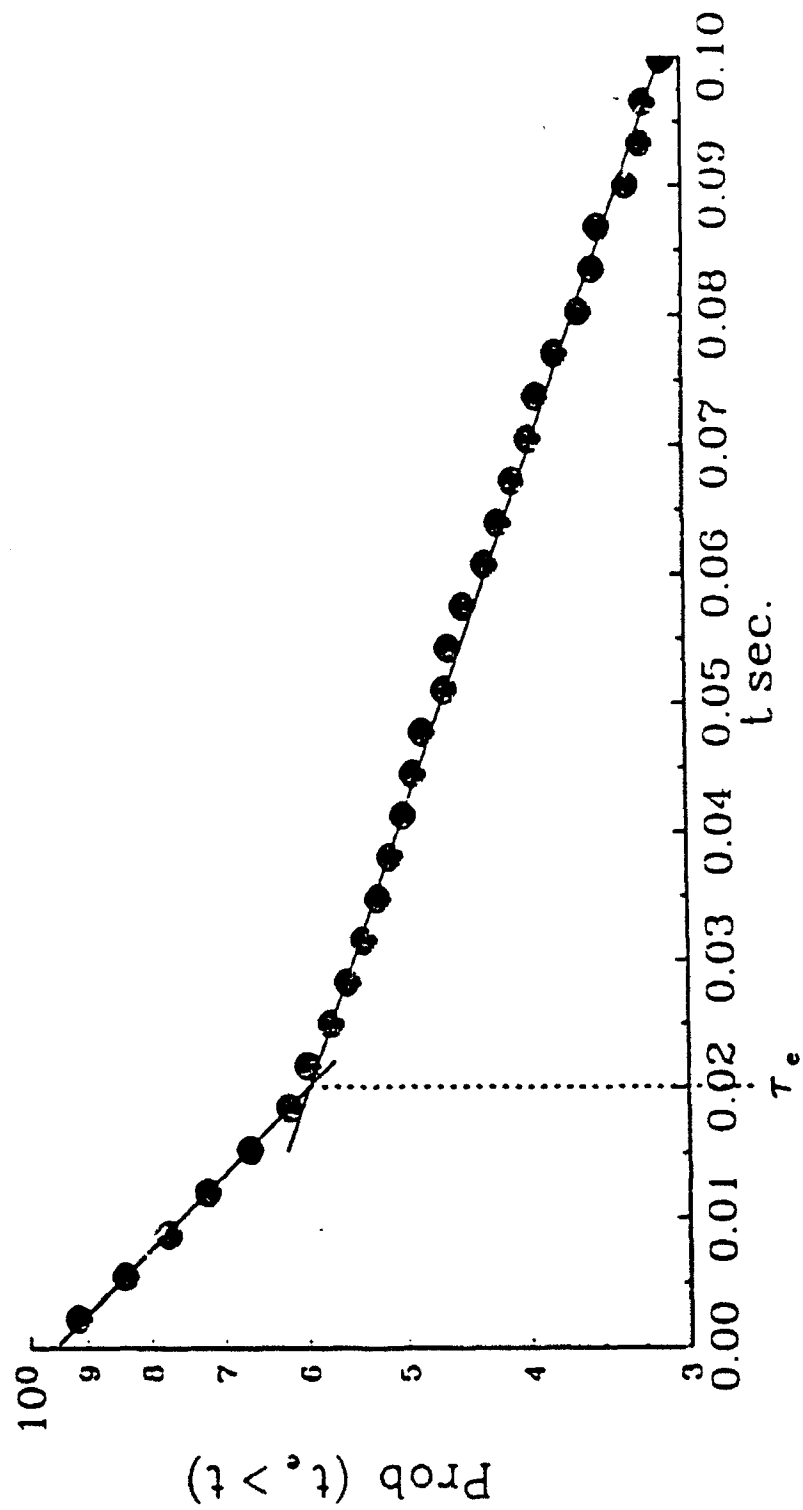


Figure 3.2 Illustration of the determination of the ejection filter time used in the time between bursts estimates

3.3.4 Relative Quadrant Analysis of the uv Reynolds Stress

The relative uv quadrant analysis results are computed by the method of Lu and Willmarth (1973). The instantaneous velocity data are sorted into quadrants depending on the signs of the u and v velocity fluctuations. The four quadrants are defined in Figure 3.3. The relative contribution of each uv_i to the total uv correlation is obtained by summing the uv_i product in each quadrant i and normalizing by the total number of ensembles and the average total uv.

3.3.5 Turbulent Velocity Spectra

Turbulent velocity fluctuation frequency spectra of the three velocity components and their cross-correlations are computed from measured three-component, coincident, single-point velocity data. The velocity auto-spectra are computed from data records of 300,000 ensembles acquired over a sampling period of 176.5 seconds, or approximately 4200 integral time scales. The term integral time scale used here refers to an approximate time scale of the largest scales in the flow and is used throughout as a measure of the length of time over which velocity statistics are estimated from. It is defined here as the ratio of the pipe diameter to the bulk velocity in the pipe. The velocity records are split into 300 separate ensembles containing 1000 velocity samples each. The auto-spectra for each 1000 velocity sample ensemble are computed and then ensemble averaged over the 300 independent auto-spectra results. Bendat and Piersol (1986) indicate that this procedure for computing auto-spectra from measured data results in very good bias free estimates of the actual auto-spectra within an uncertainty of $\pm 1/(N_e)^{1/2}$, where N_e is the number of auto-spectral ensembles. The uncertainty in the present auto-spectral calculations is less than 6% by this formula. The number of independent ensembles are chosen to provide a desired bandwidth resolution; in

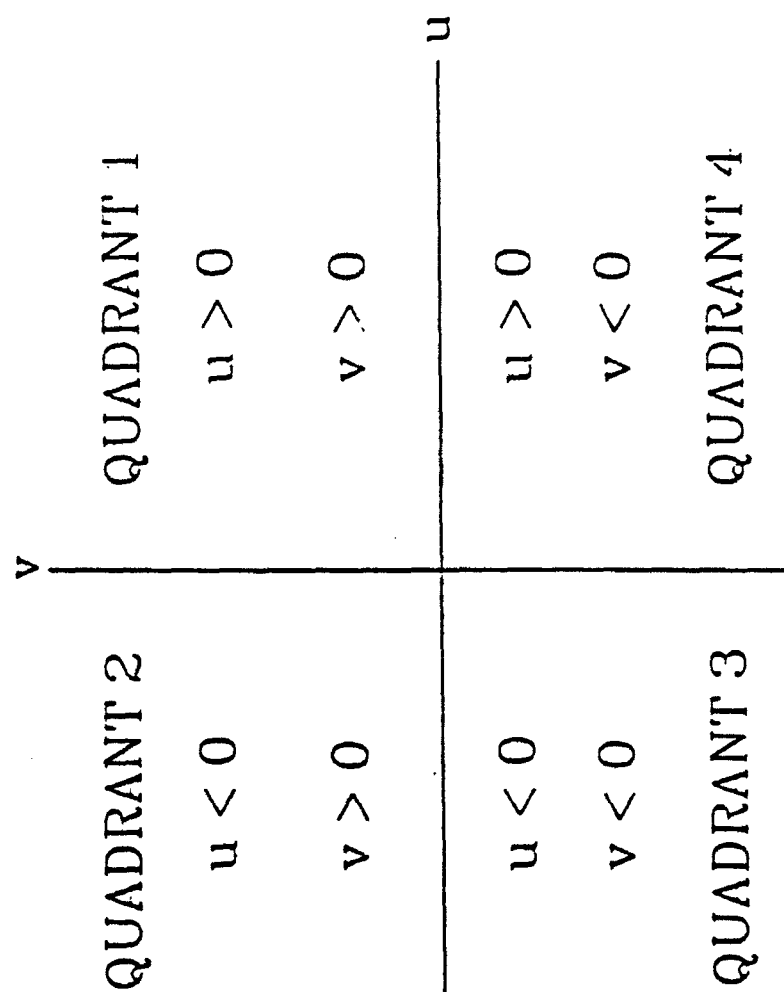


Figure 3.3 Definitions of the four quadrants used in the uv quadrant analysis technique

this particular case it is 1.7 Hz. The integrating time for each auto-spectra calculated from a 1000 velocity sample record is approximately 17 integral time scales. Tennekes and Lumley (1972) indicate that this is sufficient to insure the independence of the 300 auto-spectral ensembles. The Fourier transforms of the velocities are estimated by computing the finite Fourier transform of the velocity signals on an IBM RISC 2000 computer. A Hanning window function is used to suppress side lobe leakage effects. The algorithm used is the recommended method by Bendat and Piersol (1986) and is shown on pages 391-395 of Bendat and Piersol (1986).

The cross-spectra are estimated by a similar procedure as that described for the auto-spectral estimates. The uncertainty in the cross-spectral estimates is given by Bendat and Piersol (1986) as $\pm 1/(N_s \gamma_{ij})^{1/2}$, where γ_{ij} is the coherence function between the two velocity components. The coherence function can be approximated by the correlation coefficient R_{ij} for the estimates of the uncertainty. The uncertainty in the cross-spectral estimates will be dependent on the location in the boundary layer.

Chapter 4

GLYCERIN TUNNEL TURBULENT PIPE FLOW CHARACTERIZATION

4.1 Introduction

The undisturbed glycerin tunnel turbulent boundary layer is used as a baseline for comparisons with the modified turbulent boundary layer. Therefore, the undisturbed turbulent boundary layer must be carefully characterized. In addition, the purpose of this chapter is to quantify sources of error and determine the limitations of the LDV and data acquisition systems. Velocity profile measurements obtained in the undisturbed turbulent boundary layer are compared to published results of data from similar turbulent boundary layers. Table 2.1 lists the relevant flow parameters at the tunnel operating conditions. Excellent agreement is obtained between the velocity results measured using the TSI coincident mode of acquisition and the results measured using the external digitization method. Unless otherwise noted, the externally digitized LDV data is plotted. Estimated uncertainties in the measured data are indicated by error bands on representative points in the figures throughout the manuscript. In the event the error band is smaller than the symbol size used in the figure or the uncertainty is specified in the text, the error bands are not displayed.

4.2 Axial Pressure Surveys

The test pipe is equipped with twenty pressure transducers along the first 7.1 m of pipe length. The axial pressure gradient at operating conditions can be obtained from these transducers and is shown in Figure 4.1. The curve in Figure 4.1 is the average gradient obtained from ten independent pressure surveys measured over a period of approximately three hours. The results indicate that the axial pressure gradient asymptotes to a constant

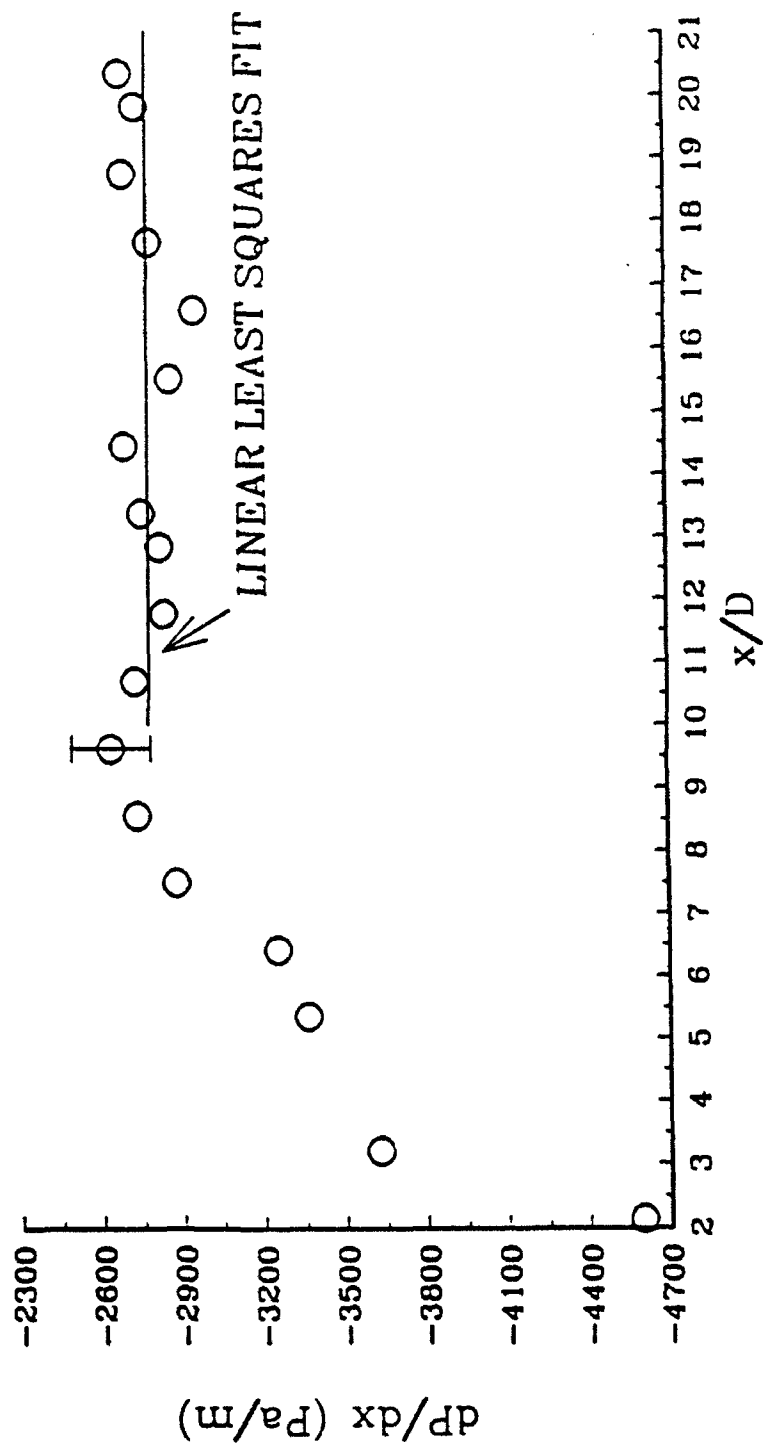


Figure 4.1 Measured axial pressure gradient along the test pipe of the glycerin tunnel

value approximately eleven pipe diameters from the entrance of the test pipe, or nearly nine pipe diameters upstream of the test section. This indicates that the flow in the test section can be considered to be fully developed. A linear least squares fit to dP/dx from $9.7 \leq x/D \leq 20.3$ gives $dP/dx = -2773.03 \pm 147 \text{ Pa/m}$.

In fully developed pipe flow, the wall shear stress τ_w can be calculated from the axial pressure gradient by application of the momentum equation. The momentum equation for a horizontal fully developed pipe flow reduces to $\tau_w = -\frac{1}{2} R dP/dx$. An estimate of the friction velocity u^* can be obtained from the measured pressure gradient using the momentum equation and the definition of u^* . The value of u^* obtained from the pressure gradient is $0.399 \pm 0.01 \text{ m/s}$.

4.3 Velocity Profile Statistics

The friction velocity calculated from the mean streamwise velocity profile in the viscous sublayer is approximately 0.402 m/s . This value of the friction velocity is in excellent agreement with the value obtained from the axial pressure gradient measurements. Mean streamwise velocity profiles are in good agreement with the turbulent boundary layer logarithmic law of the wall and the profile of Spalding (1961). A typical undisturbed mean velocity profile, normalized with wall variables, is shown in Figure 4.2. The logarithmic law of the wall, viscous sublayer profile and Spalding's profile are shown for comparison. Measured mean circumferential and radial velocity components are found to be zero within experimental uncertainty, as is expected in a fully developed pipe flow.

Profiles of the measured rms velocities, u' , v' and w' , are shown in Figure 4.3. The data of Karlsson and Johansson (1988) and the direct numerical simulation data of Antonia et al. (1992) are also shown in Figure 4.3 for comparison. The reference curves of

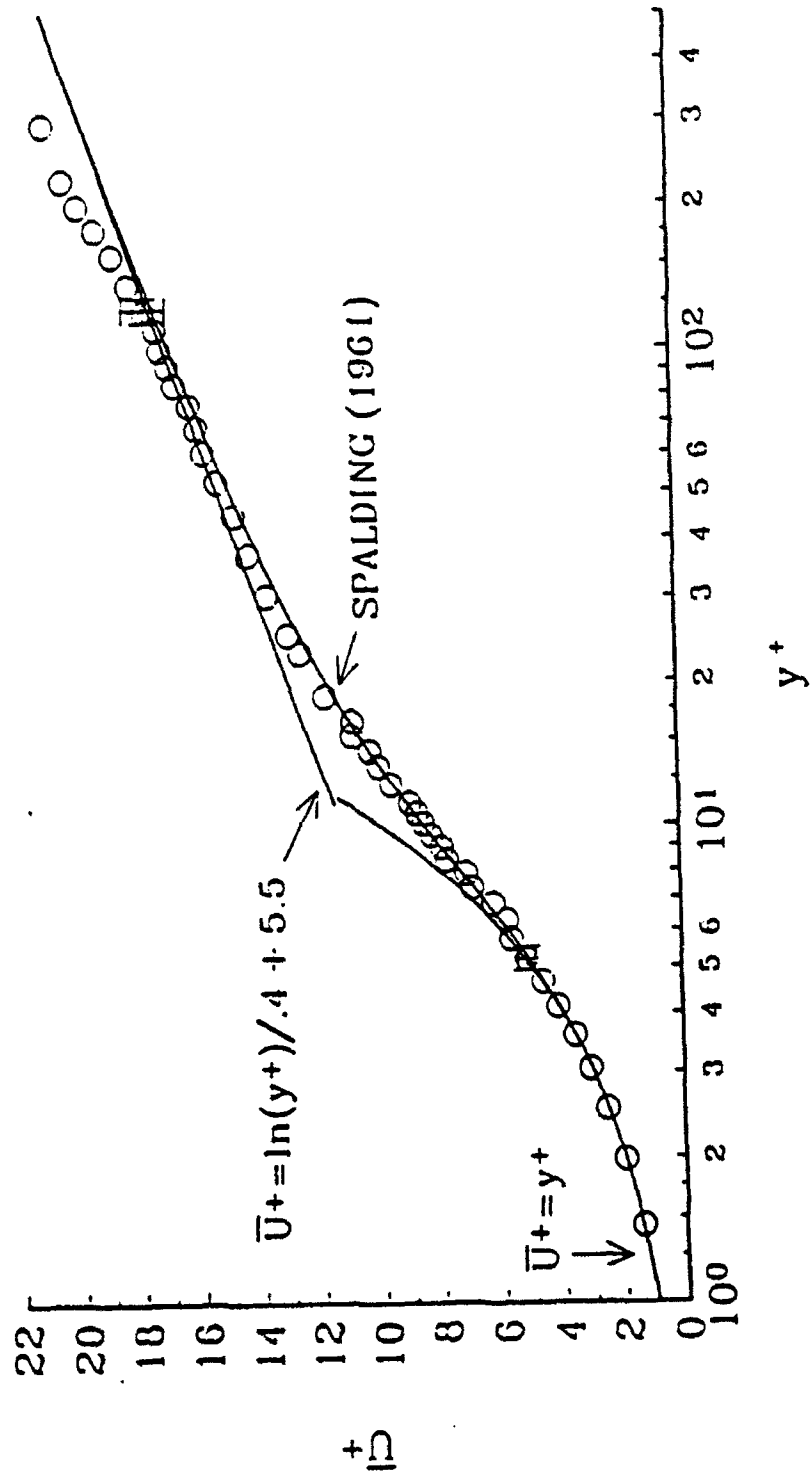


Figure 4.2 Typical streamwise mean velocity profile in the undisturbed glycerin tunnel turbulent boundary layer. The profile is plotted in wall variables

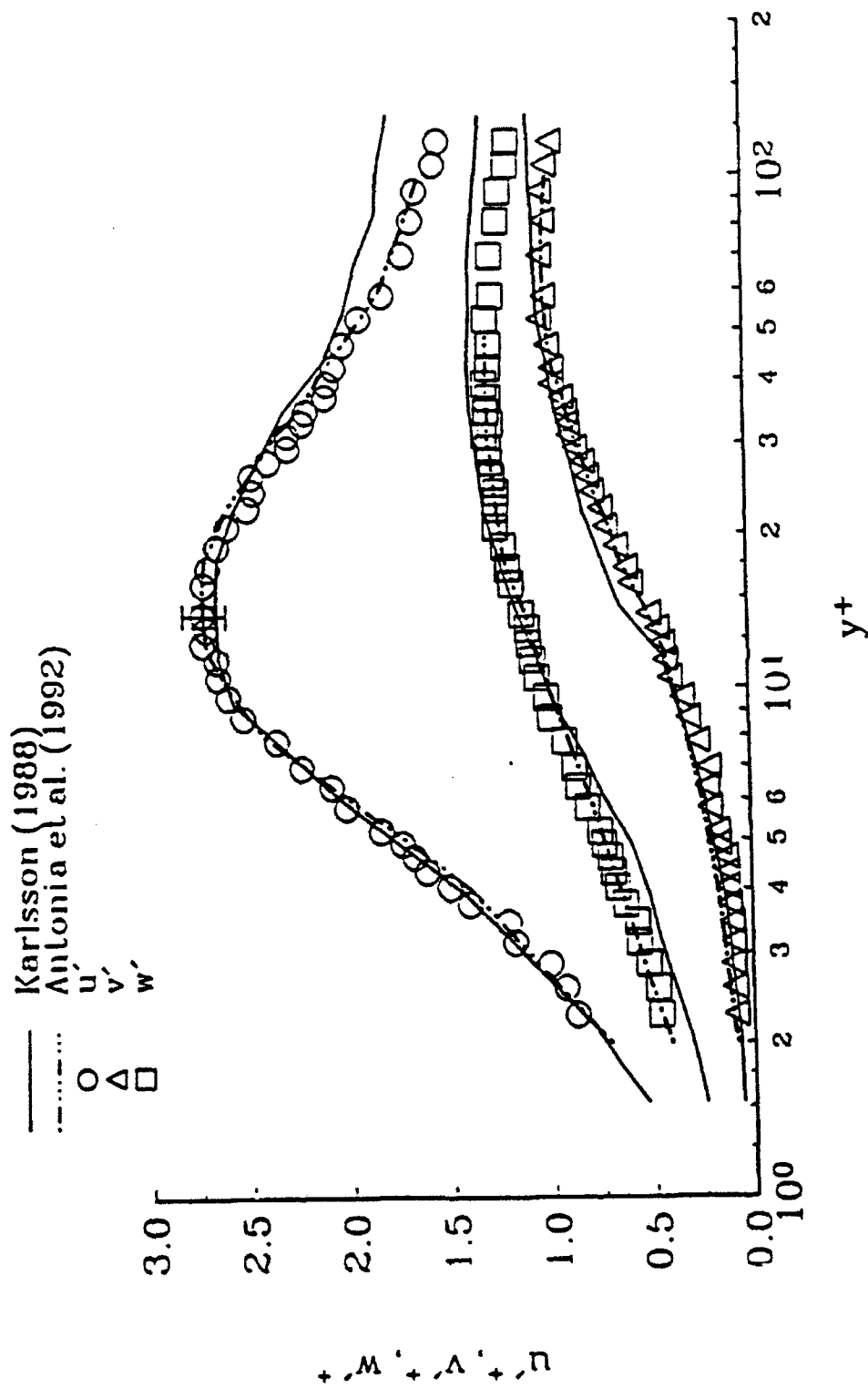


Figure 4.3 Measured rms velocities in the undisturbed glycerin tunnel turbulent boundary layer. Data are normalized by wall variables

Karlsson and Johanson (1988) were measured in a flat plate turbulent boundary layer with a momentum thickness Reynolds number, $Re_\theta = 1450$. The data of Antonia et al. (1992) was from a direct numerical simulation of a fully developed channel flow at $Re_\theta = 700$. The estimated momentum thickness Reynolds number of the current measurements is $Re_\theta = 730$. Excellent agreement is obtained between the $Re_\theta = 700$ simulation results of Antonia et al. (1992) and the current data. The present v' data are slightly lower than the simulation data for $y^+ < 10$. If the simulation data is assumed to be correct, the percent error in the measured v' data is approximately 26% low at $y^+ = 2.5$ and the error continually decreases with increasing y^+ . This error may be attributed to the refraction effects near the wall. A reduction in the half angle of approximately 0.5° , which may be reasonable at $y^+ = 2.5$, would amount to a 26% decrease in the measured v' data. The disagreement of the present data with Karlsson's data at large y^+ is a Reynolds number effect. Antonia et al. (1992) and Wei and Willmarth (1989) indicate that the velocity statistics, when normalized by viscous scales, are dependent on Re_θ for $y^+ > 15$. The effect of increasing Re_θ is that the normalized intensities increase.

A typical uv Reynolds stress profile measured in the unmodified turbulent boundary layer is shown in Figure 4.4 along with the reference data of Karlsson and Johanson (1988) and Antonia et al. (1992). Very good agreement is once again obtained between the measured uv profile in this investigation and the simulation data of Antonia et al (1992) for $y^+ \geq 5$. The present data is low below $y^+ = 5$ and this may also be attributed to the refraction effect on the radial velocity measurement. The peak in the measured uv profile is located at $y^+ = 35$ to 40. This agrees with the location determined from the empirical relation derived by Sreenivasan (1990),

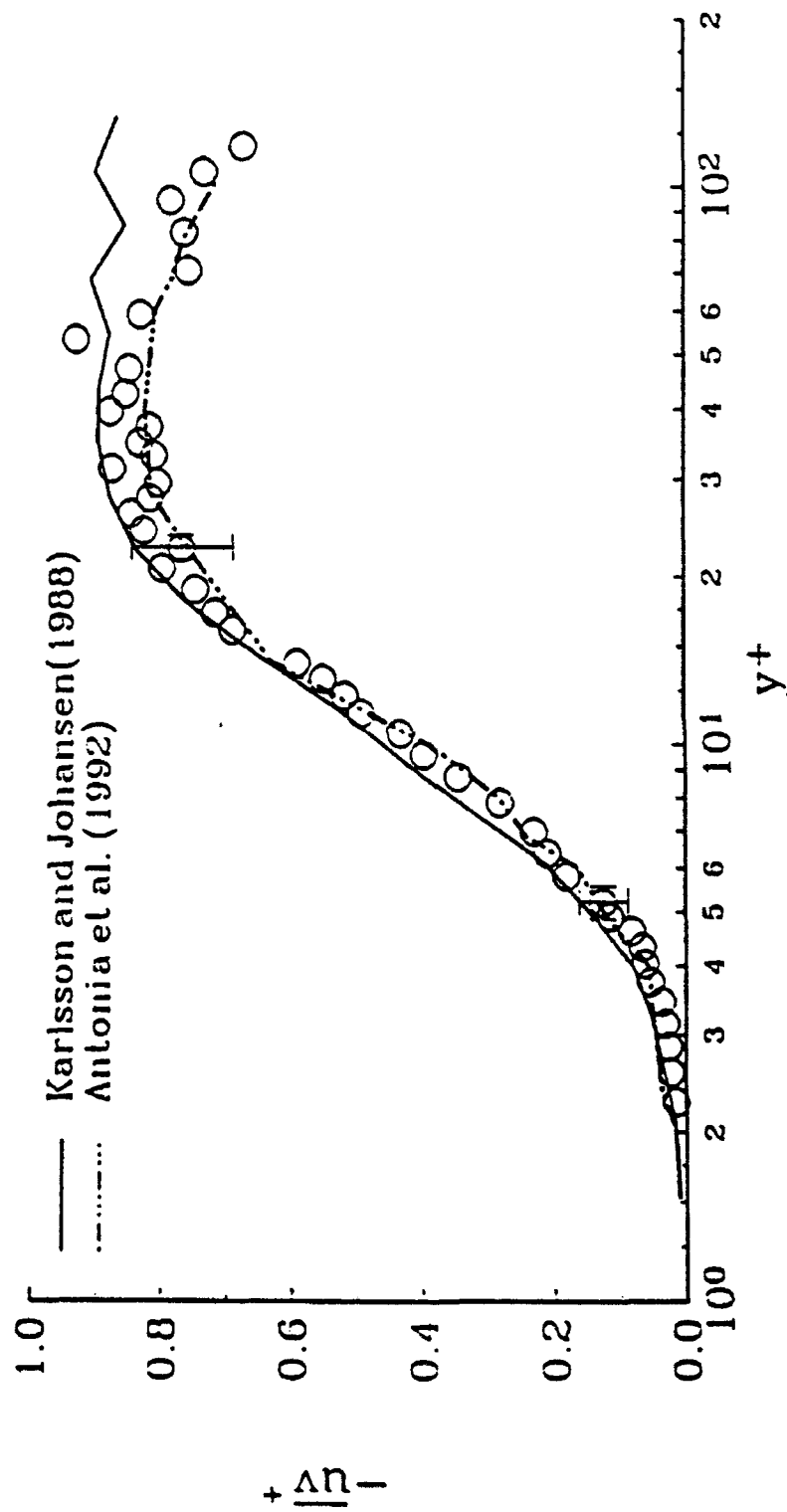


Figure 4.4. Typical uv Reynolds stress profile measured in the undisturbed glycerin tunnel turbulent boundary layer. Data normalized by wall variables

$$y_{\max}^+ = 2 \sqrt{R^+}.$$

In the current experiment where $R^+ = 306.5$, this relation yields a $y_{\max}^+ \approx 35$. The Reynolds number effect on these profiles is apparent from a comparison of this data with the results of Karlsson and Johanson (1988). The other Reynolds stress components are zero in a fully developed turbulent pipe flow and are measured as such within the experimental uncertainty. Selected triple correlation profiles, normalized by viscous scales, are compared with the data of Karlsson and Johanson (1988) in Figure 4.5a and b. Skewness and kurtosis profiles are plotted in Figure 4.6a and b. The $Re_\tau = 287$ simulation skewness and kurtosis results of Kim et al. (1987) are provided for comparison.

4.4 Post Processed Results

Turbulent boundary layer time between bursts, T_b , profiles are estimated from the measured externally digitized, time resolved uv velocity data. The time between burst estimates agree with published results. A constant $T_b^+ \approx 100$ to 110 is obtained below $y^+ = 10$ with a gradual decrease for $y^+ > 10$. By $y^+ = 100$, the value of T_b^+ is decreased to approximately 70. The uncertainty in T_b^+ is estimated by Student-T tests at approximately $\pm 17\%$.

Relevant quadrant analysis results of the uv velocity data are compared with the results of Kim et al. (1987). Very good agreement is observed between the measured data and the computations of Kim (1987) beyond $y^+ = 5$. However, the externally digitized data and the TSI coincident mode data show an increasing error with decreasing y^+ for $y^+ < 5$. This error is due to the measurement of the radial velocity component with the violet laser beams. The current measurements are compared with an earlier uv measurement set and with

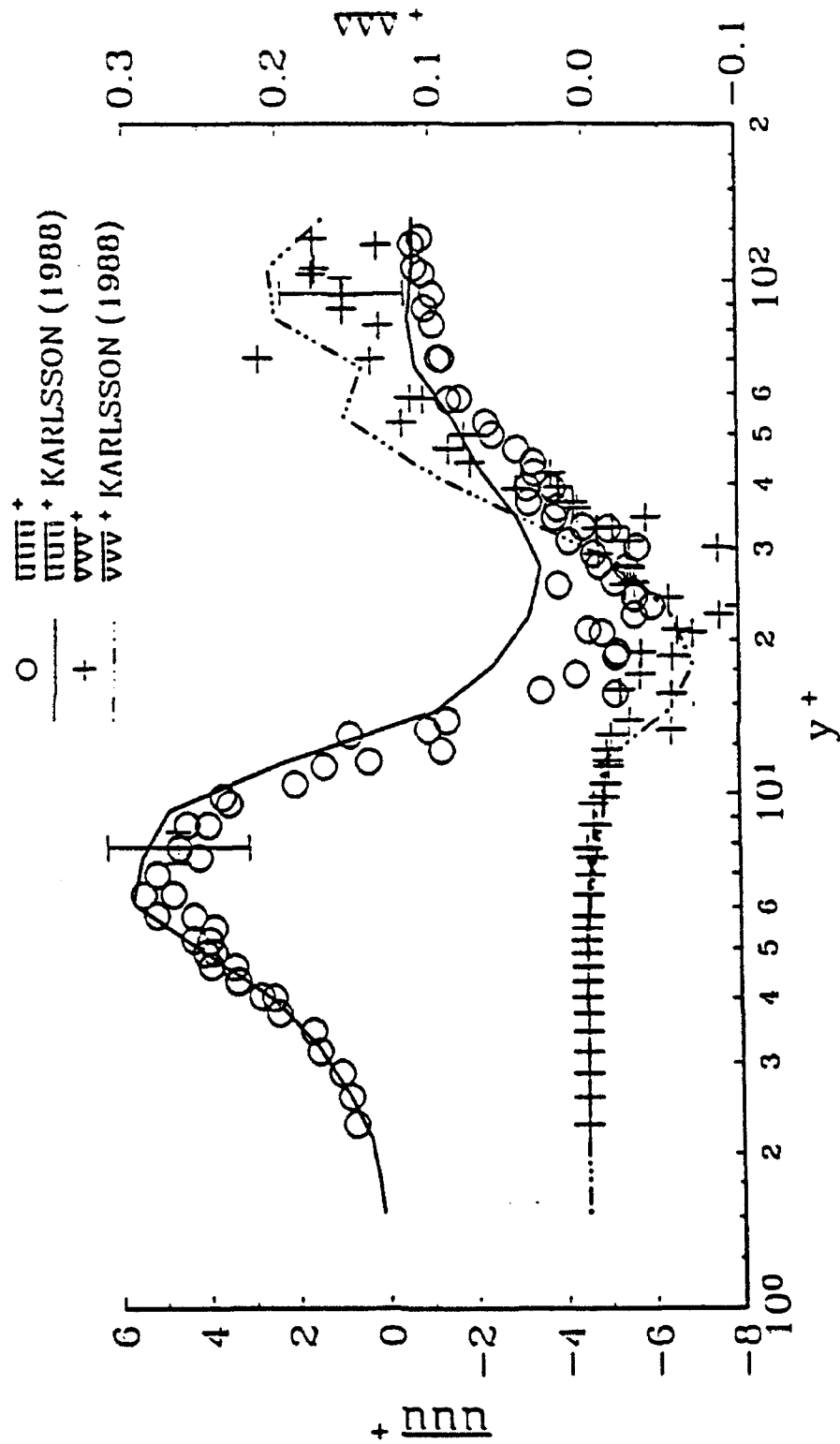


Figure 4.5 Measured triple correlation profiles in the undisturbed glycerin tunnel turbulent boundary layer. Data normalized by wall variables. a) uuu and vvv

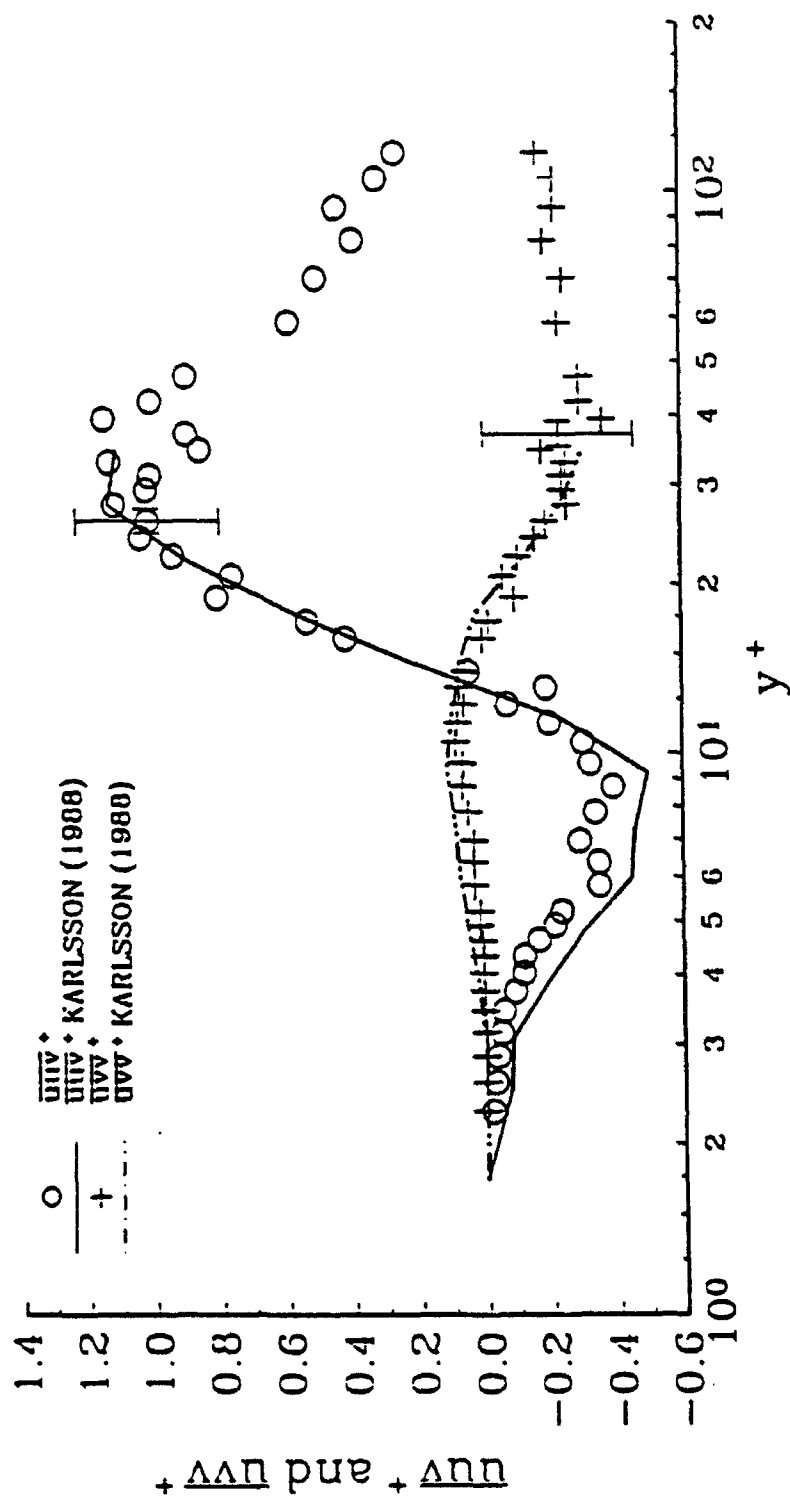


Figure 4.5(cont.) b)uuv, and uvv

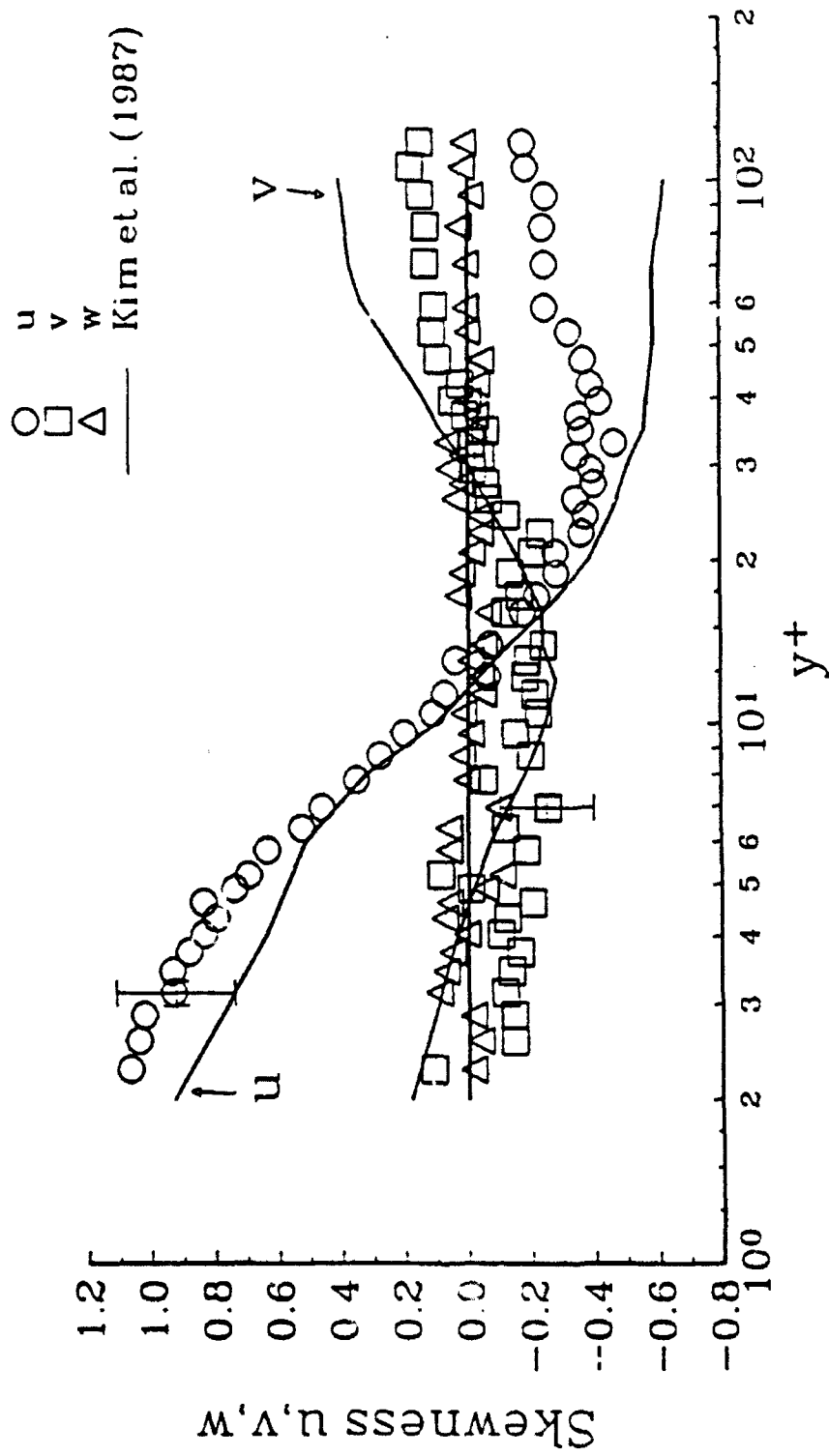


Figure 4.6 Typical profiles of the undisturbed glycerin tunnel turbulent boundary layer
a) velocity fluctuation skewness levels

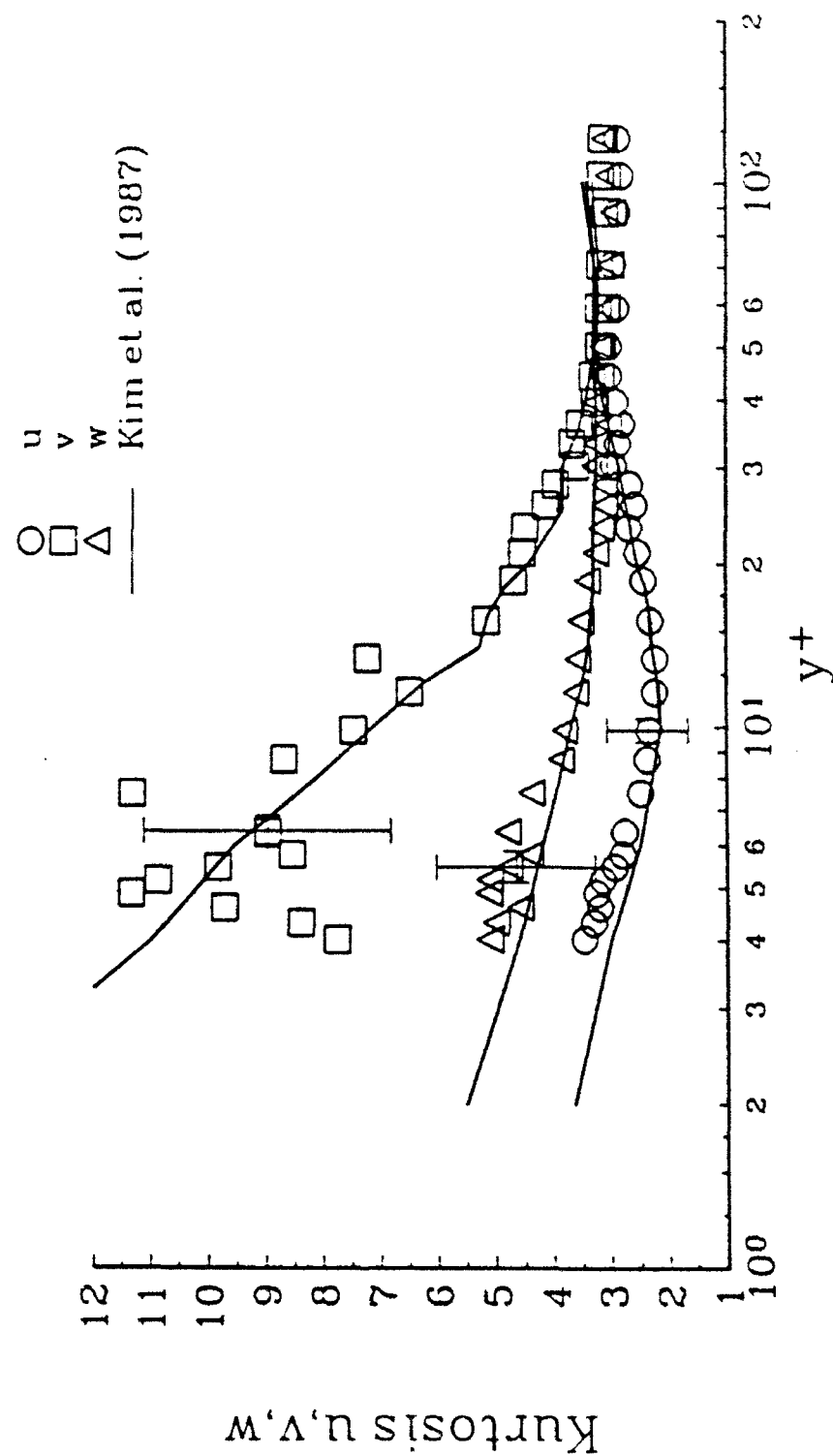


Figure 4.6(cont.) b) velocity fluctuation kurtosis levels

the data of Kim (1987) in Figure 4.7. The earlier data set, labeled TSI-1, is TSI coincident mode data, which used the green laser line to measure the radial velocity component. The TSI-2 data is measured with the fiber-optic setup described in Chapter 2.

A comparison of the TSI-1 results with the TSI-2 and externally digitized results indicates that the use of the 476.5 nm laser beams coupled to the 488 nm component of the fiber-optic probe introduces an error in the radial velocity measurements near the wall. The elevated results below $y^+ = 5$ are not an Re_τ effect since Antonia et al. (1992) indicate that the relative quadrant analysis results are nearly independent of Re_τ for low Reynolds numbers. The possibility of an error in the near wall radial velocity measurements is discussed in Section 2.2. As the wall is approached, the counter-processor amplifier gain is increased to offset the decreasing data rates near the wall. More amplifier gain is needed with the violet beams than with the green beams because of the lower power in the violet beams. As mentioned in Section 3.1.2, this increases the effective length of the fiber-optic probe volume. The increased gain coupled with the refraction effect below $y^+ = 5$, which is also discussed in Section 2.2, will intensify any error or noise due to the not perfectly collimated violet laser beams. This explains why the errors in the TSI-2 and the externally digitized data in Figure 4.7 are limited to $y^+ < 5$.

The experimental data used for comparison by Kim et al. (1987) do not show nearly as good an agreement with their results as do the present data. This suggests that a more stringent test of the quality of uv Reynolds stress data would be a comparison of the relative quadrant contribution to the total uv, rather than merely comparing profiles of the rms velocities and the total uv data. It should be noted that the error in the $\langle uv_i \rangle$ levels for $y^+ < 5$ are very repeatable and that it is not simply a random day to day procedural error. The velocity measurements in the modified boundary layer are all obtained with the violet

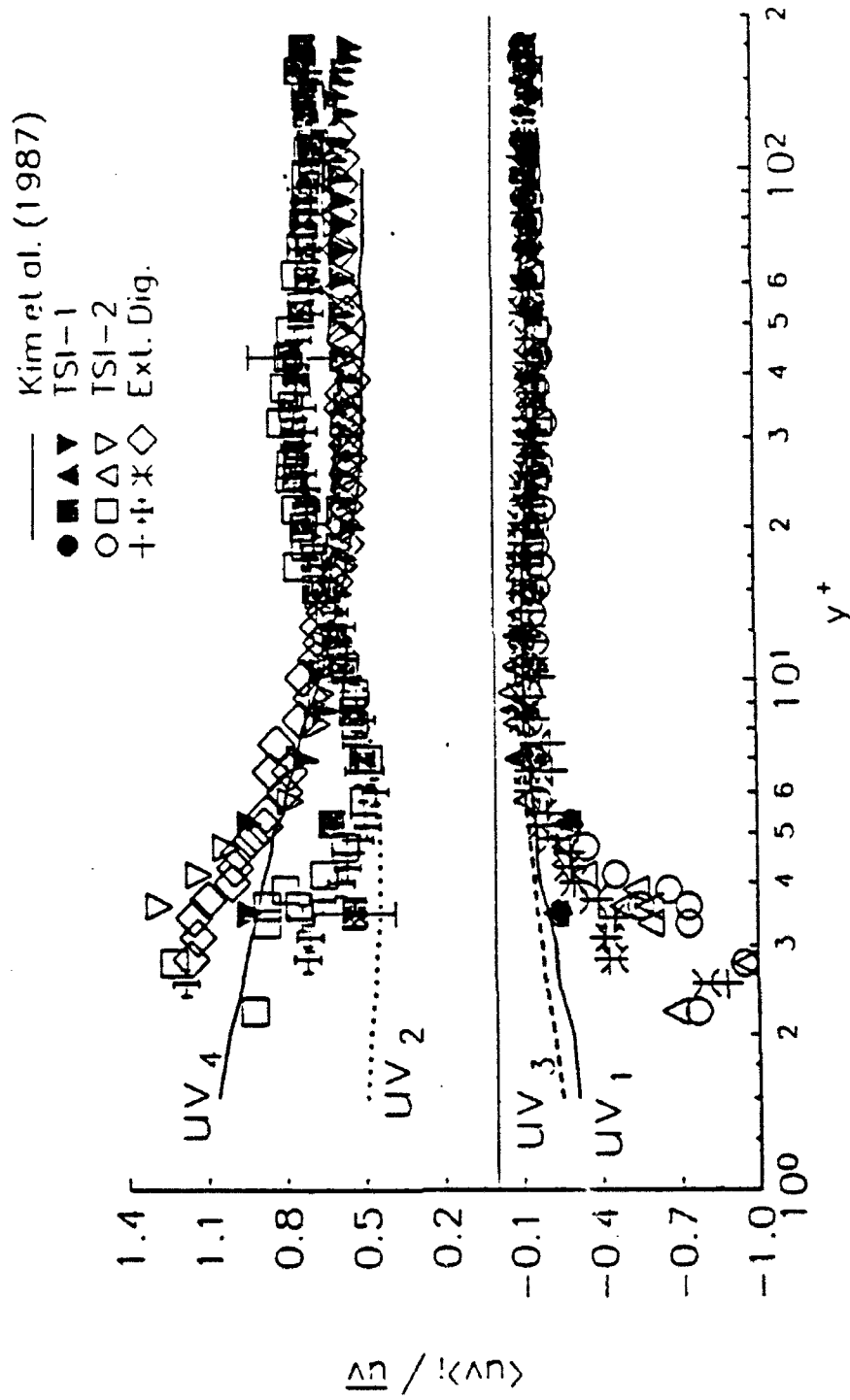


Figure 4.7 Relative quadrant analysis of the uv signal in the undisturbed glycerin tunnel turbulent boundary layer. TSI-1, TSI-2 and ext. dig. data represent three different LDV system configurations

beams coupled to the fiber probe. Therefore, the externally digitized data is used as the reference.

Estimates of several terms of the turbulent kinetic energy balance are obtained by differentiating the measured velocity profile data. The turbulent kinetic energy balance in cylindrical coordinates is given by:

$$C + P + DV + DT + Pr + DI = 0$$

4.1

$$C = \text{Convection by mean flow} \rightarrow -(\bar{V} \cdot \nabla) \bar{q}$$

$$P = \text{Production by mean strain rate}$$

$$\begin{aligned} \rightarrow & -\frac{1}{r} \overline{wu} \frac{\partial \bar{U}}{\partial \theta} - \overline{wv} \frac{\partial \bar{V}}{\partial \theta} - \frac{1}{r} \overline{w^2} \frac{\partial \bar{W}}{\partial \theta} - \overline{uv} \frac{\partial \bar{U}}{\partial r} - \overline{v^2} \frac{\partial \bar{V}}{\partial r} \\ & - \overline{vw} \frac{\partial \bar{W}}{\partial r} - \frac{\bar{V} \bar{w}^2}{r} + \frac{2\bar{W}}{r} \overline{wv} - \overline{u^2} \frac{\partial \bar{U}}{\partial x} - \overline{uv} \frac{\partial \bar{V}}{\partial x} - \overline{uw} \frac{\partial \bar{W}}{\partial x} \end{aligned}$$

$$DV = \text{Viscous diffusion} \rightarrow +\nu \left[\frac{1}{r} \frac{\partial r}{\partial r} \frac{\partial \bar{q}}{\partial r} + \frac{1}{r^2} \frac{\partial^2 \bar{q}}{\partial \theta^2} + \frac{\partial^2 \bar{q}}{\partial x^2} \right]$$

$$DT = \text{Turbulent diffusion} \rightarrow -\frac{1}{r} \frac{\partial r \overline{vq}}{\partial r} - \frac{\partial \overline{uq}}{\partial x} - \frac{1}{r} \frac{\partial \overline{wq}}{\partial \theta}$$

$$Pr = \text{Pressure transport terms} \rightarrow -\frac{1}{\rho} \left[\overline{v \frac{\partial p}{\partial r}} + \overline{u \frac{\partial p}{\partial x}} + \overline{w \frac{\partial p}{\partial \theta}} \right]$$

$$DI = \text{Dissipation} \rightarrow -\nu \left[\frac{4\overline{w \partial v}}{r \partial \theta} + \left(\frac{\partial u_i}{\partial x_j} \right) \left(\frac{\partial u_i}{\partial x_j} \right) + DI_m \right]$$

$$DI_m = \text{Measurable dissipation} \rightarrow \frac{\overline{v^2}}{r^2} - \frac{\overline{w^2}}{r^2} - \frac{2}{r^2} \frac{\partial \overline{vw}}{\partial \theta}$$

$$\bar{q} = \frac{1}{2} (\overline{u^2} + \overline{v^2} + \overline{w^2}) \quad q = \frac{1}{2} (u^2 + v^2 + w^2)$$

This can be simplified to the following equation for a fully developed turbulent pipe flow:

$$-\frac{\overline{uv}}{P} \frac{\partial \overline{U}}{\partial r} - \frac{1}{r} \frac{\partial \overline{rvq}}{\partial r} + v \frac{1}{r} \frac{\partial r \partial \overline{q}}{\partial r \partial r} - v \left[\frac{\overline{v^2 + w^2}}{r^2} \right] - DI - Pr \quad 4.2$$

The first 4 terms of Equation 4.2 can be estimated from the measured data. The remaining terms cannot be estimated and are combined together as a remainder. Profiles of the turbulent kinetic energy balance are shown in Figure 4.8. The energy balance results from the numerically simulated channel flow calculations of Mansour et al. (1988) at $Re_\tau = 287$ are also shown for comparison. The measurable dissipation term, DI_m is zero within the uncertainty of the measurements. In general, the profiles of the estimated energy balance from the current measurements are in good qualitative agreement with the simulation data. There is a small discrepancy between the measured and the simulation rate of production profiles. The measured curve is slightly higher in magnitude. Antonia et al. (1992) states that the limiting value of the production of turbulent kinetic energy is 0.25. The present estimate, approximately 0.26, is slightly larger than this limiting value. The difference in the peak levels between these results and those of the simulation is more than likely an Re_τ effect, as Antonia et al. (1992) have shown that there is a slight Reynolds number effect on the rates of energy production and dissipation.

Measured turbulent velocity auto-spectra show good agreement with the auto-spectra measured by Herzog (1986) in the same facility using hot-film anemometry. Auto-spectral estimates at $y^+ = 20$ are shown in Figure 4.9 along with data of Herzog (1986). Typically, the LDV is a noisier system than the hot-wire/film anemometer and this is evident in

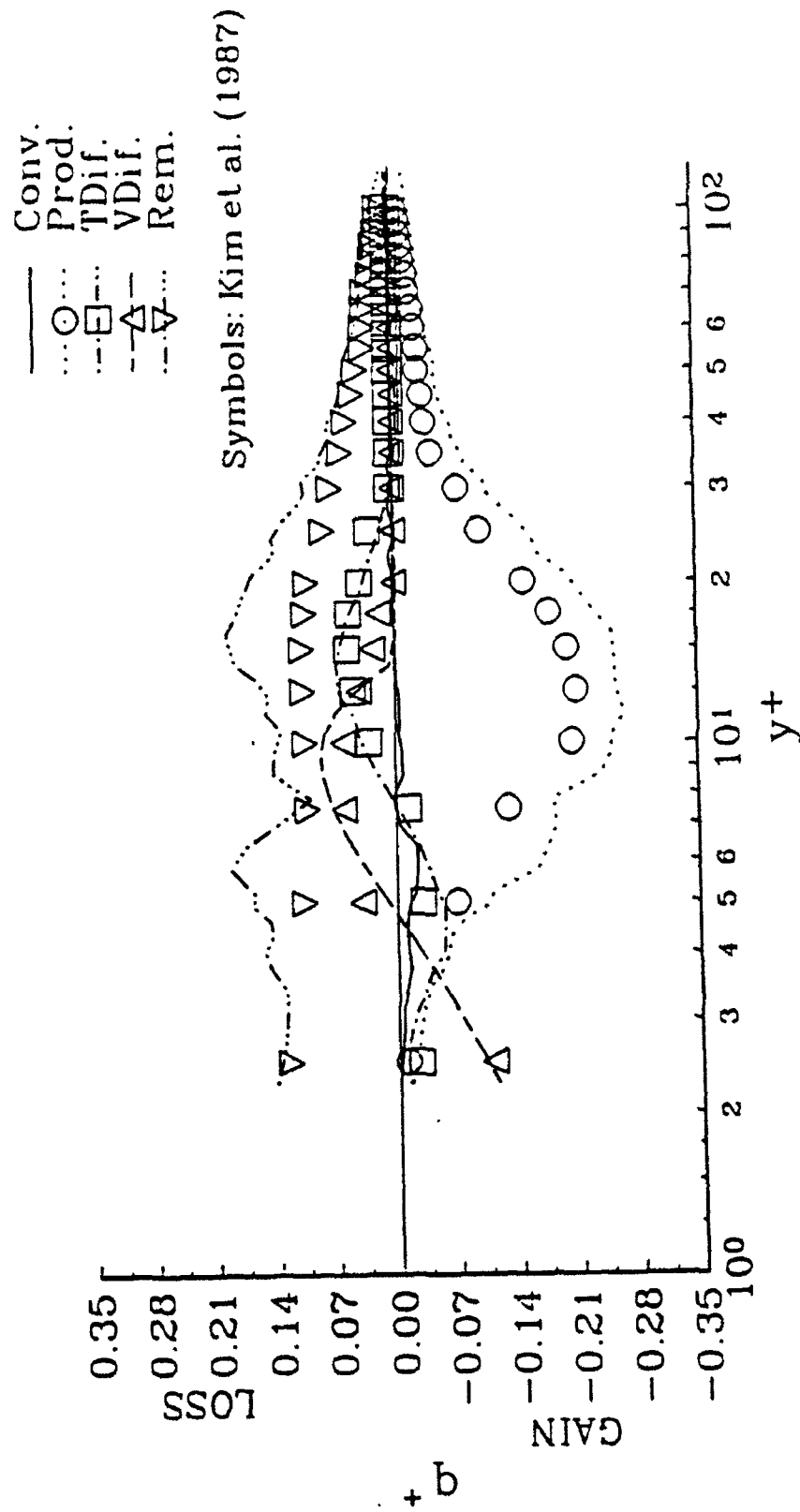


Figure 4.8 Profiles of the components of the turbulent kinetic energy transport equation, Equation 4.3, in the undisturbed glycerin tunnel turbulent boundary layer

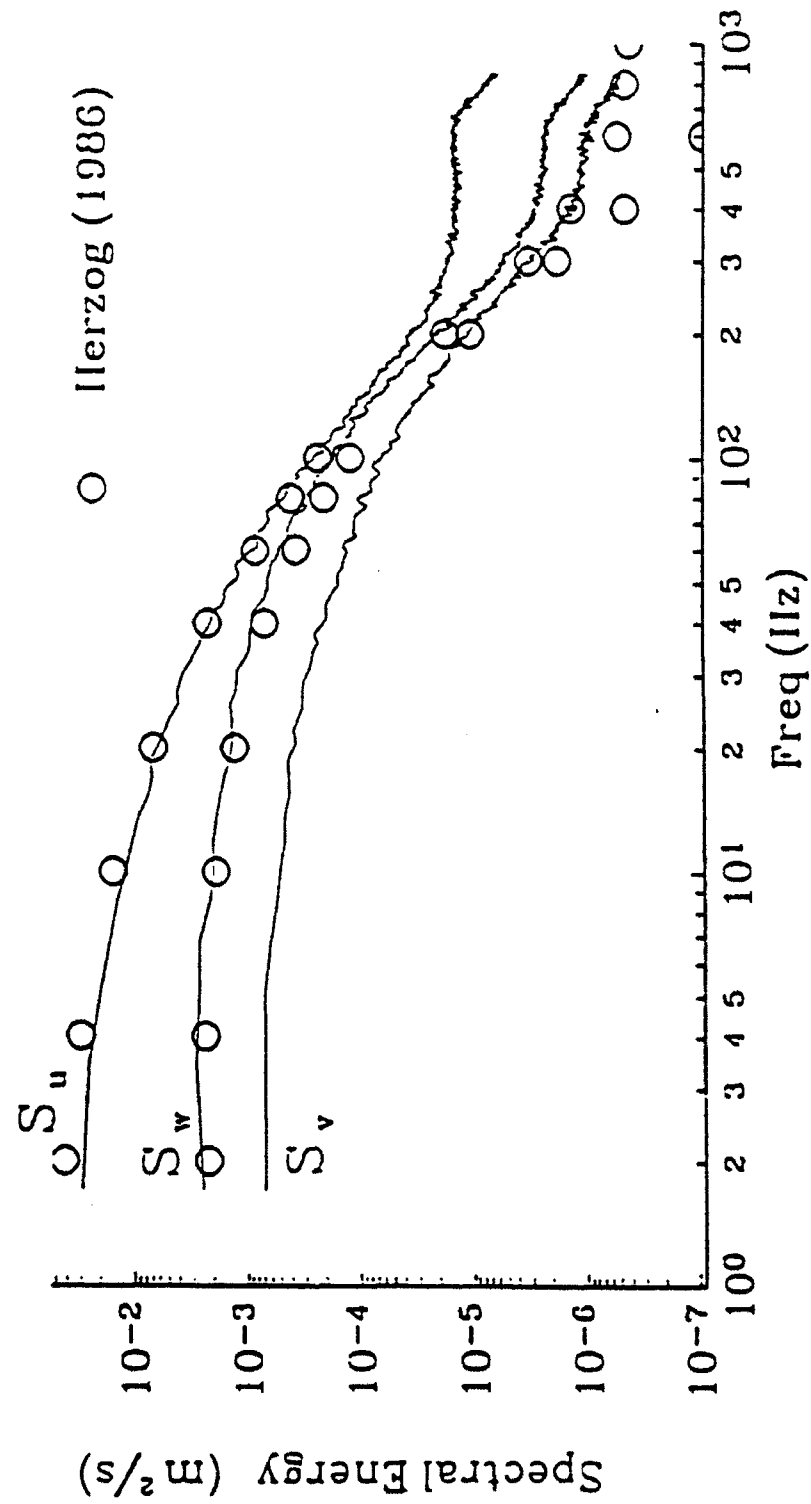


Figure 4.9 Typical auto-spectral estimates of the turbulent velocity fluctuations at $y^+ = 20$. Measured in the undisturbed glycerin tunnel turbulent boundary layer

Figure 4.9. The LDV measured spectra flattens out much sooner than the data of Herzog. This effect has been observed by Buchave et al. (1979). The sharp roll off at frequencies above 700 Hz is filter roll off due to the anti-alias low pass filters. Figures 4.10 to 4.12 show velocity auto-spectral estimates at four y^+ locations in the boundary layer. The uncertainties in the auto-spectral estimates are obtained from eight independent measurements using the Student-T test. The uncertainty estimates obtained from the Student-T tests are less than 6% which agrees with the uncertainty estimates from statistical principals as presented in Chapter 3.

4.5 Summary

The unmodified glycerin tunnel turbulent boundary layer is a typical fully developed turbulent pipe flow at an apparent $Re_\tau = 730$. The data presented in this chapter are in excellent agreement with the numerically simulated turbulent channel flow computations at $Re_\tau = 700$ and in reasonable agreement with published experimental turbulent boundary layer data. The accuracy of the externally digitized LDV and data acquisition systems is also characterized. Below $y^+ = 5$, an error in the radial velocity measurement is apparent, and is primarily due to the use of the violet laser beams and the refraction effects at the pipe walls due to imperfect refractive index match. This error occurs with both the TSI coincident and the external digitization modes, and is mostly apparent in the relative quadrant analysis results. The results for $y^+ > 5$ are fairly noise free and very repeatable. This suggests that a relative quadrant analysis of the total uv Reynolds stress is a more stringent test of the accuracy of Reynolds stress measurements. Overall, these results validate the use of the externally digitized LDV system for the proposed investigation of the modified near wall region. Excellent agreement is obtained between the TSI coincidence mode data and the

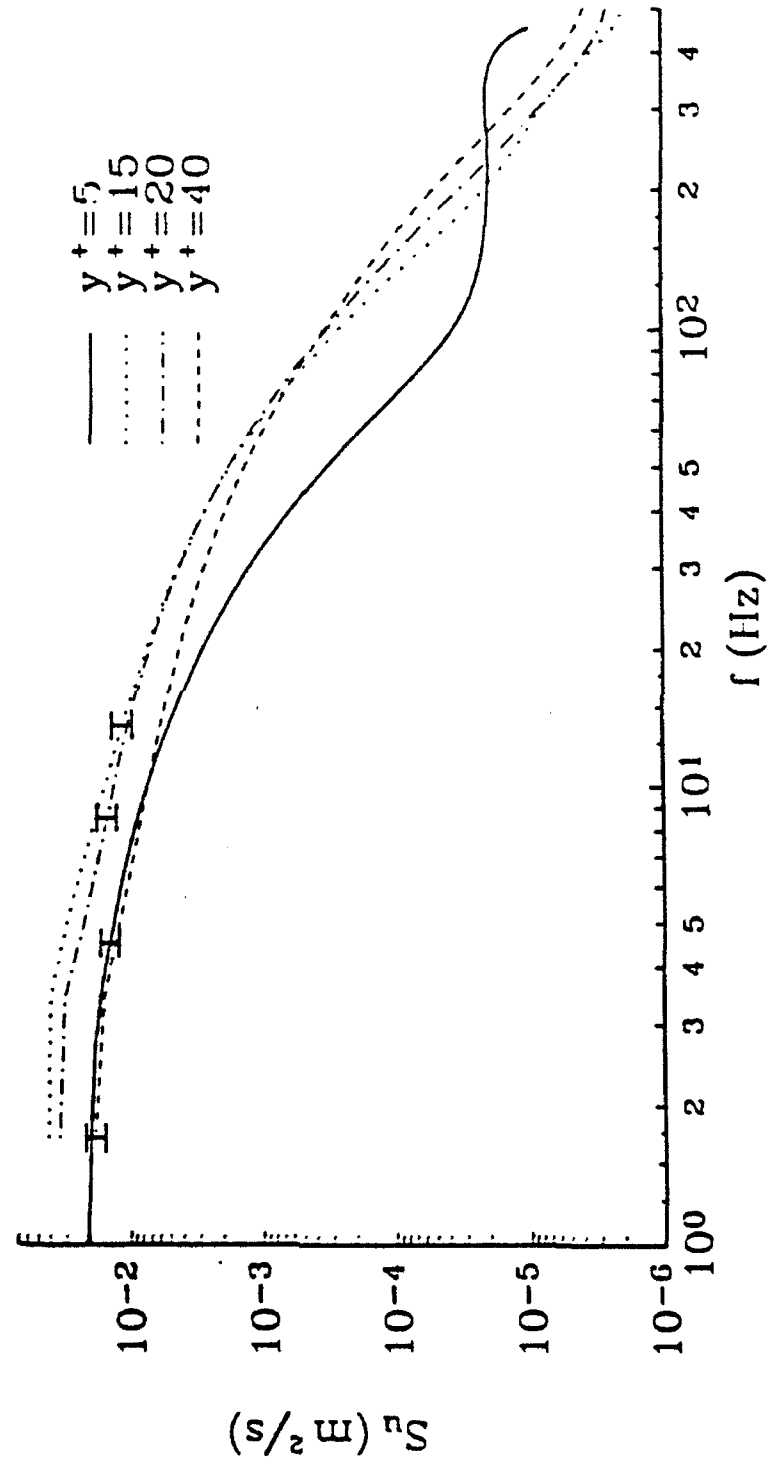


Figure 4.10 Typical auto-spectral estimates of the streamwise velocity fluctuations at four locations in the undisturbed glycerin tunnel turbulent boundary layer

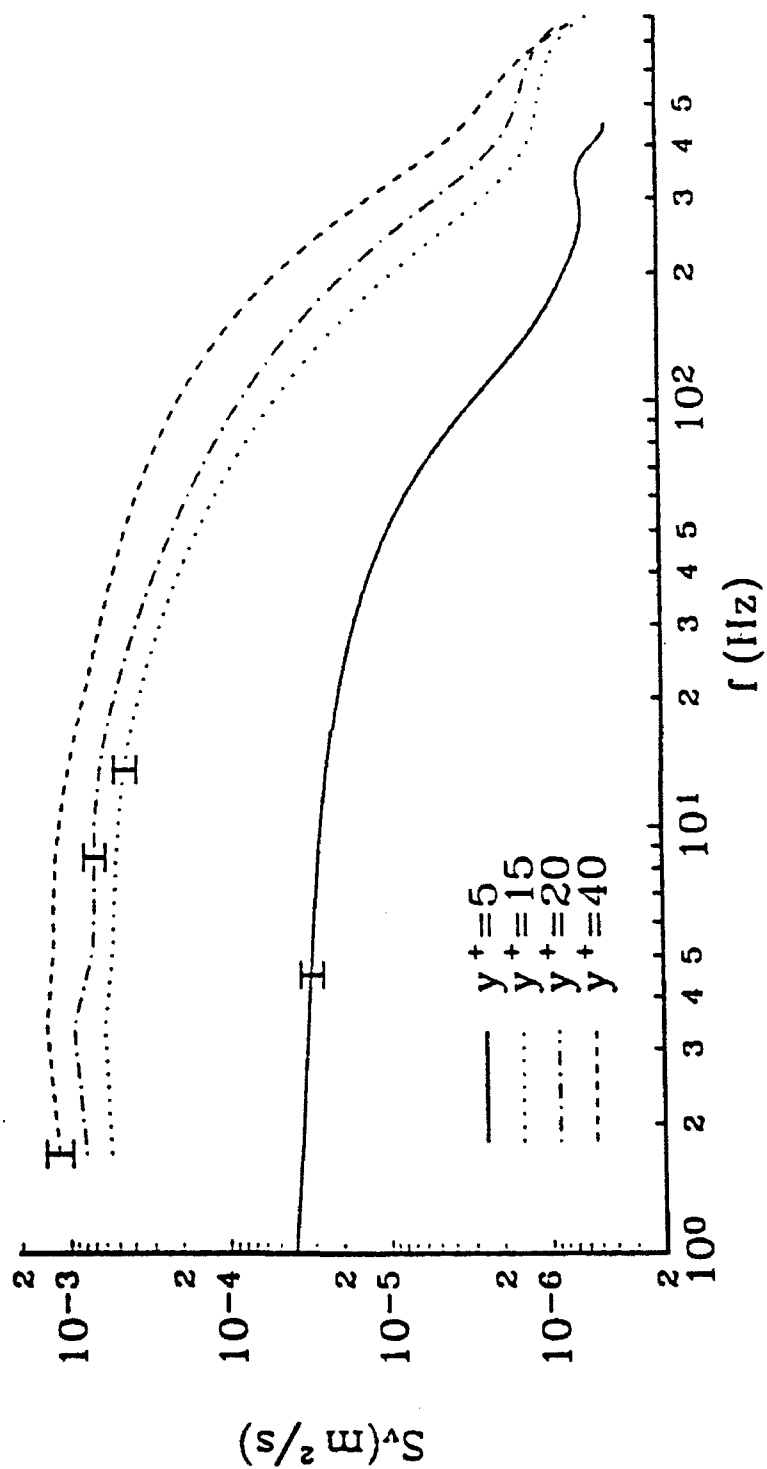


Figure 4.11 Typical auto-spectral estimates of the radial velocity fluctuations at four locations in the undisturbed glycerin tunnel turbulent boundary layer

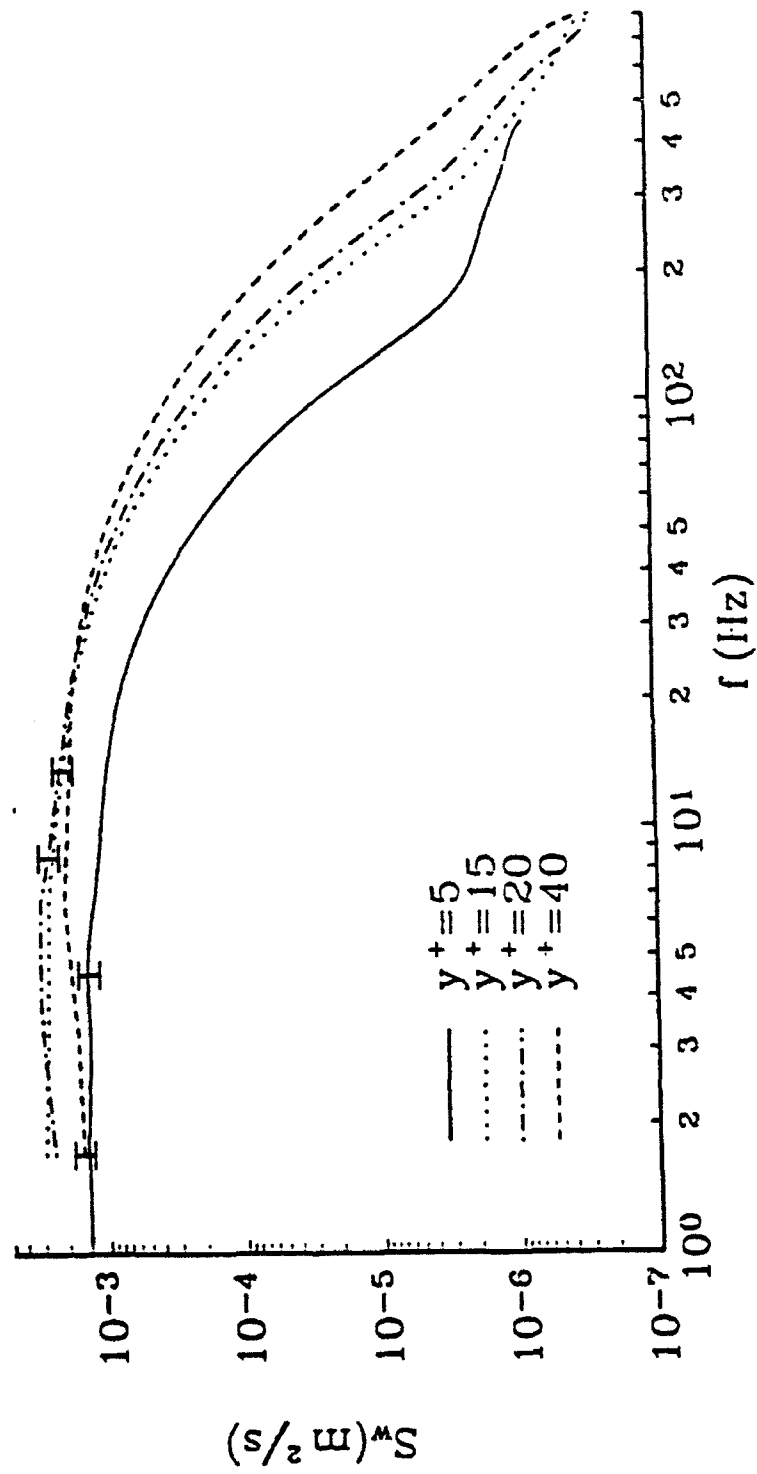


Figure 4.12 Typical auto-spectral estimates of the circumferential velocity fluctuations at four locations in the undisturbed glycerin tunnel turbulent boundary layer

external digitization mode data. However, the externally digitized data show less scatter, which probably results from the greater number of ensembles used to compute the statistics and the nearly bias free measurements.

Chapter 5

THE MODIFIED WALL REGION: SINGLE-POINT MEASUREMENTS

5.1 The Global Flow Field

5.1.1 Introduction

This chapter presents the single-point three-component velocity measurements obtained in the modified boundary layer downstream of the bump. Measurements are obtained at several streamwise locations over the range $29 \leq x^+ \leq 354$. Off-centerplane measurements are made over a limited circumferential region from $-17 \leq z^+ \leq 17$. The confirmation of the rollup of a junction vortex and the presence of a small separation region behind the bump are discussed in Section 5.2. The remainder of the chapter will focus on the velocity measurements in the development and recovery regions downstream of the bump ($58 \leq x^+ \leq 354$), which are the regions of primary interest in this investigation.

The velocity data is obtained using both the TSI coincidence mode and the external digitization method. The TSI coincidence mode measurements, obtained for $\pm z^+$, indicate that the streamwise (u) and radial (v) velocity statistics are symmetric about the centerplane, while the spanwise (w) velocity statistics are anti-symmetric. Therefore, all statistics involving odd powers of w will be anti-symmetric about the centerplane, while all others will be symmetric. With this in mind, the off-centerplane externally digitized measurements are made only for negative z^+ .

The velocity profile data are normalized by the undisturbed value of the friction velocity unless otherwise noted. This method of normalizing provides direct comparisons of the measured quantities at the same physical distance from the wall. The reference curves

appearing throughout the figures in this chapter are the undisturbed turbulent boundary layer data reported in Chapter 4.

5.1.2 Summary of the Characteristics of the Global Flow Field

The following discussion briefly describes the global flow field, as interpreted from the measurement set, around and downstream of the bump. An unscaled illustration of the global flow field is shown in Figure 5.1. A junction vortex is formed immediately upstream of the bump by the impact of the near wall boundary layer on the bump. The vortex wraps around the bump and is convected downstream forming a pair of counter-rotating quasi-streamwise vortices. The counter-rotating vortices are approximately 10 to 15 wall units in diameter and are confined to the near wall region of $y^+ < 20$. The counter-rotating vortices are observed to intermittently wander in the spanwise direction, occasionally crossing the plane of symmetry of the bump. As the vortices convect downstream, they slowly diverge in the spanwise direction increasing their spanwise separation. A second vortical structure is present at a slightly higher position in the boundary layer. The origin and cause of this second structure is speculated to be a shedding shear layer originating near the top of the bump. A significant radial and spanwise convergence of mean flow occurs over a narrow region from $0 < y^+ \leq 20$, and extends for more than 100 wall units downstream. This region plays a significant role in the dynamics of the centerplane turbulence modifications. The interpretation of a highly three-dimensional unsteady turbulent flow from single-point statistics and two-point correlations is somewhat subjective. The interpretations of the measured data to be presented are believed to best explain the measured results; however, they may not be the only possible interpretations.

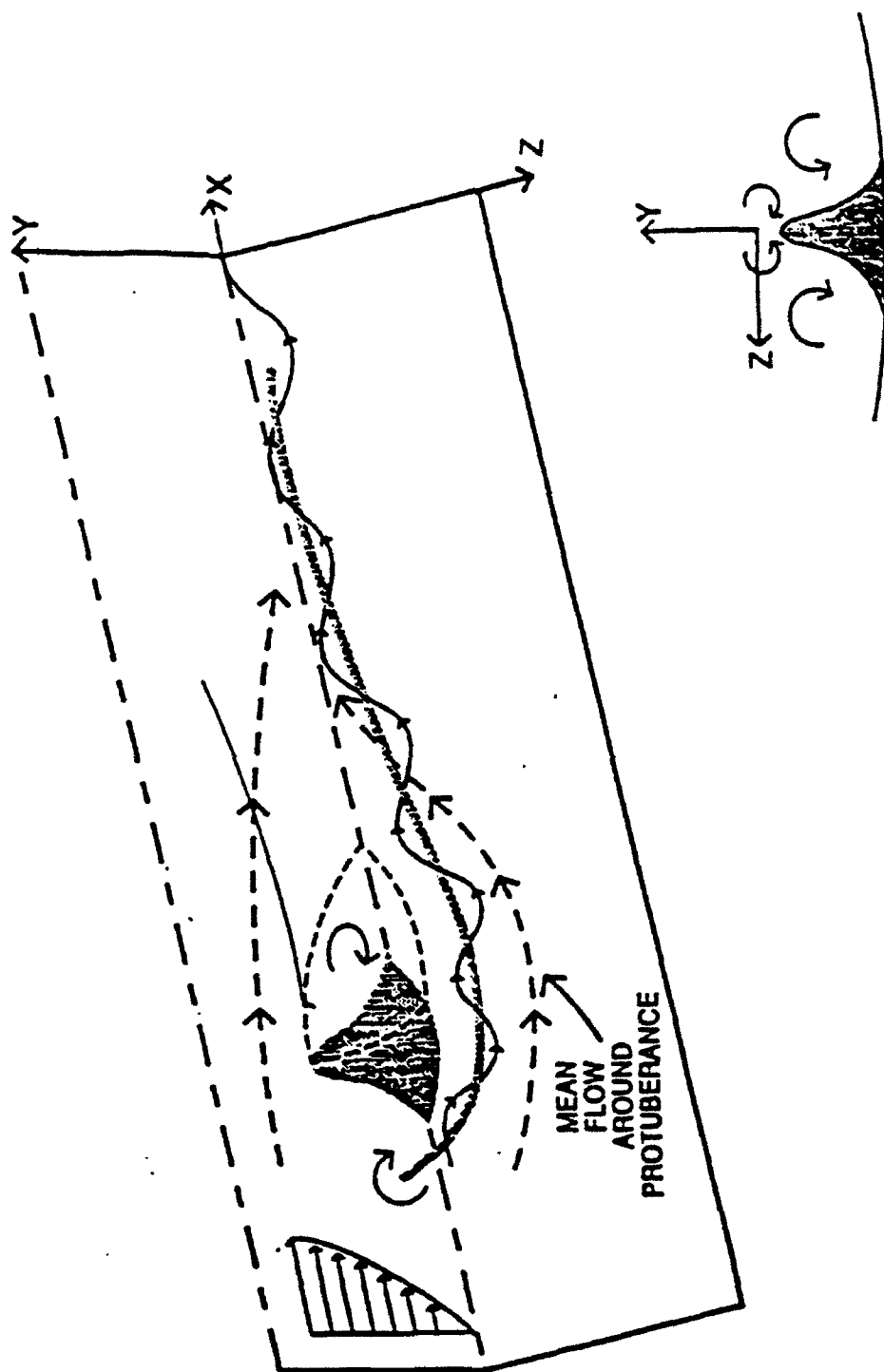


Figure 5.1 Illustration of global flow field around and downstream of the bump. Figure is not to scale

5.2 Local Velocity Measurements Around the Bump

5.2.1 Confirmation of the Junction Vortex

A limited number of two-component U and V velocity measurements are made immediately upstream of the bump to confirm the rollup of a junction vortex. Figure 5.2 shows a vector map of the measurements in front of the bump. The vectors indicate that there is a small region of reverse flow near the wall at $x^* = -10$. A weak rotational velocity pattern is apparent near the intersection of the bump with the pipe wall. Histograms of the streamwise velocity measurements along the wall $-17 < x^* < -10$ show intermittent backflow for $y^* < 3$. In addition, negative velocities are also observed in the histograms at $x^* = -10$ for $y^* \leq 6$. The negative velocity samples at $y^* = 6$ occur much less frequently and are considerably lower in magnitude than closer to the wall. A detailed characterization of the upstream junction vortex is not the focus of this investigation. The reader is referred to Devenport and Simpson (1990) and Shekarriz et al. (1992) for more complete studies of the behavior of junction vortices.

Robinson (1991) showed that the intensity of the vortical structures in a turbulent boundary layer could be characterized by a normalized vortex Reynolds number defined by;

$$\frac{R_v}{A^*} = \frac{\Gamma}{2\pi\nu A^*} \quad 5.1$$

The normalized area A^* is defined as the cross-sectional area enclosed by the path used to compute the vortex circulation Γ . An order of magnitude estimate of the circulation of the junction vortex can be obtained from the measured velocity field upstream. The circulation is estimated by integrating the velocity field around a path enclosing the vortex. Because the junction vortex is aligned with the mean spanwise vorticity of the boundary layer, this

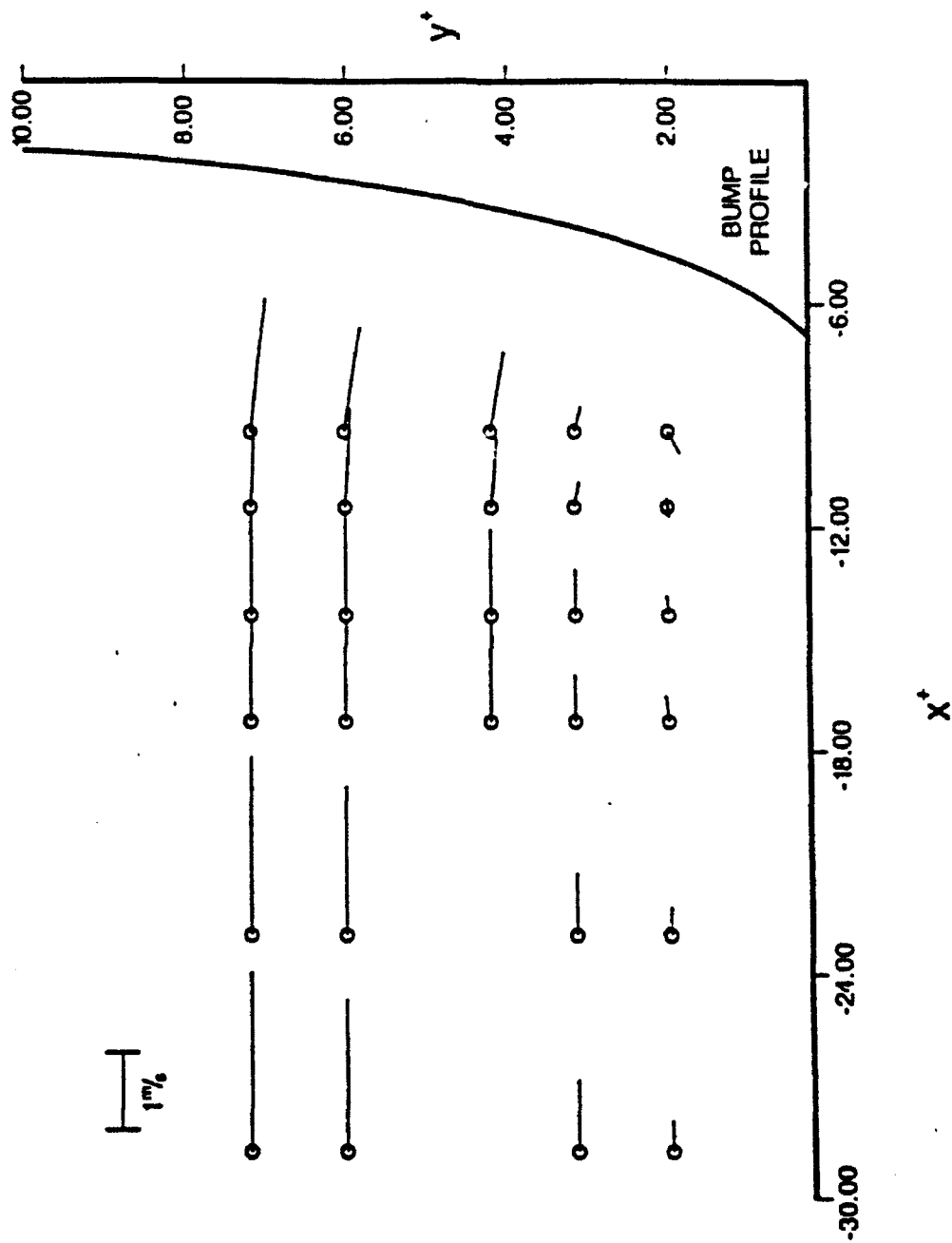


Figure 5.2 Two-component velocity vectors upstream of the bump, measured along the centerplane of the bump in the x - y plane

estimate of the circulation contains both the vortex circulation and a component due to the approaching mean velocity gradient. The circulation of the vortex can be estimated by subtracting the circulation due to the mean velocity gradient from the computed circulation of the measured velocity field in front of the bump. The mean velocity gradient circulation is obtained by integrating the approaching mean velocity profile around a similar integration path as that used for the vortex. The estimated value of R_v/A^+ for the junction vortex is approximately 0.022. This order of magnitude estimate compares favorably with the distribution of near wall vortex intensities observed by Robinson (1991) for both spanwise and quasi-streamwise vortices in the turbulent boundary layer simulation of Spalart (1988).

The junction vortex wraps around the bump forming a pair of counter-rotating quasi-streamwise vortices sharing a common flow down between them. Measurements, to be discussed shortly, indicate that the legs of the counter-rotating vortices are approximately 10 to 15 wall units in diameter. The vortices are confined to the near wall region as they convect downstream. The strength of the quasi-streamwise counter-rotating vortices should be on the order of magnitude of the junction vortex initially and decrease with increasing streamwise distance from the bump. The vortices are stretched as they convect around the bump and then slowly diffuse as they travel downstream and interact with the near wall turbulent boundary layer.

5.2.2 Confirmation of a Downstream Separation Zone

Streamwise velocity measurements obtained at several streamwise and radial locations between $13.5 \leq x^+ \leq 29$ indicate that a small separation region exists immediately downstream of the bump. Measured negative streamwise velocities near the wall confirm the

recirculation zone inside the separation bubble. The measurements indicate that the separation region extends to $x^+ \approx 25$.

5.3 Measurements in the Development and Recovery Region $58 \leq x^+ \leq 350$

5.3.1 Mean Velocity Results

A reduction in local skin friction, τ_w , is observed along the centerplane and persists approximately 180 wall units downstream of the bump. The axial and spanwise recovery of the wall shear stress is shown in Figure 5.3. The mean streamwise velocity profiles exhibit an upward shift of the log region when scaled with the reduced value of the friction velocity and plotted in wall coordinates as shown in Figure 5.4. Walker and Tiederman (1990) and Fontaine et al. (1992) among others have shown a similar behavior in skin friction reduced profiles of flows with drag reducing polymers. A gradual recovery in the mean velocity profile is observed in the axial direction. Full recovery of the wall shear stress on the centerplane occurs by $x^+ = 350$. The profiles at $x^+ = 58$ do not exhibit any noticeable distortions in their shape due to either the bump or the short separation zone behind the bump. The spanwise development of the mean velocity profiles are similar to the axial development but relax over a much smaller distance of $z^+ \approx -17$. While significant local skin friction reduction is observed over a considerable area, this is more than offset by the form drag on the element. An order of magnitude estimate of the form drag from measured velocity profiles around the element is approximately four to five times larger than the resulting skin friction reduction.

The spanwise development of the mean radial and circumferential velocity profiles at $x^+ = 58$ are shown in Figures 5.5 and 5.6. The profiles at $x^+ = 58$ clearly indicate a mean

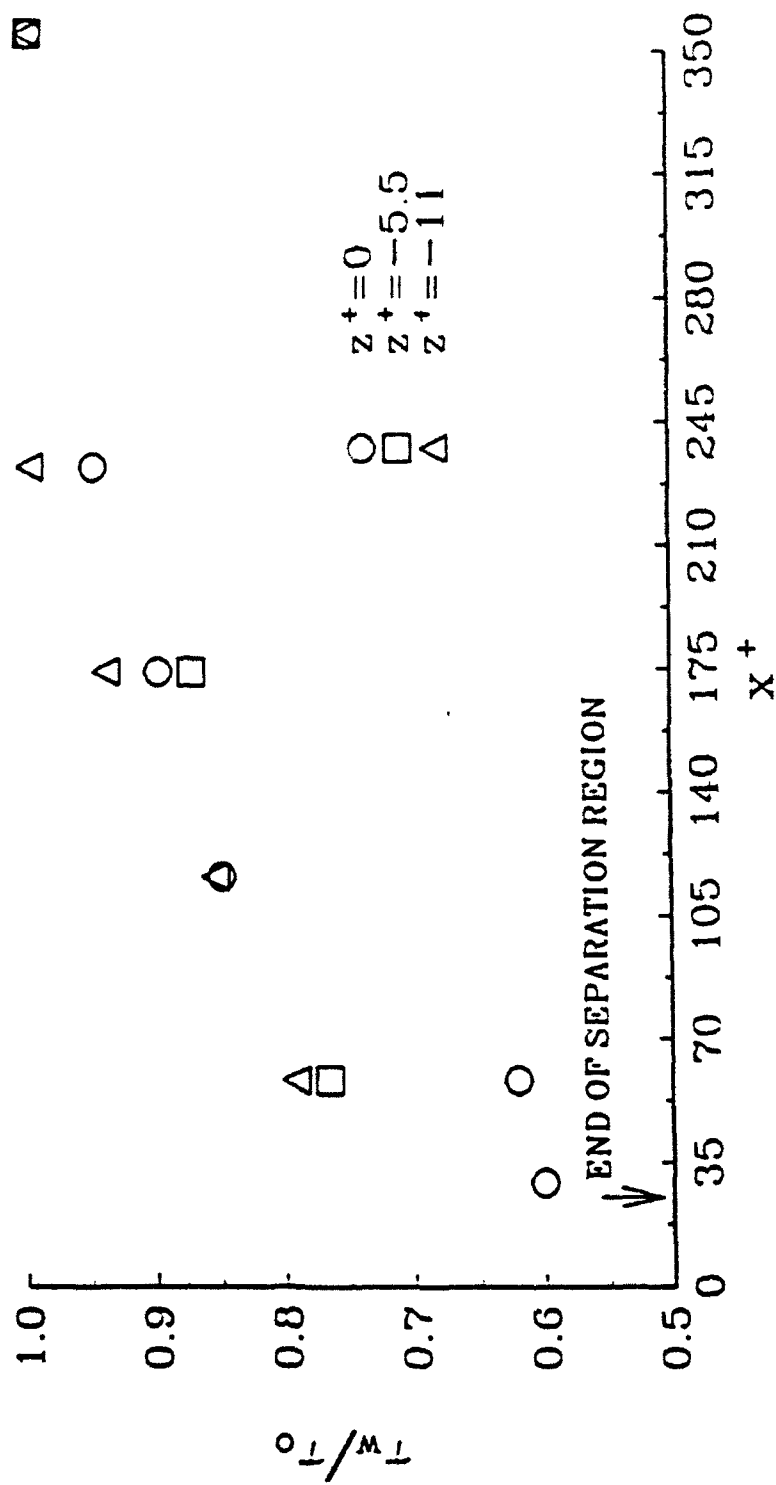


Figure 5.3 Development of the normalized wall shear stress downstream of the bump. The wall shear stress is normalized by the value obtained in the undisturbed glycerin tunnel boundary layer

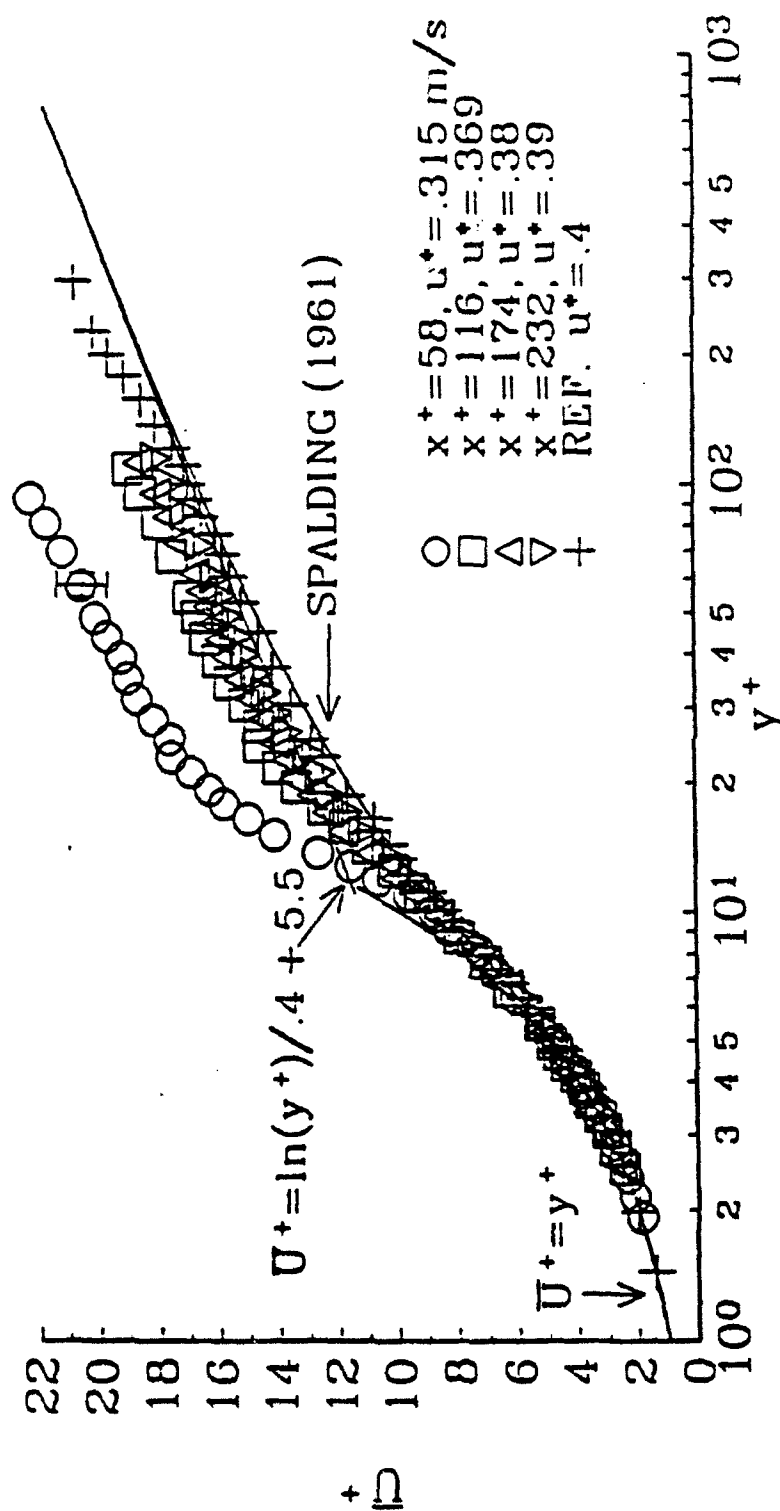


Figure 5.4 Axial development of the streamwise mean velocity profiles downstream of the bump. The profiles are measured along the centerplane and are normalized by local friction velocity

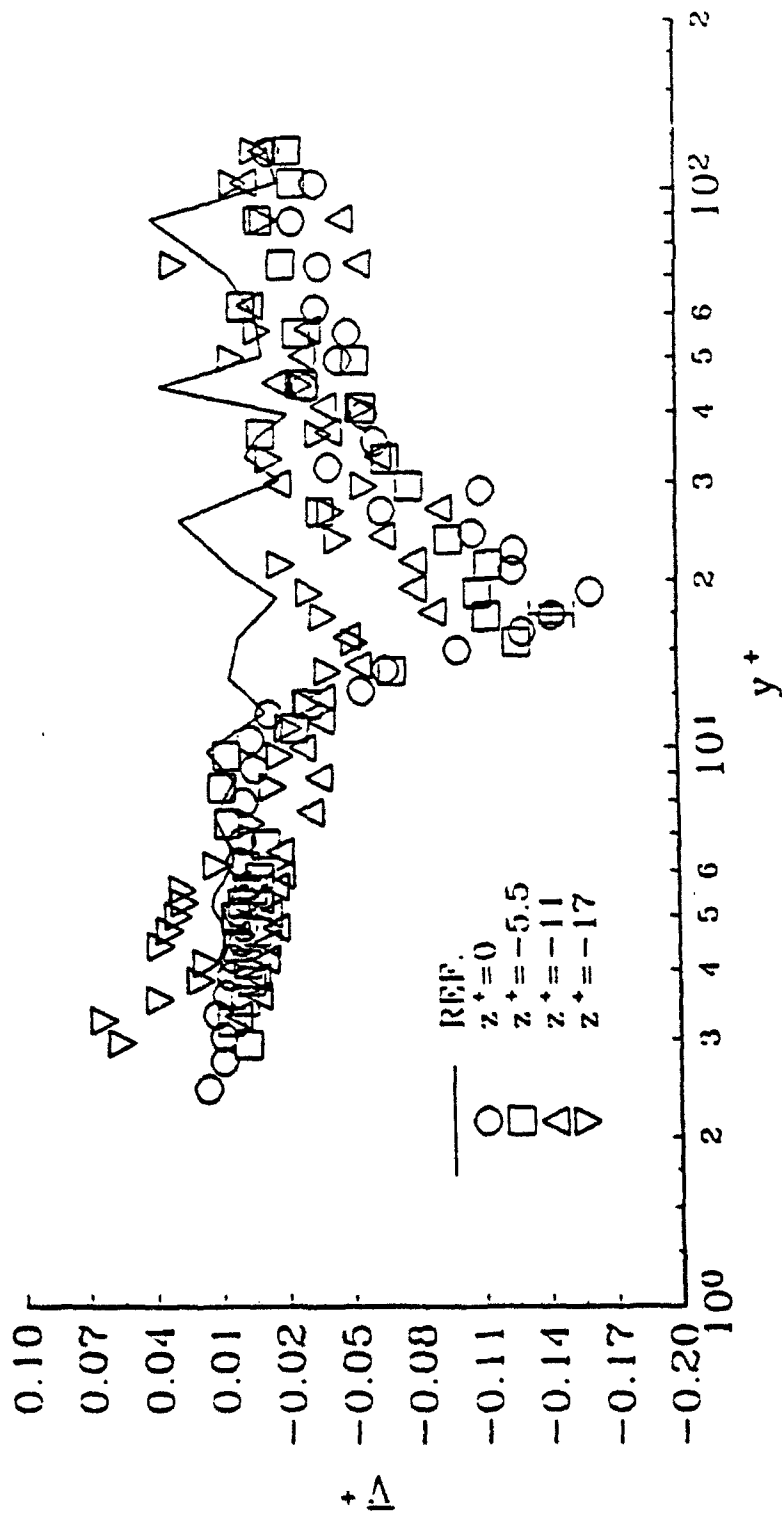


Figure 5.5 Spanwise development of the radial mean velocity profile at $x' = 58$
Normalization with ref. u'

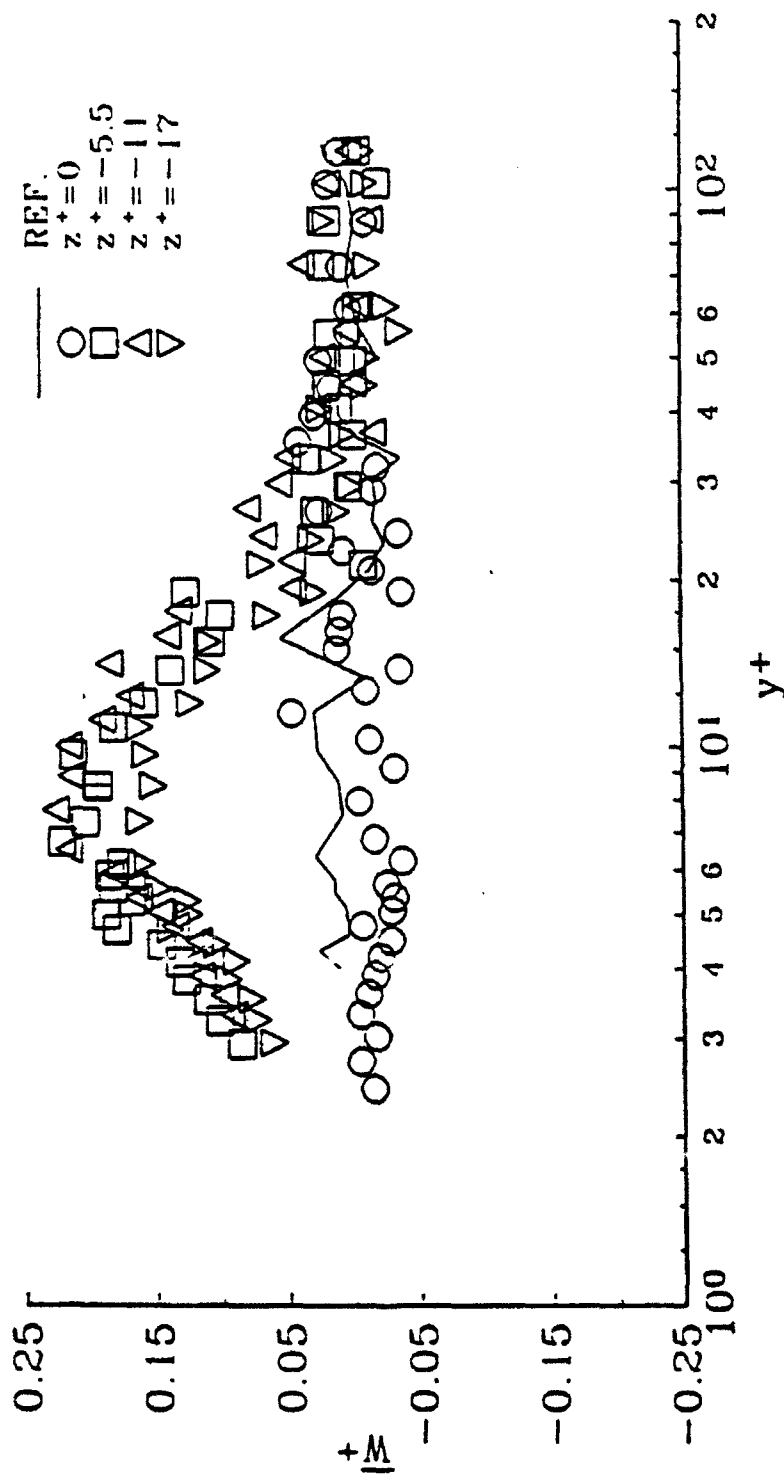


Figure 5.6 Spanwise development of the circumferential mean velocity profile at $x^* = 58$
Normalization with ref. u^*

flow converging towards the centerplane and the wall. The spanwise velocity profiles show an influx of fluid converging towards the centerplane for $y^+ < 20$, with a peak occurring over the range $7 \leq y^+ \leq 10$. A radial downwash towards the wall occurs above the spanwise influx for $10 \leq y^+ \leq 40$ and peaks at $y^+ = 20$. The mean radial velocity is approximately zero below $y^+ = 10$. Recovery of the mean radial velocity profiles occurs slowly with increasing streamwise distance, and is fully accomplished by $x^+ = 232$. The spanwise velocity profiles show a more rapid recovery with x^+ . The spanwise mean velocity is fully recovered by $x^+ = 174$, while a weak radial downflow still occurs over the region $10 \leq y^+ \leq 40$. This weak downflow is approximately 33% of the radial velocity magnitude at $x^+ = 58$.

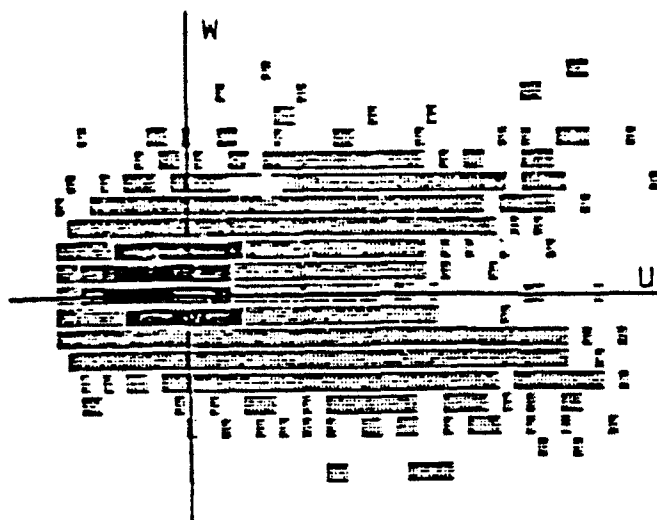
The radial velocity profiles relax with increasing spanwise distance. The radial velocity becomes positive for $y^+ < 6$, at $z^+ = -17$. The positive radial velocity near the wall may be a result of the other side of the quasi-streamwise vortex pumping fluid away from the wall. The spanwise velocity profiles show little relaxation over the same spanwise displacement. Convergence of flow towards the centerplane is a dominant feature governing the dynamics of the turbulence for $y^+ < 20$. It is speculated that in the region of mean flow convergence a suppression of radial and spanwise turbulent velocity fluctuations occurs. Outward moving fluid in the form of turbulent fluctuations must overcome the wallward and centrally oriented forces due to the spanwise and radial momentum influx.

5.3.2 Turbulent Velocity Fluctuation Statistics

5.3.2.1 Turbulent Velocity Hodographs

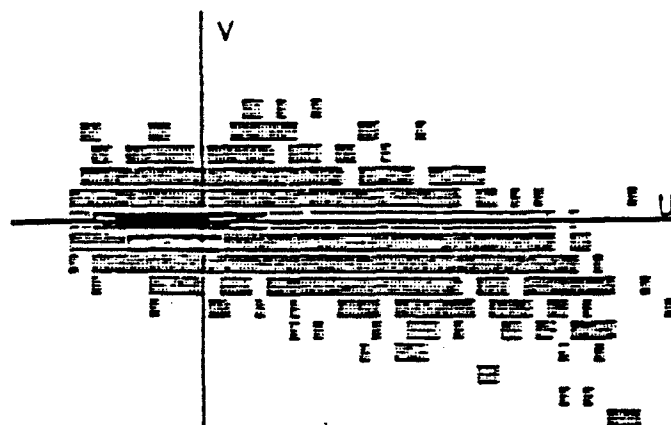
Two-dimensional hodograph planes of the turbulent velocity fluctuations, both on and off the centerplane, confirm the presence of counter-rotating vortices straddling the centerplane near the wall. Figures 5.7 - 5.10 show hodograph planes at several spanwise locations for $y^+ = 5$ and $x^+ = 58$. The hodographs shown in the figures represent contours of the joint probability density of the velocity fluctuations in two-dimensional planes. The highest probability corresponds to the darkest shading. The intersection of the axis lines in the figures represents the location of the mean value. The bin widths, defined BINW in the figures, correspond to the width of the velocity bins used to estimate the probability density. For example, the bin widths in Figure 5.7a are 0.78 m/s wide for the streamwise and 0.185 m/s high for the spanwise velocities.

The bimodal uw hodographs, on the centerplane, indicate that the vortices intermittently wander from side to side in the spanwise direction occasionally crossing the centerplane. As a leg of the vortex pair crosses the centerplane, it leaves its signature in the instantaneous velocity measurements - that is, a high positive u accompanied by a strong positive or negative w fluctuation. Off-centerplane hodographs show a change from the bimodal uw hodograph to a unimodal hodograph as the LDV probe volume slices through only one leg of the counter-rotating vortex pair. The hodographs also indicate that a downwash is created by the counter-rotating vortices. These results are observed with to persist with increasing streamwise displacement; however, the magnitudes of the velocity fluctuations associated with the wandering counter-rotating vortices decrease downstream. The near wall bimodal behavior of the u - w velocities is still evident at $x^+ = 174$.



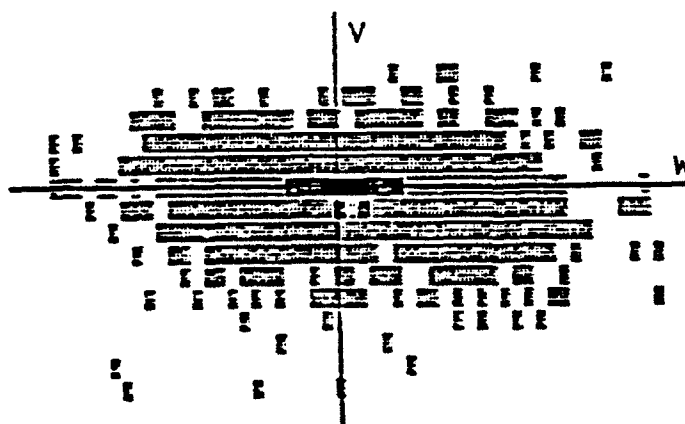
	U	W
MEAN	1.202	-.011
S.D.	.512	.261
MIN.	.298	-1.661
MAX.	4.369	1.771
BINW	.078	.185
CORR	-.048	
	<div style="display: flex; align-items: center;"> <div style="width: 10px; height: 10px; background-color: black; margin-right: 5px;"></div> > 548. Points </div>	
	<div style="display: flex; align-items: center;"> <div style="width: 10px; height: 10px; background-color: black; margin-right: 5px;"></div> > 366. Points </div>	
	<div style="display: flex; align-items: center;"> <div style="width: 10px; height: 10px; background-color: black; margin-right: 5px;"></div> > 183. Points </div>	
	<div style="display: flex; align-items: center;"> <div style="width: 10px; height: 10px; background-color: black; margin-right: 5px;"></div> > 0. Points </div>	

a)



	U	V
MEAN	1.202	-.003
S.D.	.512	.053
MIN.	.298	-.686
MAX.	4.369	.394
BINW	.078	.074
CORR	-.204	
	<div style="display: flex; align-items: center;"> <div style="width: 10px; height: 10px; background-color: black; margin-right: 5px;"></div> > 1002. Points </div>	
	<div style="display: flex; align-items: center;"> <div style="width: 10px; height: 10px; background-color: black; margin-right: 5px;"></div> > 666. Points </div>	
	<div style="display: flex; align-items: center;"> <div style="width: 10px; height: 10px; background-color: black; margin-right: 5px;"></div> > 334. Points </div>	
	<div style="display: flex; align-items: center;"> <div style="width: 10px; height: 10px; background-color: black; margin-right: 5px;"></div> > 0. Points </div>	

b)



	W	V
MEAN	-.011	-.003
S.D.	.281	.053
MIN.	-1.661	-.686
MAX.	1.771	.394
BINW	.066	.074
CORR	-.188	
	<div style="display: flex; align-items: center;"> <div style="width: 10px; height: 10px; background-color: black; margin-right: 5px;"></div> > 1603. Points </div>	
	<div style="display: flex; align-items: center;"> <div style="width: 10px; height: 10px; background-color: black; margin-right: 5px;"></div> > 1069. Points </div>	
	<div style="display: flex; align-items: center;"> <div style="width: 10px; height: 10px; background-color: black; margin-right: 5px;"></div> > 534. Points </div>	
	<div style="display: flex; align-items: center;"> <div style="width: 10px; height: 10px; background-color: black; margin-right: 5px;"></div> > 0. Points </div>	

c)

Figure 5.7 Joint probability density contours shown in the two-component hodograph planes at $x^* = 58$, $y^* = 5$ and $z^* = 0$. a) uw, b) uv, c) vw

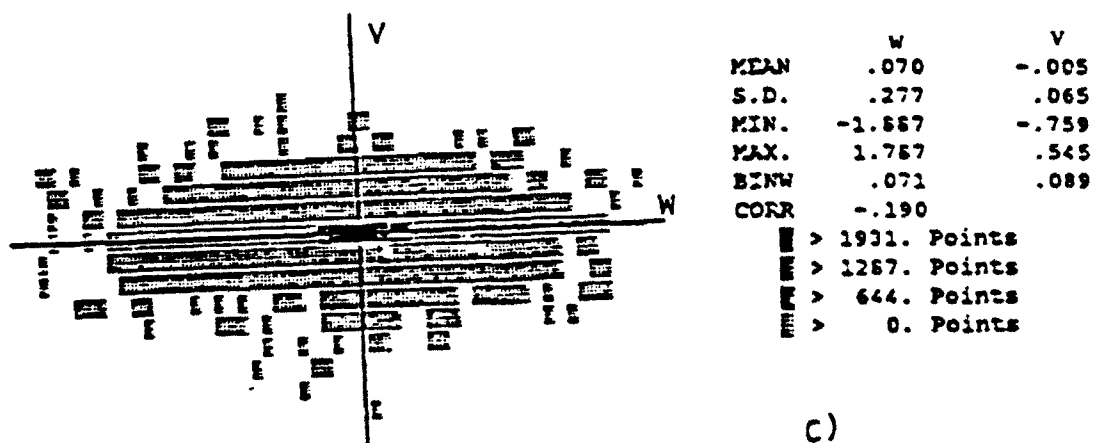
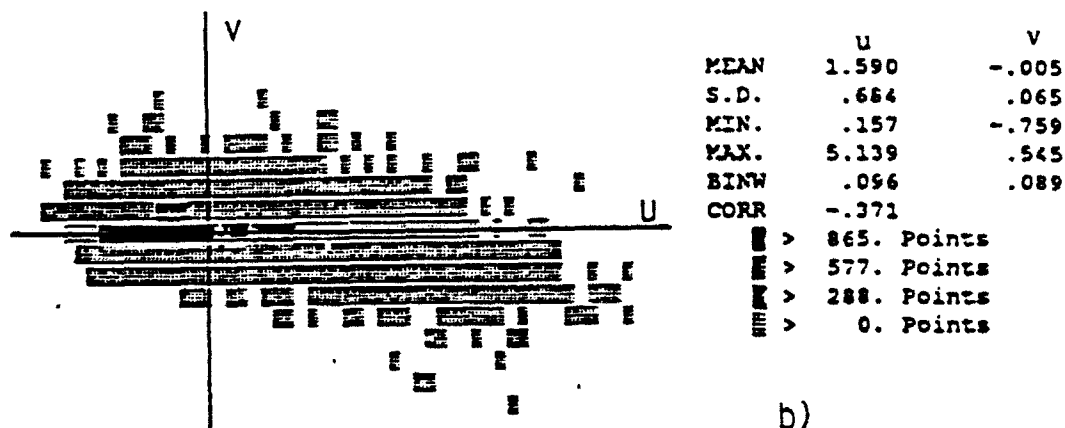
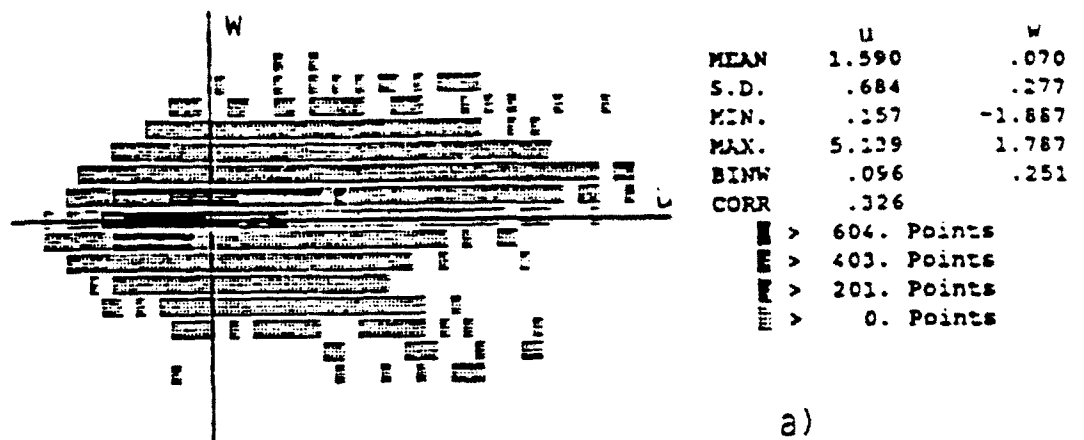
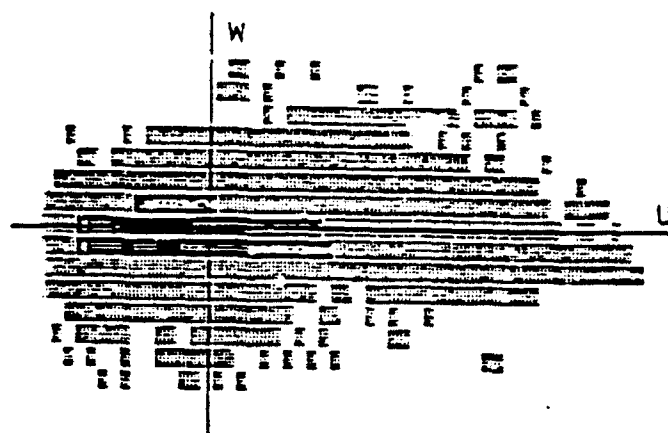


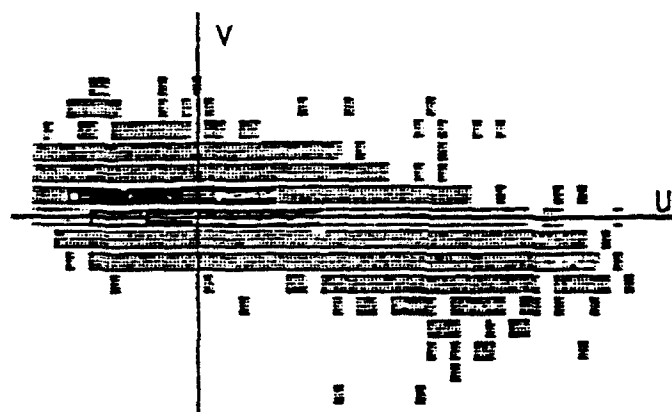
Figure 5.8 Joint probability density contours shown in the two-component hodograph planes at $x^* = 58$, $y^* = 5$ and $z^* = -5.5$. a) uw, b) uv, c) vw



	U	W
MEAN	1.619	.047
S.D.	.699	.239
MIN.	.338	-1.520
MAX.	4.839	1.661
BINW	.087	.217
CORR	.095	

█ > 459. Points
 █ > 306. Points
 █ > 153. Points
 █ > 0. Points

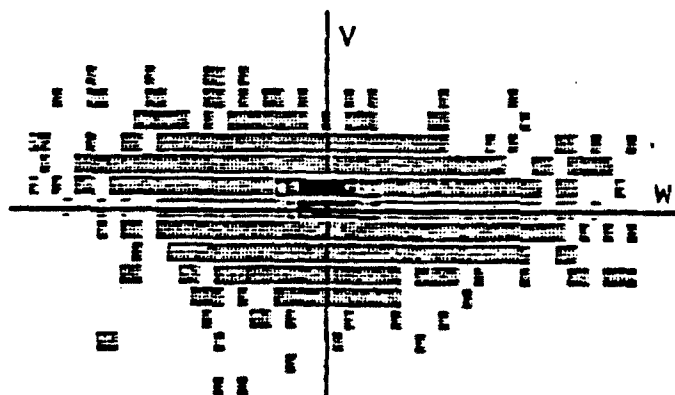
a)



	U	V
MEAN	1.619	-.013
S.D.	.699	.062
MIN.	.338	-.698
MAX.	4.839	.424
BINW	.087	.076
CORR	-.510	

█ > 668. Points
 █ > 446. Points
 █ > 223. Points
 █ > 0. Points

b)



	W	V
MEAN	.047	-.013
S.D.	.229	.062
MIN.	-1.520	-.698
MAX.	1.661	.424
BINW	.061	.076
CORR	-.097	

█ > 1311. Points
 █ > 874. Points
 █ > 437. Points
 █ > 0. Points

c)

Figure 5.9 Joint probability density contours shown in the two-component hodograph planes at $x^* = 58$, $y^* = 5$ and $z^* = -11$. a) uw, b) uv, c) vw

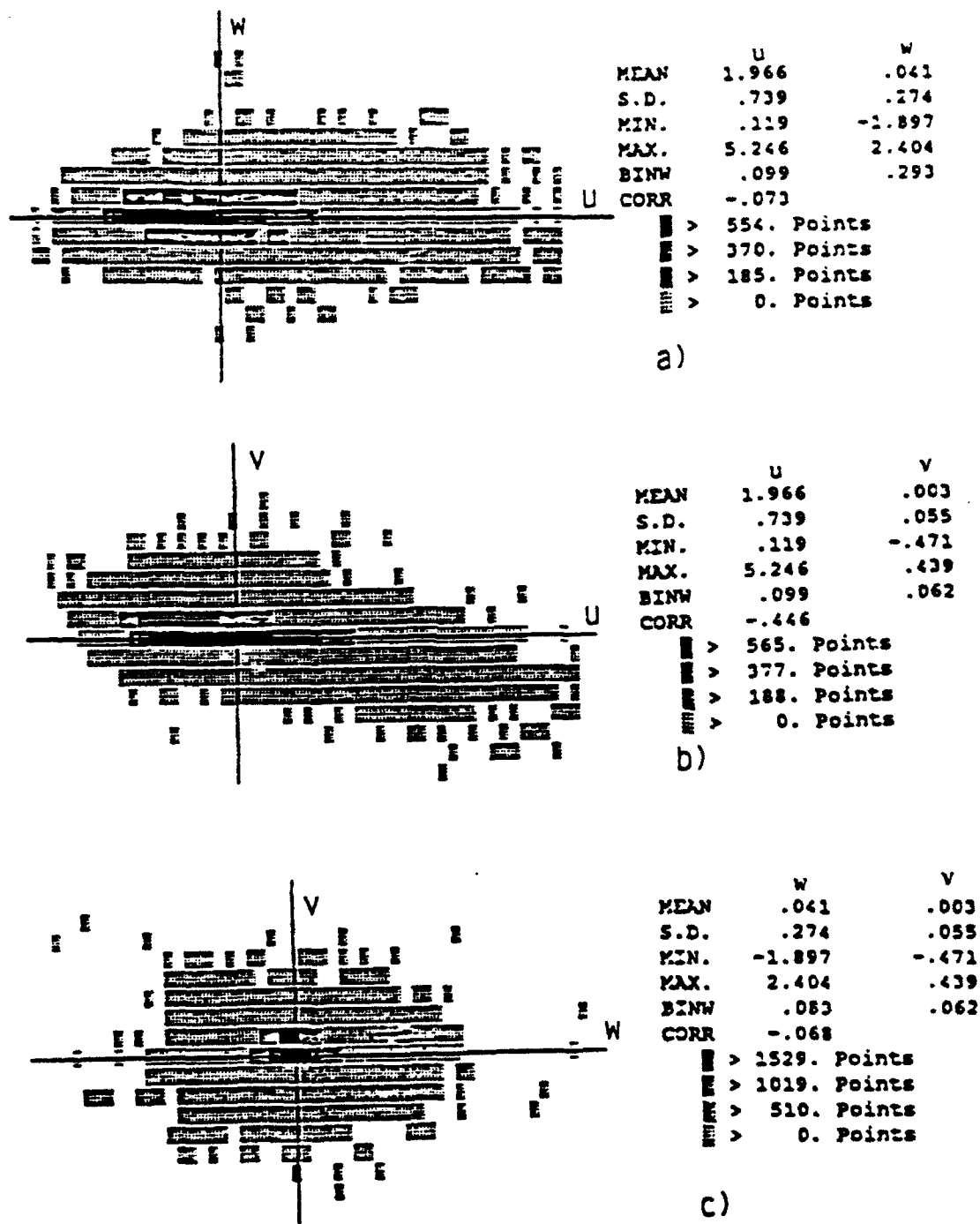


Figure 5.10 Joint probability density contours shown in the two-component hodograph planes at $x^* = 58$, $y^* = 5$ and $z^* = -17$. a) uw, b) uv, c) vw

5.3.2.2 RMS Velocity Measurements

Centerplane profiles of the streamwise rms velocity, u' , are plotted as a function of axial position in Figure 5.11. The profiles indicate that the u' peak is shifted farther from the wall and its magnitude is slightly higher than the reference peak levels. The magnitude of the u' levels are decreased for $y^+ < 20$. The peak occurring at $y^+ \approx 25$ is slightly elevated over the magnitude of the peak levels in the reference curve. These results suggest that the effective size of the sublayer and buffer region has increased, thus shifting the profiles in y^+ . This behavior in the u' profiles is similar to that reported by Fontaine et al. (1992) for drag reduced turbulent boundary layers with polymers, except that the magnitude of the peak in the u' profiles does not increase with polymers. The profiles show a continual recovery beyond 232 wall units in the axial direction and appear to overshoot the reference levels below $y^+ = 4$, at the last measurement location. The spanwise recovery of the u' profiles is complex. At $x^+ = 58$, the u' profiles relax towards reference levels with increasing $|z^+|$ and slightly overshoot the reference levels at $z^+ = -17$. However, at $x^+ = 116$, spanwise relaxation of the u' profiles is not observed from $-11 \leq z^+ \leq 0$. The u' profiles at $x^+ = 174$, shown in Figure 5.12, first decrease with increasing spanwise displacement and then rapidly relax and overshoot the reference levels near the wall, at $z^+ = -17$.

Surprisingly, the radial rms velocity, v' , profiles indicate little change from the reference levels in both centerplane and off-centerplane measurements. Figure 5.13 shows centerplane recovery as a function of axial position. The v' levels may be slightly lower than reference levels for $17 \leq y^+ \leq 30$ at $x^+ = 58$ and may show a slight increase for $y^+ < 20$, at $x^+ = 174$. However, these small changes are within the uncertainty of the measurements.

The axial development of the spanwise rms velocity profiles is shown in Figure 5.14. A small decrease in the near wall levels, below $y^+ = 5$, is observed at $x^+ = 58$. The near

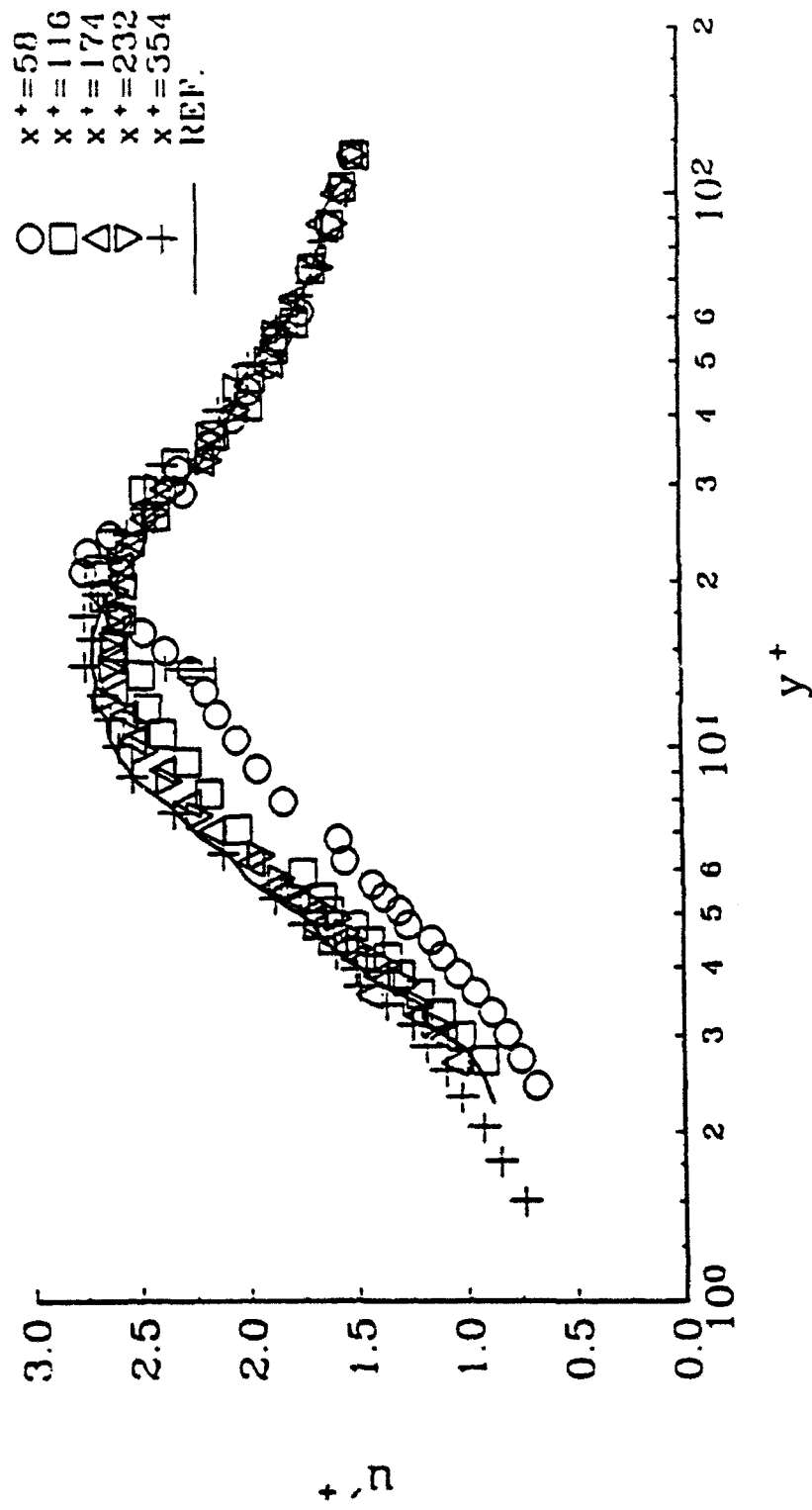


Figure 5.11 Axial development of the streamwise rms velocity profiles along the centerplane.
Normalization with ref. u^+

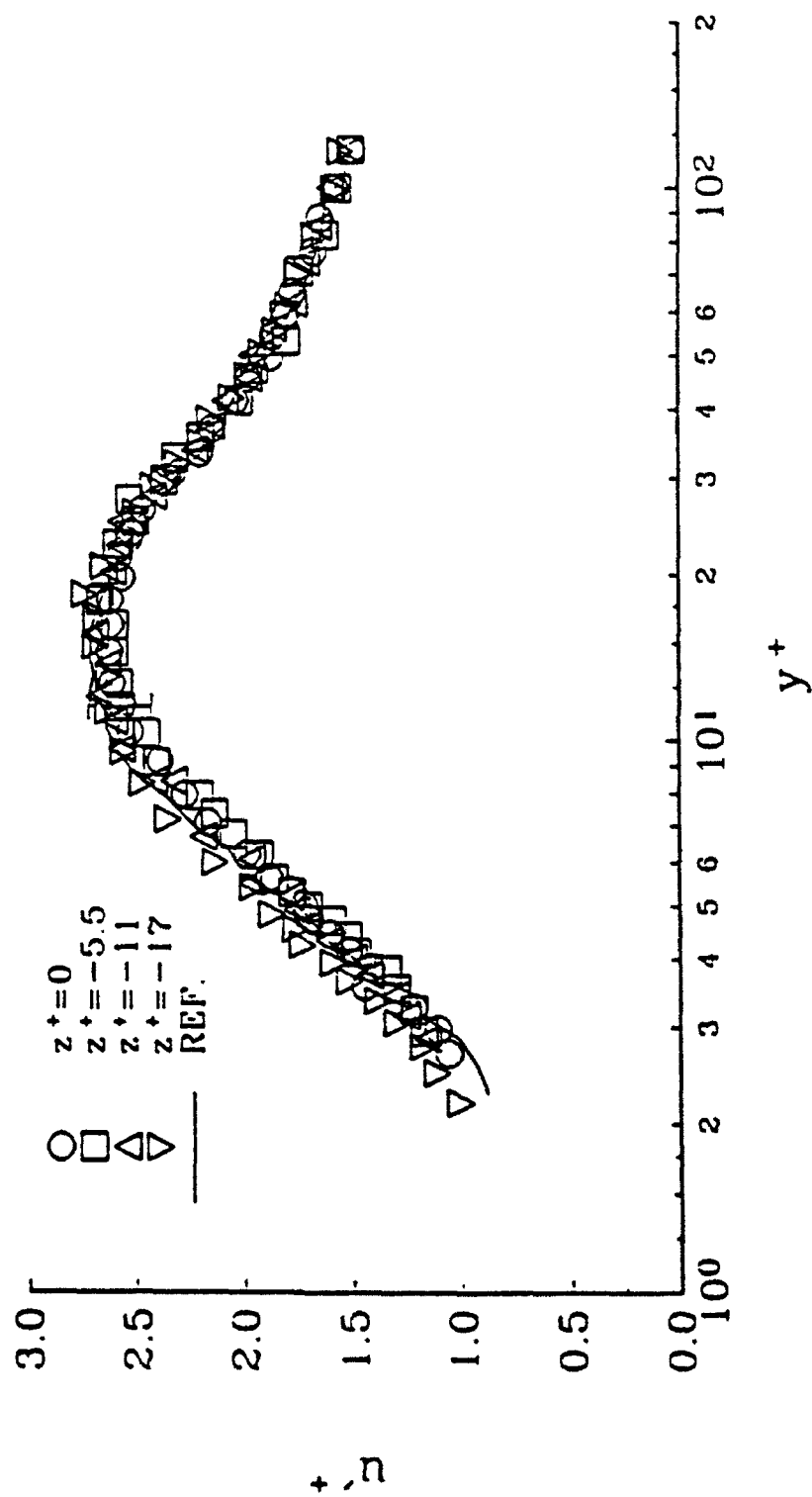


Figure 5.12 Spanwise development of the streamwise rms velocity profiles at $x^+ = 174$.
Normalization with ref. u^+

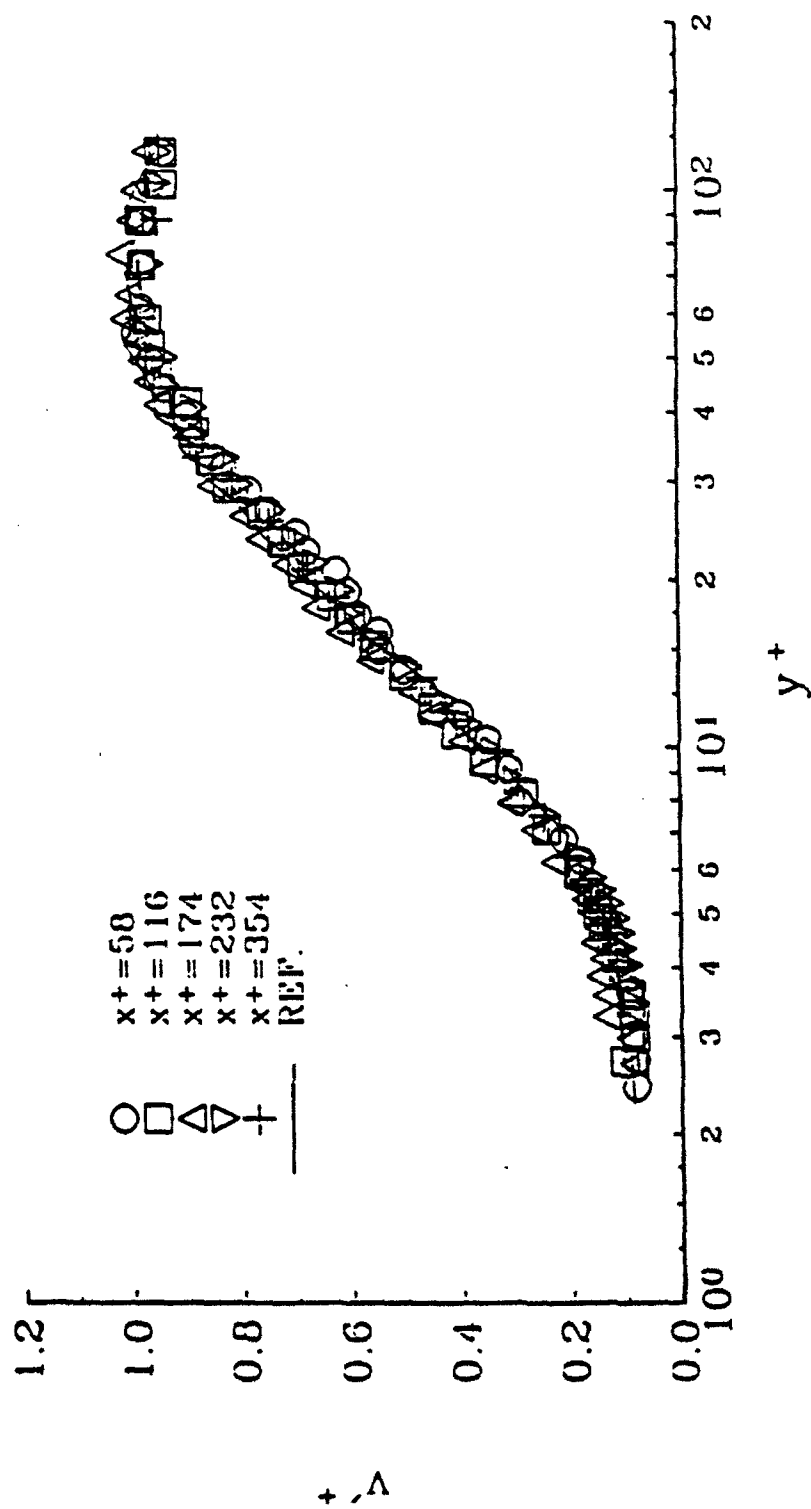


Figure 5.13 Axial development of the radial rms velocity profiles along the centerplane.
Normalization with ref. u^*

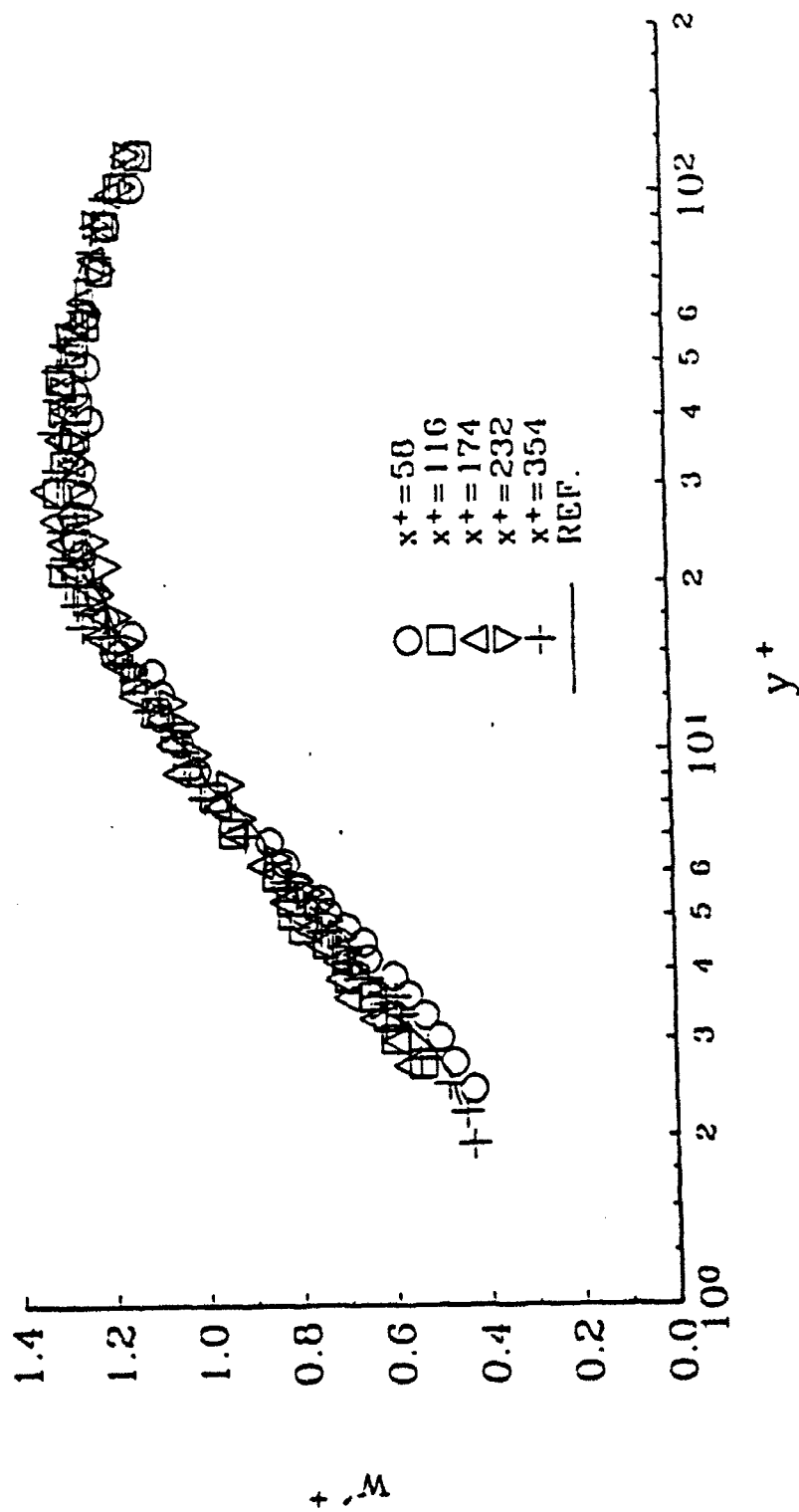


Figure 5.14 Axial development of the circumferential rms velocity profiles along the centerplane.
Normalization with ref. u^+

wall region relaxes with increasing x^+ and overshoots reference levels slightly below $y^+ = 20$, at $x^+ = 116$ and 174 . However, the magnitude of these changes is small, approaching the experimental uncertainty of the measurements. Full recovery of the w' profiles is observed by $x^+ = 354$. Figure 5.15 illustrates the off-centerplane behavior of the spanwise rms levels at $x^+ = 58$. The w' levels are observed to continually decrease to $z^+ = -11$, then increase with further spanwise displacement. This trend with increasing spanwise displacement persists with x^+ but with smaller changes in the magnitudes of the w' profiles compared to reference levels. The w' profiles are independent of spanwise position by $x^+ = 174$.

The near wall behavior in the rms velocities is due to a combined effect of the mean flow convergence towards the centerplane and the presence and wandering of the vortices off the centerplane. The reduced centerplane u' levels result from inhibited turbulent fluctuations due to the mean flow convergence. It is speculated that the converging mean flow has a similar effect on the v' and w' levels. However, the vortices act to increase turbulent transport which results in increasing these rms levels. The intermittent wandering of the vortices continually brings velocity fluctuations into the centerplane and off-centerplane near wall region. Radial and circumferential fluctuations are directly created by the rotational motion of the counter-rotating vortices. Streamwise fluctuations are created by the entrainment of high velocity fluid from above toward the wall. In addition, it is likely that the vortices become skewed with respect to the axial direction as they wander. This generates a streamwise fluctuation which is proportional to the magnitude of the spanwise fluctuation and the skew angle. It is particularly interesting that the increased turbulence activity, by the vortices, is sufficient to offset any centerplane reductions in the radial and spanwise rms levels due to the mean flow convergence. However, the reduction of the streamwise rms levels is

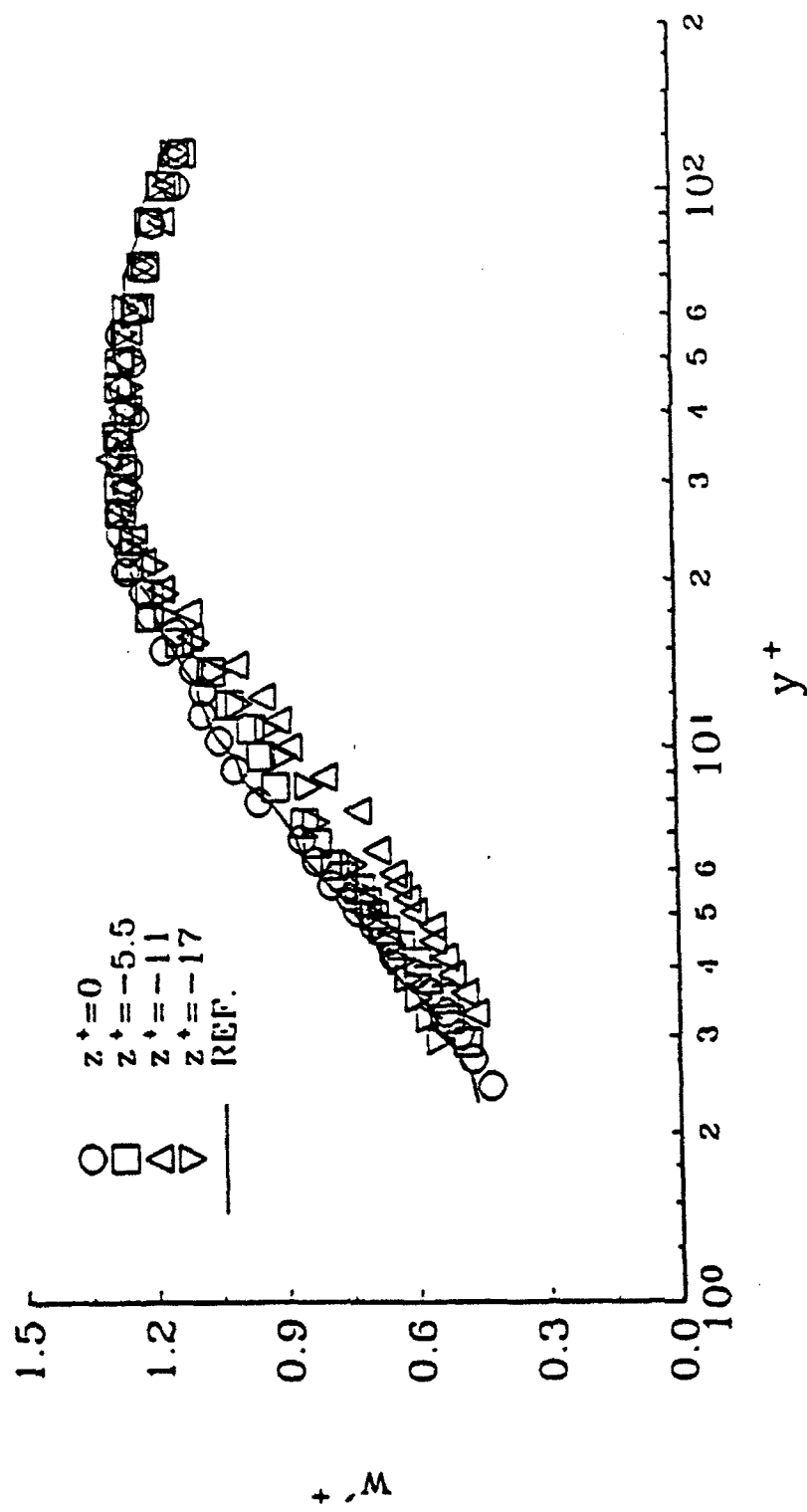


Figure 5.15 Spanwise development of the circumferential rms velocity profiles at $x^* = 58$.
Normalization with ref. u^*

not completely offset by the increased turbulent activity.

The circumferential rms velocity behavior in the spanwise direction is directly related to the wandering of the vortices. An examination of the uw probability density contours in Figures 5.7 - 5.10 indicate that the width of the high probability w contours are a maximum on the centerplane and decrease with increasing spanwise movement to $z^+ = -11$. A slight increase is observed in the contour widths from $z^+ = -11$ to $z^+ = -17$. The presence of the other vortex, in the form of negative w fluctuations, is felt less and less with increasing spanwise movement due to the finite span over which the vortices can wander. On the centerplane there is a high probability for both positive and negative w fluctuations, which increases the variance in the data.

5.3.2.3 Reynolds Stress Data

The Reynolds stress profiles are significantly modified downstream of the bump. The axial development and recovery of the uv component of the Reynolds stress along the centerplane is shown in Figure 5.16. At $x^+ = 58$, a significant decrease in the uv levels is observed for $y^+ < 15$, with an increase over reference levels at $y^+ \approx 23$. A relaxation towards reference levels is observed with increasing streamwise distance and full recovery occurs by $x^+ = 232$. At $x^+ = 116$, a small reduction is still observed below $y^+ = 9$, while the peak at higher y^+ is broader and shifted further from the wall to $y^+ \approx 30$. The significant decrease in uv near the wall results from a suppression of burst type motions caused by the convergence of fluid towards the centerplane and the wall. The increased levels at $y^+ > 20$ indicate that a second structure is present. The broadening and shift of the increased uv levels, from $x^+ = 58$ to 116, suggests that the structure increases in size and

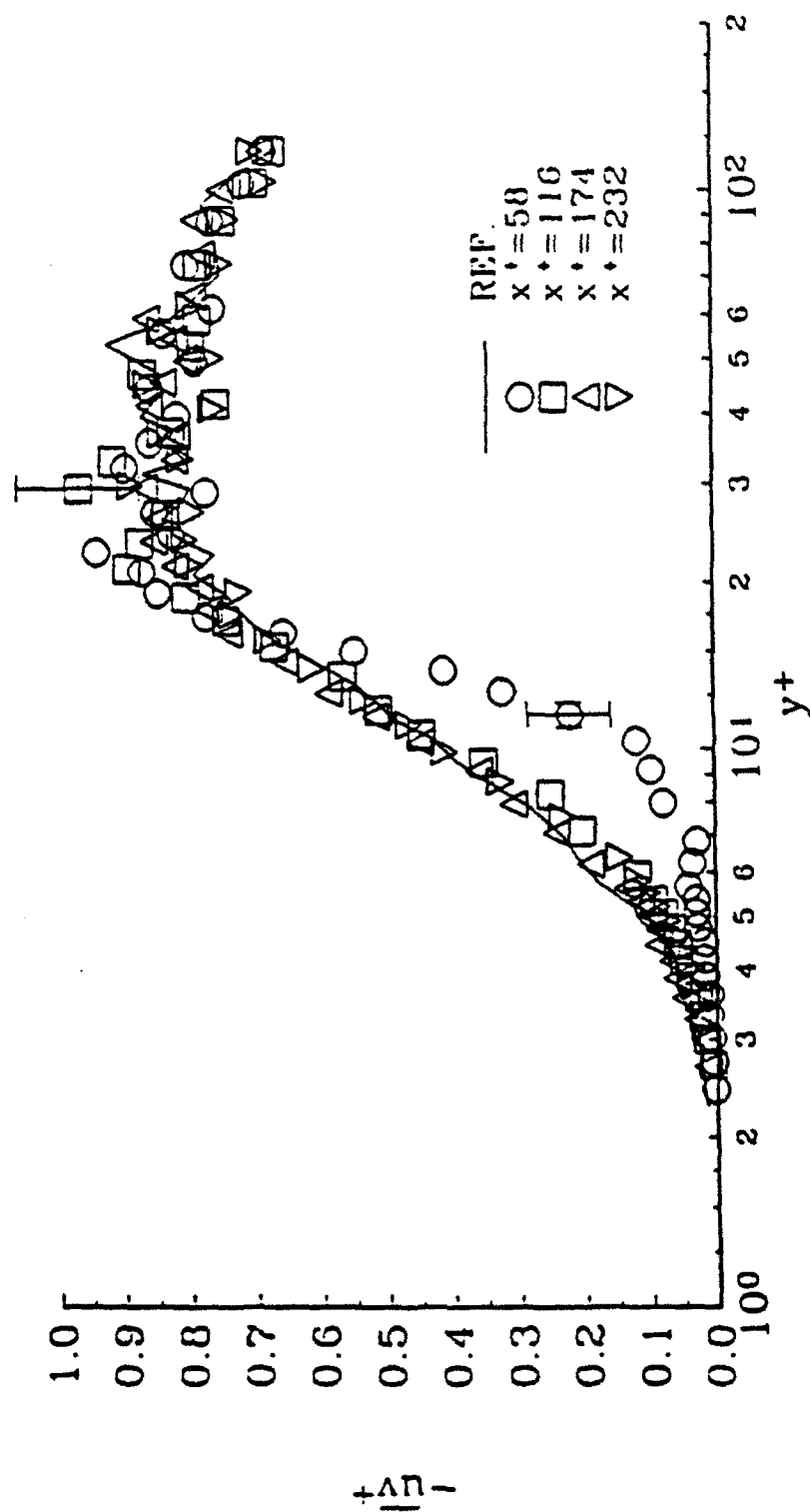


Figure 5.16 Axial development of the uv^+ Reynolds stress profiles along the centerplane. Normalization with ref. u^+

moves away from the wall or becomes tilted at an angle with respect to the wall as it convects downstream.

It is speculated that the second structure originates as a shear layer forming near the top of the bump. This shear layer sheds off of the bump and evolves into a counter-rotating vortex structure as shown in Figure 5.1. The interface between the mean flow convergence and the second structure is a region of increased shear and increased uv . Figure 5.17 illustrates this shear layer. This figure shows the non-dimensionalized radial gradient of the mean streamwise velocity, on the centerplane, plotted as a function of wall distance at $x^* = 58$. An increase in the gradient is observed from $12 \leq y^* \leq 40$ with a local peak at $y^* \approx 15$. The decreased gradient at the wall is indicative of the reduced local skin friction. The remaining centerplane gradients of the mean velocity, which are small, are also shown in Figure 5.17. Secondary counter-rotating vortical structures have also been observed by Hunt et al. (1978) and Schofield and Logan (1990) for turbulent boundary layer flow over bumps. These authors consider bumps which are greater than half the boundary layer thickness, however, considerably larger than the present bump.

The uv profiles quickly recover to reference levels with increasing spanwise displacement. At $x^* = 58$, the off-centerplane profiles at $z^* = -5.5$ show a small decrease in uv levels below $y^* = 6$, similar to that observed in the centerplane profile at $x^* = 116$. The peak at $y^* > 20$ persists to $z^* = -5.5$ and is broader in radial extent over the region $15 \leq y^* \leq 30$. The magnitude of the peak is reduced slightly from the levels observed on the centerplane. This indicates that the region of influence of the second structure is approximately 11 wall units in spanwise extent.

The suppression of near wall bursting events at the locations of reduced uv is confirmed by an increase in the time between bursts. Figure 5.18 shows centerplane profiles

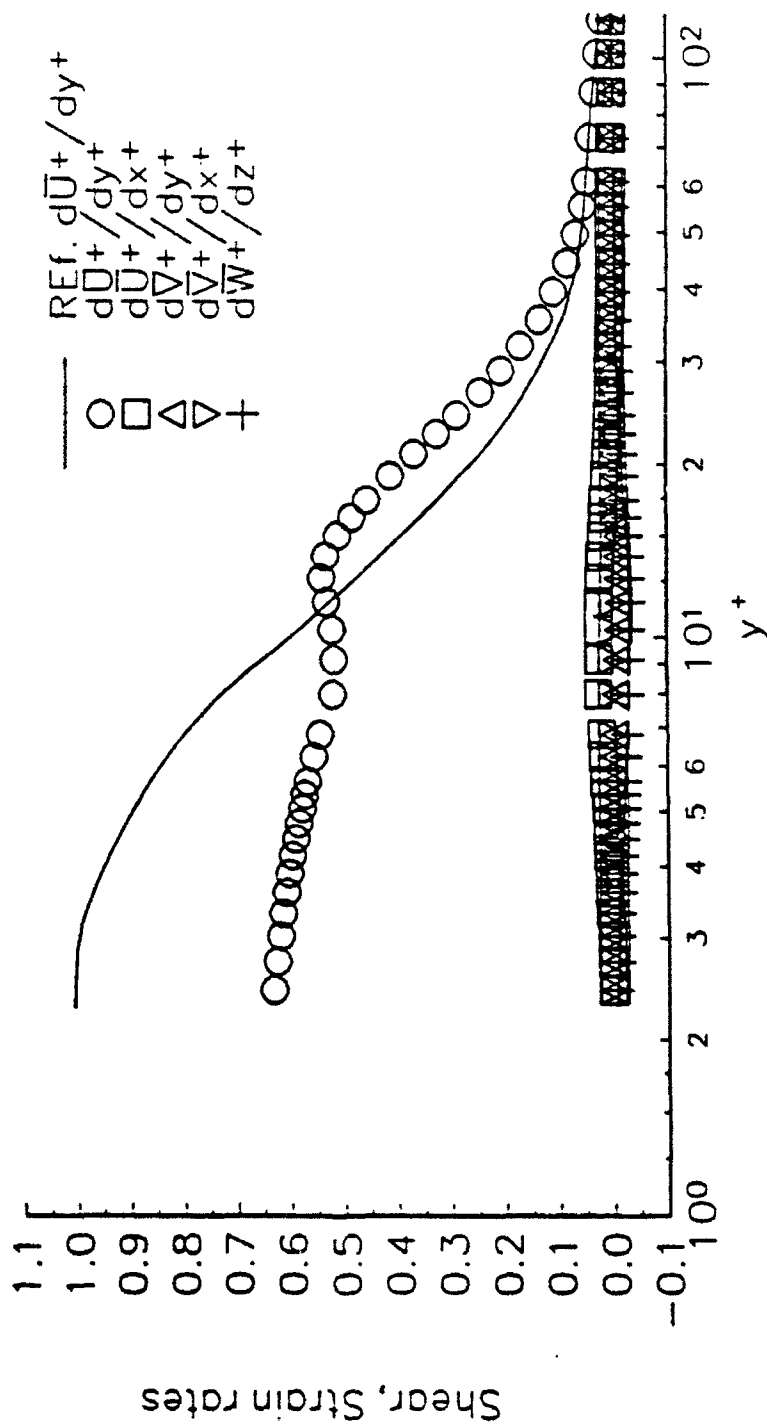


Figure 5.17 Profiles of the mean velocity strain rates at $x' = 58$ and $z' = 0$.
Normalization with ref. u^*

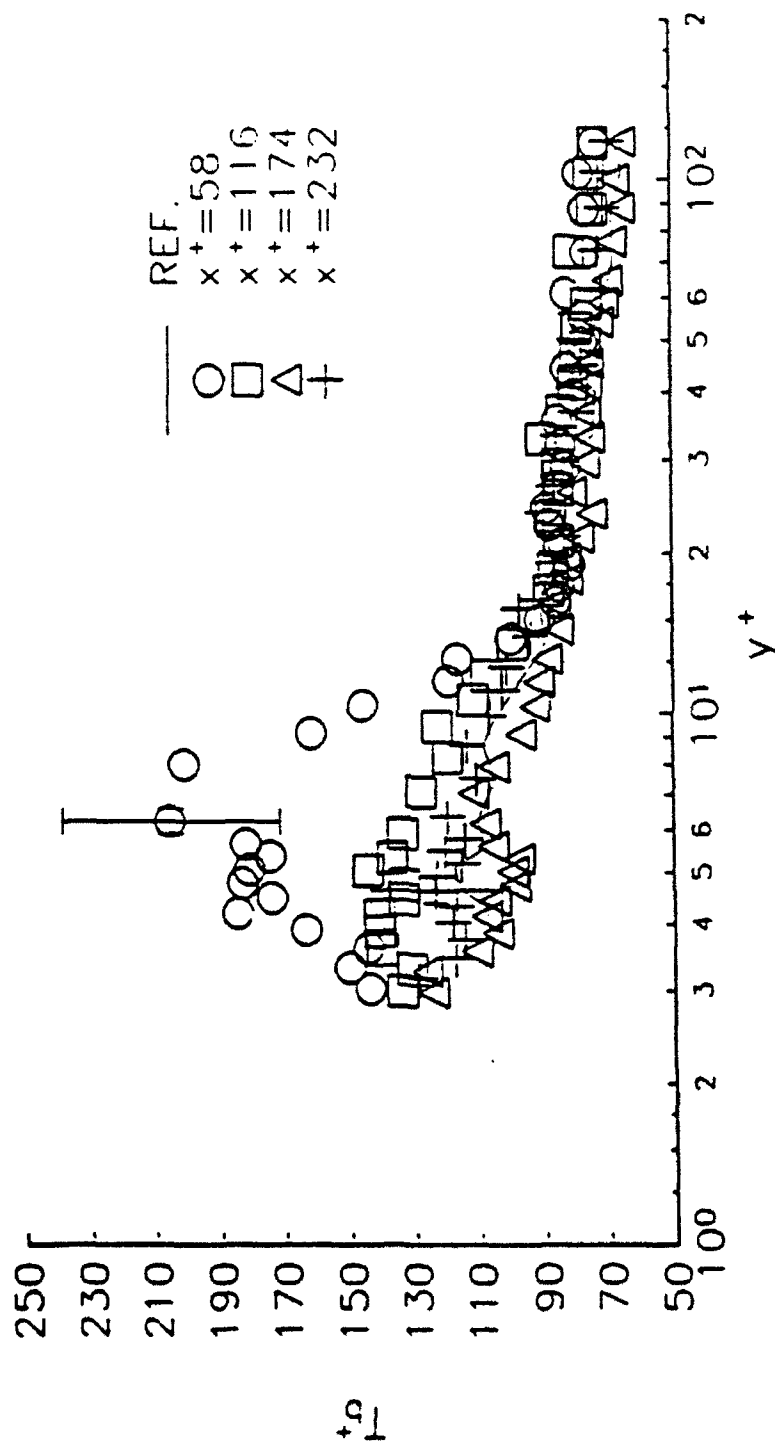


Figure 5.18 Axial development of profiles of the time between bursts estimates along the centerplane.
Normalization with ref. u^+

of the time between bursts estimates. A significant increase in T_b^+ is observed over the region of reduced uv . Likewise, a small decrease in T_b^+ is observed at $y^+ = 20$ corresponding to the increased uv levels at this radial location. The increased T_b^+ results are similar to those observed by Koskie and Tiederman (1992) in polymer drag reduced flows. These authors find that the time between bursts doubles for a 33% skin friction reduction. This closely parallels the present results of a near doubling of the time between bursts at a location with an approximate 38% local skin friction reduction. The spanwise recovery of the bursting time is similar to that observed with the centerplane axial recovery. The increased bursting times imply that the number of bursts, quadrant two events, is decreased.

The generation of Reynolds stress is governed by the time scales of the bursting process. This provides an estimate of the characteristic time scale of the Reynolds stress producing structures. The reference time between bursts is on the order of 0.1 s or 10 Hz. The increased time between bursts in the modified boundary layer suggests that the mean flow convergence inhibits large scale outward motions. However, this does not exclude the possibility of small scale inhibition by the mean flow convergence.

The relative quadrant analysis of the uv signal confirm the suppression of quadrant two and four events. Figure 5.19a and b show the axial development of the relative quadrant profiles of the uv signal. In these figures, the reference total uv signal instead of the measured local value, at the corresponding y^+ , is used to normalize the individual quadrant averages. This method of normalizing provides a more direct comparison of the modifications to each quadrant relative to the undisturbed results. The contributions of quadrant two and four events are decreased below $y^+ < 15$ and are slightly increased over reference values from $15 \leq y^+ \leq 25$, at $x^+ = 58$. Furthermore, the contributions of quadrant one and three events are increased below $y^+ = 20$. This acts to decrease the total

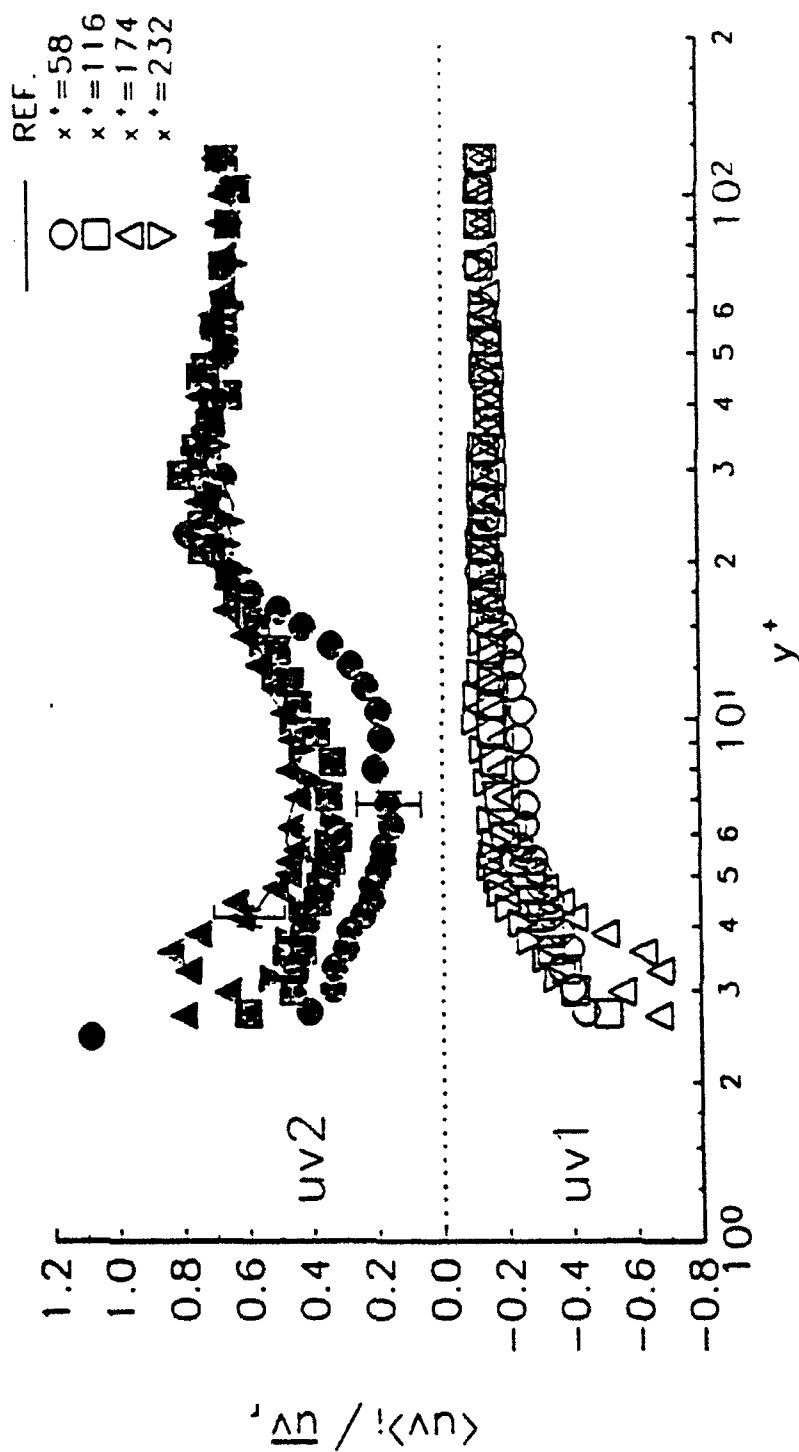


Figure 5.19 Axial development of profiles of the uv relative quadrant analysis results. The quadrant averages are normalized by the undisturbed total uv level and u^* . a) quadrants 1 and 2

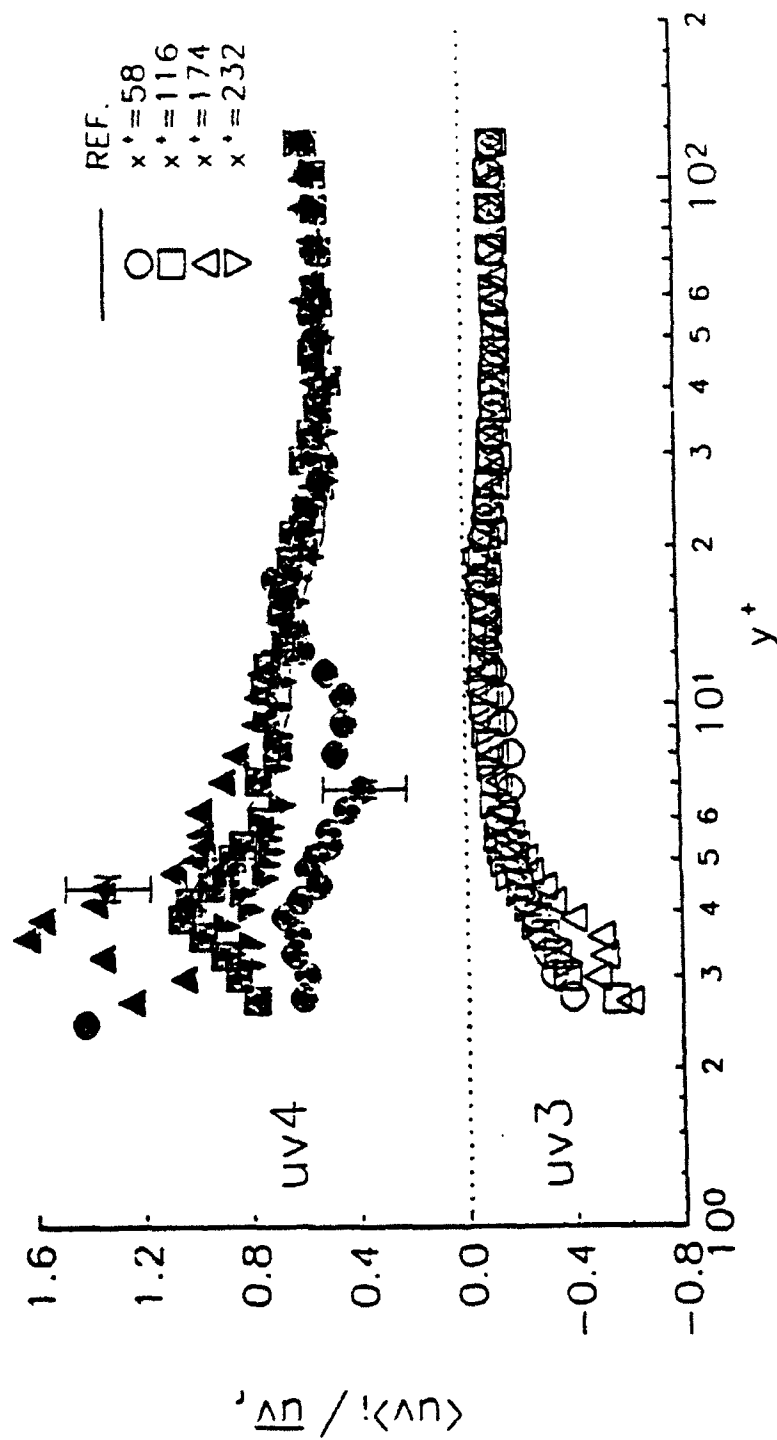


Figure 5.19(cont.) b) quadrants 3 and 4

negative uv levels. Quadrant one and three results quickly recover with increasing x^+ . Quadrant two and four levels are higher than reference levels at $x^+ = 174$ and return to reference levels by $x^+ = 232$. A rapid spanwise recovery is observed at all axial measurement locations.

Strong non-zero uw and vw correlations are measured at off-centerplane positions downstream of the bump. These correlations are normally zero in a fully developed pipe flow and are measured as such, within the experimental uncertainty, in the unmodified boundary layer. Figures 5.20 and 5.21 show off-centerplane uw and vw Reynolds stress profiles at $x^+ = 58$. The vw data, shown in Figure 5.21, is TSI coincidence mode data. The spatial filtering of the externally digitized v velocity is most apparent in the off-centerplane vw correlations and corresponding triple correlations due to the large circumferential gradients of the spanwise velocity component about the centerplane. Although the externally digitized vw correlation profiles are qualitatively similar to the TSI coincident mode profiles, the sharp features of the profiles are smoothed due to spatial averaging. The cause of this spatial averaging of the externally digitized data, from the fiber-optic probe, has been discussed in Chapter 3.

Zero uw and vw correlations are measured along the centerplane. This is expected due to the anti-symmetry of the w velocity fluctuations. Figure 5.20 supports the existence of a counter-rotating vortex structure near the wall, where a strong correlation exists between positive u and positive w fluctuations for $z^+ < 0$. The profiles suggest that the vortices are approximately 15 wall units in diameter. The vw profiles suggest the presence of a second structure located at $y^+ \approx 20$. The uw and vw correlations persist for $x^+ > 174$ and remain confined to the near wall region. The off-centerplane uw profiles at $x^+ = 116$ and 174 indicate that the counter rotating vortices separate in the spanwise direction as they convect

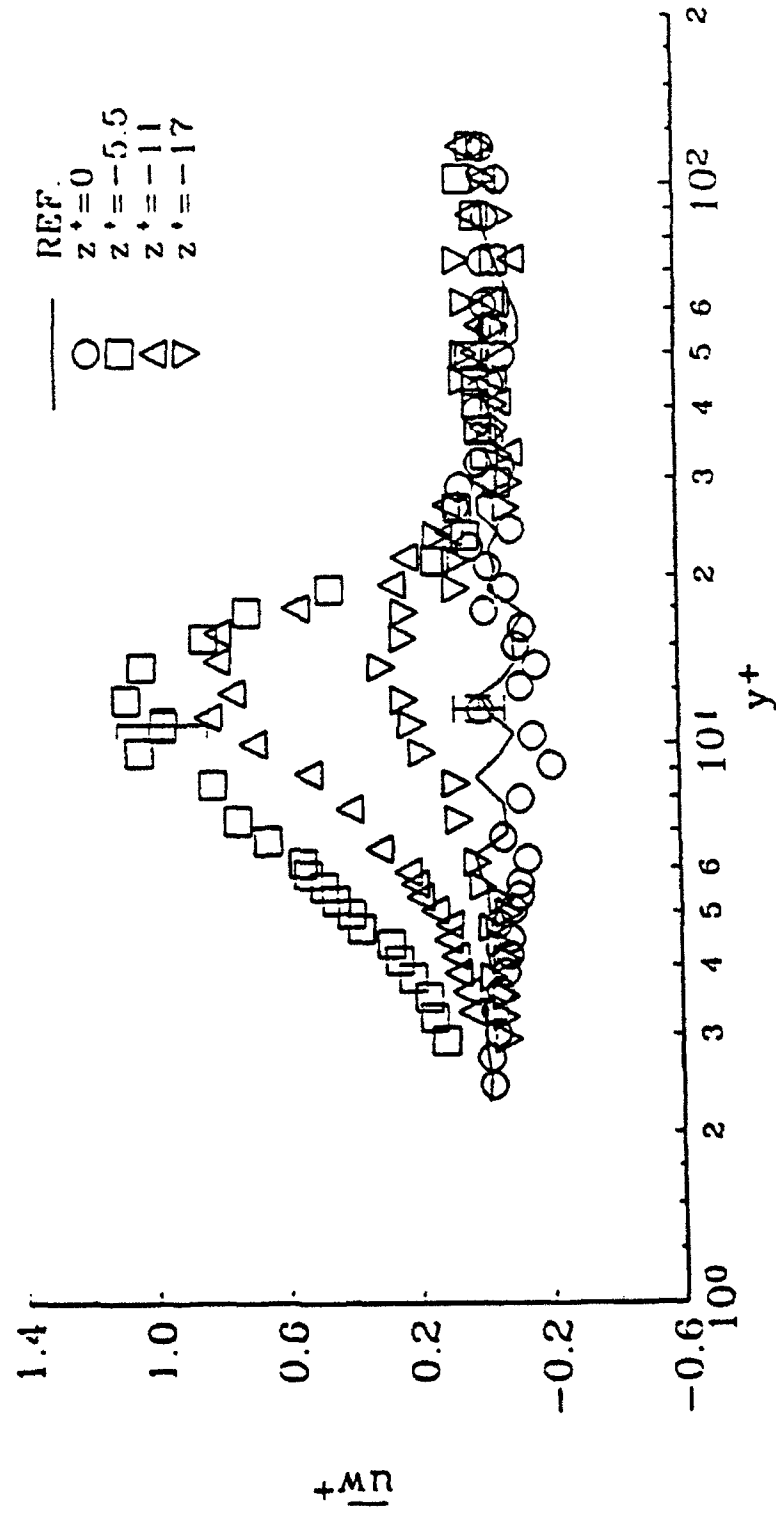


Figure 5.20 Spanwise development of the uw Reynolds stress component at $x^* = 58$.
Normalization with ref. u^*

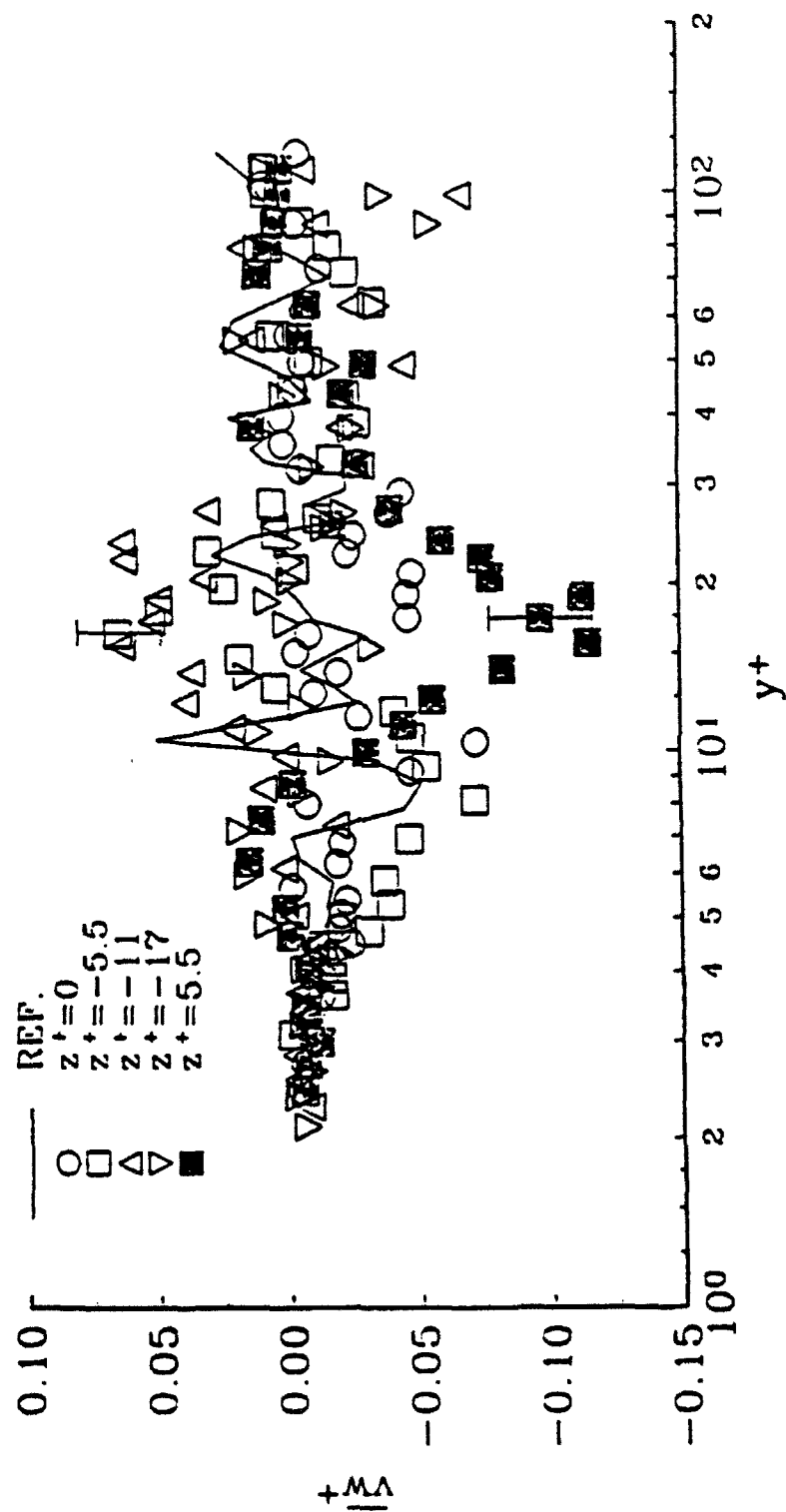


Figure 5.21 Spanwise development of the wv Reynolds stress component at $x^* = 58$.
Normalization with $ref\ u^*$

downstream. This behavior of the junction vortex legs has also been observed by Schofield and Logan (1990). The turbulent velocity fluctuation statistics imply that the vortices remain coherent over a longer streamwise distance from the bump than does the mean flow convergence.

5.3.2.4 Velocity Skewness and Kurtosis

The modifications of the velocity skewness profiles are consistent with the presence of a pair of quasi-streamwise counter-rotating vortices confined to the near wall region. The axial development of the streamwise and radial skewness profiles are shown in Figure 5.22. The streamwise fluctuating velocities are more positively skewed than reference levels for $y^+ \leq 15$, while the radial skewness profiles are more negatively skewed compared to reference levels. These skewness profiles are indicative of larger positive streamwise velocity fluctuations and larger negative radial velocity fluctuations from the mean compared to reference conditions. The hodographs shown in Figures 5.7 to 5.10 support these conclusions. Kurtosis values are increased below $y^+ = 15$ for both the streamwise and radial velocities. This indicates that the magnitudes of the intermittently occurring positive streamwise and negative radial velocity fluctuations are significantly greater than the magnitude of the mean velocities. The skewness and kurtosis levels show a continual recovery with both increasing axial and spanwise displacement. A full recovery in the near wall radial skewness levels is observed by $x^+ = 174$, but is not observed until $x^+ = 354$ in the streamwise skewness profiles. At $x^+ = 58$, both the streamwise and radial skewness profiles return to reference levels by $z^+ = -17$. Off-centerplane streamwise skewness levels show a slow recovery with spanwise distance at $x^+ = 174$. Elevated u skewness levels are still observed at $z^+ = -17$ for the $x^+ = 174$ axial position. The behavior of the kurtosis

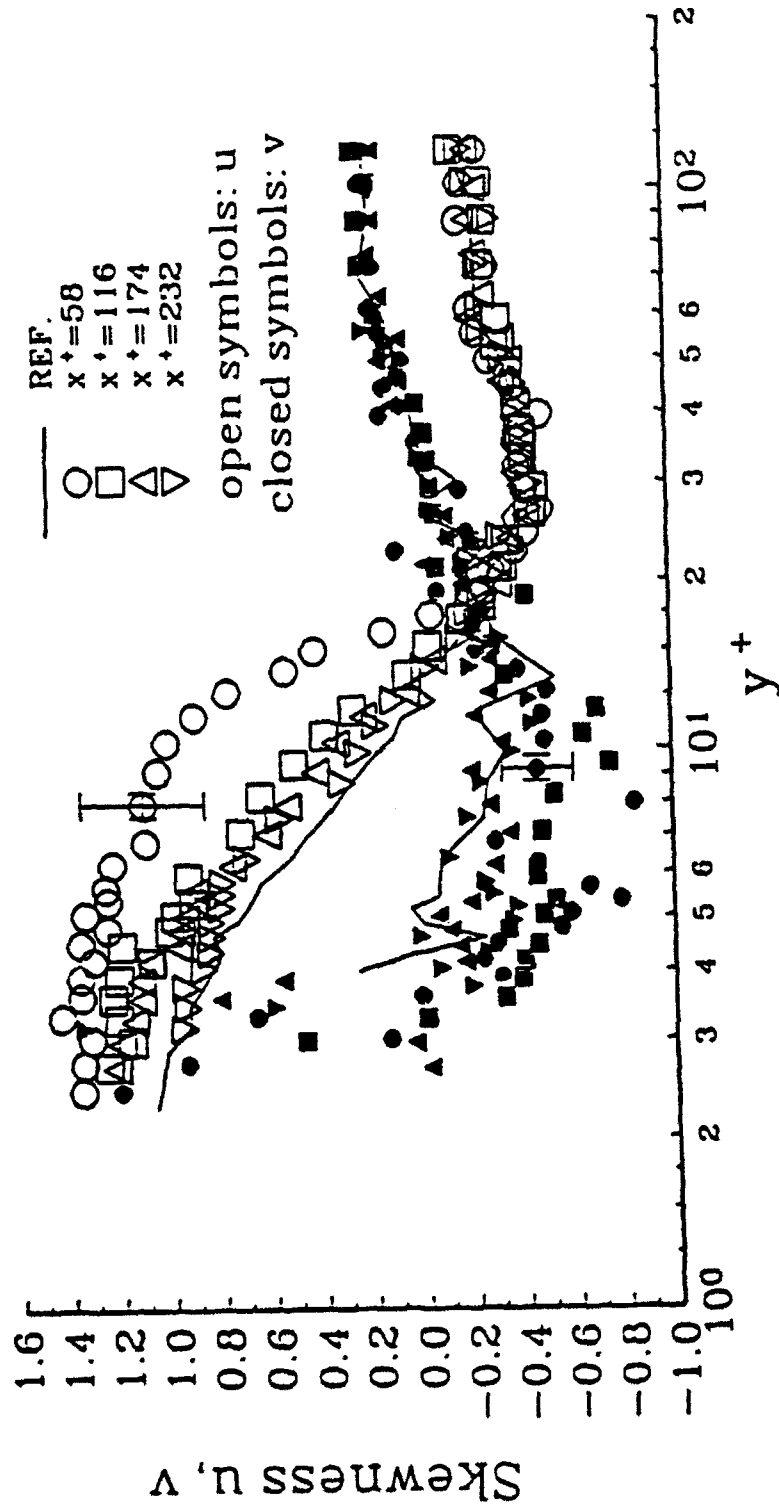


Figure 5.22 Axial development of profiles of the streamwise and radial velocity skewness levels.
 Normalization with ref. u^+

profiles with streamwise and spanwise displacement is similar.

Centerplane spanwise velocity skewness levels are zero, as they should be, for the intermittent anti-symmetric w velocity fluctuation distribution. This is clear from the centerplane uw hodographs. The off-centerplane measurements of the spanwise skewness profiles, shown in Figure 5.23, are dominated by the spanwise wandering of the vortices. This can be illustrated by referring to the off-centerplane uw hodographs shown in Figures 5.7 to 5.10. The uw hodographs become increasingly unimodal with increasing spanwise displacement. The uw hodographs at $z^+ \approx -5.5$ still show some bimodal behavior at high u fluctuations. This indicates that the streamwise vortex on the other side of the centerplane penetrates into the measurement field of the LDV probe at this negative z^+ location off the centerplane. The increased negative skewness levels correspond to the large negative velocity excursions from the mean. With increasing spanwise displacement in the negative z^+ direction, the LDV probe moves outside of the penetration region of the other vortex from the positive z^+ side of the centerplane. The uw hodographs show an increasing tilt towards high positive w fluctuations which result in increased positive skewness. The off-centerplane skewness profiles combined with the uw hodographs at $x^+ = 174$ indicate that the vortices are displaced farther apart from one another and that they wander over a greater spanwise extent than they did at the upstream location. At $x^+ = 174$, negative w skewness levels are observed to a $z^+ = -17$, with peak levels occurring at $z^+ = -11$. The increased spanwise distance over which the other vortex penetrates, at $x^+ = 174$, may be due to the loss of significant spanwise mean flow velocity towards the centerplane. The streamwise development of the circumferential skewness profiles at $z^+ = -11$ is shown in Figure 5.24. Kurtosis profiles of the spanwise velocity show increasing values with increasing $|z^+|$, which is consistent with a decrease in the number of rare negative w fluctuations from the

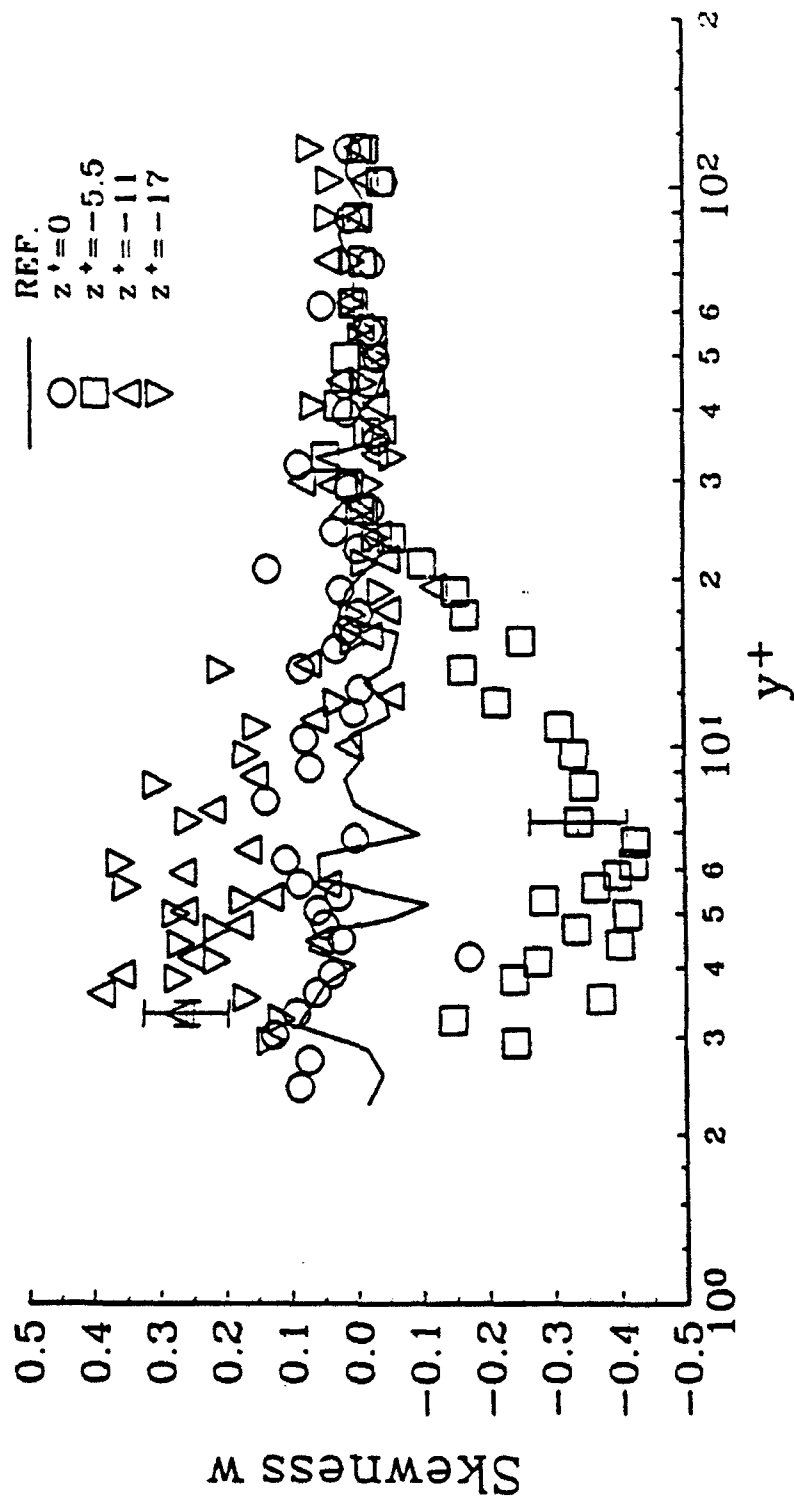


Figure 5.23 Spanwise development of profiles of the circumferential velocity skewness levels at $x^* = 58$.
Normalization with ref. u^*

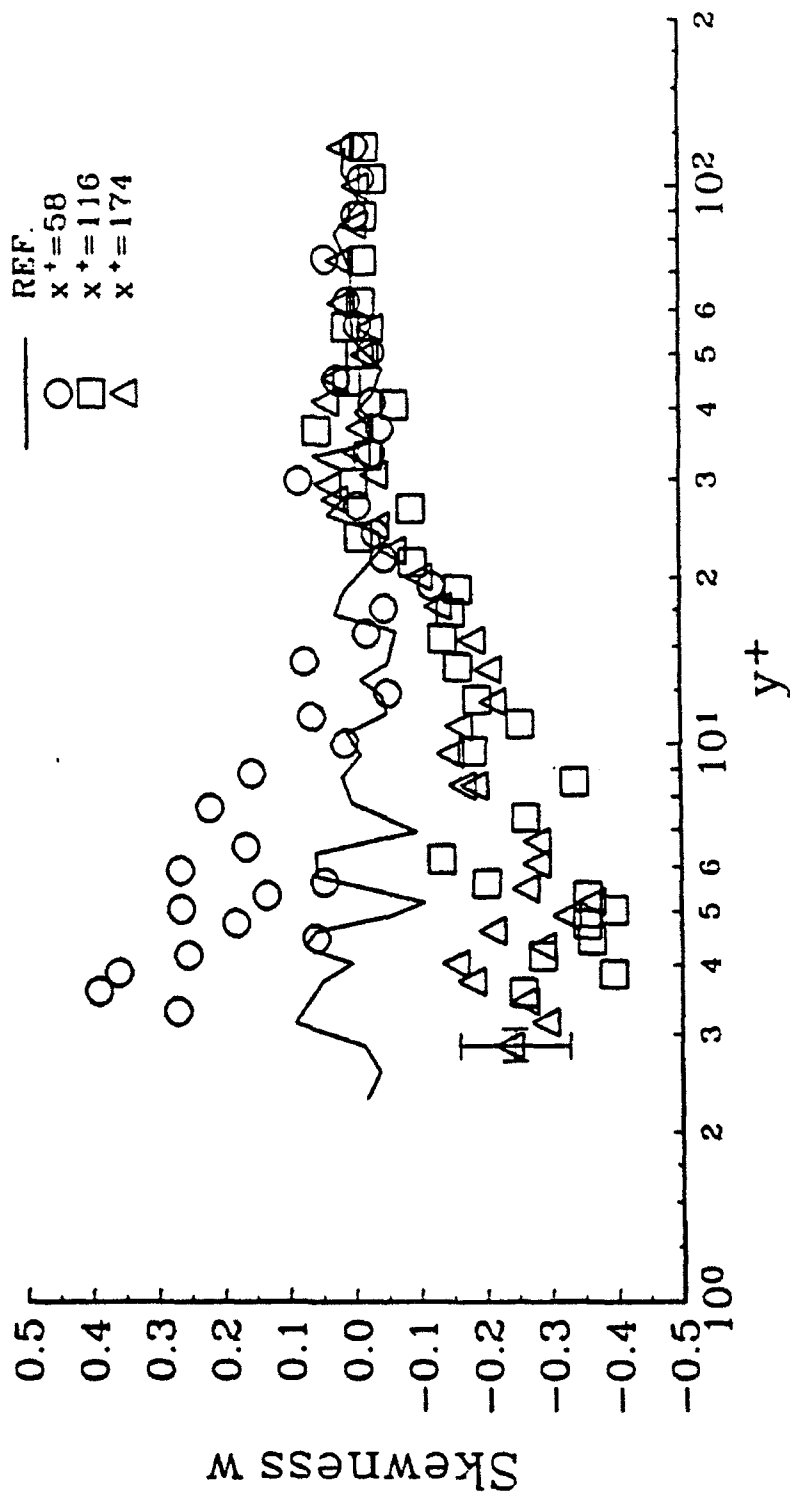


Figure 5.24 Axial development of profiles of the circumferential velocity skewness levels at $z^+ = -11$.
Normalization with ref. u^+

other vortex as it crosses the centerplane into the measurement field of the LDV probe.

The measured triple correlation profiles are also strongly modified and confirm the presence of the counter-rotating vortices. In addition, these changes imply that the transport, or turbulent diffusion, of Reynolds stress and turbulent kinetic energy (TKE) is modified in the near wall region. The triple correlations will be examined in the context of the transport of the turbulent kinetic energy in Chapter 6.

5.4 Summary of the Single-Point Statistics

Upstream velocity measurements confirm the rollup of a junction vortex in front of the wall-mounted bump. The junction vortex is convected around the bump forming a pair of counter-rotating, quasi-streamwise vortices, which are confirmed by the velocity profile statistics. Three-component, coincident, time resolved LDV measurements are made in the development region downstream of the bump. The measurements indicate that the counter-rotating vortices are confined to the near wall region and that the legs are approximately 10 to 15 wall units in diameter. The vortices are observed to persist for more than 174 wall units downstream of the bump. Fluctuating velocity measurements indicate that these vortices wander from side to side occasionally crossing the centerplane. A second vortical structure, probably a counter-rotating vortex pair, occurs at a $y^+ \approx 20$ and is probably generated near the top of the bump.

A radial and circumferential mean velocity convergence is measured toward the wall and the centerplane. This convergence region is approximately 15 to 20 wall units high and persists for more than 100 wall units downstream of the bump. This region plays a dominant role in the dynamics of the near wall flow on the centerplane. Turbulent momentum transport in the form of ejections and sweeps is retarded within this region. A reduction in rms

velocities and a significant decrease in the near wall uv correlation is observed. Both a burst rate analysis and a relative quadrant analysis of the uv signal support this interpretation. The reduction in Reynolds stress generation yields a reduction in the local wall shear stress with mean streamwise velocity profiles similar to those observed in drag reduced boundary layers with polymers. However, the resulting form drag on the element more than offsets the local skin friction reduction. The counter-rotating vortices increase turbulent transport and bring increased velocity fluctuations into the near wall convergence region by wandering across the centerplane. This acts to increase the rms levels, which are reduced by the mean flow convergence. It is particularly interesting that increased turbulent transport nearly offsets exactly any reductions in the radial and spanwise rms fluctuations by the mean flow convergence. A rapid spanwise recovery is observed in all the velocity statistics, which indicates the modifications are confined to a region of influence on the order of the sizes of the counter-rotating vortices.

The interaction of the second vortical structure at $y^+ = 20$ with the near wall mean flow convergence region causes an increased shear at the interface. This shear layer produces higher uv levels than normally observed at $y^+ = 20$. As a result, increased rms levels and reduced bursting times are observed locally. The second structure moves away from the wall with increasing streamwise distance, which indicates that it may be a counter-rotating vortical structure.

The modifications in some of the velocity profile statistics in the convergence region are very similar to those observed in polymer drag reduced boundary layers. Polymers increase the size of the small scale turbulence by effectively adding an energy sink to the turbulent kinetic energy producing buffer region. The polymers locally increase the viscosity by adding elongational viscoelastic properties to the fluid. This additional elongational

viscosity retards the small scale fluctuations, interrupts the turbulent momentum transport near the wall, and reduces the velocity gradient at the wall. In addition, the streamwise rms levels are reduced and the radial rms levels are considerably reduced.

As discussed above, the mean flow convergence may reduce the radial and spanwise rms levels as much as it does the streamwise rms levels. There is no reason to believe that the converging forces, due to the mean velocity momentum toward the centerplane and wall, will inhibit streamwise fluctuations without inhibiting both radial and spanwise velocity fluctuations as well. In this light, it appears that the skin friction reducing mechanism in the present investigation is similar to that observed in polymer drag reduction. Both systems include additional forces which inhibit momentum transport, although the processes generating these forces are quite different. However, the presence of the counter-rotating vortices and the thin shear layer considerably modify the effects of the mean flow convergence and produce results which are quite different from those observed in polymer drag reduction. In particular, the increased levels in uv^+ and u' , and the lack of a change in v' levels are different from what is observed in polymer drag reduction.

Chapter 6

TURBULENT KINETIC ENERGY BALANCE AND SPECTRA

6.1 Turbulent Kinetic Energy Balance

Several of the terms appearing in Equation 4.1 can be estimated from the measured velocity data. The pressure-velocity correlations and several components of the dissipation term cannot be estimated from the present data. In addition, the lack of a fine measurement grid in both the axial and circumferential directions prohibits acceptable estimates of the viscous diffusion terms in these directions. However, an order of magnitude analysis and examination of the data shows that the axial component of the viscous diffusion term is negligibly small compared to the other two terms. The terms that are not directly estimated are combined and referred to as the remainder term.

Unlike the classical fully developed pipe flow, the flow field about the bump contains near wall inhomogeneities in all three coordinate directions which cannot be neglected. Thus, the simplifications made in deriving Equation 4.2 cannot be applied to the present problem. The only simplification that can be made without reservation is to neglect the circumferential gradient of symmetric terms on the centerplane.

The axial and spanwise development of the time averaged turbulent kinetic energy, defined in Equation 4.1, is shown in Figures 6.1 and 6.2. The development of the q^+ profiles is similar to that of the u' profiles, which is not surprising considering the variance of u is the dominant term of q^+ . A significant decrease in q^+ is observed at $x^+ = 58$ along the centerplane. The decrease in q^+ comes from a significant reduction in the turbulent kinetic energy production near the wall. The profiles appear to be shifted away from the wall with the peak moving to $y^+ \approx 20$. However, the magnitude of the peak is greater than peak levels

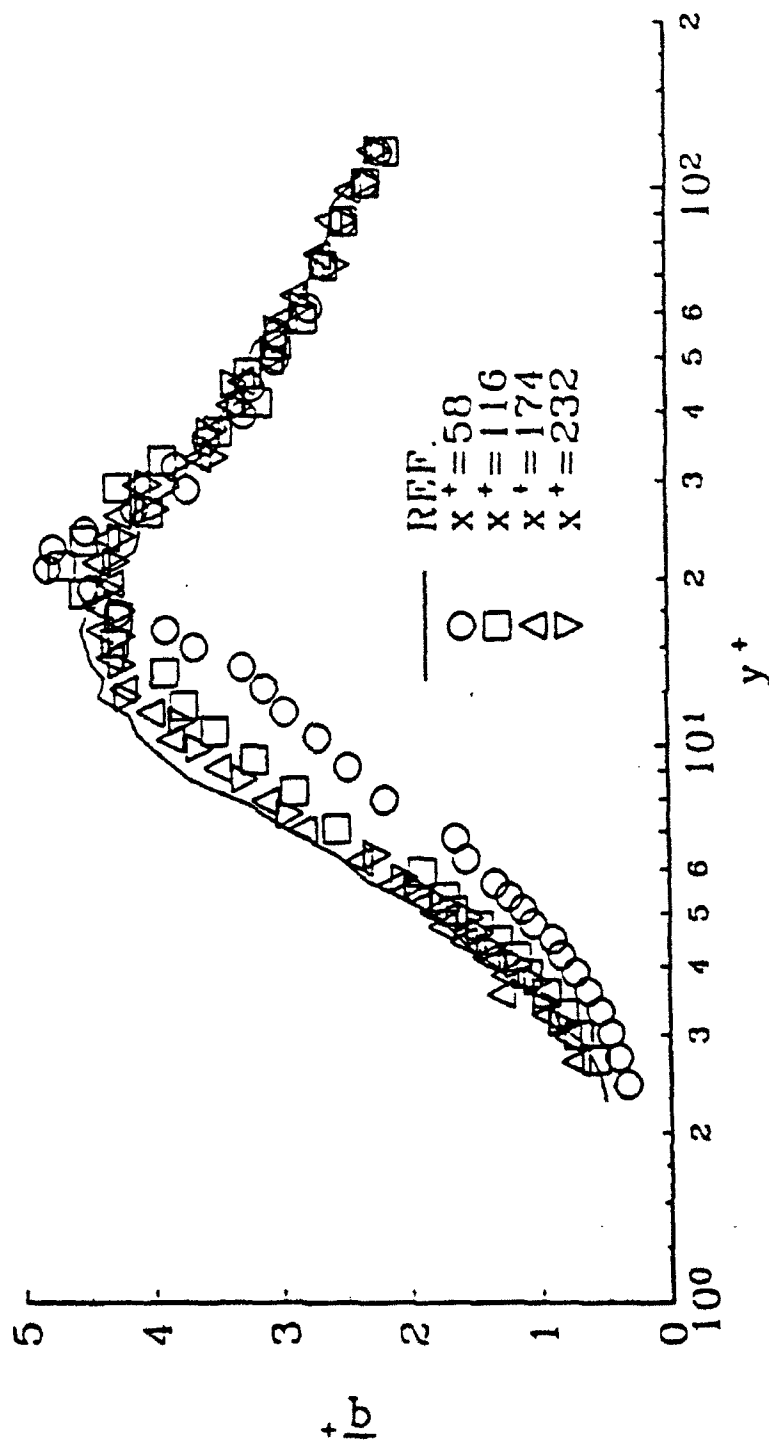


Figure 6.1 Axial development of profiles of the time averaged turbulent kinetic energy along the centerplane.
Normalization with ref. u^*

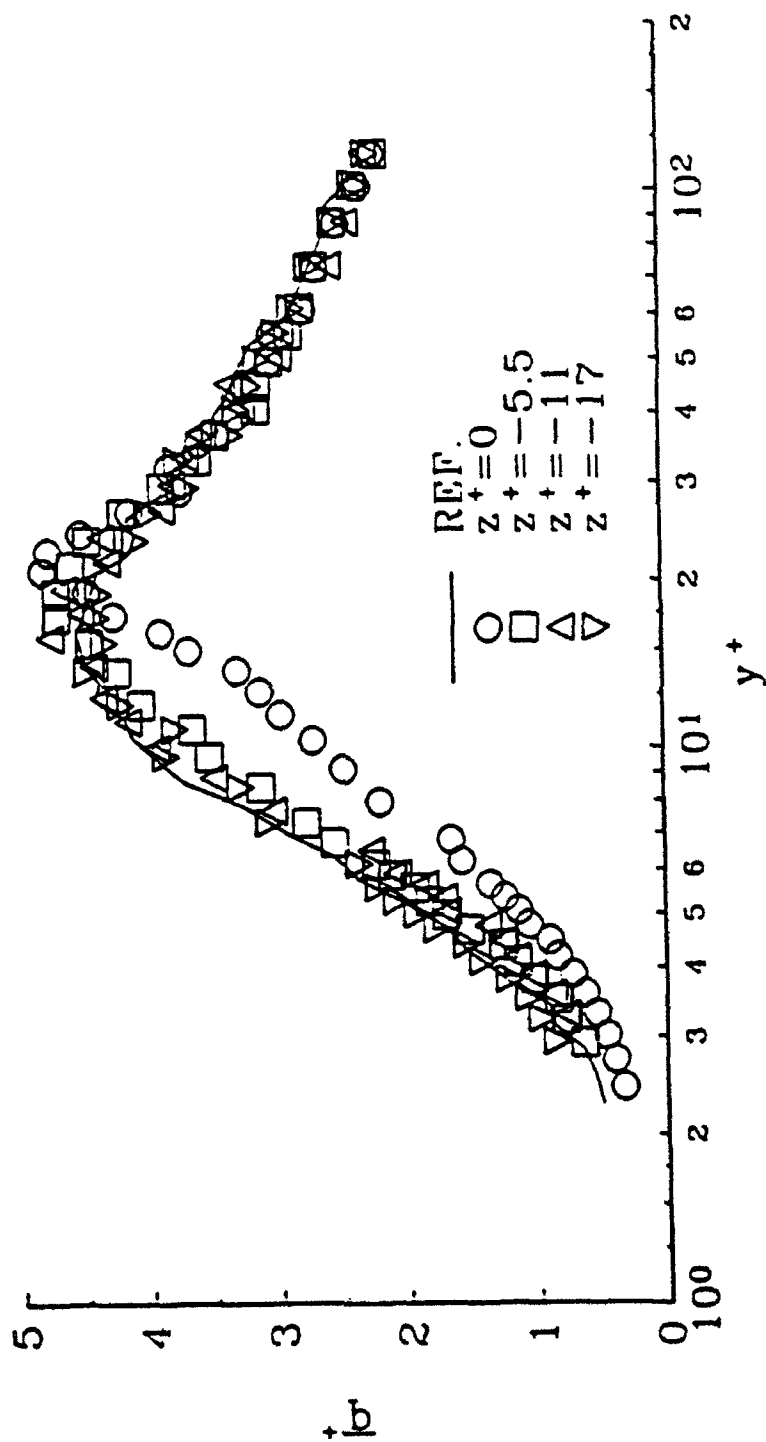


Figure 6.2 Spanwise development of profiles of the time averaged turbulent kinetic energy at $x^* = 58$.
Normalization with ref. u^*

in the reference boundary layer. These increased levels at $y^+ \approx 20$ are from the second vortical structure and the thin shear layer located there.

Centerplane profiles of the components of the turbulent kinetic energy balance, at $x^+ = 58$, are shown in Figure 6.3. The reference profiles shown in Figure 4.8 are reproduced here in Figure 6.4 for convenience. Similar to the reference boundary layer, the measurable dissipation term, DI_m , is zero within the measurement uncertainty. A complete analysis of the dynamics of the near wall turbulent energy transfer is not possible given the experimental and measurement limitations in the highly three-dimensional inhomogeneous flow field. Several interesting observations can, however, be made from Figure 6.3.

The centerplane balance at $x^+ = 58$ indicates that a significant reduction in the rate of production of q^+ occurs below $y^+ = 13$. This is accompanied by an increase in the rate of turbulent diffusion, which is directly related to the modifications of the triple correlations. Farther out in the boundary layer, at $13 < y^+ < 40$, production is increased above reference levels with the peak occurring at $y^+ \approx 20$. The magnitude of this peak is marginally greater than the magnitude of the peak in the reference boundary layer. The combination of the reduction in the uv correlation and the decrease in the mean strain rate, as is shown in Figure 5.17, is probably the dominant factor responsible for the decrease in the rate of production for $y^+ < 13$. In addition, a positive axial gradient of the streamwise velocity in the near wall region contributes to the reduction in the overall rate of production of q^+ . Figure 6.5 illustrates the contributions of the different components to the total rate of production term in Equation 4.1. Clearly the terms involving the gradients of the streamwise velocity are the dominant contributors to the total rate of production. The positive streamwise gradient of the axial velocity component is a reflection of the local skin friction reduction and recovery with increasing x^+ . The decrease in the rate of production of q^+ directly

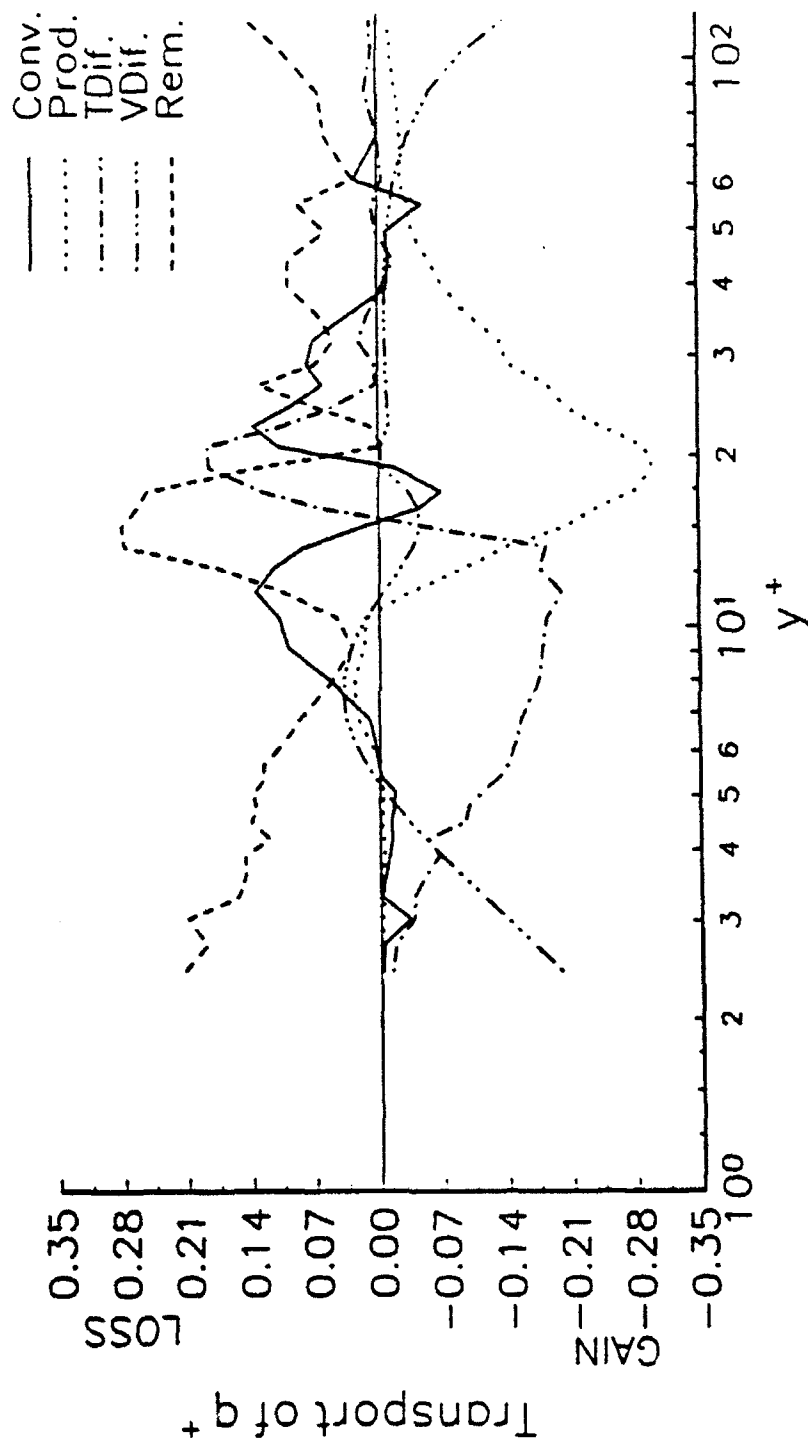


Figure 6.3 Profiles of the terms of the turbulent kinetic energy balance, Equation 4.2, at $x^* = 58$ and $z^* = 0$
Normalization with ref. u^*

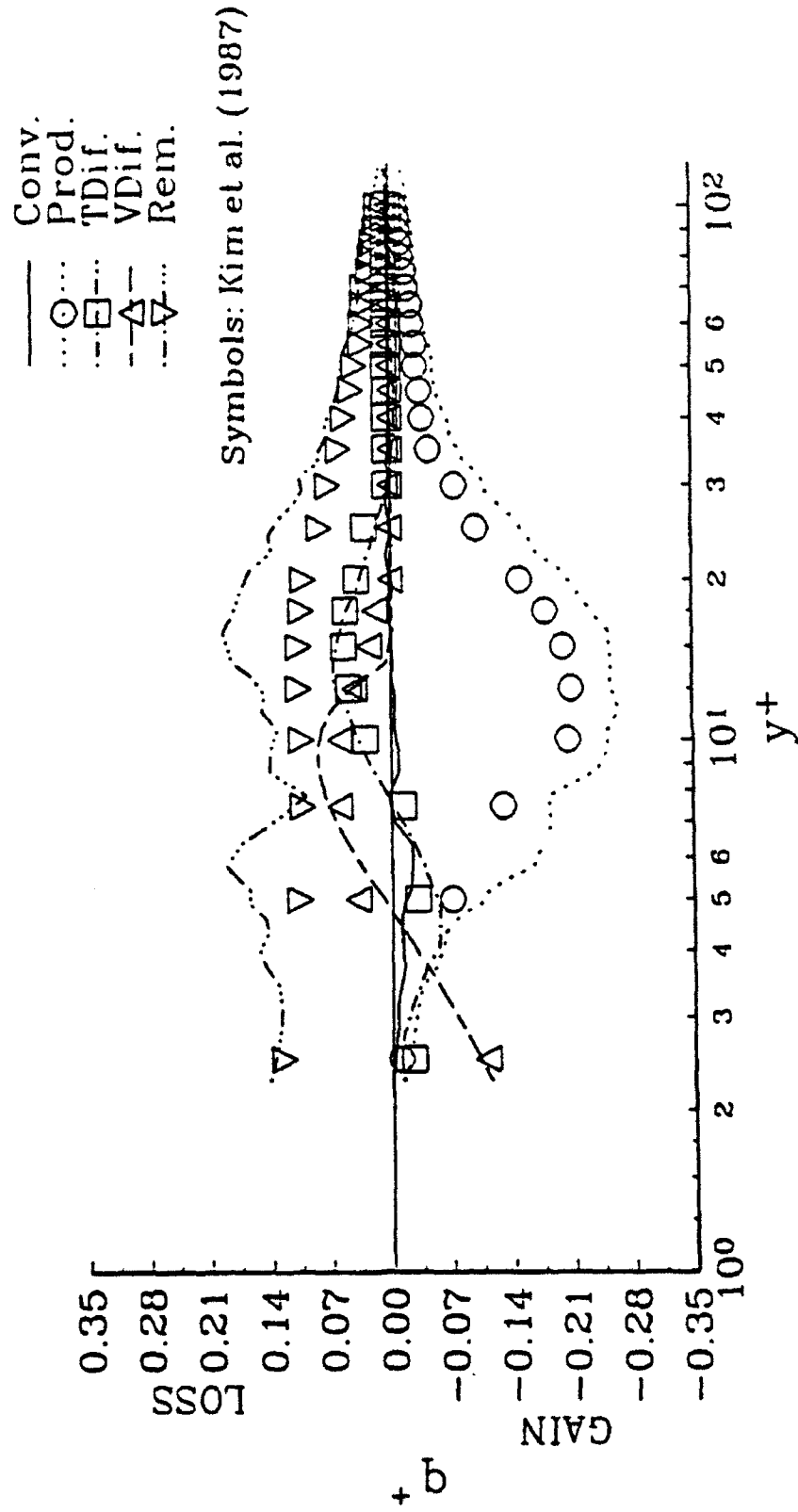


Figure 6.4 Profiles of the components of the turbulent kinetic energy transport equation, Equation 4.3, in the undisturbed glycerin tunnel turbulent boundary layer. Normalization with ref. u^*

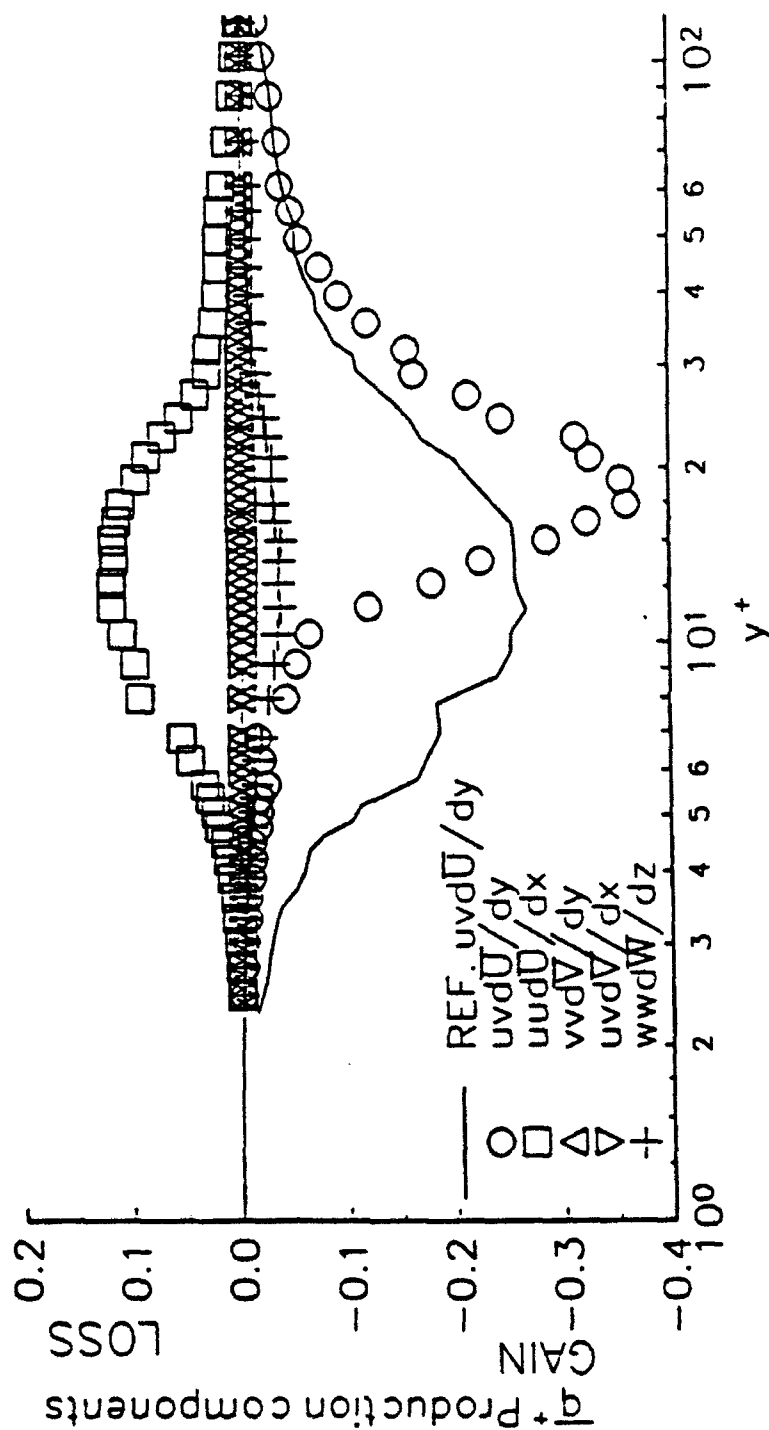


Figure 6.5 Contributions of the components of the rate of production of turbulent kinetic energy at $x^* = 58$ and $z^* = 0$. Normalization with ref. u^*

corresponds to suppression of burst type events in the mean flow convergence region.

Kim et al. (1971) has shown that the bursting event is the dynamic feature generating nearly all of the production of q^+ below $y^+ = 100$. The suppression of the bursting events causes a decrease in the uv generation, reduced turbulent kinetic energy production and a reduction in the local skin friction near the wall. The burst rate is approximately proportional to the frequency of the Reynolds stress producing structures. In the undisturbed pipe flow, the mean burst rate is approximately 10 Hz. The inhibition of the Reynolds stress producing events implies that the large scale, low frequency, turbulent scales are retarded by the mean flow convergence. Thus the significant reduction in the rate of production is due to a suppression of fluctuations which scale with the bursting time. This does not imply that the small scale, high frequency turbulence is not inhibited also.

The increased levels of the rate of production at $y^+ \approx 20$ are from the presence of the second vortical structure centered at this location. The interaction of the near wall convergence region and the second vortical structure produces a thin shear layer at the interface. This is evident from the strain rate profile shown in Figure 5.17, where a local increase in the strain rate occurs from $15 \leq y^+ \leq 25$. The increased shear results in a small increase in the uv correlation as shown in figure 5.16. The increased uv correlation combined with the increased strain rate produces a net increase in the rate of production of q^+ over reference levels.

In addition to the modifications to the rate of production, an increase in the levels of the rate of turbulent diffusion are observed. Although the qualitative trends in the profile of the rate of turbulent diffusion are not significantly modified, the magnitude of the peak levels are increased. It is speculated that these increased levels are caused by the wandering of the counter-rotating vortices across the centerplane. The vortices redistribute energy from the

high production area at $y^+ \approx 18$ and from locations off the centerplane to the near wall centerplane region of little energy production. As the vortices cross the centerplane, velocity fluctuations of all three components are convected into the centerplane region and contribute to the local energy within this region. The radial and circumferential transport of fluctuating velocity is apparent from the circulating velocity pattern of the vortices in the y - z plane. However as the vortices wander, they are likely skewed with the axial direction or their axes of rotation become tilted with respect to the axial direction. This produces streamwise fluctuations. In addition, the circulating motion of the vortices entrains high streamwise velocity fluctuations from higher y^+ and significant velocity fluctuations associated with the shear layer located over the region $15 \leq y^+ \leq 17$ down toward the wall.

The steady state assumption implied in Equation 4.2 does not permit changes in the time averaged energy levels at a point. These profiles merely represent the rate of transport or generation of energy by the different dynamical processes in the boundary layer at a given point. The increased rate of turbulent diffusion over reference levels at $y^+ = 5$ implies that it is the transport by the turbulent velocities which is contributing most to the energy levels observed at this location. This does not imply that the overall energy levels at $y^+ = 5$ are increased above reference levels. Figure 6.1 shows that q^+ is actually reduced at this location.

An interpretation, similar to that provided by Laufer (1954), can be invoked to help explain the results shown in Figure 6.3. In contrast to the relatively simple fully developed pipe flow of Laufer (1954), however, an interpretation of this highly three-dimensional inhomogeneous flow field is greatly complicated. The following interpretation is therefore speculative at best and somewhat simplified.

The profiles indicate that considerable energy gains are locally generated through production and by mean flow convection at $y^+ \approx 19$. Energy is transported away from this region by turbulent diffusion. This energy is transported towards the wall along the energy gradient. The increase in the rate of turbulent diffusion towards a loss in energy at $y^+ \approx 19$ implies that some process has increased the rate at which energy is transported from this location to surrounding regions. This transport of energy by the turbulent velocity fluctuations can occur in the radial direction as well as in the axial and spanwise directions due to the strong gradients in these directions. This diffusion of energy towards the wall by turbulent fluctuations is consistent with a transport mechanism due to the spanwise movement of the vortices across the centerplane.

The profile of the rate of convection by the mean flow indicates that energy is also convected into the near wall layer below $y^+ \approx 12$. In addition, an increase in the remainder term occurs over a region of $12 \leq y^+ \leq 18$. The mean radial velocity is strongly retarded within this region, where the radial velocity magnitude sharply decreases from a maximum at $y^+ \approx 20$ to nearly zero at $y^+ \approx 10$. It is probable that an increase in the rate of dissipation contributes to the increased remainder. However, the remainder term contains other processes which may also be altered.

Additional insight can be gained by considering the transport of the individual components making up the turbulent kinetic energy. Figures 6.6 to 6.8 show profiles of the balance of the transport of $u'^2/2$, $v'^2/2$ and $w'^2/2$ energy in the reference boundary layer. The $u'^2/2$ results are in good agreement with the simulation results published by Mansour et al. (1988), while the $v'^2/2$ and $w'^2/2$ profiles are qualitatively in agreement with these simulation results. The very small magnitudes of the quantities in Figures 6.7 and 6.8 make estimation of these quantities difficult. In a fully developed pipe flow, there is no

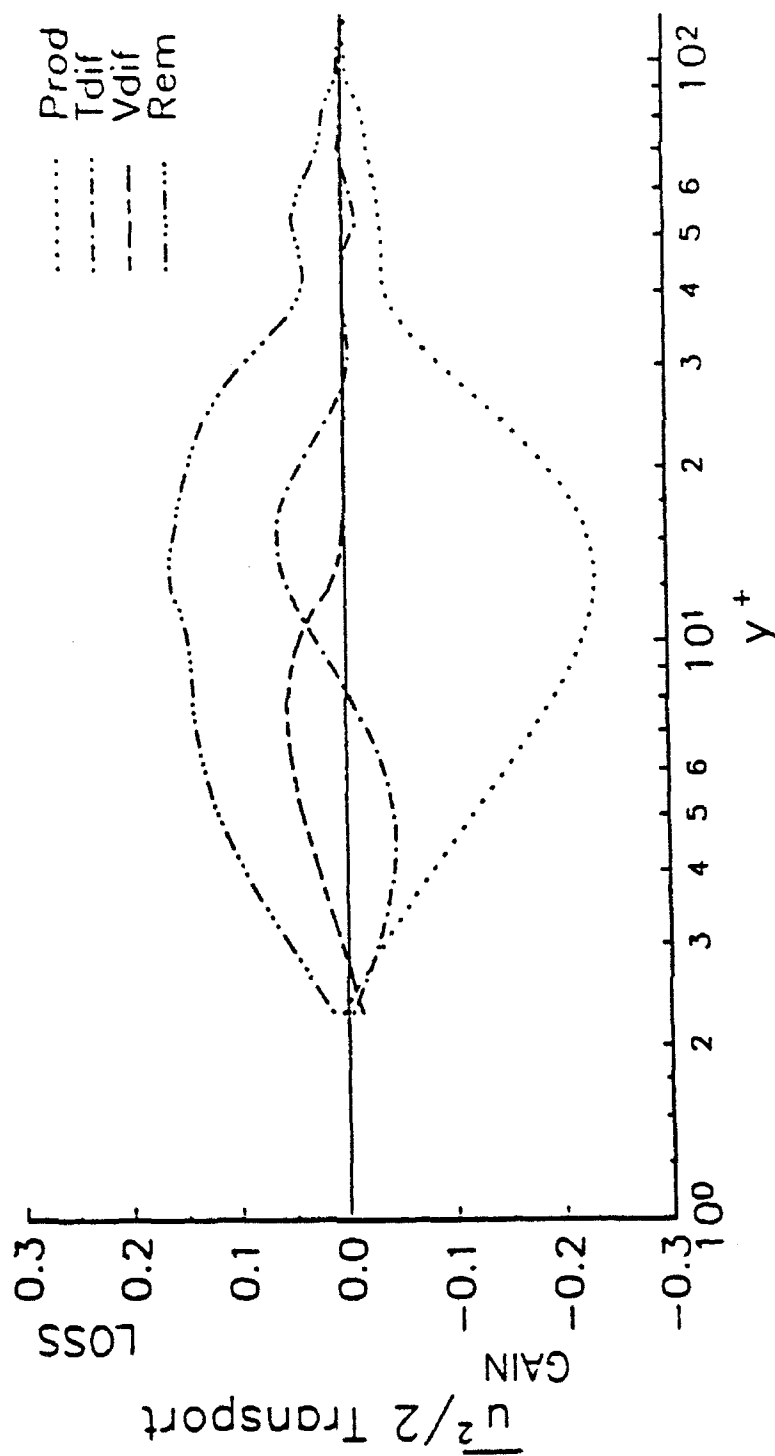


Figure 6.6 Profiles of the terms of the $u'^2/2$ transport equation in the undisturbed glycerin tunnel turbulent boundary layer

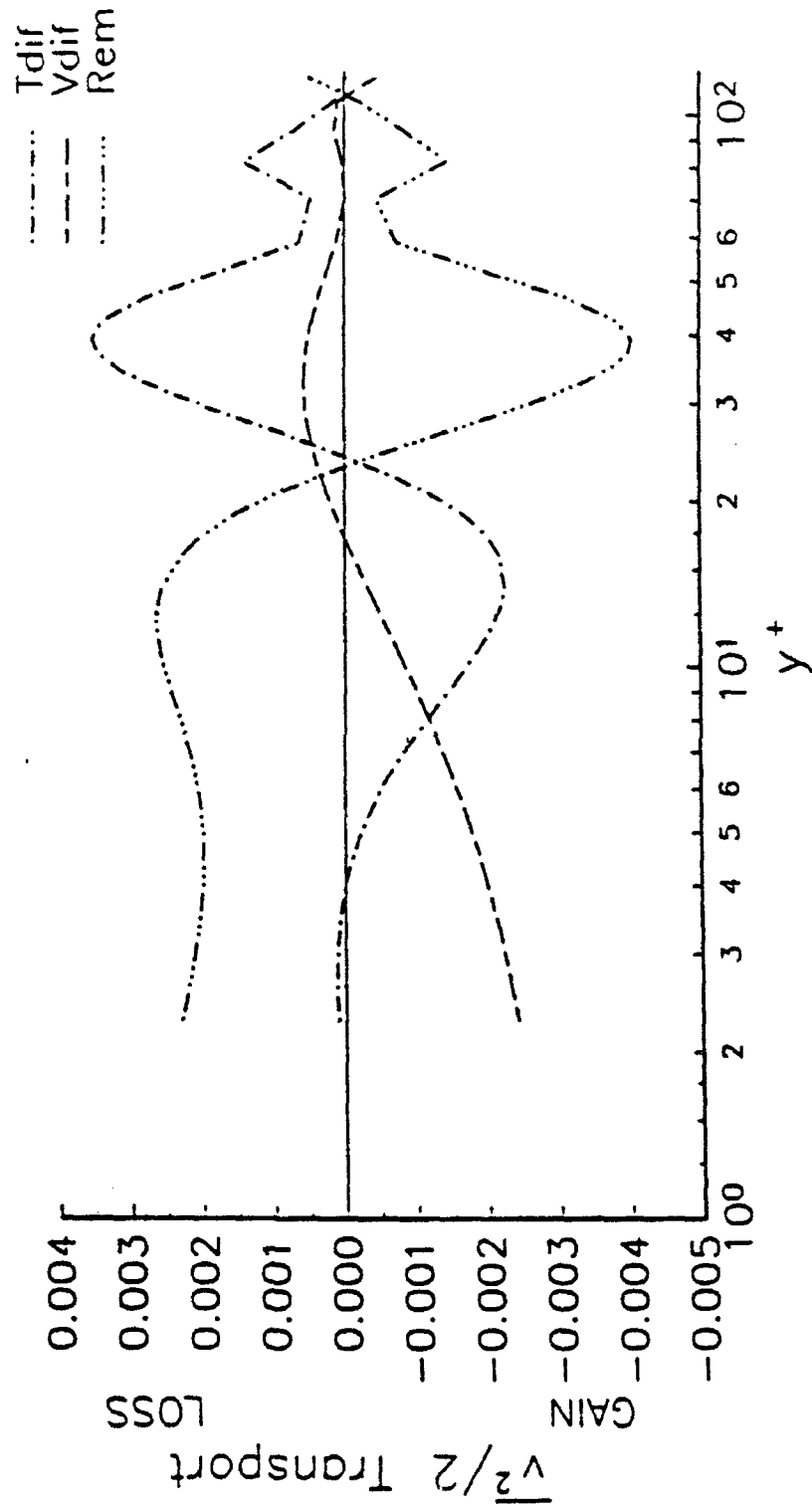


Figure 6.7 Profiles of the terms of the $v^2/2$ transport equation in the undisturbed glycerin tunnel turbulent boundary layer

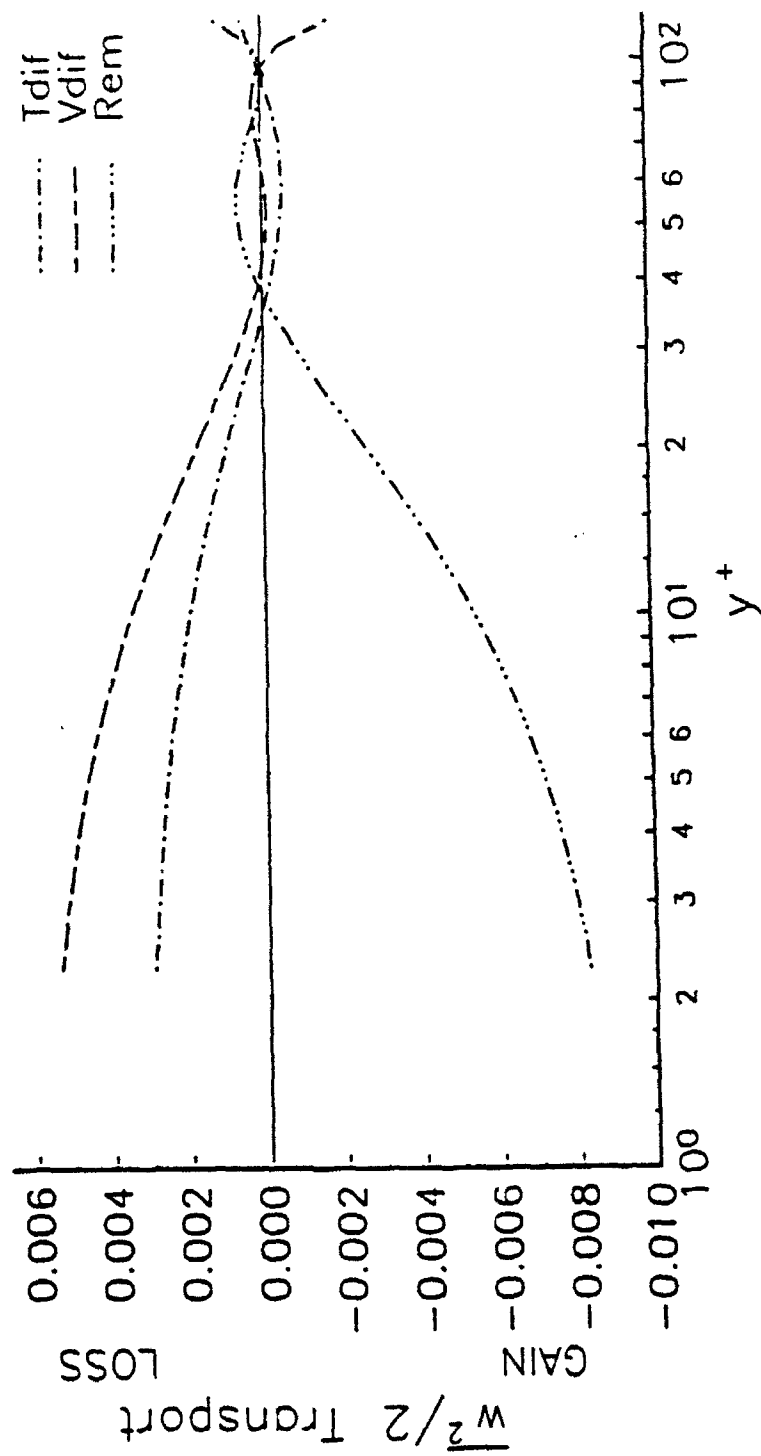


Figure 6.8 Profiles of the terms of the $w^2/2$ transport equation in the undisturbed glycerin tunnel turbulent boundary layer

contribution from convection, and the only production occurs in the $u'^2/2$ component. Energy is transmitted from the $u'^2/2$ component to the other two components through the pressure velocity correlations. The viscous diffusion and turbulent diffusion terms distribute energy amongst the scales within a particular component. The higher levels in the spanwise components compared to the levels of the radial components indicate that the direction of energy transfer across the components travels from u to w to v . Thus u' levels are greater than w' levels which in turn are larger than the v' levels as is shown in Figure 4.3. The modified transport profiles for the components of q^+ , at $x^+ = 58$, are shown in Figures 6.9 to 6.11. Note the change of scale of the ordinates in these figures.

The $u'^2/2$ profiles in Figure 6.9 indicate that this component is the dominant contributor to the observed modifications in the profiles of the rates of production, convection and turbulent diffusion of q^+ . The significant reduction in the rate of production below $y^+ = 15$ is caused by the mean flow convergence. Similar to the rate of turbulent diffusion of q^+ , the $u'^2/2$ rate of turbulent diffusion is increased below $y^+ = 10$. However, the decrease in the rms levels in this region indicate that the transport of energy into the near wall region is not sufficient to completely offset the decreased energy levels resulting from the reduction in the rate of production of $u'^2/2$ energy.

Figure 6.10 indicates that there is a significant increase in the rate of production of $v'^2/2$ at $y^+ = 15$. In addition there is a contribution to the rate of energy gain due to mean flow convection at larger y^+ . The increase in the rate of mean flow convection is offset by a negative production increase which implies that the mean flow gradients of the radial velocity are extracting energy from the turbulence. It may be that the lack of change in the radial rms profiles of Figure 5.13 results from the transport of energy into the mean flow convergence region by the counter-rotating vortices. The vortices bring radial velocity fluctuations into the

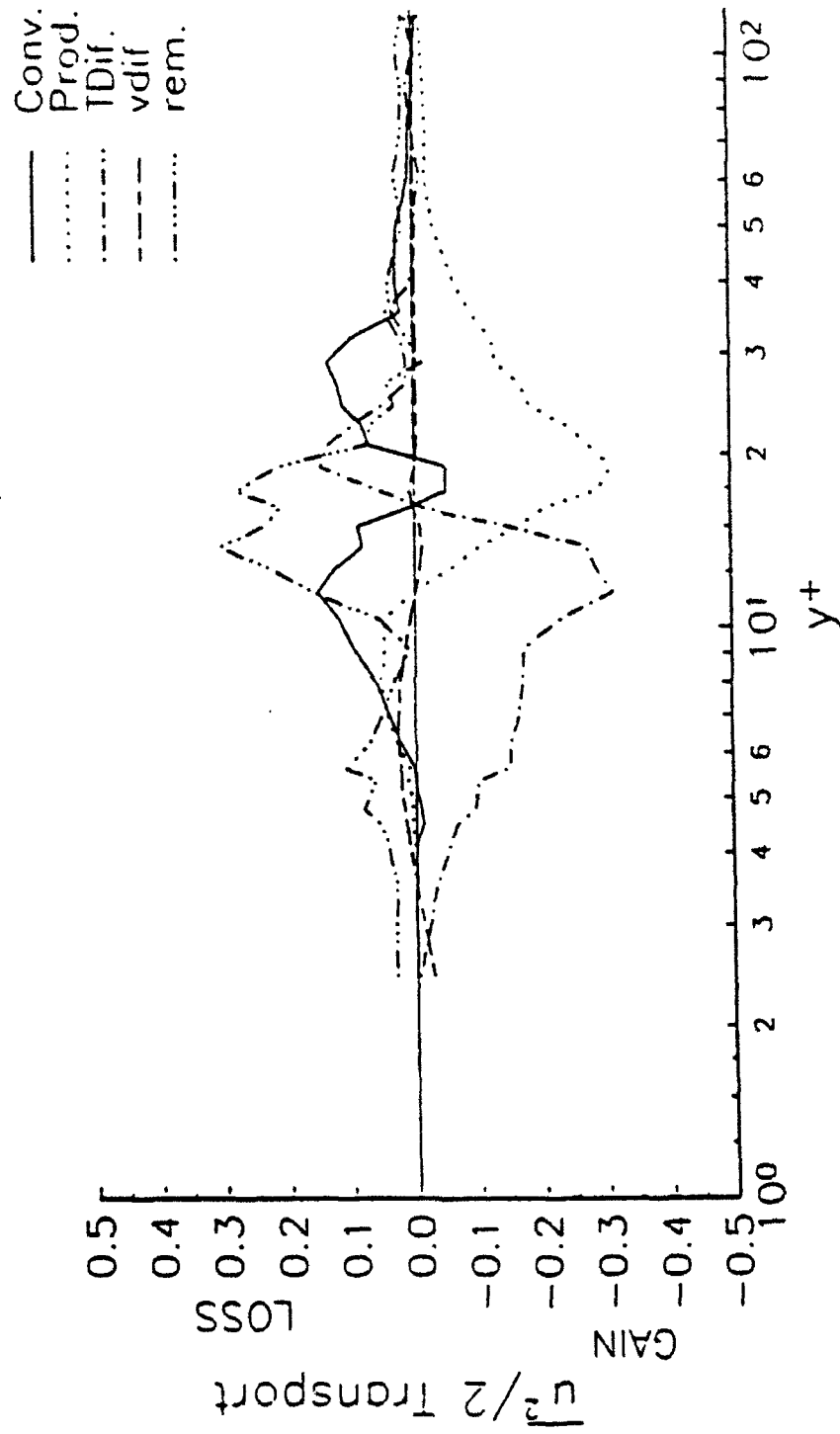


Figure 6.9 Profiles of the terms of the $u'^2/2$ transport equation at $x' = 58$ and $z' = 0$.
Normalization with ref. u'

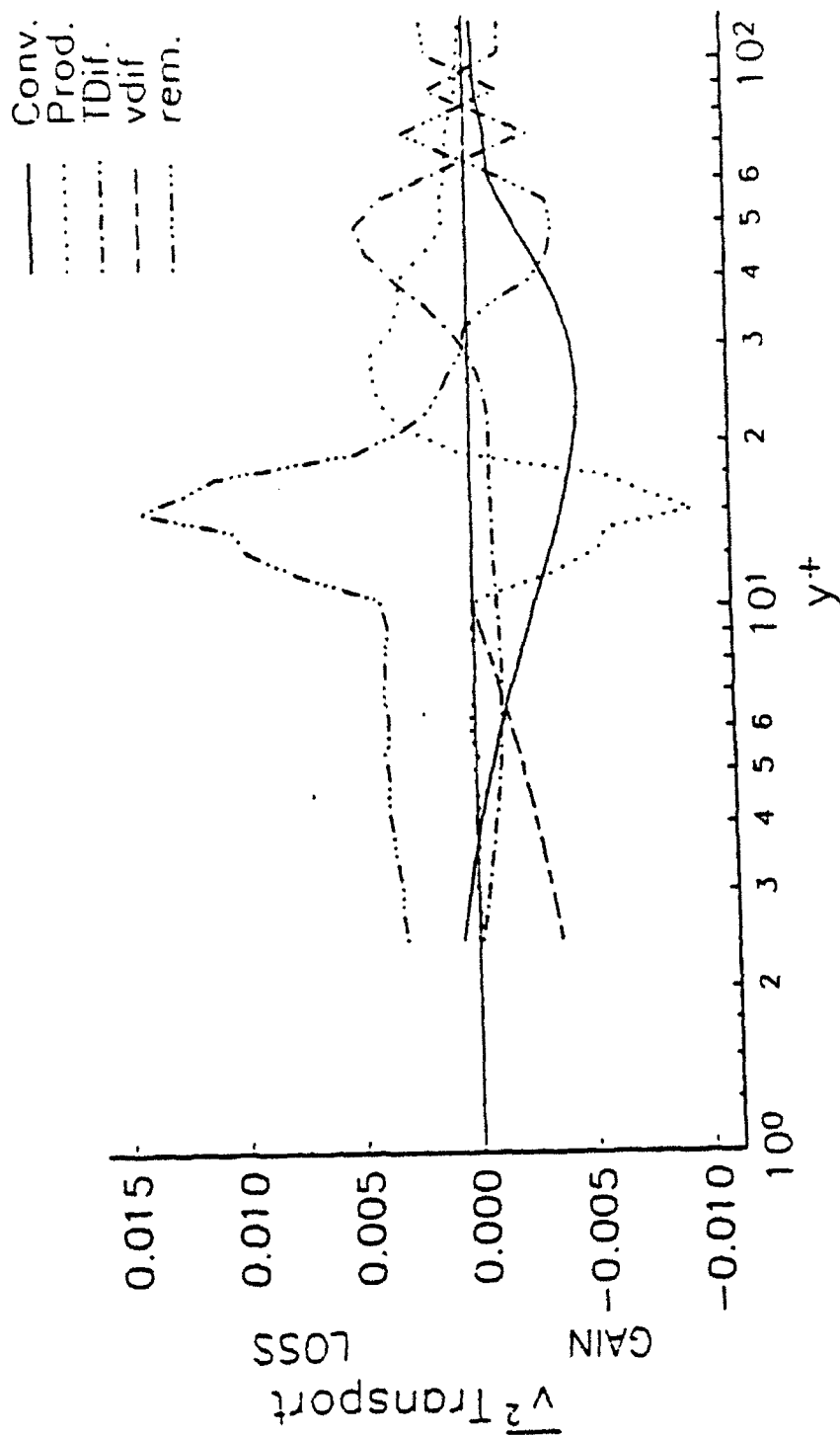


Figure 6.10 Profiles of the terms of the $\frac{v^2}{2}$ transport equation at $x^* = 58$ and $z^* = 0$.
Normalization with ref. u^*

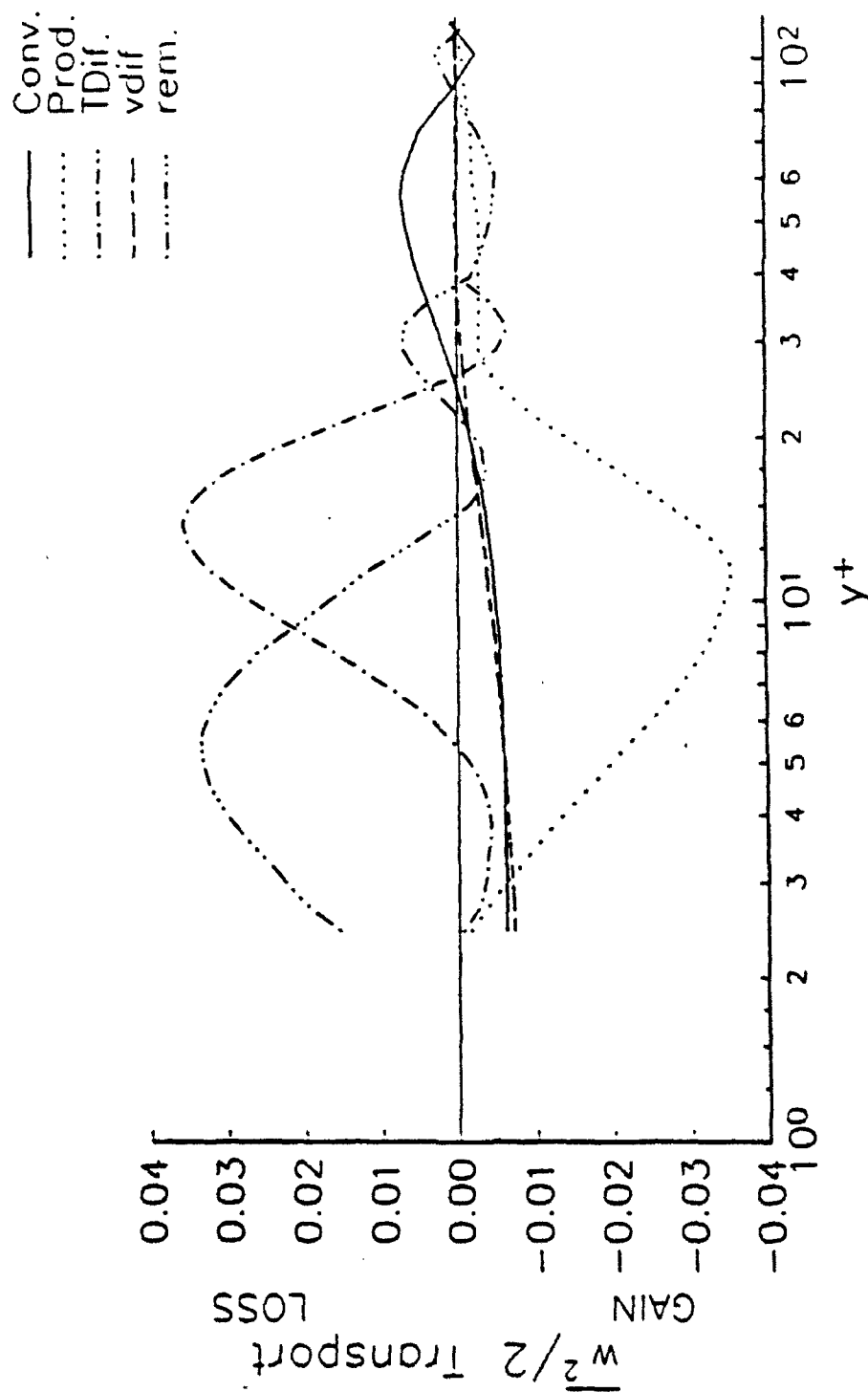


Figure 6.11 Profiles of the terms of the $w^2/2$ transport equation at $x^* = 58$ and $z^* = 0$.
Normalization with ref. u^*

wall region as they wander across the centerplane. In addition, the rotational velocity distribution of the vortices entrains high energy fluctuations from the region of production at $y^+ \approx 15$. It is speculated that this added energy offsets any reduction in energy due to the inhibition of turbulence by the mean flow convergence. This results in no net change in the rms levels within experimental uncertainty, which is a surprising result.

The counter-rotating vortices and the mean flow convergence directly affect the profiles of the transport of $w^2/2$ shown in Figure 6.11. The rate of production is significantly increased over the entire near wall region by the addition of spanwise gradients of the mean velocities. The profile of the rate of turbulent diffusion indicates that energy is transported from the region of high production towards the wall. The viscous diffusion term is opposite that observed in the reference condition from a loss to a gain in energy. An increase in convection is observed below $y^+ = 30$ towards an energy gain in this region. These modifications in $w^2/2$ are consistent with transport of turbulent energy in the form of velocity fluctuations by the intermittent wandering of the vortices crossing the centerplane. As mentioned in Chapter 5, the vortices bring high positive and negative spanwise velocity fluctuations into the centerplane as they wander. By an argument similar to that just used for the radial component, the increased energy from the production and the transport of energy by the vortices offsets reductions in energy caused by the mean flow convergence. Thus a negligible change in the spanwise rms levels, within experimental uncertainty, are observed on the centerplane. A comparison of Figures 6.10 and 6.11 indicate that on the centerplane the vortices influence the circumferential components of q^+ more than they influence the radial components.

A gradual recovery in the turbulent kinetic energy, q^+ , is observed with increasing streamwise distance from the bump. The centerplane profiles of the estimates of Equation 4.2

at $x^+ = 116$ are shown in Figure 6.12. The rate of production and rate of turbulent diffusion have nearly recovered. The peak in the profile of the rate of production is moving closer to the wall and is approximately equal to the reference value. Transport of q^+ by the mean flow convection is still observed, which indicates that considerable mean radial velocities and streamwise gradients of q^+ persist. The effects of the shear layer, which has moved to $y^+ = 30$, is no longer observed in the profile of the rate of production. This indicates that the shear layer considerably weakens as it convects downstream.

Off-centerplane profiles of the transport terms of q^+ are shown in Figure 6.13. These profiles are measured at $x^+ = 58$ and $z^+ = -11$. The peak in the rate of production of q^+ is moved towards the wall, while the magnitude of the peak is still slightly elevated above reference levels. The effects of the shear layer at $y^+ = 20$ are not observed, which indicates that the shear layer is relatively narrow in spanwise extent. The off-centerplane uv^+ results, described in Chapter 5, indicate that the shear layer is on the order of 11 wall units wide. The increased production levels are a result of both the additional Reynolds stresses and the associated mean velocity gradients. In particular, the $uw\partial U/r\partial\theta$ and the $uw\partial W/\partial x$ terms increase the rate of turbulent kinetic energy production. The convection by the mean flow is increased below $y^+ = 25$ resulting in a gain of energy, while a decrease is observed beyond $y^+ = 25$ which results in a loss of energy. It is speculated that the absence of a convergence region and the addition of the $uw\partial U/r\partial\theta$ term to the rate of production of $u'^2/2$ results in increasing u' levels for $z^+ < 0$. The major contributor to the production of $w'^2/2$ is the $w'^2\partial W/\partial\theta$ component. At $z^+ = -11$, the circumferential gradient of the mean spanwise velocity is smaller than its value at the centerplane. The terms $vw\partial W/\partial r$ and $uw\partial W/\partial x$, which are zero on the centerplane, contribute to the production, but are small relative to the $w'^2\partial W/r\partial\theta$ term. In addition, it is also possible that the turbulent diffusion of $w'^2/2$ is reduced

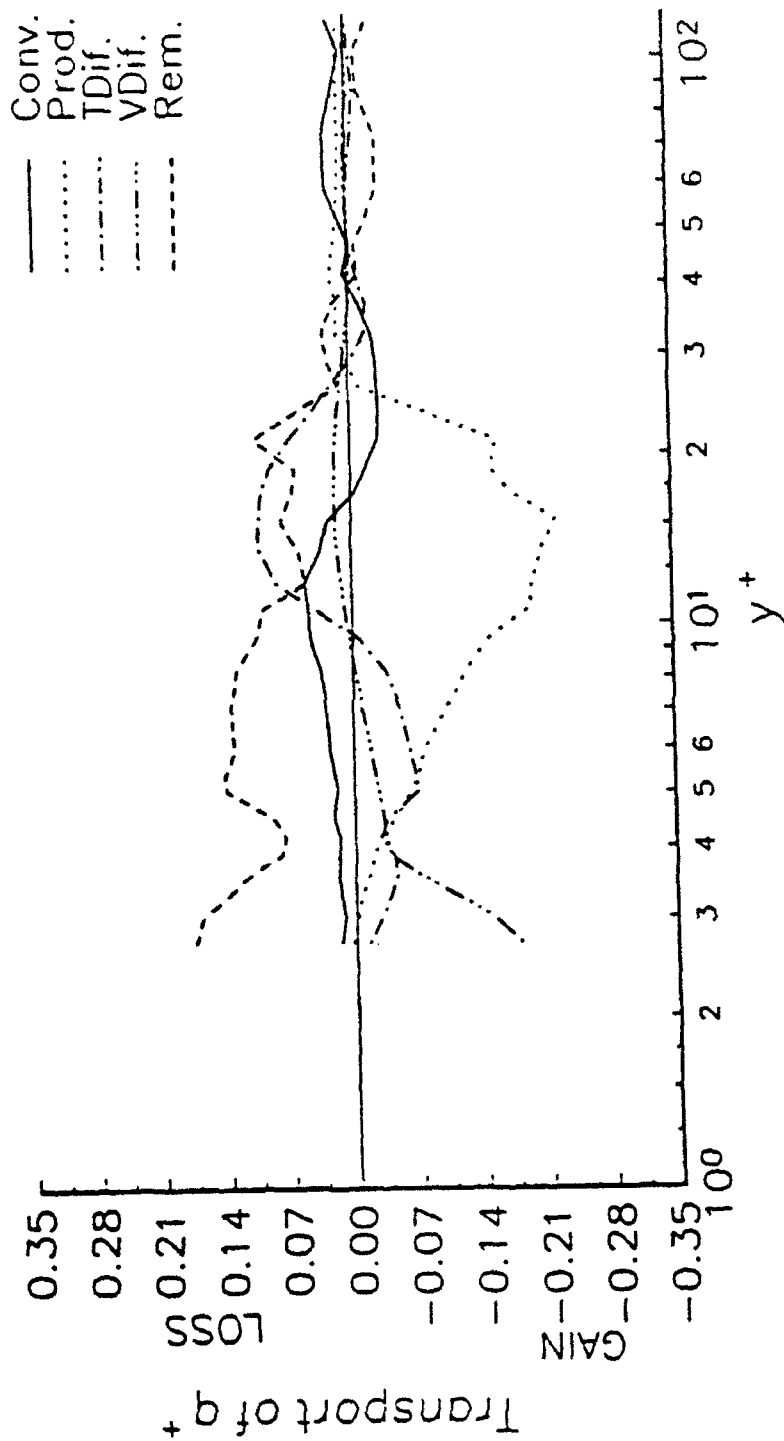


Figure 6.12 Profiles of the terms of the turbulent kinetic energy balance, Equation 4.2, at $x^+ = 116$ and $z^+ = 0$.
Normalization with ref. u^*

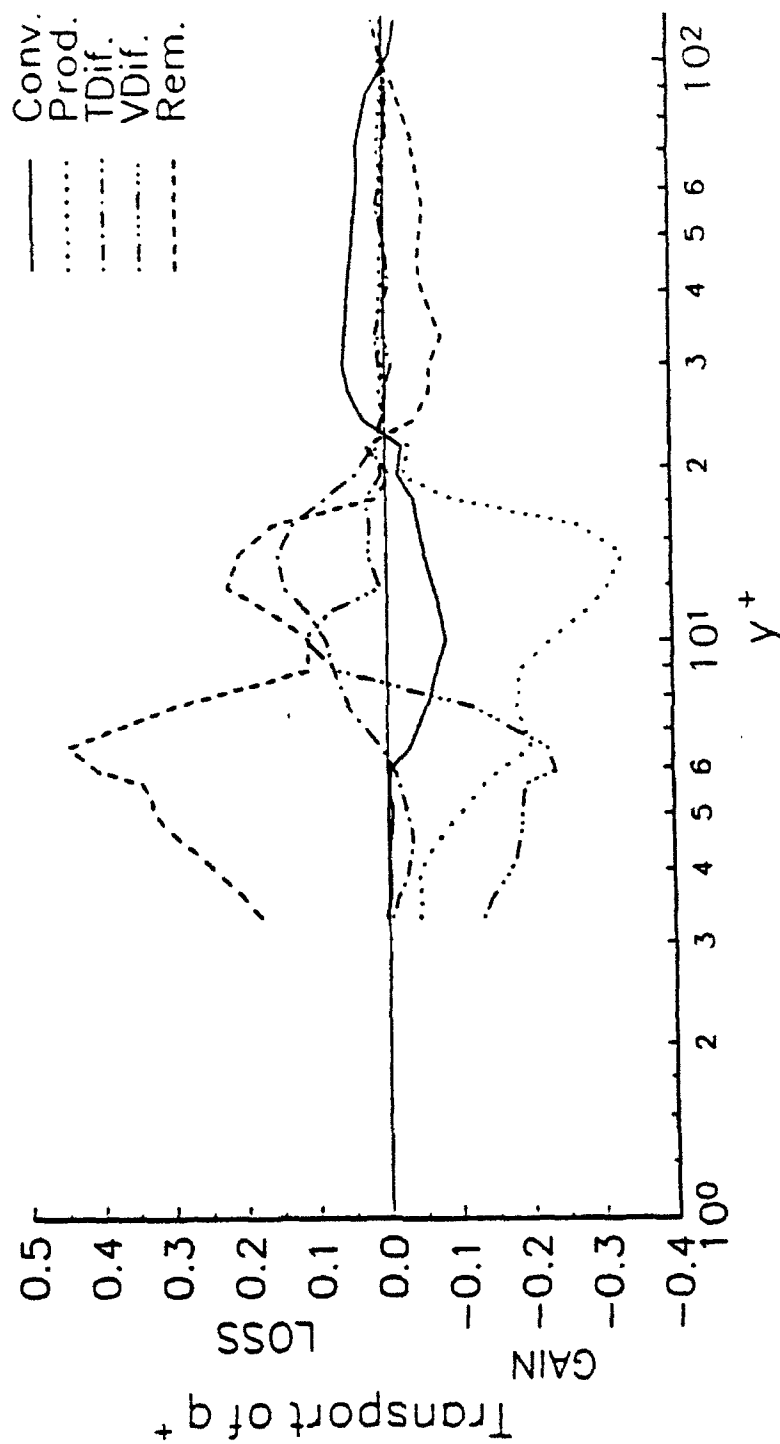


Figure 6.13 Profiles of the terms of the turbulent kinetic energy balance, Equation 4.2, at $x^+ = 58$ and $z^+ = -11$.
Normalization with ref. u^*

by moving outside the region of penetration of the other vortex. The combination of these effects may result in a reduction in w' levels with increasing z^+ . The observed increasing streamwise and decreasing circumferential rms levels with increasing spanwise displacement may also suggest that a transfer of energy may occur between the two velocity components with increasingly negative displacement from the centerplane.

6.2 Velocity Spectra

Turbulent velocity energy spectra are estimated from three-component, coincident, single-point velocity measurements at several locations downstream of the bump. The measurements are made at two axial locations, $x^+ = 58$ and 116 , for $z^+ = 0, -5.5$ and -11 . At each of these positions, four radial locations in the boundary layer are investigated at $y^+ = 5, 15, 20$ and 40 . The velocity measurements for the spectral estimates and the spectral estimation procedure are described in Section 3.3.4.

The estimated frequency spectra confirm the conclusion that the mean flow convergence inhibits large scale motions which leads to a decrease in energy at low frequencies. In addition, the transport of energy by the counter-rotating vortices occurs at higher frequencies. Figures 6.14 to 6.16 show the frequency auto-spectra for the three velocity components at $y^+ = 5$. The auto-spectra of the streamwise and radial velocity components indicate that a reduction in the energy at frequencies below approximately 30 Hz occurs on the centerplane at $x^+ = 58$. This corresponds to the location of significant reductions in the uv^+ correlation and the rate of production of q^+ . In contrast, the auto-spectra of the spanwise velocity component at this location does not show any significant departure from the reference levels below 30 Hz. The axial and radial component auto-spectral estimates show increasing low frequency energy levels with both increasing

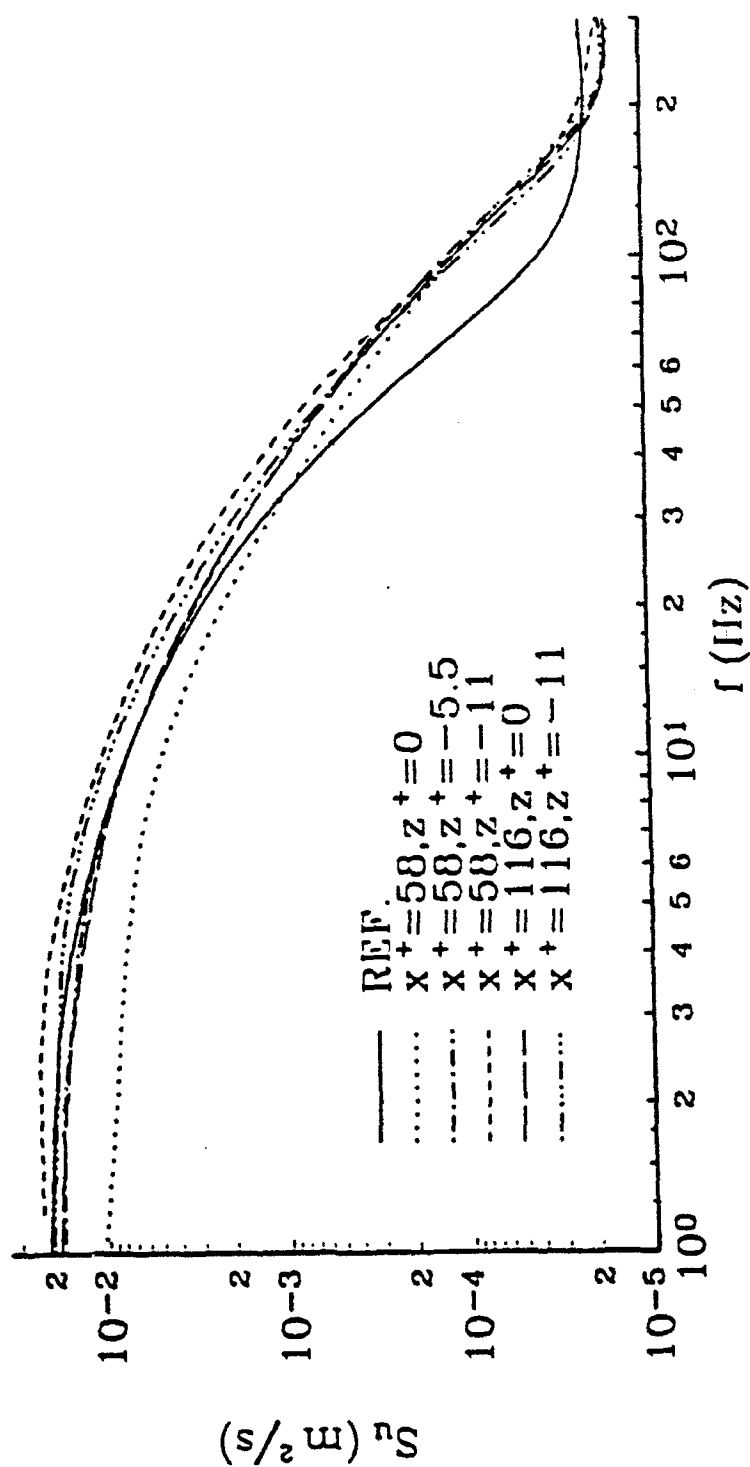


Figure 6.14 Auto-spectral estimates of the streamwise velocity component at $y^* = 5$.
Lines are curve fits to the estimated auto-spectra

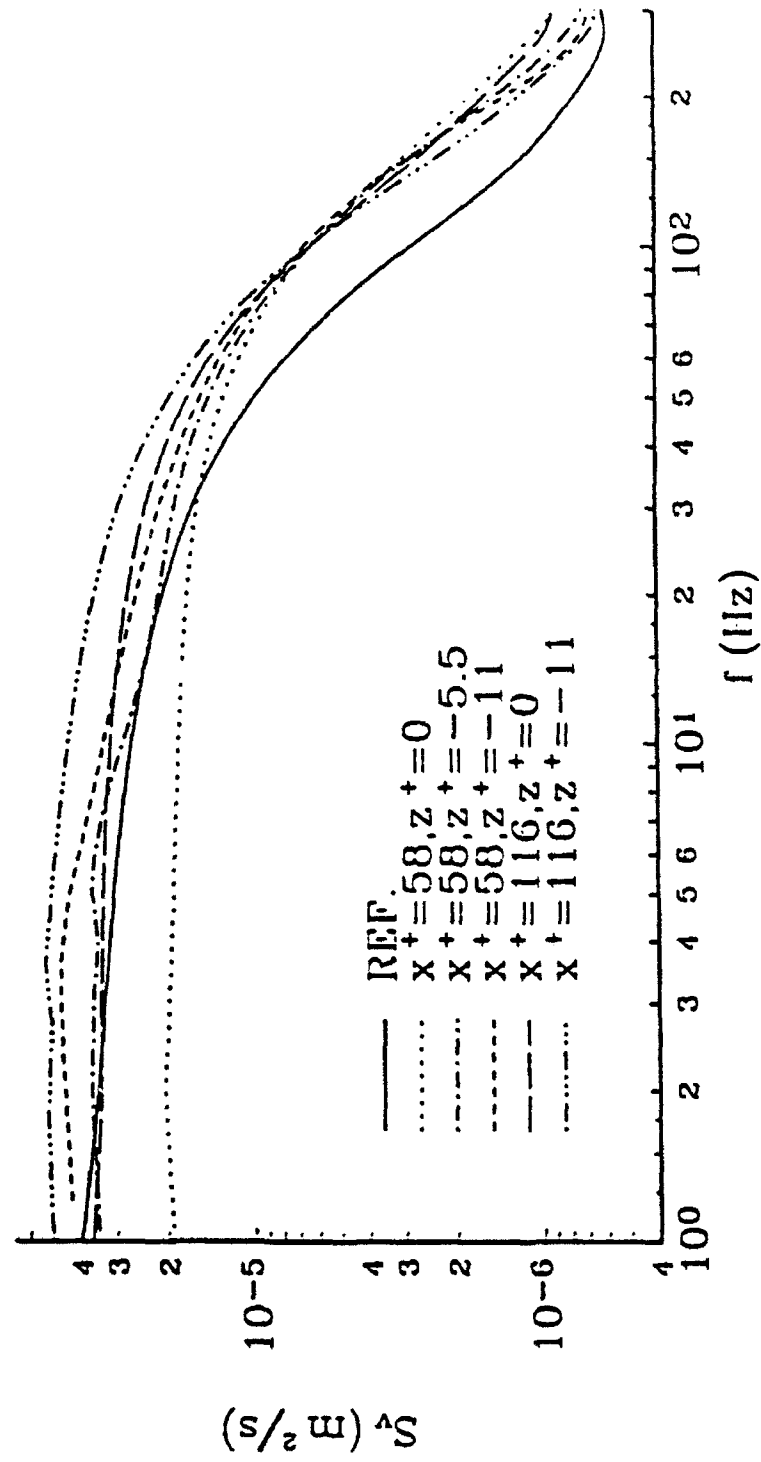


Figure 6.15 Auto-spectral estimates of the radial velocity component at $y^* = 5$.
Lines are curve fits to the estimated auto-spectra

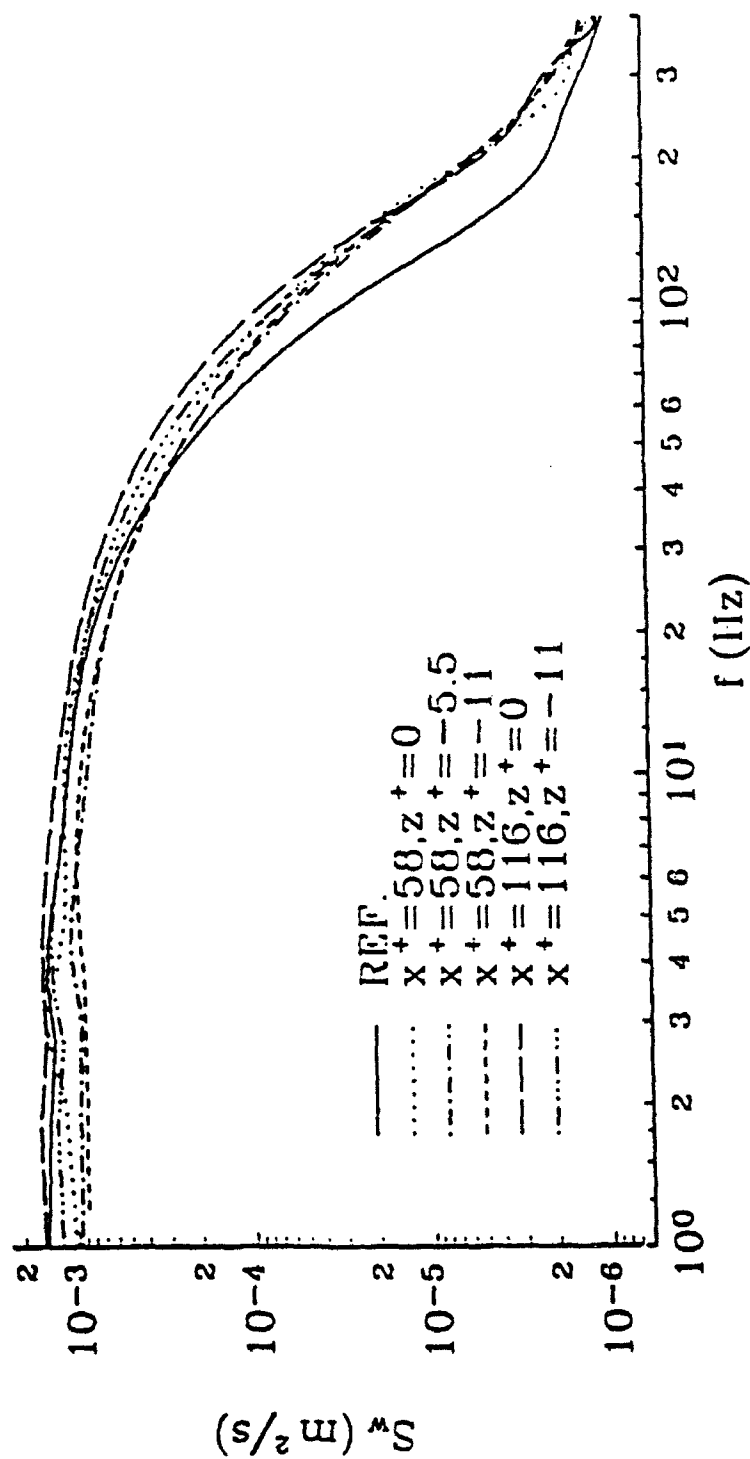


Figure 6.16 Auto-spectral estimates of the circumferential velocity component at $y^* = 5$.
 Lines are curve fits to the estimated auto-spectra

streamwise and spanwise displacement. At $z^+ = -11$, both the streamwise and radial energy levels are increased above reference levels at low frequencies. The spanwise auto-spectra exhibit an opposite behavior with spanwise displacement where a reduction in low frequency energy is observed with increasing z^+ . Increasing levels in the spanwise velocity auto-spectra are also observed with increasing x^+ along the centerplane. The high frequency energy levels of all the velocity component auto-spectra are elevated above reference levels.

These results are consistent with the conclusions drawn from the turbulent kinetic energy balance presented in Section 6.2. At $x^+ = 58$, a significant reduction in the production of $u'^2/2$ is observed on the centerplane, below $y^+ = 10$. As in the reference case, there is no production of $v'^2/2$ for $y^+ \leq 10$. The production of energy occurs at frequencies of approximately 10 Hz. The lack of production in these components suggests that there may be little low frequency energy available to offset or add to the reduced energy levels due to the mean flow convergence. Thus, the streamwise and radial velocity auto-spectral levels should be lower than reference levels at low frequencies. This is indeed observed in the streamwise and radial velocity auto-spectra at $y^+ = 5$. The energy balance of $w'^2/2$ shown in Figure 6.11 indicates that production of this component of q^+ occurs throughout the wall layer, and correspondingly the low frequency spanwise velocity auto-spectra is nearly unchanged.

The increased energy at high frequencies is a result of the transport of energy into the sublayer region by the counter-rotating vortices. The frequency range over which the transport of energy by the vortices occurs is limited at the low frequency end by the rate at which the vortices wander and cross the centerplane. This rate will be a minimum frequency at which the turbulent transport of energy by the vortices can occur. As the vortex wanders across the centerplane, the frequency of the fluctuations will be dependent on the speed at

which the vortex is traveling, the turnover time of the vortex and the size of the structures being entrained by the vortex.

A rough estimate of the wandering frequency may be obtained by performing a time between burst analysis on the uw correlation signal. The bimodality of the distribution at large streamwise fluctuations is used as the conditioning event. The results are quite scattered but range between 4 and 11 Hz. These low frequency estimates are consistent with visual observations of the vortices when the tunnel is densely seeded with air bubbles for flow visualization purposes. The auto-spectral energy estimates shown in Figures 6.14 to 6.16 indicate that the increased energy levels occur over a continuous range of frequencies greater than 40 Hz. An order of magnitude estimate of the turnover frequency of the counter-rotating vortex leg can be obtained by assuming a vortex 14 wall units in diameter with a rotational velocity proportional to the friction velocity. This gives an estimate of 19 Hz. The convection speed of the vortices past the LDV measurement volume will effectively increase the measured frequencies beyond the vortex turnover rate. It is also likely that as the vortex convects across the centerplane, it entrains velocity fluctuations from the thin shear layer at $y^+ \approx 20$ which probably has characteristic time scales much smaller than those of the counter rotating vortex. This will also contribute to the high frequency velocity fluctuations.

The increase in off-centerplane streamwise auto-spectra at low frequencies is consistent with the observed recovery in the rate of production of q^+ at $y^+ = 5$ in the $z^+ = -11$ profile shown in Figure 6.13. It would appear from examination of some of the auto-spectral estimates in Figures 6.15 and 6.16 that an increase in the radial and spanwise rms levels should be observed at several locations, since the variance of a velocity component is equal to the integral of the auto-spectra over all frequencies. However, caution must be advised in interpreting the high frequency auto-spectral estimates because of the relatively low

frequency cutoff due to the high noise ceiling of the LDV system. A close examination of the radial spectra, in Figure 6.15, indicates that at approximately 110 Hz the spectral curves cross. It appears that the rate at which energy is cascaded to the higher frequencies is greater in the curves with elevated low frequency energy. The off-centerplane radial velocity spectral curve at $x^+ = 116$ may be used as an example. At the LDV cutoff frequency, this curve appears to fall off at a faster rate with increasing frequency than the reference curve does. In fact, this curve must cross under the reference curve at higher frequencies than resolved, as the integral is equal to the variance which is unchanged from the reference. The faster rate of energy reduction with increasing frequency indicates that the rate of dissipation may be higher.

The energy spectra at $y^+ = 15$ is shown in Figures 6.17 to 6.19. The auto-spectral estimates are closer to reference levels for all velocity components at this location. The streamwise and spanwise auto-spectra at $y^+ = 15$ show similar trends as that observed at $y^+ = 5$, but with a smaller percent variation in the energy levels with varying axial and spanwise locations. In contrast to that observed at $y^+ = 5$, the radial auto-spectra show a similar behavior to the spanwise auto-spectra at this location. The peak in the production of $v^2/2$ occurs at this location on the centerplane and is probably related to the thin shear layer centered at $y^+ = 17$. The high frequency energy levels in the radial and spanwise components show a rapid recovery towards reference levels with increasing y^+ . However, the streamwise component shows a relatively slow recovery in the high frequency auto-spectra. Elevated levels are still observed beyond frequencies of 50 Hz. By comparing Figures 6.6 and 6.9, the increased levels are caused by a higher rate of turbulent diffusion into this region. The high frequency energy is transported into this location by the entrainment of high streamwise velocity from above the vortex; in particular, from the high frequency streamwise

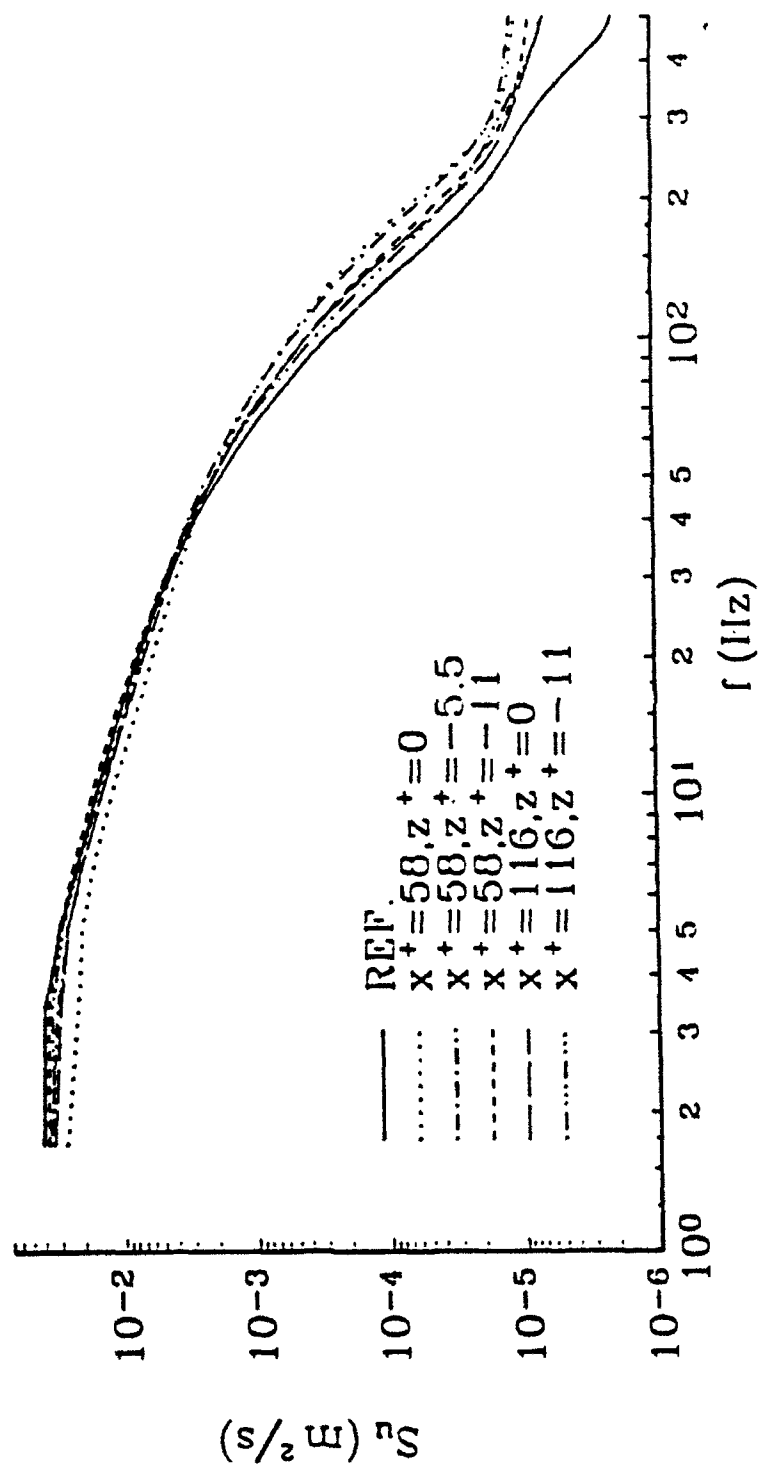


Figure 6.17 Auto-spectral estimates of the streamwise velocity component at $y^+ = 15$.
Lines are curve fits to the estimated auto-spectra

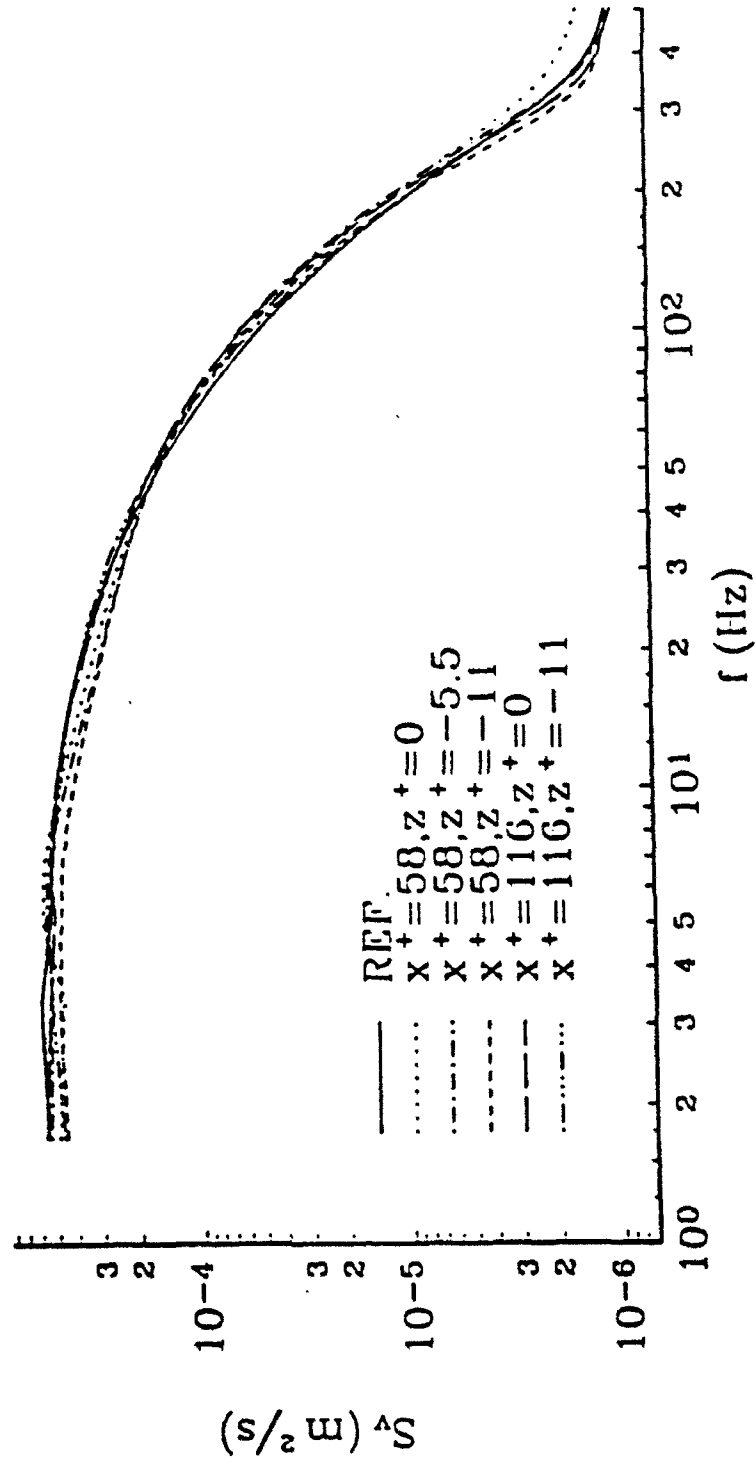


Figure 6.18 Auto-spectral estimates of the radial velocity component at $y' = 15$.
Lines are curve fits to the estimated auto-spectra

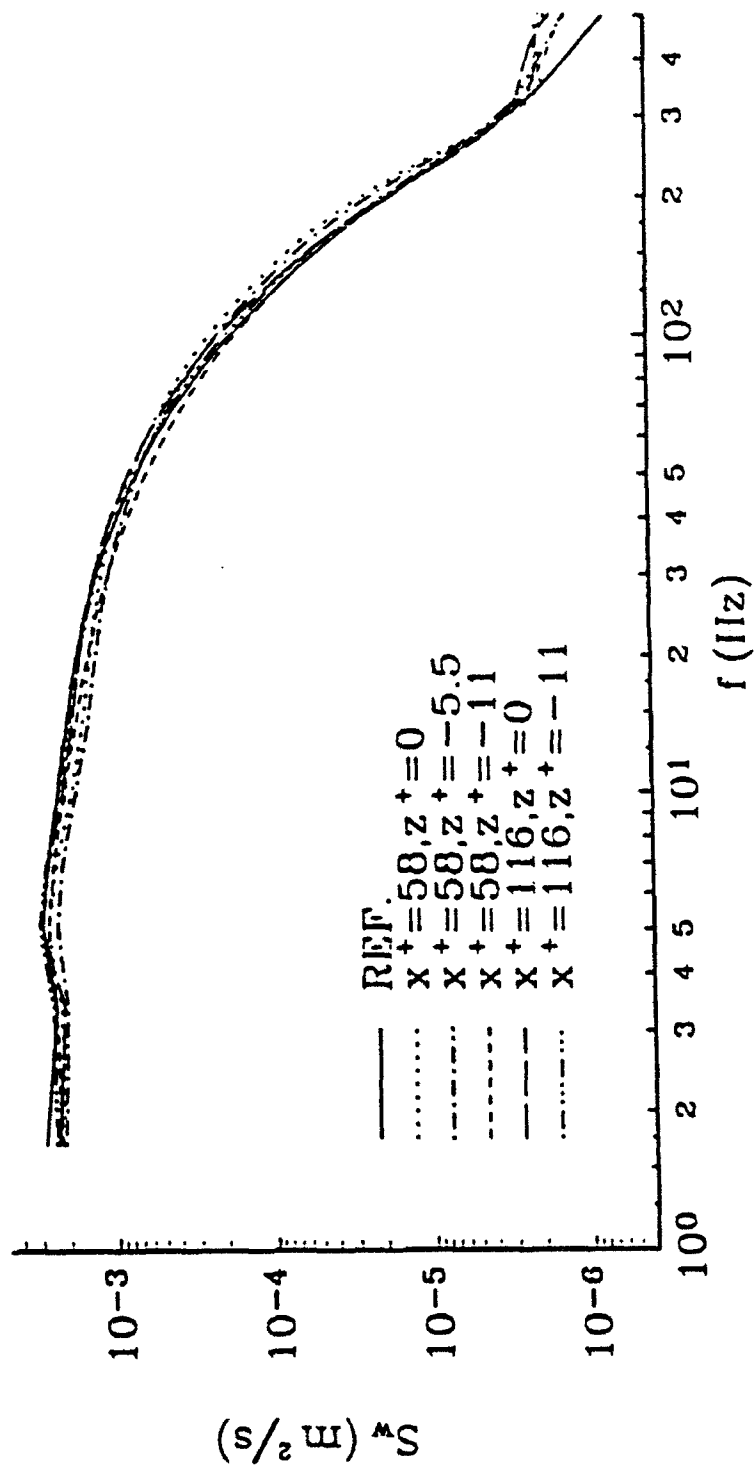


Figure 6.19 Auto-spectral estimates of the circumferential velocity component at $y^+ = 15$.
Lines are curve fits to the estimated auto-spectra

velocity fluctuations contained in the thin shear layer. The rate at which these curves fall off with increasing frequency is similar to the behavior observed in the example of the radial velocity auto-spectra at $y^+ = 5$. By $y^+ = 20$, the energy spectra are nearly recovered to reference levels, and full recovery is observed by $y^+ = 40$. These data indicate that the vortices are effective at transporting fluctuations with frequencies larger than the characteristic frequency of the vortices, which is estimated at approximately 19 Hz.

The single-point, coincident velocity measurements enable the estimation of the one sided cross-spectra between two of the three velocity components. The magnitude of the cross-spectra between the streamwise and radial velocities at $y^+ = 5$ is shown in Figure 6.20. The reference curves which indicate that the uv Reynolds stress producing events are large scale low frequency events are consistent with the observations presented in Chapter 5 and 6. These curves clearly illustrate the reduced correlation in the uv signal at $x^+ = 58$ on the centerplane. The uv cross-spectra rapidly recovers with increasing z^+ while a slow recovery is observed along the centerplane with increasing x^+ . Increased cross-spectra are observed at $z^+ = -11$ for both axial locations. While these increased cross-spectra indicate an increase in the Reynolds stress production, the integral must be equal to the magnitude of the uv correlation which is unchanged.

A recovery in the cross-spectra is observed with increasing y^+ . The centerplane cross-spectra at $y^+ = 15$ is shown in Figure 6.21. Reductions in the cross-spectra are still observed, although the magnitude of the changes in these curves is lower. By $y^+ = 20$, the cross-spectra, shown in Figure 6.22, are higher than reference which results from the presence of the second vortex structure and shear layer, and is consistent with the increased uv^+ levels measured at $y^+ = 20$.

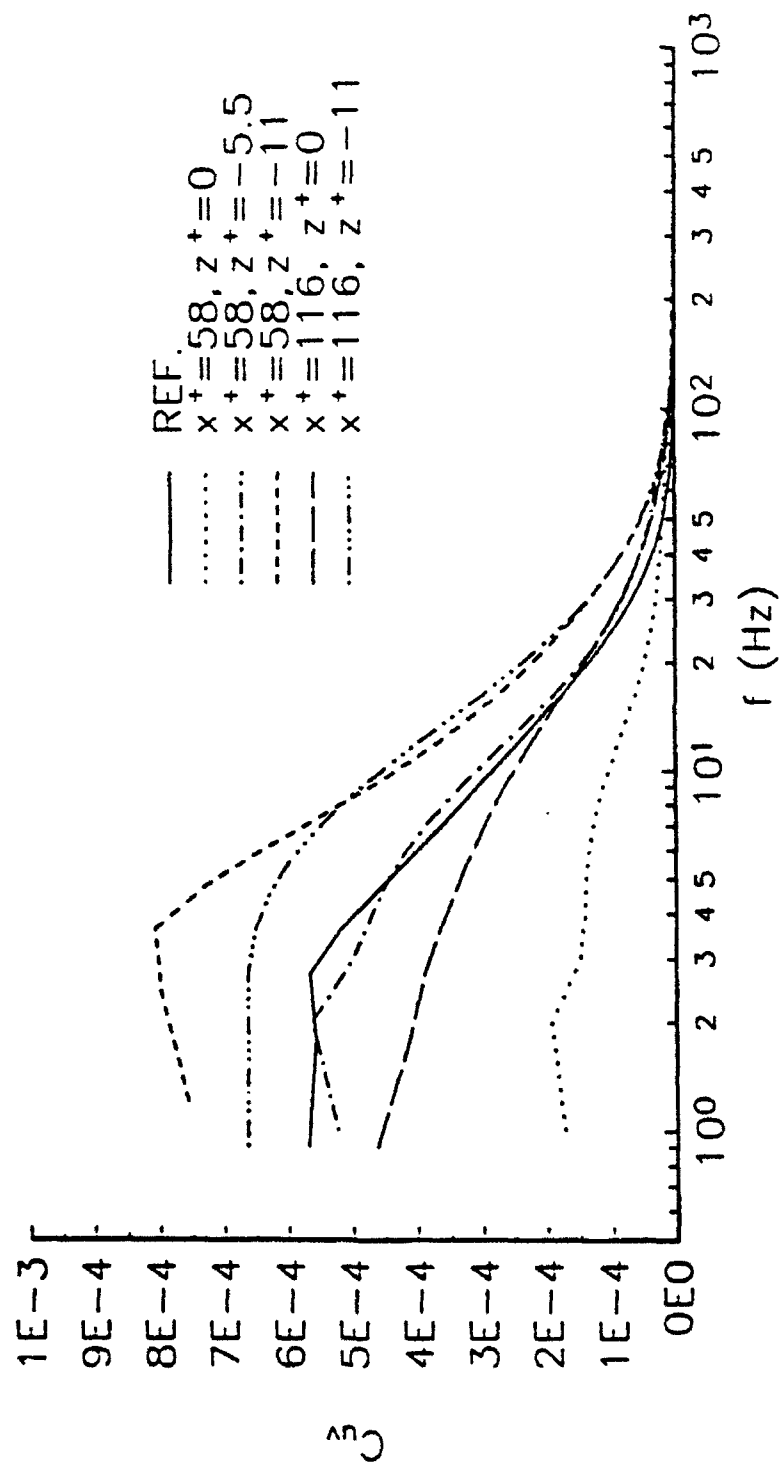


Figure 6.20 Magnitude of the one-sided cross-spectral estimates of the u and v velocities at $y^+ = 5$

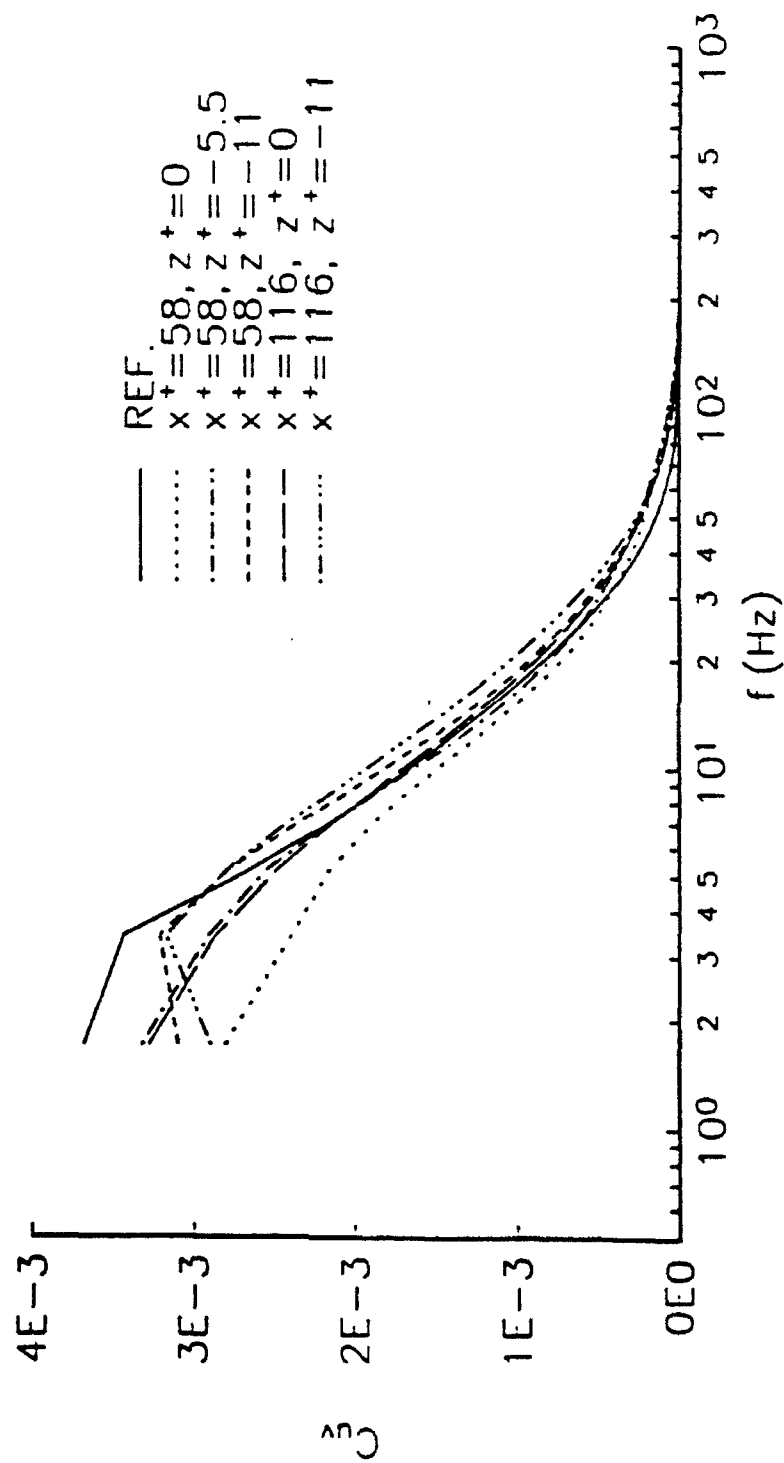


Figure 6.21 Magnitude of the one-sided cross-spectral estimates of the u and v velocities at $y^* = 15$

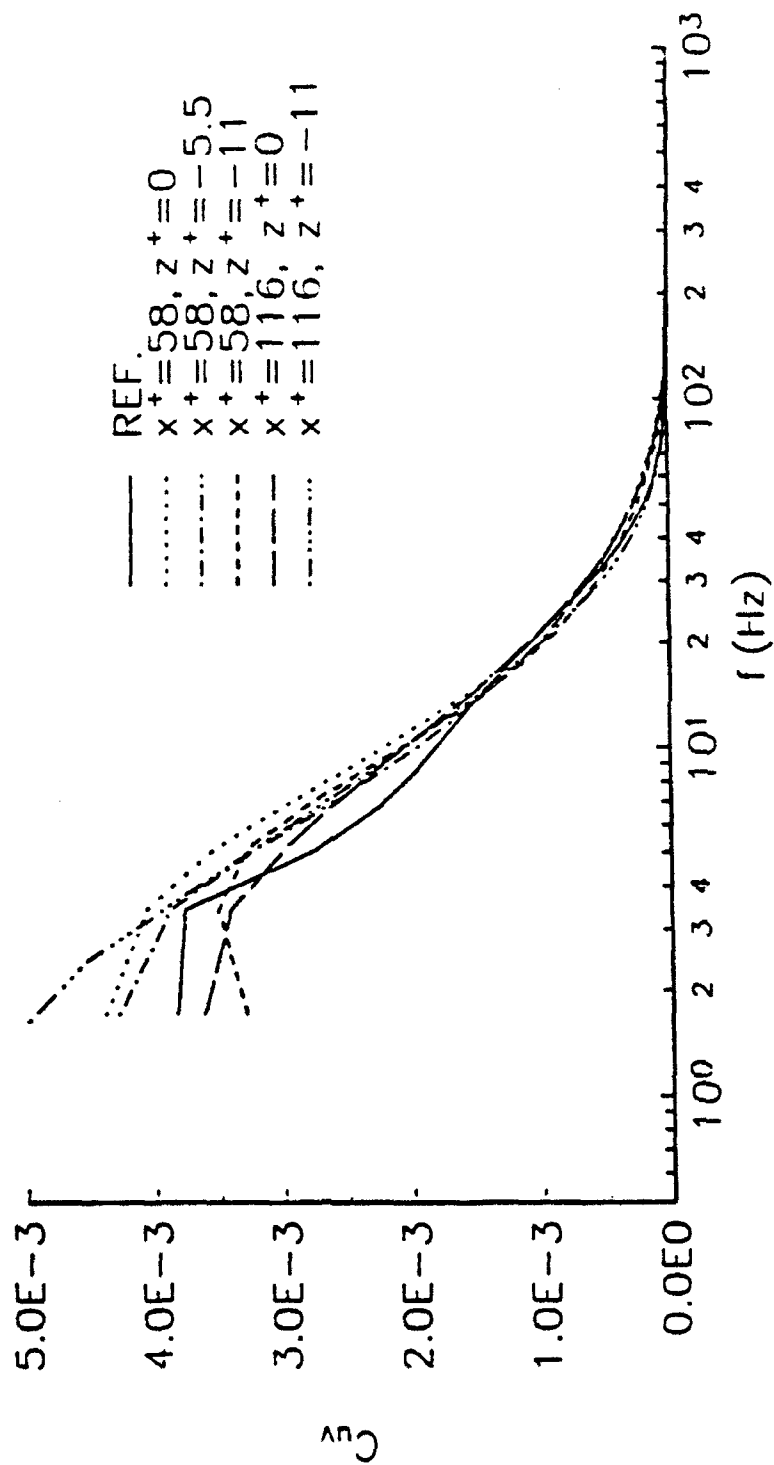


Figure 6.22 Magnitude of the one-sided cross-spectral estimates of the u and v velocities at $y^+ = 20$

Cross-spectra of the uw and vw velocity components show no change from reference levels on the centerplane and an increase in energy with increasing spanwise displacement. This is consistent with the increased correlations which are observed off the centerplane. Figures 6.23 and 6.24 show the uw and vw cross-spectra at $y^* = 5$, respectively. The recovery of these cross-spectra is very similar to that observed in the velocity correlations and was discussed in Chapter 5. These components of the cross-spectra are a consequence of the presence of the counter-rotating vortices. From Figures 6.23 and 6.24, it may be observed that the frequency range of significant uw and vw generation also occurs over low frequencies. Since the counter-rotating vortices are responsible for the generation of the uw and vw correlations, the cross-spectra provide an approximate range of frequencies over which the time scale of the vortices is likely to occur.

6.3 Summary

In general, the centerplane energy balance can be describe as follows. The strong mean flow convergence induces additional forces, due to the mean flow momentum, which are aligned towards the wall and centerplane. These additional forces inhibit outward velocity fluctuations by the turbulence and reduce overall turbulent momentum transport. It is shown that the mean flow convergence inhibits large scale fluctuations. This results in a decrease in Reynolds stress with a corresponding decrease in the local strain rate. These combined effects appear as a significant reduction in the local turbulent kinetic energy.

A thin shear layer is formed at the interface between the mean flow convergence and a second vortical structure at $y^* = 20$. Turbulent energy production in the streamwise and radial components is increased locally around this shear layer as shown in Figures 6.9 and 6.10. This generated turbulence results in a local increase in Reynolds stress and streamwise

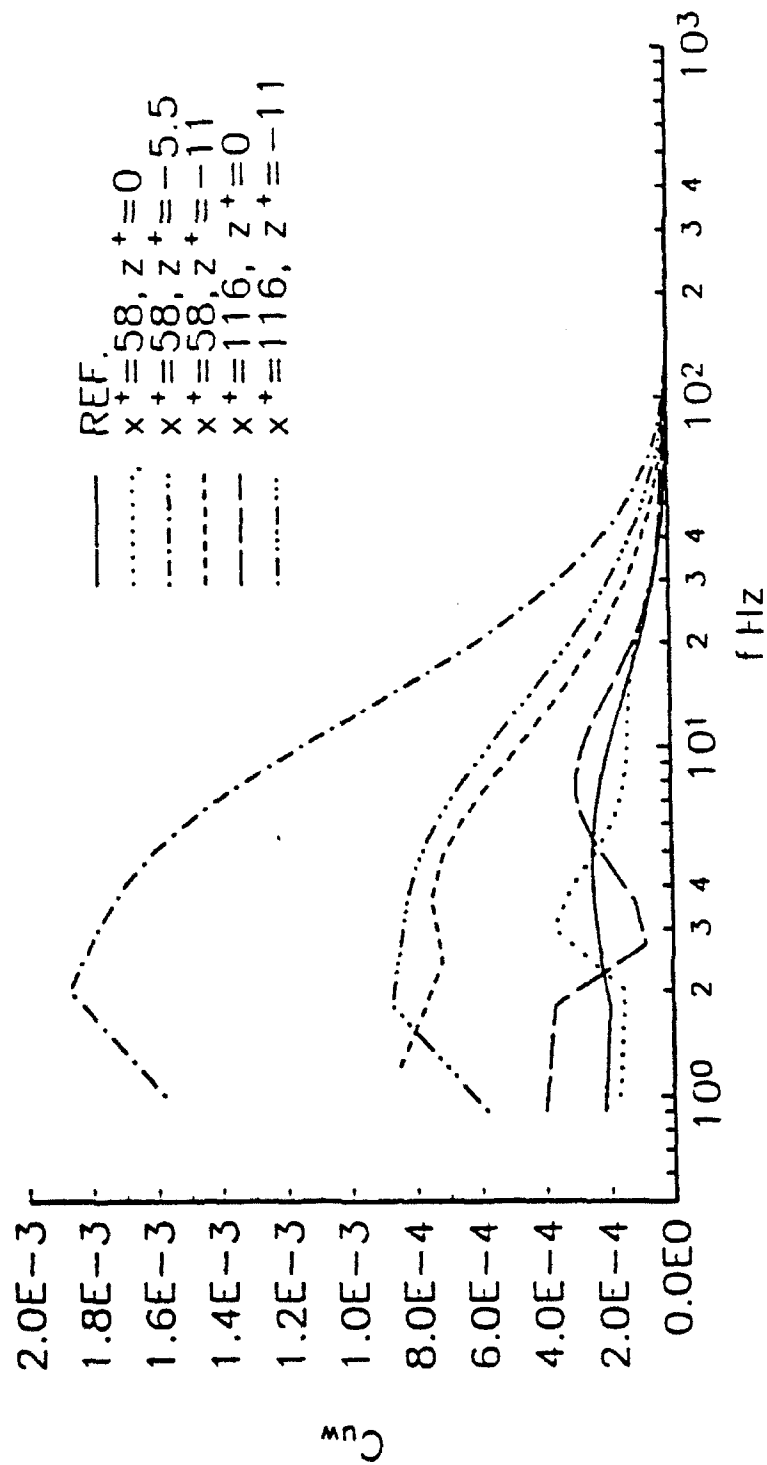


Figure 6.23 Magnitude of the one-sided cross-spectral estimates of the u and w velocities at $y^* = 5$

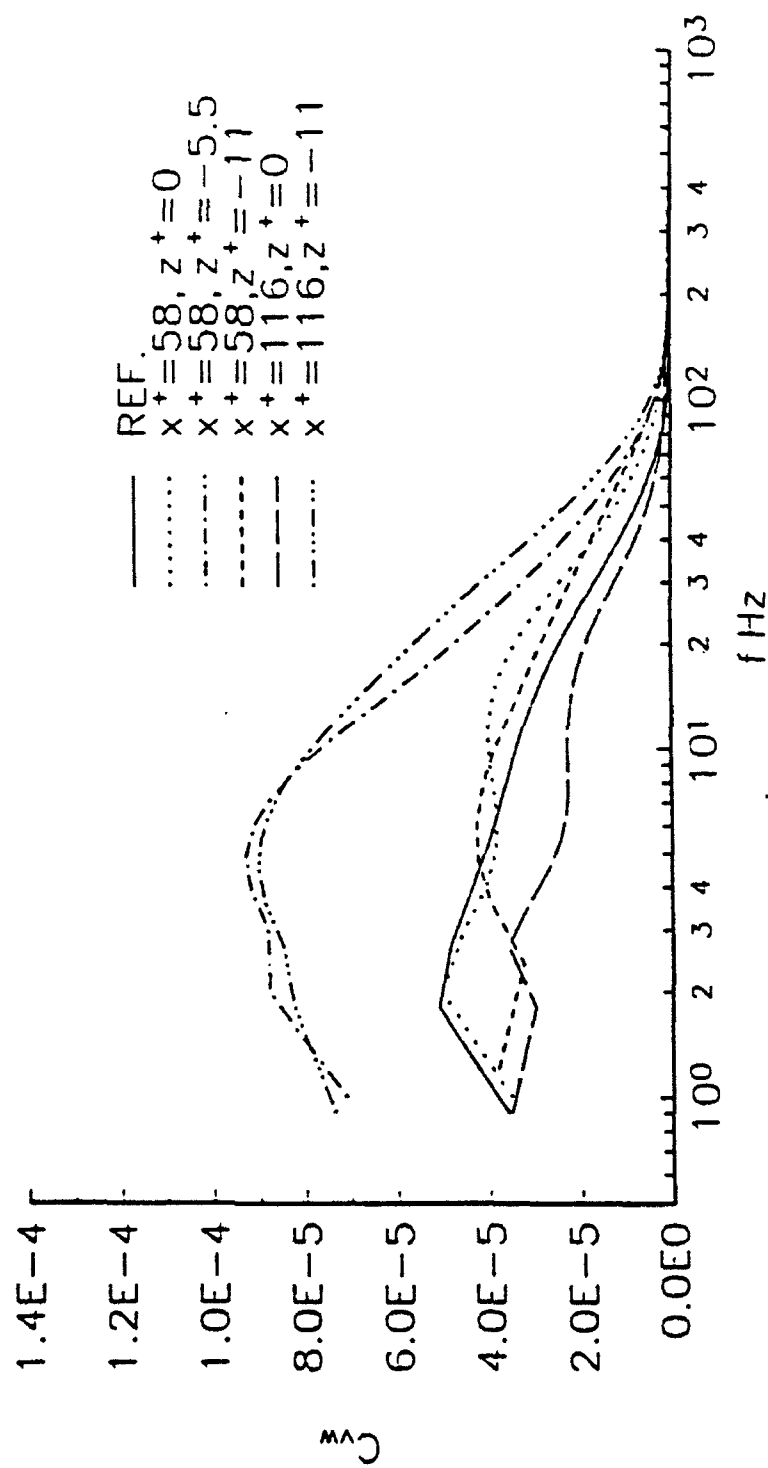


Figure 6.24 Magnitude of the one-sided cross-spectral estimates of the w and v velocities at $y^* = 5$

rms velocities. The strong radial mean flow directed towards the wall peaks at the location of this shear layer. It may be that this wallward motion retards large radial turbulent fluctuations. Thus, no change in the radial rms levels is measured.

Superimposed on the mean flow convergence region is the pair of counter-rotating vortices which intermittently wander and cross the centerplane. These vortices transport energy in the form of turbulent velocity fluctuations into this centerplane region. This energy is transported in the form of small scale (no larger than the size of the vortices) high frequency velocity fluctuations. As the vortices cross into the centerplane region, they carry large positive and negative spanwise velocity fluctuations, negative radial fluctuations and positive axial fluctuations. The axial fluctuations result from any mis-alignment of the vortices from the streamwise direction and from the entrainment of high streamwise velocity above the vortices. Below $y^* = 15$, the vortices have a greater effect on the spanwise velocity component than on the radial component. This occurs because negative radial velocity fluctuations are strongly inhibited by the wall, while the spanwise velocity fluctuations are not.

It may be that the inhibition of turbulence by the convergence region causes a reduction in energy in all components of q^* . However, the increased transport of energy by the counter-rotating vortices adds to these decreased energy levels. This increased energy by the vortices must offset any decrease in the energy of the radial velocity components, as the measured radial rms velocity levels are approximately equal to the undisturbed levels. The transport of energy by the vortices and the increased production of $w^2/2$ produces a similar effect on the circumferential rms levels at $z^* = 0$.

The velocity auto-spectral and cross-spectral estimates support the conclusions drawn from the turbulent kinetic energy analysis. The reduced low frequency energy in the

streamwise and radial velocity auto-spectra and the uv cross-spectra confirm the inhibition of large scale low frequency turbulence by the mean flow convergence. The transport of turbulence by the vortices occurs over a continuous frequency range of greater than 40 Hz.

Chapter 7

STOCHASTIC ESTIMATION

7.1 Introduction

The purpose of this chapter is to present the linear stochastic estimation technique, developed by Adrian (1979), and provide an example of its use in the current investigation. In addition, procedures and proposals for future use of this technique are provided. In complex flows where the form of the dominant structures is unknown, conventional conditional averaging techniques can require a considerable data reduction effort. The linear stochastic estimation technique is an analytical tool which can extract conditionally averaged information in a more efficient manner. Linear stochastic estimation uses the unconditional multi-point correlation tensor to extract the conditionally averaged information. To this end, two-point space/time correlation measurements are made in the modified near wall region downstream of the bump.

A brief description of the two-point correlation measurements are presented in the next section. Contour maps are shown and briefly discussed in the context of the modifications observed in these measurements compared to what is expected in a canonical turbulent boundary layer. The linear stochastic estimation technique is discussed in Section 7.3 and is applied to the measured zero time lag two-point correlations.

7.2 Two-Point Correlation Measurements

Two-point space/time velocity correlation measurements are obtained downstream of the bump. The current measurements are confined to the centerplane region, zero spanwise probe separation, due to measurement limitations of the facility. In the ideal situation, the

two-point correlation measurements would be made in the cross-stream, y - z , plane at several axial locations. These measurements would permit a more thorough determination of the characteristics of the quasi-streamwise vortices, since the vortex cross-sections are aligned with this cross-stream plane. However, the purpose of this work is to develop a working understanding of the stochastic estimation procedure. In this light, the centerplane zero time lag correlation measurements are sufficient to provide an example for the application of linear stochastic estimation. Throughout this chapter, the notation for the two-point measurements is defined such that when referring to a two point correlation, such as uw , the first variable is the velocity component measured at the fixed probe location and the second variable is the velocity component measured at the moving probe location. In the example given, uw , the fixed probe measures the axial velocity component and the moving probe measures the spanwise component.

The measurement of the two-point correlations involves using the LDV system in the manner described in Section 2.3. Two uv contour maps at fixed probe locations of $y^+ = 2$ and 12 are measured in the undisturbed glycerin tunnel to determine the accuracy of the LDV system. These measurements are compared to the uv two-point correlation data measured by Chevrin (1988) in the same facility. Both sets of correlations are obtained using the LDV systems operated in the TSI coincident mode. The data of Chevrin (1988) were measured using a similar LDV setup as that used here, with the exception that the fiber-optic probe was used in the back-scatter mode of operation. This greatly limited Chevrin's (1988) coincident data rates. The current uv correlation contour maps are shown in Figures 7.1 and 7.2. The axes represent the relative displacement of the moving probe from the fixed probe. In this notation the fixed probe is located at $\Delta x = \Delta y = 0$. The plus symbols in the figures represent the locations at which the velocity correlation measurements are obtained.

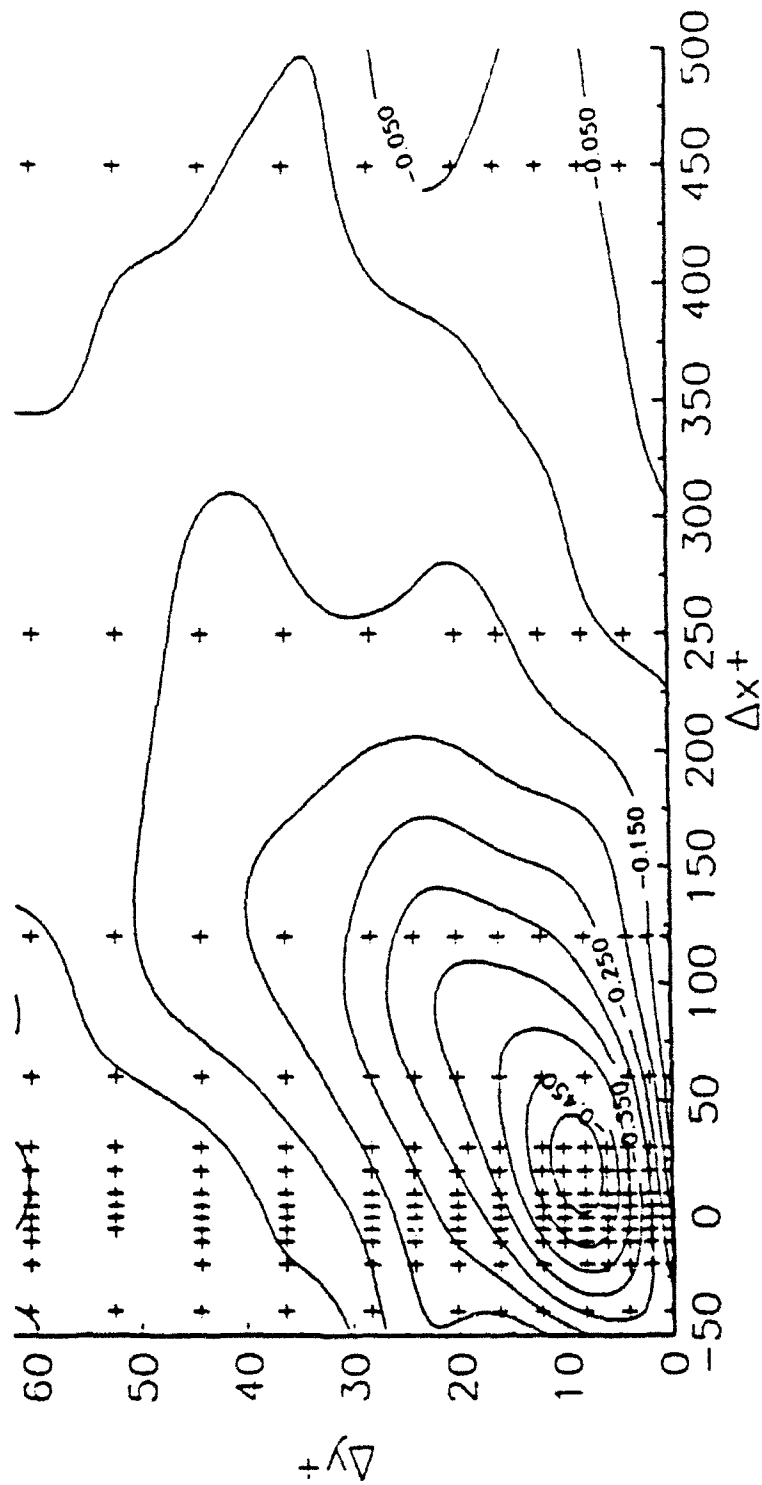


Figure 7.1 Two-point correlation contour map of the u-v velocity correlation at $y_r^+ = 2$. Measured in the undisturbed glycerin tunnel turbulent boundary layer. Symbols represent the locations of the moving probe measurements

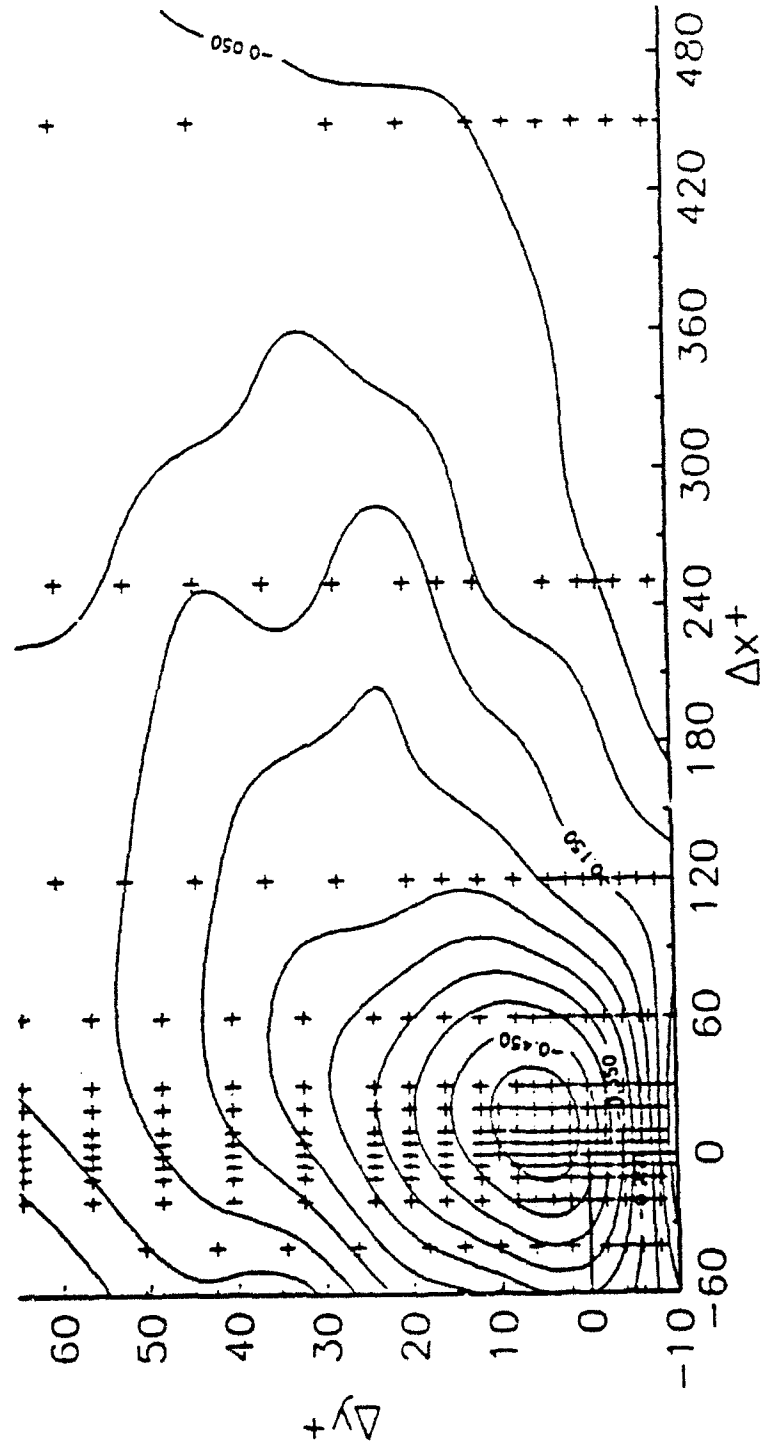


Figure 7.2 Two-point correlation contour map of the u - v velocity correlation at $y_t^+ = 12$. Measured in the undisturbed glycerin tunnel turbulent boundary layer. Symbols represent the locations of the moving probe measurements

The currently measured contour maps show good qualitative agreement with the contours measured by Chevrin (1988). The angle of inclination of the uv peak from the fixed probe location and the length of the vector connecting the peak to the fixed probe location are in agreement with the results presented by Chevrin (1988). However, the $y^+ = 2$ data of the present investigation show higher values in the uv correlation peak than what was measured by Chevrin (1988). The grid over which measurements were obtained by Chevrin (1988), however, had approximately 2.5 times fewer measurement locations than the grid in the present investigation. Furthermore, Chevrin's (1988) $y^+ = 2$ contour maps indicate that there are no measurements in the region of highest correlation. In the present investigation, time constraints prohibited the measurement of additional two-point correlations in the undisturbed boundary layer. It was anticipated that these measurements in canonical turbulent boundary layers were widely available in the open literature.

The two-point correlations behind the bump are measured using the LDV system in the external digitization mode of operation. This provides both spatial and temporal resolution in the correlation measurements. The accuracy and validity of using the LDV in the external digitization mode of operation is confirmed in Chapter 4. Eight of the nine terms in the two-point correlation tensor are directly measured along the centerplane behind the bump. The vv two-point correlation can not be measured with the current LDV setup in the test section.

The correlation maps are measured at $x^+ = 58$ for the two fixed probe locations, $y_1^+ = 5$ and 15. To fully investigate this three-dimensional inhomogeneous flow field, two-point correlation maps would have to be made with the fixed probe located at numerous downstream positions in the axial, circumferential and radial directions. That task is beyond the scope of the present investigation. The two y_1^+ locations are selected based on the

single-point results presented in Chapter 5, and correspond approximately to radial locations where the vw correlations show local peaks. These locations also correspond to a region within the radial extent of the counter rotating vortices and to the approximate location of the shear layer. The measurement grids for the two fixed probe locations are shown in Figures 7.3 and 7.4. The symbols indicate the locations of the moving probe for each measurement making up the two-point correlation contour map.

As mentioned earlier, it was anticipated that sufficient two-point correlation measurements in canonical turbulent boundary layers would be available for comparison with the measured correlations. This is not the case. The amount of published two-point correlation data is very scarce, and is mostly limited to large y_t^+ locations and generally to separations in one direction only. Some limited two-point correlation results from the Stanford University low Reynolds number turbulent channel flow simulations, $Re_\tau = 287$, are available in Kim and Hussain (1992). The effect of Reynolds number on the quantitative distributions of the contour maps is uncertain. These authors present results for fixed probe locations of approximately 5 and 12 wall units. At $y_t^+ = 5$, only the radial variations of the uu , vv and ww correlations for zero axial separation are supplied by Kim and Hussain (1992). The $y_t^+ = 12$ simulation results are full contours of the uu , vv , and ww correlations in the x - y plane, and are used for comparison with the current $y_t^+ = 15$ measurements. While direct comparisons of these data sets is not possible, a qualitative comparison of the shape of the contours is possible.

The contour maps of the uu correlations at $y_t^+ = 5$ and 15 are shown in Figures 7.5 and 7.6 respectively. These maps show that the uu correlation contours are more compact in the radial and axial directions than the results obtained in the channel flow simulations presented in Kim and Hussain (1988). The current $y_t^+ = 15$ measurements are approximately

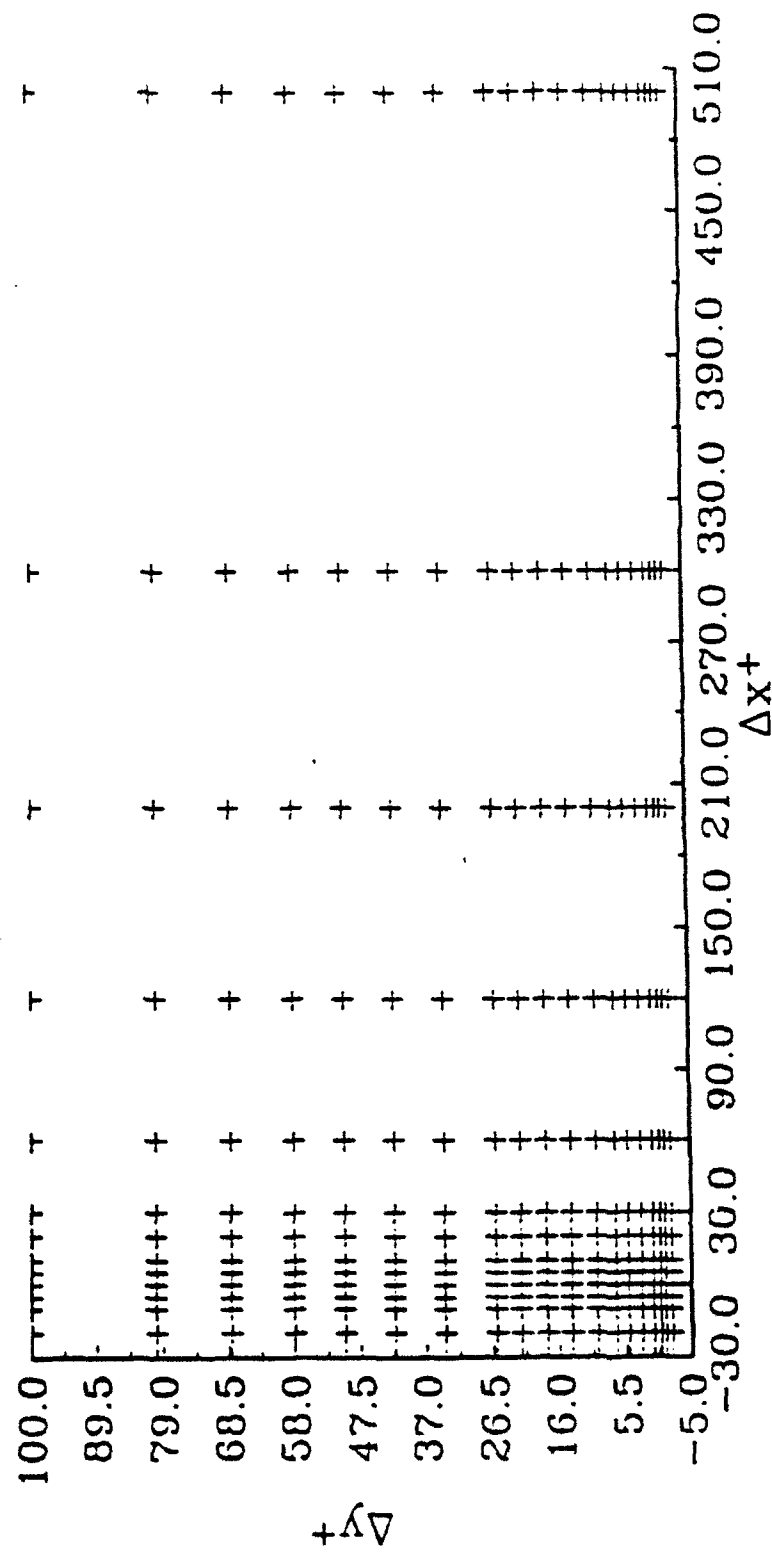


Figure 7.3 Locations of the moving probe velocity measurements for the two-point correlation measurements at $y_t^+ = 5$, $x^+ = 58$. Normalization with ref. u^*

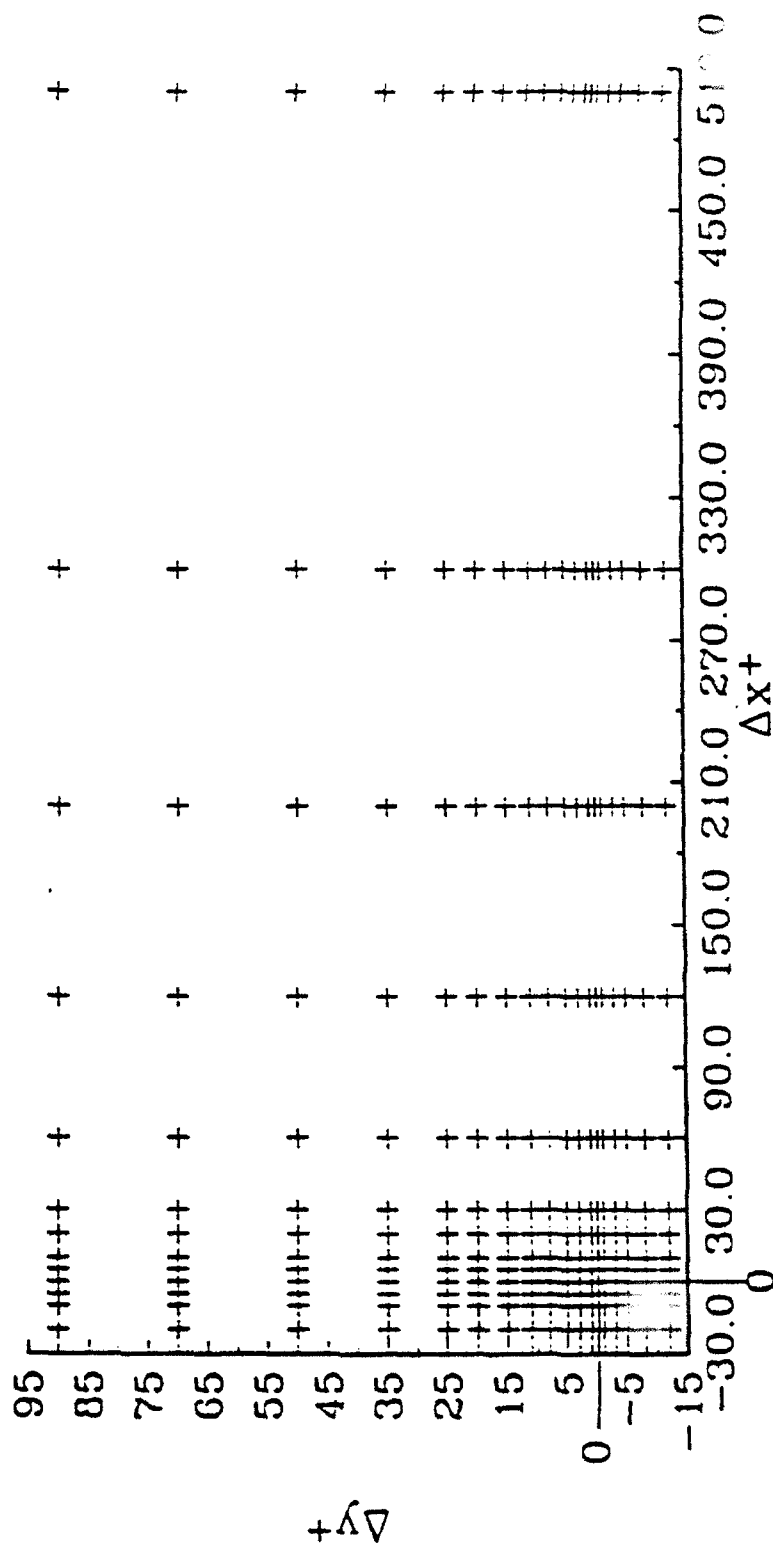


Figure 7.4 Locations of the moving probe velocity measurements for the two-point correlation measurements at $y_r^+ = 15$, $x^+ = 58$. Normalization with ref. u^+

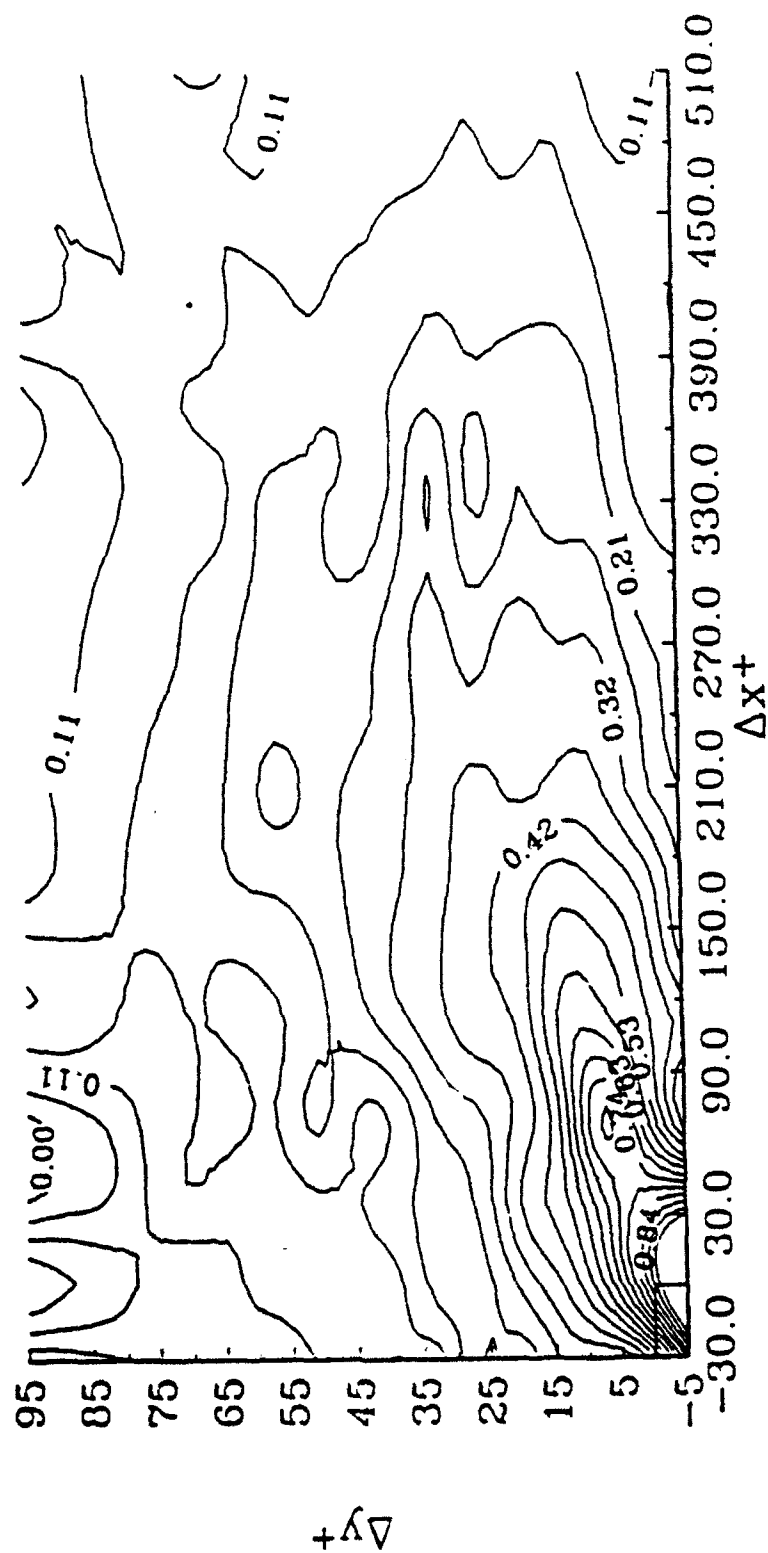


Figure 7.5 Contour maps of the uu two-point correlation at $y_r^+ = 5$, $x^+ = 58$.
Normalization with ref. u'

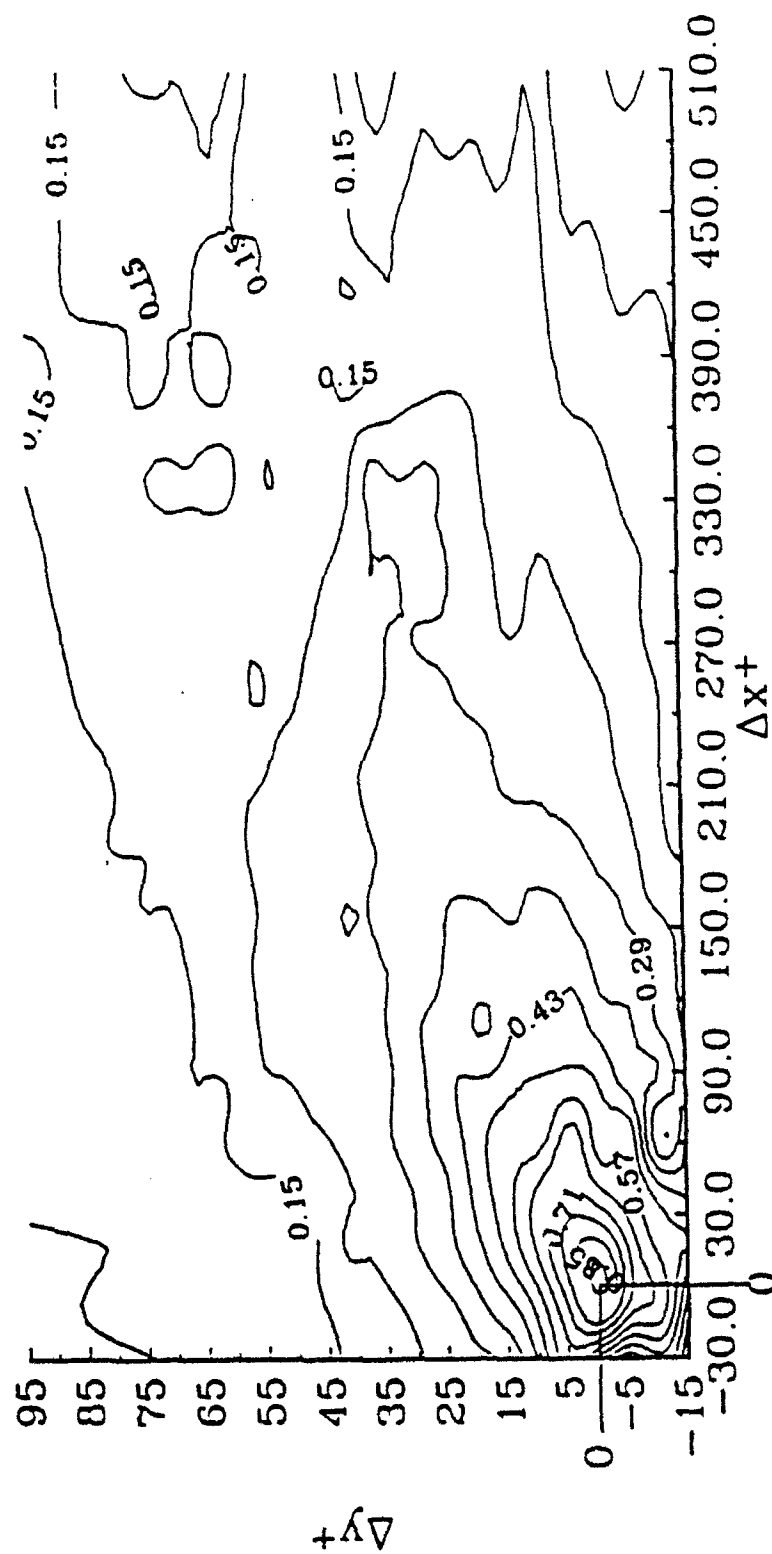


Figure 7.6 Contour maps of the uu two-point correlation at $y'_r = 15$, $x' = 58$.
Normalization with ref. u'

15 to 20 wall units narrower in radial extent and on the order of 50 wall units shorter in axial extent compared to the simulation results. In addition, these uu correlation contours appear to be bent downstream, which is not observed in the simulation results. The $y_r^+ = 5$ contours show a similar behavior but the magnitudes of the differences are much smaller, with a radial change of about 5 wall units. These changes in the shape of the contours are a consequence of the counter-rotating vortices near the wall, and of the second vortical structure and shear layer at $y^+ = 15$ to 20. The contours at $y_r^+ = 15$ appear to be well correlated with the second structure. The contours at $y_r^+ = 5$ show a region of high correlation over a radial span of approximately $5 \leq y^+ \leq 15$, which is the region of influence of the near wall counter-rotating vortices. These results imply that there may not be much communication between the counter-rotating near wall vortices and the second vortices at higher y^+ .

Figures 7.7 and 7.8 show the ww correlation contour maps behind the bump. The ww contours show similar modifications as those observed in the uu contours. They are compacted in the radial direction compared to the simulation results. However at $y_r^+ = 15$, the high correlation (> 0.5) contours have an axial extent about 40 wall units shorter than those of the simulations, while the low correlation (< 0.2) contours have a longer axial extent by approximately 30 wall units. The ww contours are bent and stretched downstream in a similar manner as that observed in the uu contours.

The uv correlations are shown in Figures 7.9 and 7.10. These correlations can be qualitatively compared to the measured correlations in the unmodified turbulent boundary layer shown in Figures 7.1 and 7.2. The contours of the uv correlation at $y_r^+ = 5$ show reduced peak correlation levels, which is consistent with the reduced uv Reynolds stress below $y^+ = 10$. The contours at $y_r^+ = 5$ also exhibit a bent profile downstream. The elongated shape of the high correlation contour makes it difficult to determine the inclination angle of

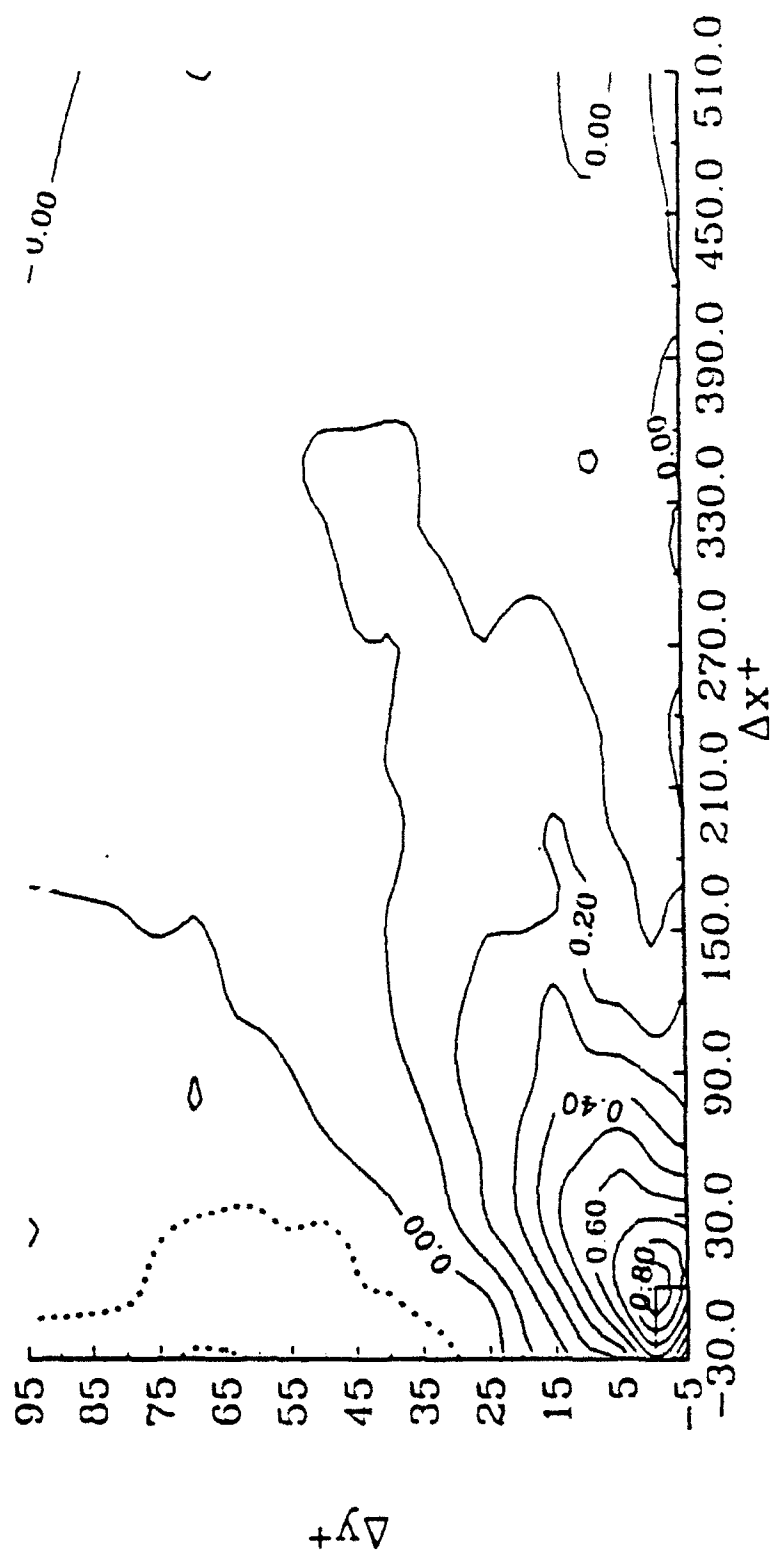


Figure 7.7 Contour maps of the ww two-point correlation at $y_r^+ = 5$, $x^+ = 58$.
Normalization with ref. u^*

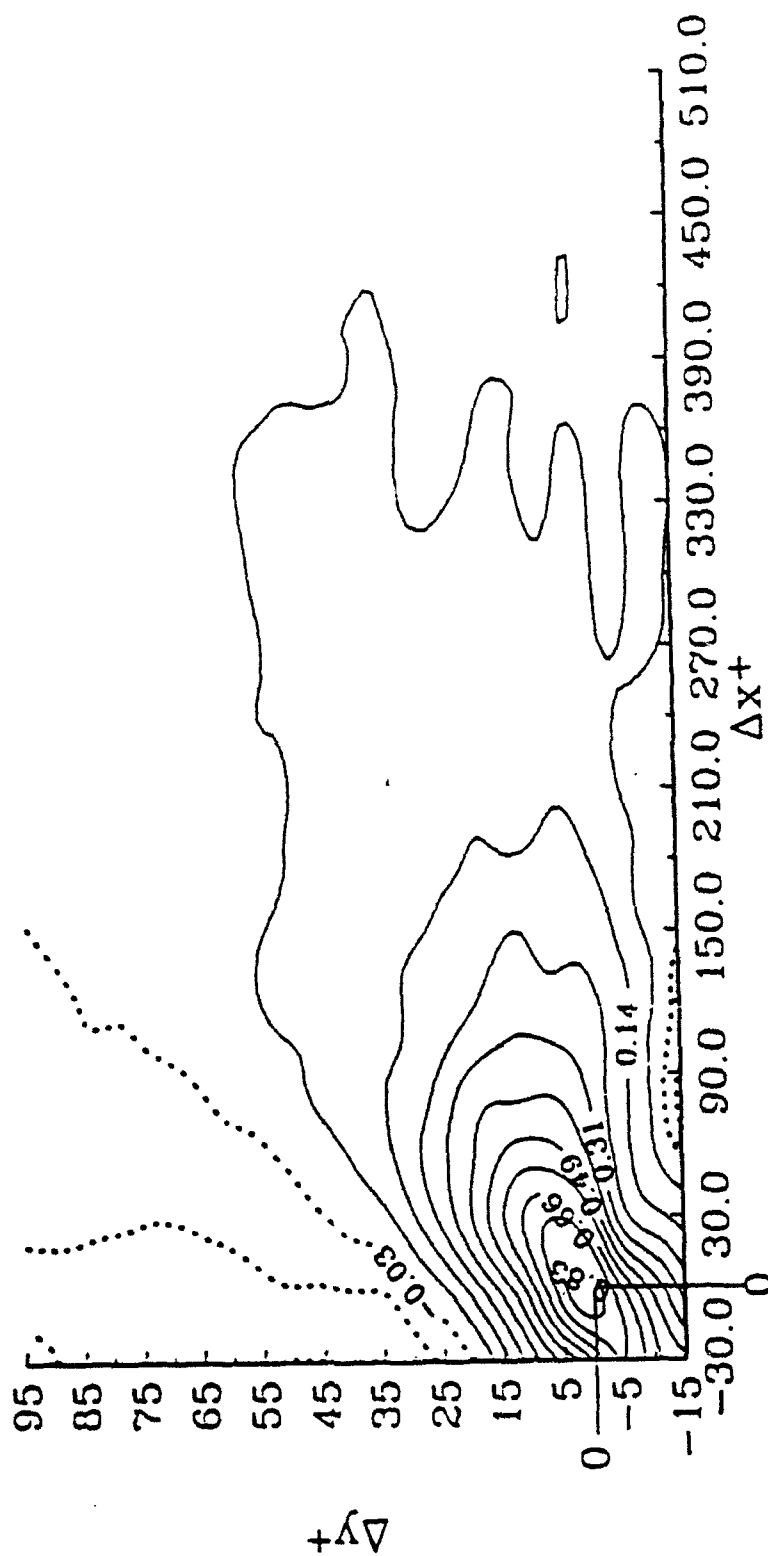


Figure 7.8 Contour maps of the ww two-point correlation at $y_t' = 15, x' = 58$.
Normalization with ref. u^*

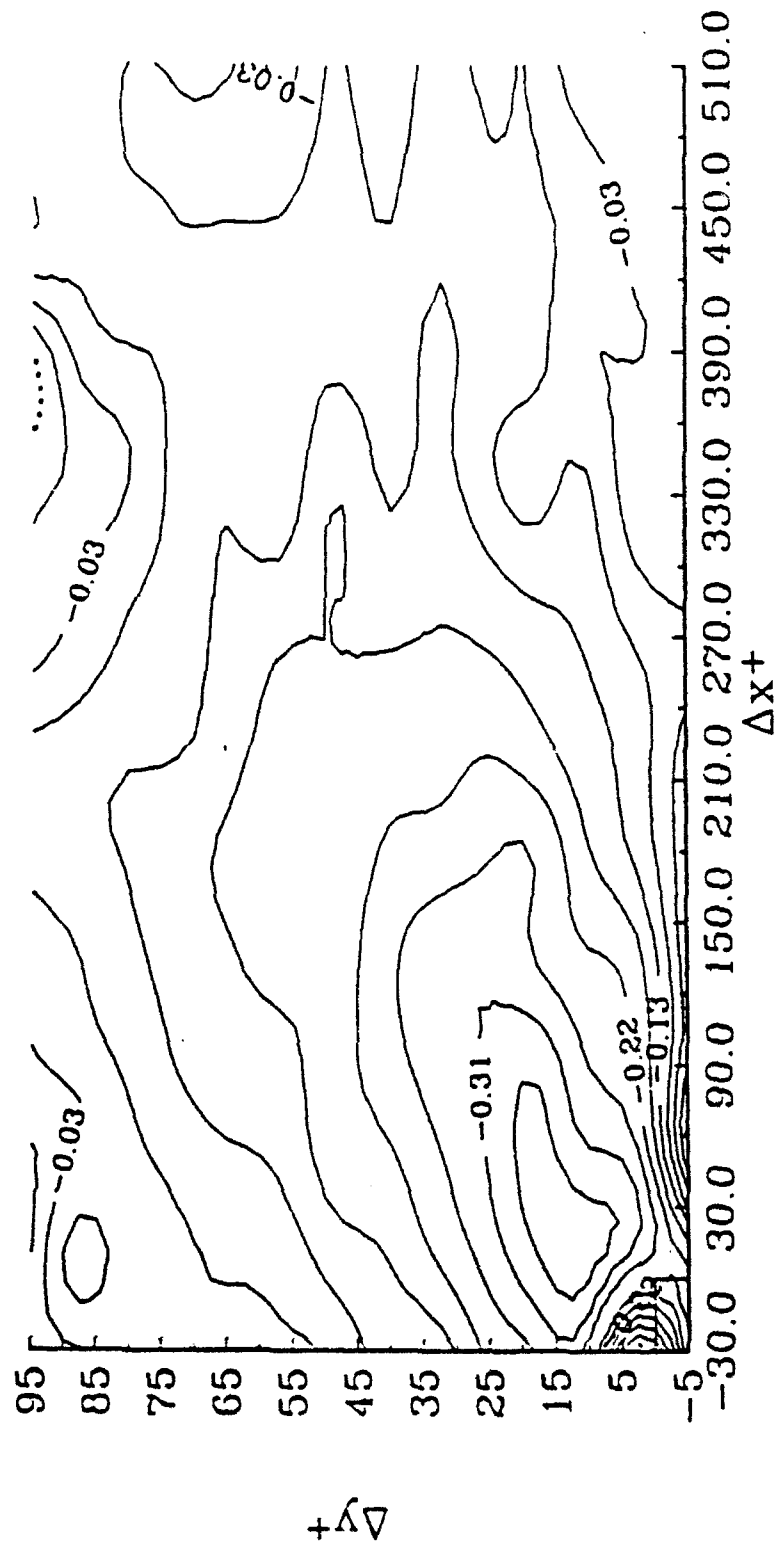


Figure 7.9 Contour maps of the uv two-point correlation at $y_r^+ = 5$, $x^+ = 58$.
Normalization with ref. u^+

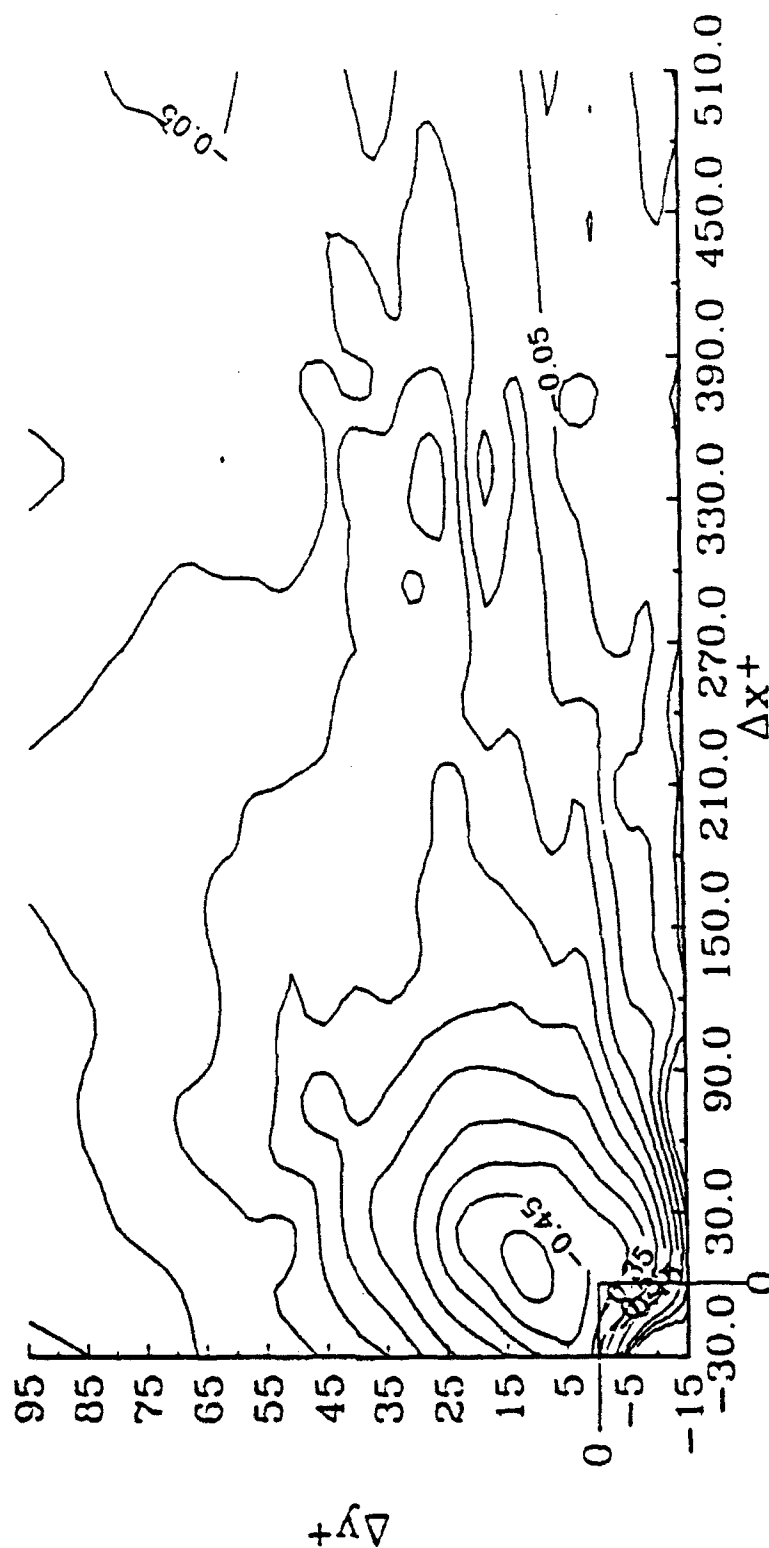


Figure 7.10 Contour maps of the uv two-point correlation at $y^+ = 15$, $x^+ = 58$.
Normalization with ref. u^*

the peak and the distance of the peak from the fixed probe. The $y_1^+ = 15$ contours are similar in shape to the $y_1^+ = 12$ contours shown in Figure 7.2. However, the location of the peak contour is shifted slightly upstream and to a higher y^+ . The inclination angle is approximately 10 degrees steeper and the length of the vector from y_1^+ to the location of the peak is slightly longer.

The vu contours show some interesting behavior, unfortunately reference contours are not available for comparison. The vu contours at $y_1^+ = 5$ and 15 are shown in Figures 7.11 and 7.12 respectively. Near the wall at $y_1^+ = 5$, the correlation levels are very small with peak levels reaching approximately -0.15. A significant region of positive correlation exists both downstream and upstream of the fixed probe location. The very small correlations more than likely result from the reduced uv Reynolds stress near the wall. The vu contours at $y_1^+ = 15$ show an elongated region of high vu correlation with the peak occurring well upstream of the fixed probe. This distribution is believed to be a result of a high correlation with the second vortex structure at $y^+ \approx 15$ to 20. The uw , wu , wv and vw two-point correlations are zero, within experimental uncertainty, in the long time averaged zero time lag statistics. This is not surprising considering the anti-symmetry of the w velocity on the centerplane.

The present correlation maps indicate that the flow field has been modified. However, the resulting changes in most of the correlations are small. The small changes are a result of the averaging of the velocity fluctuations over a time period sufficiently long compared to the frequency of the intermittent wandering of the vortices across the centerplane region. It may be that very short time averages or instantaneous correlation contours are quite different from the long time averaged picture. It is concluded in Chapter 6 that the vortices wander at a frequency in the range of 4 to 11 Hz. The nature of the wandering is

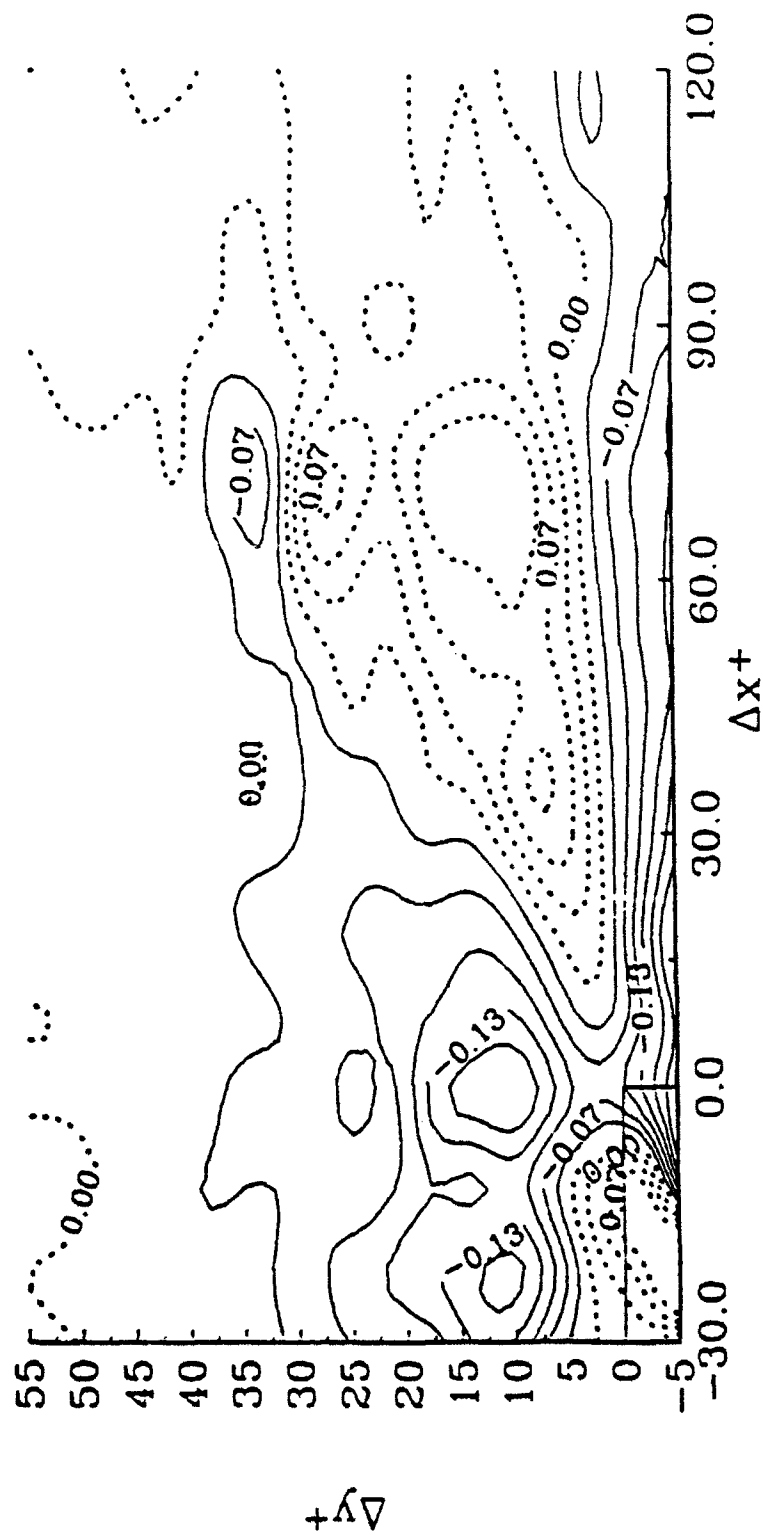


Figure 7.11 Contour maps of the v_u two-point correlation at $y_+^* = 5$, $x^* = 58$.
Normalization with ref. u^*

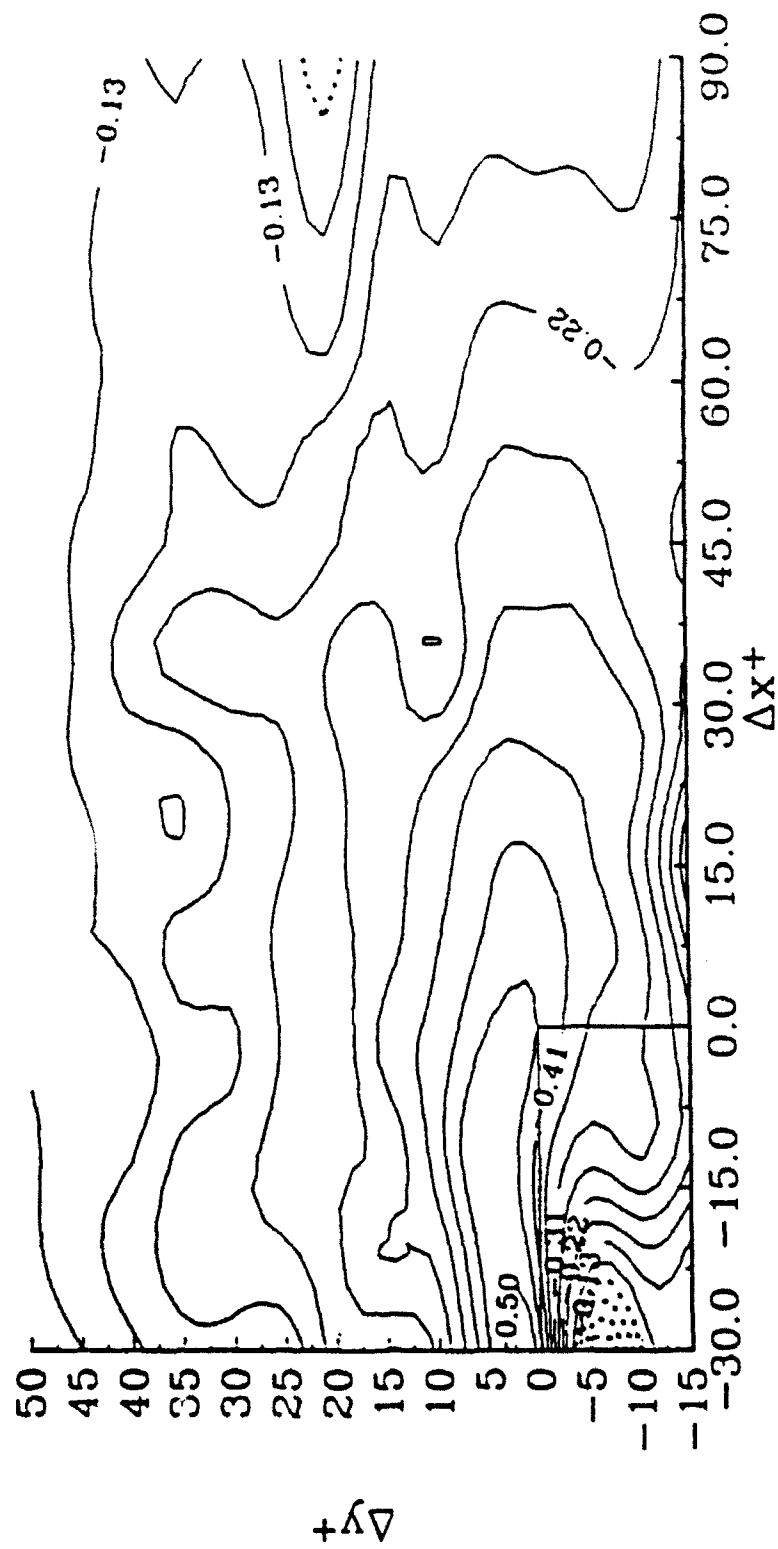


Figure 7.12 Contour maps of the vu two-point correlation at $y_t' = 15$, $x' = 58$.
Normalization with ref. u''

unclear; however, it may be that the vortices wander in a serpentine like fashion in the axial direction, similar to a shedding vortex street off of a cylinder in cross-flow. With this motion in mind, it is also anticipated that the space/time correlation maps will be different with time lag.

The continuity equation can be used to estimate the vv correlation tensor from measurements similar to those presented here, as in the work of Herzog (1986). For a two-point correlation, the continuity equation can be written as

$$\frac{\partial u_i u_j(r_c, \tau)}{\partial x_j} = 0$$

In this equation, differentiation is with respect to the moving probe location at separation r_c .

The expansion of this equation yields the following set of equations.

$$\frac{1}{r} \frac{\partial(ruv)}{\partial r} + \frac{1}{r} \frac{\partial(uw)}{\partial \theta} + \frac{\partial(uu)}{\partial x} = 0$$

$$\frac{1}{r} \frac{\partial(rvv)}{\partial r} + \frac{1}{r} \frac{\partial(vw)}{\partial \theta} + \frac{\partial(vu)}{\partial x} = 0$$

$$\frac{1}{r} \frac{\partial(rwv)}{\partial r} + \frac{1}{r} \frac{\partial(ww)}{\partial \theta} + \frac{\partial(wu)}{\partial x} = 0$$

The notation used for the two-point correlations is adopted in these equations. Integration of the second equation over r from the wall outward, yields the vv two-point correlation. In the canonical pipe flow, the spanwise gradient is zero and the vv correlation is obtained by integrating the streamwise gradient of the vu correlation. The present flow field is inhomogeneous, however, and thus requires the estimation of the circumferential gradient of the vw correlation on the centerplane. This gradient is not zero due to the anti-symmetry of the w velocity and unfortunately is not measured. As a result, the full two-point correlation

tensor is not determined on the centerplane. This restricts the application of the linear stochastic estimation technique to the estimation of two velocity components, axial and circumferential.

7.3 Linear Stochastic Estimation

To extract structural information from complex flows using conditional averaging techniques requires a considerable data reduction effort and a very large data base when the form of the dominant structures or their signature is unknown. This is also true for the extraction of the dynamics of the flow structures. The development of linear stochastic estimation has simplified the application of conditional averaging to large data bases and complex flows. Adrian (1979), Adrian and Moin (1988) and Guezennec (1989) review the details and properties of linear stochastic estimation.

The mathematical definition of the conditional average, U'_i , of a velocity field, U_i , given the conditioning event vector E_j can be written as,

$$U'_i = \int \frac{f(U_i, E_j)}{f(E_j)} U_i dU_i \quad 7.1$$

Here the terms $f(E_j)$ and $f(U_i, E_j)$ are the probability density function of the event vector E_j and the joint probability density function between the velocity field and E_j respectively. Stochastic estimation theory represents the integral in Equation 7.1 by a polynomial expression in powers of the event vector E_j written as,

$$\hat{U}'_i = A_{ij}E_j + B_{ijk}E_jE_k + \dots \quad 7.2$$

The estimate of the conditional average in Equation 7.1 is denoted by \hat{U}'_i . The coefficient matrices in Equation 7.2 are determined by minimizing the mean square error between the

estimated conditional average, \hat{U}'_i , and the actual conditional average defined by

Equation 7.1. In linear stochastic estimation, the higher order terms appearing on the right in Equation 7.2 are neglected and the Equation is truncated to the first term as

$$\hat{U}'_i = A_i E_f \quad 7.3$$

It is shown by Adrian (1979) and Guezennec (1989) that the estimated conditional averages reproduce the actual conditionally averaged flow field quite well. In addition, Adrian et al. (1980) show that the addition of the higher order terms from Equation 7.2 produce negligible corrections to the linear estimate in most flow situations.

In the present investigation, the conditioning vector will be a three component velocity vector at a point (x_c, y_c, z_c) and time (t_c) in the flow field, $U_j(x_c, y_c, z_c, t_c)$. The conditional average velocity can be obtained at any point in the flow. Let r_c be the separation vector between the location of the conditional estimate and the location of the conditioning vector x_c , y_c and z_c . In addition, the conditional average can be obtained over any time delay τ from the conditioning event time t_c . Since, the long time average of U_i at any point is a constant and is a non-random number in the flow field of interest, the conditional average of the total velocity \hat{U}'_i at a specific location is equivalent to the superposition of the mean velocity U_i on the estimate of the conditional average of the zero-mean fluctuation u_i at the same location. The form of the governing equations for the stochastic estimation technique reduces to a function of the unconditional velocity correlations when the estimation is performed on the fluctuating velocities. Therefore, the zero-mean fluctuating velocities will be used in place of the total velocity for the remainder of this chapter. Incorporating the above definitions into Equation 7.3, the equation can be written,

$$\hat{u}'_i(r_c, \tau) = A_{ij} \mu_j(x_c, y_c, z_c, t_c). \quad 7.4$$

The mean square error of the estimate of the conditional average is written as,

$$e_i = \langle (u'_i(r_c, \tau) - \hat{u}'_i(r_c, \tau))^2 \rangle = \langle (u'_i(r_c, \tau) - A_{ij} \mu_j(x_c, y_c, z_c, t_c))^2 \rangle. \quad 7.5$$

The A_{ij} are determined by minimizing the mean squared error given by Equation 7.5. A set of equations involving the unconditional single and two-point correlation tensors of the velocity field arises. After performing the error minimization, the following equation is obtained,

$$\langle u'_i(r_c, \tau)' u'_k(x_c, y_c, z_c, t_c) \rangle = A_{ij} \langle u_j(x_c, y_c, z_c, t_c) u_k(x_c, y_c, z_c, t_c) \rangle. \quad 7.6$$

The data, to be presented, are limited to zero spanwise displacement and zero time delay. In addition, the conditioning velocity is specified at $z^+ = 0$, and the initial time t_c of the conditioning event is set to zero for convenience. With these simplifications, Equation 7.6 becomes,

$$\langle u'_i(r_c)' u'_k(x_c, y_c) \rangle = A_{ij} \langle u_j(x_c, y_c) u_k(x_c, y_c) \rangle. \quad 7.7$$

The ensemble averaged term on the left in Equation 7.7 is the unconditional two-point correlation tensor about the point x_c and y_c , while the ensemble averaged term on the right is the Reynolds stress tensor measured at x_c and y_c . The A_{ij} coefficient matrix is obtained by post multiplying both sides of Equation 7.7 by the inverse of the measured Reynolds stress tensor.

The coefficient matrix is computed for every location of the event vector in any inhomogeneous coordinate direction. For example, a separate A_{ij} matrix is needed for each y_c location that conditional averaging is to be applied if the flow field is inhomogeneous in the y -coordinate direction. The A_{ij} coefficient matrix is a function of the separation vector r_c , and

in the case of temporal data the time delay τ . Once the A_{ij} matrix is obtained for a given event vector location, the construction of the estimated conditionally averaged velocity field can be performed by applying Equation 7.2. Expanding Equation 7.2 yields,

$$\hat{u}' = A_{11} u + A_{12} v + A_{13} w, \quad 7.8a$$

$$\hat{v}' = A_{21} u + A_{22} v + A_{23} w, \quad 7.8b$$

$$\hat{w}' = A_{31} u + A_{32} v + A_{33} w. \quad 7.8c$$

In the current investigation, the A_{ij} coefficient matrix is determined twice, once for each of the two event vector locations of $x_c^+ = 58$ and $y_c^+ = 5$ and 15. These locations are the fixed probe locations from the two-point correlation results presented in Section 7.2.

The lack of the vv two-point correlations precludes the calculation of the A_{21} , A_{22} and A_{23} coefficients of the A_{ij} matrix. This prevents the estimation of a radial velocity component of the conditional average, which is determined from Equation 7.8b. However, the streamwise and circumferential velocity components of the conditional average can still be estimated.

The linear stochastic estimation technique is applied to the correlation measurements presented in Section 7.1. The number of conditioning velocity vectors which can be chosen to estimate the conditionally averaged velocity field is considerably large. For the purpose of demonstration of the linear stochastic estimation technique, conditioning velocity events are selected to coincide with the bimodal distributions observed in the uw joint probability density contours shown in Figure 5.7a. At $y^+ = 5$, a conditioning event is selected for each leg of the high streamwise velocity fluctuation, and positive and negative spanwise velocity fluctuation distributions. The uw probability density distributions at $y^+ = 15$ also show a similar bimodal behavior as that observed at $y^+ = 5$. Therefore, a similar guideline is

followed for selection of the conditioning vector event at $y^+ = 15$. These conditioning events are selected because the bimodal behavior is a direct result of the counter-rotating vortices.

The zero-mean conditioning velocity vector is obtained by bandpass filtering the streamwise and spanwise components of the three-component, single-point velocity ensembles measured at each y_c^+ location. The conditioning velocity perturbations, u_c , v_c and w_c , are obtained by ensemble averaging the bandpassed data. The zero-mean velocity fluctuations are bandpassed filtered at $4.25u' \leq u \leq 4.75u'$ and $-2.75w' \geq w \geq -3.25w'$ for $y^+ = 5$, where u' and w' are the local standard deviations of the streamwise and spanwise velocity components. The bandpass filtering is performed over $2.25u' \leq u \leq 2.75u'$ and $-2.75w' \geq w \geq -3.25w'$ at $y^+ = 15$. The following conditioning velocity perturbations are obtained, $u_c = 2.2$ m/s, $v_c = -0.27$ m/s and $w_c = -0.85$ m/s for $y_c^+ = 5$, and $u_c = 2.35$ m/s, $v_c = -0.93$ m/s and $w_c = -1.45$ m/s for $y_c^+ = 15$. Conditioning velocity events are also selected to coincide with the positive w fluctuations as well.

Figures 7.13 and 7.14 show the resulting conditionally averaged streamwise and spanwise velocity perturbation fields obtained from the stochastic estimation at $y_c^+ = 5$. The conditional velocity perturbation contours shown in the figures are normalized by the magnitude of the velocity perturbation at the location of the velocity event vector. This location is denoted in the figures by the intersection of the horizontal and vertical lines emanating from $\Delta x = \Delta y = 0$. This form of presenting the data illustrates the structural form of the perturbation velocity field for different conditioning velocities. The axes notation and the actual locations of the conditional velocity perturbation estimates are the same as that used for the two-point correlation measurements of Figures 7.5 to 7.12. The total conditionally averaged velocity fields are obtained by superimposing the long time averaged

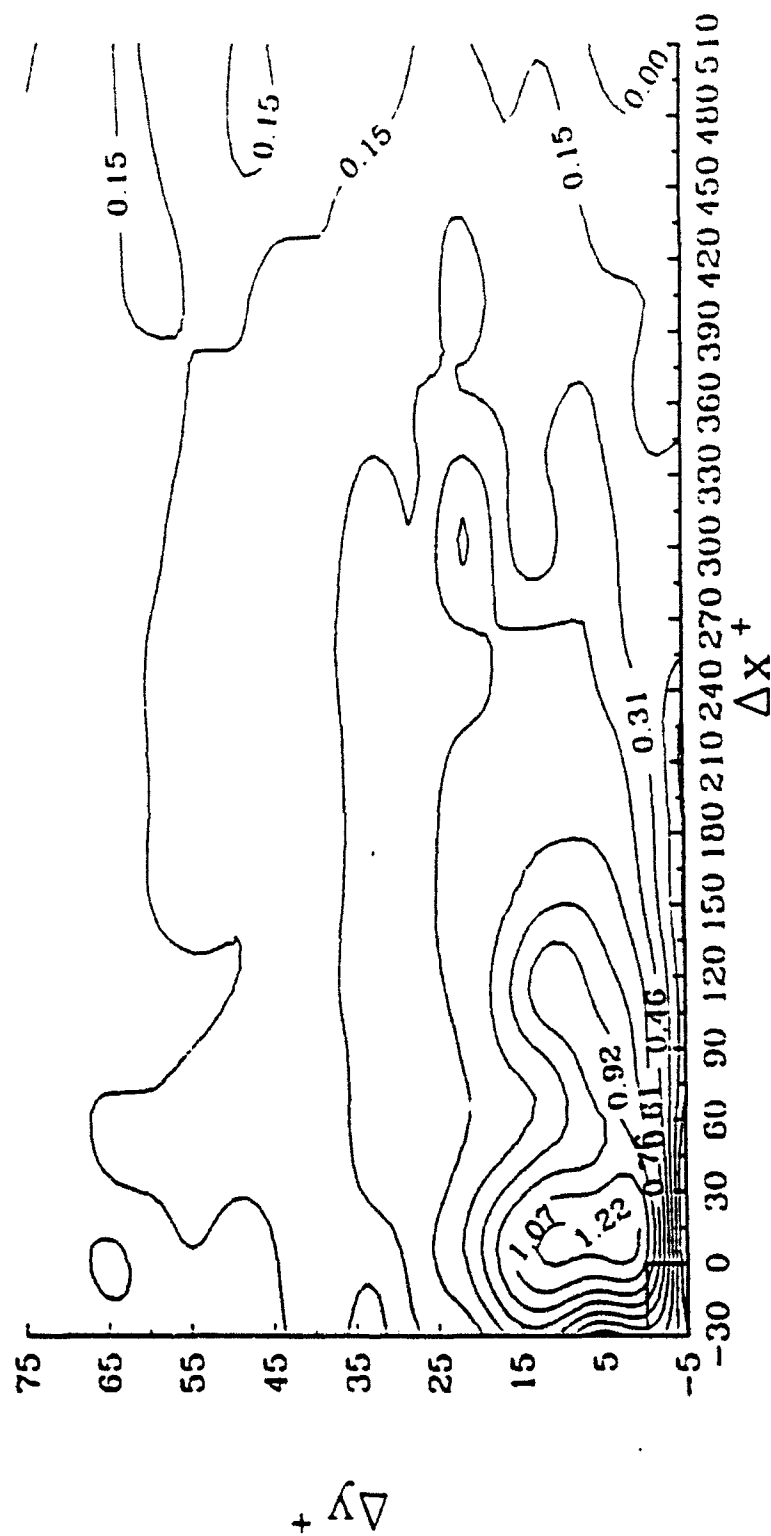


Figure 7.13 Streamwise conditionally averaged velocity perturbation contours obtained from linear stochastic estimation for $y_r^+ = 5$. $u_r = 2.2$ m/s, $v_r = -0.27$ m/s and $w_r = -0.85$ m/s. Velocity contours are normalized by the magnitude of the velocity perturbation at $\Delta x = \Delta y = 0$, which is $u = 2.32$ m/s

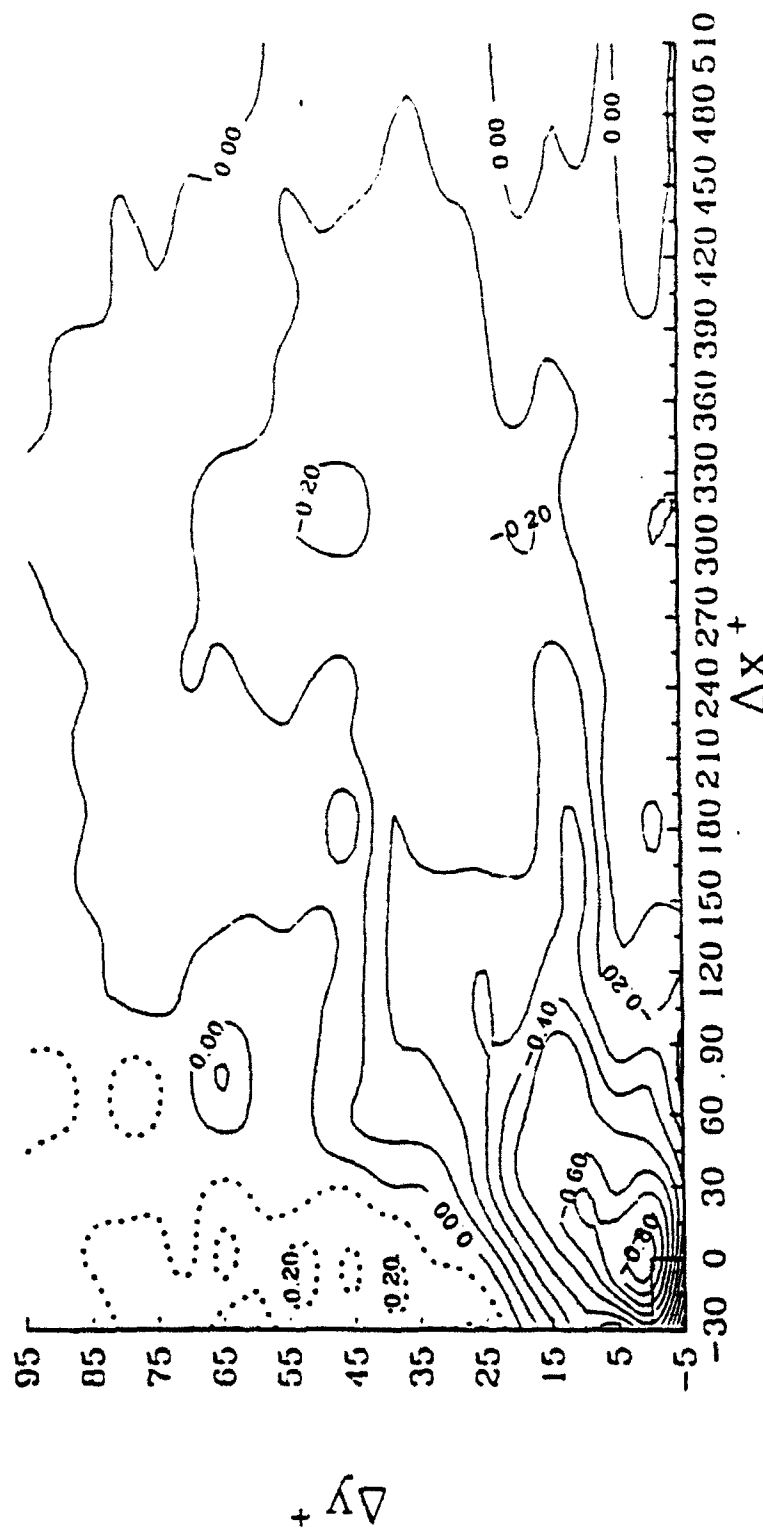


Figure 7.14 Spanwise conditionally averaged velocity perturbation contours obtained from linear stochastic estimation for $y_t^+ = 5$, $u_t = 2.2$ m/s, $v_t = -0.27$ m/s and $w_t = -0.85$ m/s. Velocity contours are normalized by the magnitude of the velocity perturbation at $\Delta x = \Delta y = 0$, which is $w = -1.08$ m/s

mean velocity field onto the conditionally averaged velocity perturbations shown in these figures.

The streamwise and spanwise conditional velocity perturbation contours show some interesting features. The streamwise contours shown in Figure 7.13 indicate that an elongated region of high velocity perturbation exists over nearly 180 wall units in the axial direction. The contours are considerably kinked at approximately 30 wall units downstream of x_c^+ and 15 wall units higher than y_c^+ . These contours suggest that a strong sweep type motion occurs as a leg of the counter-rotating vortices crosses the centerplane region. The increasing streamwise velocity perturbations with increasing radial position indicates that the gradient of the conditionally averaged total velocity profile in this region is greater than the long time averaged result. This implies that the local wall shear stress is higher during periods when the counter-rotating vortices are crossing the centerplane. The spanwise contours in Figure 7.14 show a similar shape as those observed in the w - w two-point correlation contours. That is the shape of the contours are elongated in the streamwise direction and bent downstream.

Unfortunately, the radial conditional velocity perturbation could not be estimated. It is reasonable to expect, however, that the radial velocity field is directed towards the wall in the sweep type motions illustrated in Figure 7.13. It is likely that as a vortex leg crosses the centerplane, it entrains, down towards the wall, high velocity fluid from above and from the shear layer located at $y^+ \approx 15$ to 20.

The conditional streamwise velocity perturbation contours corresponding to the positive w conditioning event are nearly identical to those shown in Figure 7.13; whereas, the spanwise conditional velocity perturbation contours for the positive w condition are the negative of the contours shown in Figure 7.14. This behavior is expected from the anti-symmetry of the uw probability density contours shown in Figure 5.7a. It also suggests

that the legs of the counter-rotating vortex pair are nearly identical except for opposite circulation.

Conditional averages of the actual velocity data are performed at several locations to check the uncertainty in the estimated velocity perturbations from the stochastic estimation. In general, the stochastic estimation results are within 20% of the conditionally averaged velocity perturbations. This is quite good when considered in light of the 20% to 30% uncertainty in the correlation coefficients.

Figure 7.15 shows streamwise conditionally averaged estimates at $y^+ = 5$, for a velocity event of $u_c = -0.5$ m/s and $v_c = w_c = 0$. This corresponds to the high probability region located in the probability density contours of Figure 5.7. This condition may be interpreted as a condition for which the vortices are more or less straddling the centerplane and not crossing it. Additionally, the probability density contours indicate that there is very little burst activity at this location. The spanwise conditional velocity perturbation estimate is approximately zero within data scatter, and is not shown. The contours in Figure 7.15 also show an elongated shape in the axial direction. The elongated region is consistent with a pair of long quasi-streamwise vortices straddling the centerplane. Surprisingly, the streamwise velocity perturbation contours show increasingly more negative streamwise velocity perturbation magnitudes with increasing radial distance from the wall. This indicates that the gradient of the streamwise conditionally averaged total velocity profile is lower than the long time averaged mean velocity gradient below $y^+ \approx 10$. This implies a reduction in the wall shear stress.

The stochastic estimation results for $y_c^+ = 15$ are shown in Figures 7.16 and 7.17. The streamwise conditional velocity perturbation estimates are shown in Figure 7.16. These contours show a considerable region which is elongated in the axial direction and somewhat

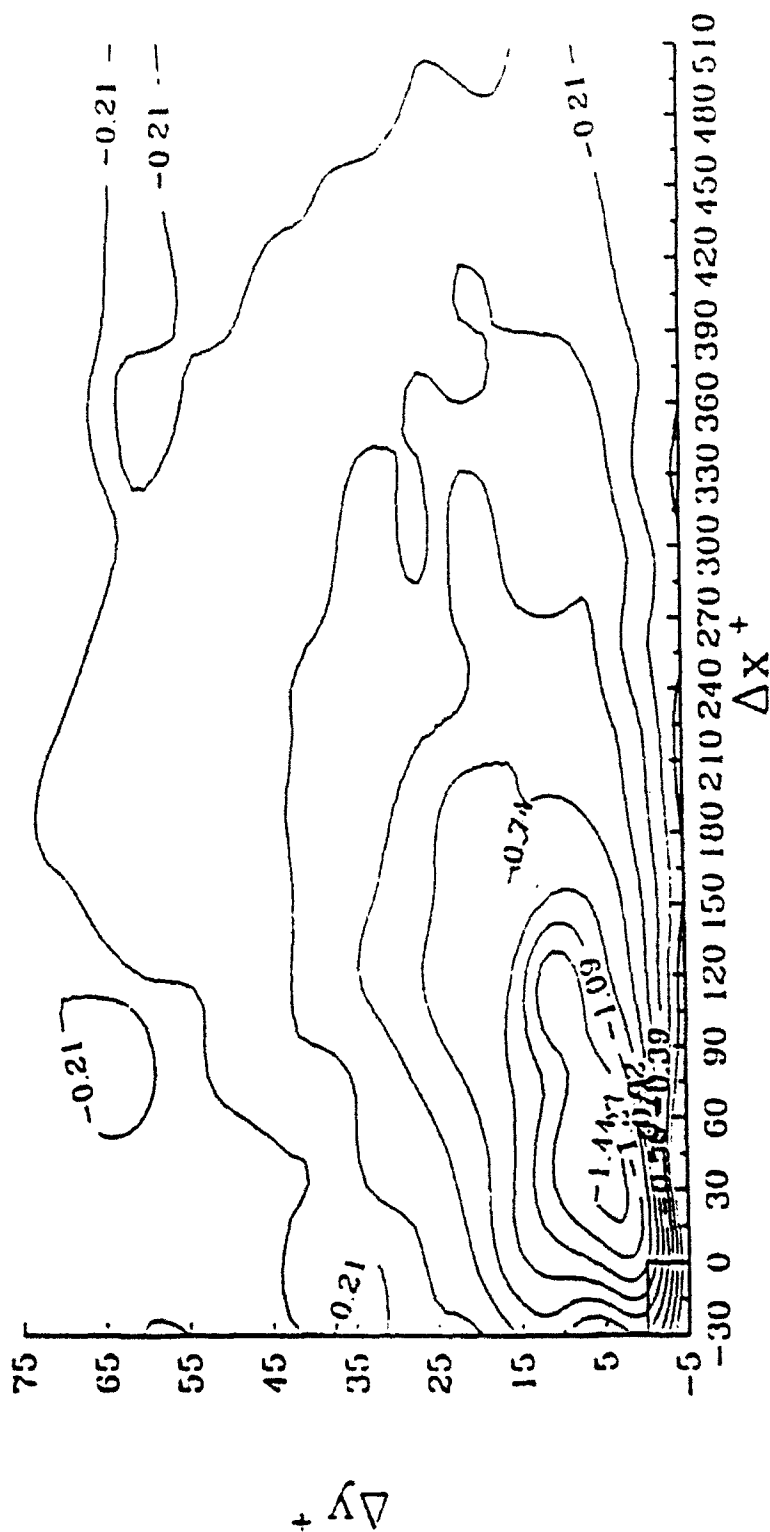


Figure 7.15 Streamwise conditionally averaged velocity perturbation contours obtained from linear stochastic estimation for $y_i^* = 5$, $u_e = -0.5$ m/s, $v_e = w_e = 0$ m/s. Velocity contours are normalized by the magnitude of the velocity perturbation at $\Delta x = \Delta y = 0$, which is $u = -0.54$ m/s

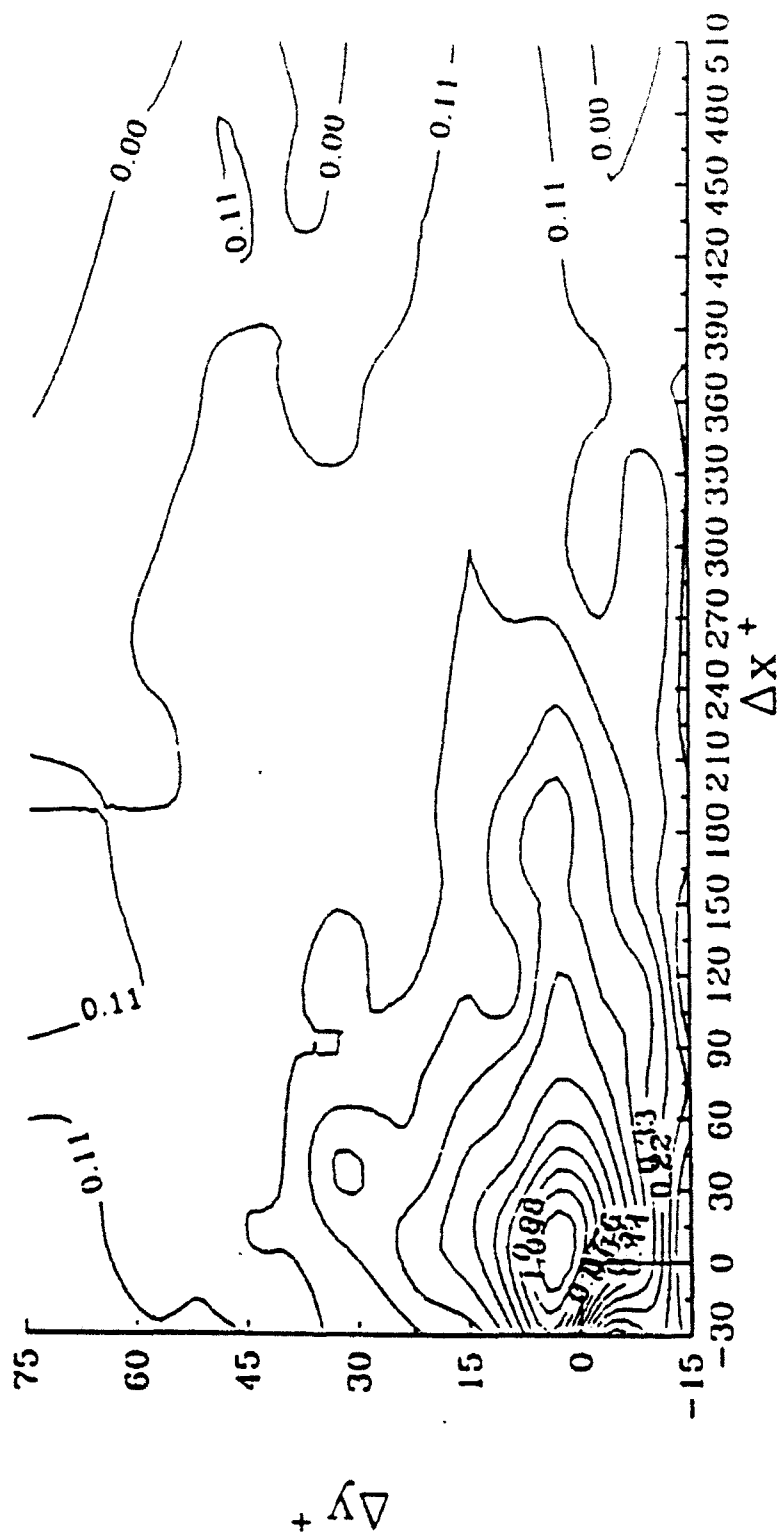


Figure 7.16 Streamwise conditionally averaged velocity perturbation contours obtained from linear stochastic estimation for $y_i' = 15$, $u_i = 2.35$ m/s, $v_i = -0.93$ m/s and $w_i = -1.46$ m/s. Velocity contours are normalized by the magnitude of the velocity perturbation at $\Delta x = \Delta y = 0$, which is $u = 2.2$ m/s

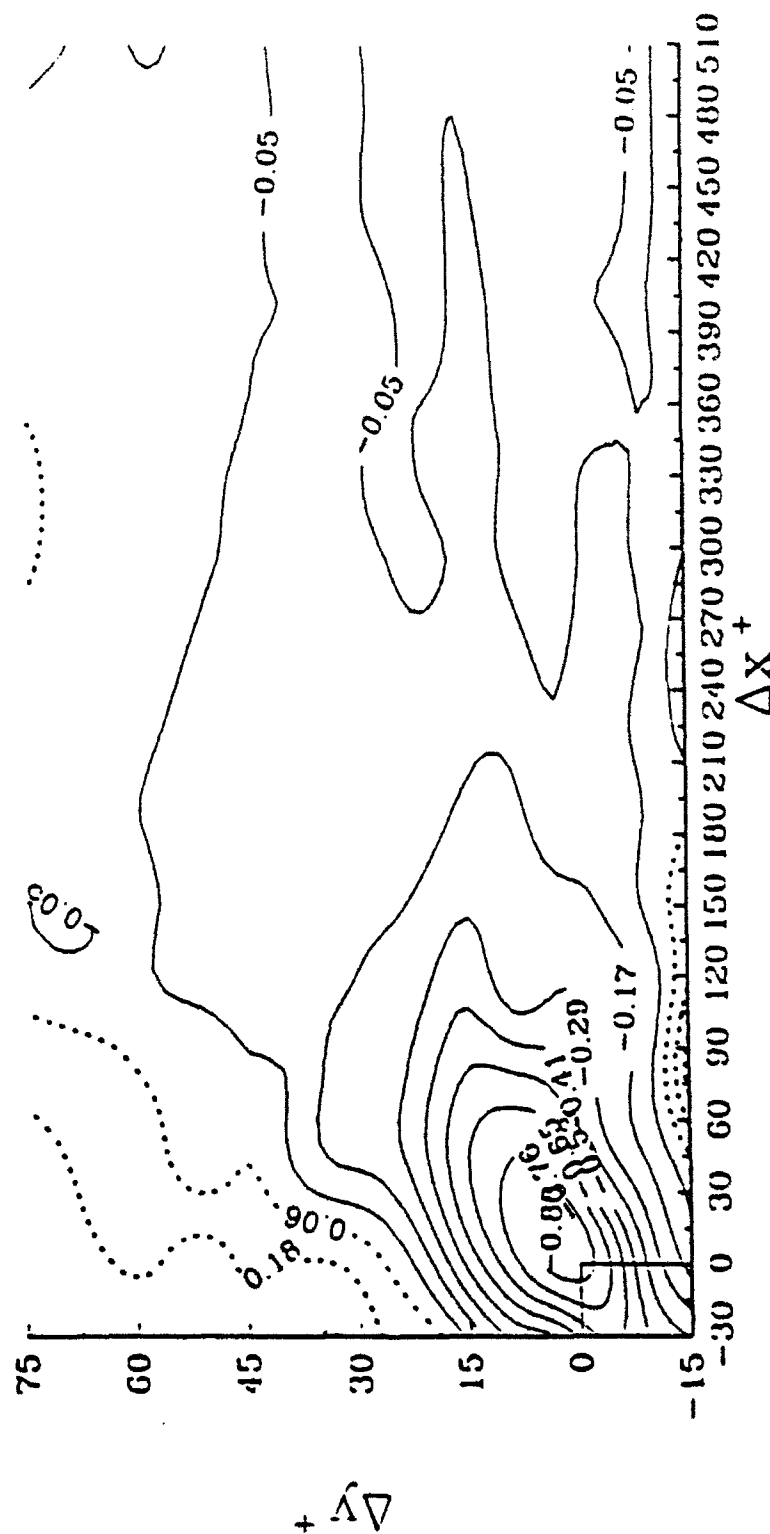


Figure 7.17 Spanwise conditionally averaged velocity perturbation contours obtained from linear stochastic estimation for $y_r^+ = 15$, $u_r = 2.35$ m/s, $v_r = -0.93$ m/s and $w_r = -1.46$ m/s. Velocity contours are normalized by the magnitude of the velocity perturbation at $\Delta x = \Delta y = 0$, which is $w = -1.2$ m/s

tilted towards the wall. The peak velocity perturbations occur at approximately the location of the shear layer and second pair of vortices at $y^+ = 20$. The sweeping type motion does not appear to be as strongly felt at this location as it is at $y_c^+ = 5$. However, the two conditioning events do not necessarily correspond to the same position of a vortex leg with respect to the centerplane. These contours also indicate that the gradient of the conditionally averaged total velocity profile is increased near the wall. The shape of these velocity contours is different from the shape of the uu two-point correlation contours shown in Figure 7.6. The spanwise conditional velocity perturbation estimate, shown in Figure 7.17, show a similar shape to the contours at $y_c^+ = 5$. The profiles show roughly the same inclination and downstream bend.

Figure 7.18 shows contours of the streamwise conditional velocity perturbations corresponding to a similar event vector as that specified for Figure 7.15. Velocity conditions are selected to correspond to the high probability regions in the $y^+ = 15$ joint probability density velocity distributions. The conditioning velocities are $u_c = -0.84$, $v_c = w_c = 0$. The velocity perturbation field is similar to the contours shown in Figure 7.15. A decrease in the gradient of the conditional velocity profile is also observed locally around the conditioning point.

The examples presented in Figures 7.13 to 7.18 illustrate the usefulness of the stochastic estimation technique in analyzing large data bases. More interesting features in the contours may result from examining off-centerplane regions of the flow field and non-zero time lag statistics. In particular, it is anticipated that the application of stochastic estimation to the time lag statistics will produce interesting results. For example, spanwise conditional velocity perturbation estimates which change sign with increasing streamwise distance may very well be observed. In this case, the temporal behavior of the counter-rotating vortices

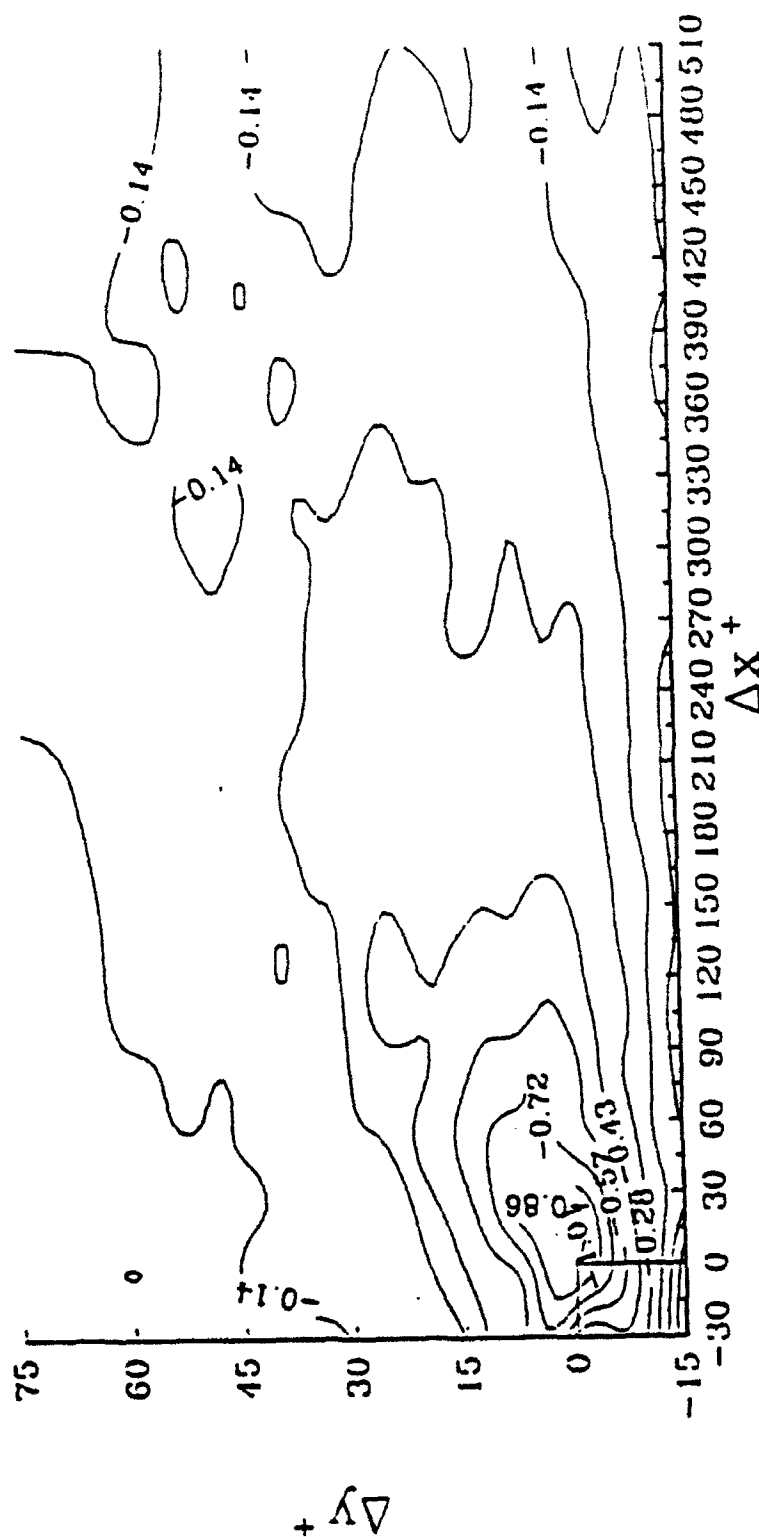


Figure 7.18 Streamwise conditionally averaged velocity perturbation contours obtained from linear stochastic estimation for $y_t^+ = 15$, $u_t = 2.35$ m/s, $v_t = 0.93$ m/s and $w_t = -1.46$ m/s. Velocity contours are normalized by the magnitude of the velocity perturbation at $\Delta x = \Delta y = 0$, which is $u = 2.2$ m/s

and how they wander may be determined.

The stochastic estimation technique can be easily extended to include multi-point conditioning events. Guezennec (1989) has successfully applied two-point stochastic estimation to a flat plate turbulent boundary layer data base. The conditionally averaged estimate is a function of conditioning events which are imposed at two or more locations simultaneously. The governing equations for this type of estimate take the form,

$$\bar{U}'_i = A_{ij}E_j(x_1) + B_{ik}E_k(x_2) \dots \quad 7.9$$

The $E_j(x_1)$ and the $E_k(x_2)$ are the conditioning events at locations x_1 and x_2 respectively. The estimation of the coefficient matrices A_{ij} and B_{ik} are performed in a similar manner as that described above for Equation 7.3. The resulting equation for the coefficient matrices involves the two-point correlation measurements around both the x_1 and x_2 fixed probe locations, the Reynolds stress tensor at x_1 and x_2 , and an additional cross correlation tensor between the velocities at x_1 and x_2 . The additional cross correlations are available in the two-point correlations measured at each fixed probe location of x_1 and x_2 . The multi-point stochastic estimation enables the control of the length scales over which the conditional averaging is performed. The length scales are determined by the magnitude of the separation of the two conditioning events. This type of analysis can be performed with the current two-point correlation data base. The separation vector would be a 10 wall unit separation in the radial direction. This would focus the stochastic estimation on structures with radial length scales of the order of 10 wall units.

In addition, Guezennec et al. (1991) have begun to use stochastic estimation to extract dynamical information from measured space/time correlation maps. The coefficient matrix A_{ij} can be computed for time delays from an initial time t_c , and for time delays around times different from the initial time. A temporally evolving picture can then be obtained by

applying the stochastic estimation procedure from time step to time step. For this case, the computation of all the A_{ij} matrices is not a trivial task. However, once the A_{ij} matrices are computed, the application of the estimation procedure to any conditioning event and the construction of the temporal results should be relatively easy.

Recently, Brereton (1992) has extended the stochastic estimation technique to include a direct procedure for estimating the uncertainty in stochastic estimations. The procedure for determining the uncertainty is quite involved and requires that data be obtained over a fine measurement grid. In the case of time delay statistics, which was the example used by Brereton (1992), this requirement can be easily met. However, the application of this estimate of uncertainty to spatial correlations would require a data base measured over such a spatially fine grid, which is more than likely impractical. In addition, the ability to tailor the stochastic estimation procedure to specific events is discussed. For example, the stochastic estimation can be applied as a bandpass filter to isolate the structures associated with specific scales. Many of these extensions to the linear stochastic estimation technique can be applied to the space/time correlation data base measured herein.

Chapter 8

SUMMARY AND RECOMMENDATIONS FOR FURTHER STUDY

8.1 Summary

A method of locally controlling the near wall burst process is investigated and presented. A significant suppression of the turbulent energy producing near wall burst process is accomplished by the generation of a converging flow field towards the wall over the region $y^+ \leq 30$. The wall directed converging flow retards outward moving ejection motions associated with the burst process. This converging flow is produced in part by a pair of counter-rotating vortices with a common flow down. The vortices are locally generated in the buffer region and sublayer of a fully developed turbulent pipe flow by a 16.4 wall unit high, wall-mounted bump. The bump also creates a converging mean flow downstream due to the approaching boundary layer being forced over and around the bump.

The investigation is conducted at a Reynolds number, based on pipe diameter, of approximately 10,000. The corresponding momentum thickness Reynolds number for the fully developed turbulent pipe flow is approximately 730. The glycerin tunnel provides large length and time scales which provide excellent spatial and temporal resolution. Multi-component, multi-point laser Doppler velocimetry is used to investigate the development and recovery regions downstream of the bump. The LDV and data acquisition systems are operated in manner which allows high resolution, time resolved, unbiased velocity measurements. The measurements include single-point, three-component velocity profiles, two-point, space/time velocity correlations and multi-component velocity spectral estimates in both the undisturbed and modified turbulent pipe flow. The two-point space/time velocity

correlations involved the direct measurement of 8 of the 9 terms of the two-point correlation tensor on the flow centerplane.

The detailed set of three-component single-point velocity measurements obtained in the undisturbed boundary layer quantified measurement uncertainties and limitations, and identified potential sources of error. These velocity measurements show excellent agreement with and validate a recent direct numerical simulation of a fully developed turbulent channel flow at a momentum thickness Reynolds number of about 700 by Antonia et al. (1992). A detailed description of the measurements of the undisturbed flow are provided in the manuscript.

The rollup of a junction vortex upstream of the bump is observed in the velocity measurements. This junction vortex is convected around the bump forming a pair of counter-rotating quasi-streamwise vortices downstream. Measurements indicate that the vortices are approximately 10 to 15 wall units in diameter and are confined to the near wall region. The vortices are observed to persist for more than 174 wall units. Turbulent velocity fluctuations indicate that these vortices wander in the circumferential direction occasionally crossing the centerplane. Velocity profile statistics also indicate a second vortical structure, possibly a counter-rotating vortex pair, is located at a $y^+ \approx 20$ and may be generated near the top of the bump.

A radial and circumferential mean velocity convergence towards the wall and the centerplane is observed. This region is approximately 15 to 20 wall units high and persists for more than 100 wall units. This convergence zone can be interpreted as a stagnation region when observed from a reference frame moving with the local streamwise velocity. This mean velocity convergence is a dominant feature of the development and recovery region downstream of the bump. Turbulent velocity fluctuations are strongly retarded within this

region, which yields a reduction in streamwise rms velocities and a significant decrease in the near wall uv Reynolds stress. Burst rate and relative quadrant analyses of the uv signal confirm that turbulent momentum transport in the form of ejections and sweeps are retarded within this mean flow convergence region.

The decrease in the number of ejections and the burst rate confirm the local inhibition of the bursting event. In addition, the decrease in sweep type events indicates that the convergence region causes a decoupling of the inner ($y^+ < 12$) and outer ($y^+ \geq 12$) near wall regions. Low speed fluid from the inner near wall region does not penetrate the buffer region, and likewise high speed fluid cannot penetrate the inner region. This result is significant in that both sweeps and ejections are suppressed which reduces the generation of uv Reynolds stress all the way to the wall. The suppression of the near wall turbulent activity produces a reduction in the local wall shear stress with resulting mean streamwise velocity profiles similar to those observed in drag reduced boundary layers with polymers. However, the form drag on this bump more than offsets the local skin friction reduction. Turbulent velocity auto- and cross-spectral estimates indicate that the low frequency Reynolds stress producing motions are inhibited within this region. In addition, small scale, high frequency motions may be inhibited by the convergence region as well.

Superimposed on this convergence region are the near wall counter-rotating vortices and the second vortical structure at $y^+ \approx 20$. Velocity statistics clearly indicate the presence of both vortical structures. These statistics indicate that the resulting modifications to the turbulent boundary layer are confined to the buffer region and sublayer. Modifications are not observed beyond $y^+ \approx 40$. Non-zero uw and vw Reynolds stress components are measured at off-centerplane locations. These additional correlations directly result from the presence of the counter-rotating vortices.

An examination of the transport of turbulent kinetic energy shows that the rate of production of energy is significantly reduced within the convergence region. However, the rate of transport of energy by turbulent fluctuations is increased. The counter-rotating vortices increase the rate of turbulent transport and bring increased velocity fluctuations into the near wall mean flow convergence region. The rotational velocity pattern of the counter-rotating vortices creates radial and circumferential velocity perturbations as the vortices wander across the centerplane. In addition, this motion entrains and transports high streamwise velocity fluctuations toward the wall. The wandering of the counter-rotating vortices intermittently brings sweep type motions into the near wall region.

Apparently, the major influence of the counter-rotating vortices is an increase in the rate of turbulent energy transport by increased turbulent diffusion. This acts to offset the favorable modifications obtained in the convergence region. This increased turbulent activity is also illustrated in increased energy levels above 40 Hz in all auto- and cross-spectral estimates near the wall. The transport of turbulence by the counter-rotating vortices occurs over a continuous frequency range larger than approximately 40 Hz. This indicates that the vortices are effective at transporting fluctuations with larger characteristic frequencies than that of the vortices, which is estimated at approximately 19 Hz, or of their wandering rate of 4 to 11 Hz.

Surprisingly, negligible changes in the radial rms profiles are observed everywhere, and only small modifications to the spanwise rms profiles are observed on the centerplane. It is likely that the mean flow convergence reduces the radial and spanwise rms levels as much as it does the streamwise rms levels. The increased transport of turbulence by the vortices and an increase in the rate of production of the spanwise component of q^* offsets any reductions in the spanwise rms levels on the centerplane. Furthermore, the increased

transport by the vortices also offsets reductions to the radial rms levels everywhere. It is particularly interesting that the increased turbulence is enough to nearly recover all energy loss in the convergence region and that radial and spanwise rms levels are approximately equal to the undisturbed levels. Clearly the second vortical structure at $y^* \approx 20$ is undesirable, and it is possible that the near wall counter-rotating vortices may be undesirable in a control scheme, at least in the non-active role in which they are introduced.

The linear stochastic estimation technique is presented and is successfully applied to the development region along the centerplane. The measured two-point correlation tensor as well as the Reynolds stress tensor are used in the stochastic estimation procedure. The high quality measurements yield uncertainty estimates of approximately 20% in the conditionally averaged velocity perturbation estimates obtained from the linear stochastic estimation. Unfortunately, the vv two-point correlations could not be obtained and this restricted the application of the technique to the estimation of only the streamwise and spanwise velocity perturbations. The stochastic estimation results illustrate the dominance of the sweep type motions created by the counter-rotating vortices. Velocity perturbation contours indicate that centerplane values of τ_w may be lower than the long time average value when the vortices are straddling the centerplane and higher than the long time average value when a leg of the counter-rotating vortices crosses the centerplane. This has the important implication that the mean flow convergence region may produce more favorable modifications to the near wall burst process in the absence of the counter rotating vortices.

8.2 Major Significance of the Present Results

The major significance of the current investigation is the reinforcement of the importance of the bursting process to the generation of Reynolds stress and turbulent kinetic energy in the near wall region, below $y^+ \approx 15$. The main objective of the study, which is the local modification of the bursting mechanism to produce a reduction in the generation of turbulence, is accomplished. The results indicate that the driving mechanism responsible for the suppression of the burst process is the convergence of mean flow downstream of the bump. Ejection type motions must overcome the wallward directed forces imposed by the radially converging flow. The spanwise convergence also produces a decoupling of the near wall region, $y^+ < 15$, from the rest of the buffer region and log layer. This decoupling is evident by the suppression of quadrant four Reynolds stress producing motions below $y^+ \approx 12$. The suppression of these quadrant four events yields significant reductions in the total uv signal right near the wall.

This control scheme, at least in the non-active role applied here, is not practical due to the increased form drag on the bump. However, the results do imply that a significant suppression of turbulence can be achieved by locally influencing the turbulence generating mechanism. It is possible that in a more active role, the following scheme may produce net positive gains in skin friction reduction.

It is probable that the generation of the counter-rotating vortices is undesirable in the current control scheme. While the vortices may increase the flux of fluid toward the wall, the current results indicate the vortices are more effective at increasing the transport of turbulent fluctuations. This result agrees with the accepted association of vortices with the significant transport of momentum in the turbulent boundary layer. Since the vortices are relatively fixed in space, this particular flow problem has the potential of allowing, in a fairly direct

manner, the study of the dynamics associated with quasi-streamwise vortices in the near wall region. Unfortunately, the current measurements are limited in spanwise extent and the upflow sides of the counter-rotating vortices could not be investigated. Considering the current knowledge associated with quasi-streamwise vortices in the near wall region, it is likely that increased burst rates and ejection activity would be encountered on the upflow sides at larger spanwise displacements off the centerplane.

The application of the linear stochastic estimation technique to the centerplane region confirms the association of the counter-rotating vortices with sweep type motions and thus with an increased transport of turbulence. The results also imply that a further suppression of turbulent motion and a resulting further decrease in local skin friction may be achieved if the wandering of the vortices is prevented. This together with the information presented in the preceding paragraph suggests that the vortices are clearly undesirable and probably do not supplement the burst suppressing capabilities of the mean flow convergence. Although the stochastic estimation technique is used only in a limited fashion here, the versatility of the technique in the study of complex turbulent flow structure is evident.

As a final note of significance, a high quality, high resolution, velocity data base is compiled for both the undisturbed and modified turbulent pipe flows. Detailed three-component, single-point, time resolved velocity measurements in the near wall and log regions of a $Re_\tau = 730$ canonical turbulent pipe flow are presented. These measurements are in excellent agreement with a recent direct numerical simulations of a $Re_\tau \approx 700$ fully developed turbulent channel flow by Antonia et al. (1992). The combination of these measurements and the measurements of the modified near wall region provide a unique measurement set for use in the validation of turbulent boundary layer computational codes. The modified results provide a good test case considering the relatively simple boundary

conditions of fully developed pipe flow at the upstream and far downstream inflow and outflow boundaries. The author is unaware of any three-dimensional data sets which provide the accuracy and the temporal and spatial resolution of the current measurements in a $Re_\tau > 500$ canonical turbulent boundary layer.

8.3 Recommendations for Further Study

The present measurements are limited to small displacements off the centerplane. It would be of interest to increase the current data base to include measurements on the upflow sides of the counter-rotating vortices. This would allow the testing of the speculations raised in Section 8.2 concerning the kinematics of the counter-rotating vortices and increased ejection motions.

Off-centerplane two-point correlations would be a welcome supplement to the current data base. In addition, the vv correlations on the centerplane would be of interest. The current data base can be further analyzed to include time delayed statistics. It may be that the time lag statistics will provide additional information about the characteristics of the vortices and their spanwise wandering. The linear stochastic estimation technique can be applied to these time lag statistics, and potentially enable the temporal analysis of the centerplane modifications. This knowledge may lead to a more efficient method of applying the burst suppression scheme introduced here. In addition, this may lead to a better understanding of the dynamics of the both the near wall counter-rotating vortices and the second pair of vortices at $y^+ = 20$. What is the process governing the observed motions of these vortices? Do the two pairs of vortices interact with each other, and if so, how? The answers to these questions may lead to a better understanding of the transport mechanisms of the vortices and

to methods of control of quasi-streamwise vortices. This may have implications in active control schemes which seek to control the quasi-streamwise vortices.

The influence of bump shape should be studied. Streamlining the bump would reduce the effects of increased form drag and may possibly produce more favorable results. Similarly the influence of the counter-rotating vortices should be investigated in more detail. Can a similar mean flow convergence be set up with the generation of a weaker pair of vortices and does this new situation produce favorable results? Furthermore, are the observed reductions in the burst process dependent on the combined effects of both the counter-rotating vortices and the mean flow convergence? The influence on the bursting process of just a mean flow convergence flow field without the vortices, if it can be generated, should be investigated. And most importantly, this control scheme must be investigated in an active role. It is possible that when applied in a short time, almost instantaneous manner, the benefits obtained from the reduced turbulent activity may be more than enough to offset any short time unfavorable disturbances created by the bump.

REFERENCES

- Adrian, R.J., 1975, "On the Role of Conditional Averages In Turbulence Theory," Proc. 4th Biennial Symp. on Turbulence in Liquids, 1975, Univ. of Missouri Rolla, pp. 323-332.
- Adrian, R. J., 1979, "Conditional Eddies In Isotropic Turbulence," *J. Phys. Fluid*, Vol. 22, No. 11, pp. 2065-2070.
- Adrian, R. J. and Earley, W. L., 1975, "Evaluation of LDV Performance Using Mie Scattering Theory," Symp. on Laser Anem., University of Minnesota, Minnesota.
- Adrian, R. J. and Moin, P., 1988, "Stochastic Estimation of Organized Turbulent Structure: Homogenous Shear Flow," *J. Fluid Mech.*, Vol. 190, pp. 531-559.
- Adrian, R. J. and Yao, C. S., 1987, "Power Spectra of Fluid Velocities Measured By Laser Doppler Velocimetry," *Exp. Fluids*, Vol. 5, pp. 17-28.
- Antonia, R. A., 1981, "Conditional Sampling in Turbulence Measurements," *Ann. Review Fluid Mech.*, Vol. 13, pp. 131-156.
- Antonia, R. A., Teitel, M., Kim, J. and Browne, L.W.B., 1992, " Low Reynolds Number Effects in a Fully Developed Turbulent Channel Flow," *J. Fluid Mech.*, vol. 236, pp. 579-605.
- Aubry, N., Holmes, P., Lumley, J. L. and Stone, E., 1988, "The Dynamics of Coherent Structures in the Wall Region of a Turbulent Boundary Layer," *J. Fluid Mech.*, vol. 192, pp. 115-173.
- Bakewell, H. P., 1966, *An Experimental Investigation of the Viscous Sublayer In a Turbulent Pipe Flow*, Ph.D. Thesis, The Pennsylvania State University.
- Bakewell, H. P. and Lumley, J. L., 1967, "Viscous Sublayer and Adjacent Wall Region In Turbulent Pipe Flow," *J. Phys. Fluids*, Vol. 10, No. 9, pp. 1880-1889.
- Baldwin, J. T. 1990, *An Investigation of the Mean Fluid velocity and Reynolds Stress Fields within an Artificial Heart Ventricle*, Ph.D. Thesis, The Pennsylvania State University.
- Bendat, J. S. and Piersol, A. G., 1986, *Random Data, Analysis and Measurement Procedures*, Second Ed., J. Wiley and Sons Inc.
- Blackwelder, R. F. and Eckelmann, H., 1979, "Streamwise Vortices Associated With the Bursting Phenomenon," *J. Fluid Mech.*, Vol 94, pp. 577-594.
- Bloch, A. M. and Marsden, J. E., 1989, "Controlling Homoclinic Orbits," *Theoret. Comput. Fluid Dynamics*, vol 1, pp. 179-190.

Bogard, D. G. and Tiederman, W. G., 1987, "Characteristics of Ejections In Turbulent Channel Flow," *J. Fluid Mech.*, Vol. 179, pp.1-19.

Brereton, G.J., 1992, " Stochastic Estimation as a Statistical Tool for Approximating turbulent conditional averages," *Phys. Fluids*, vol. A4, no. 9, pp. 2046-2054.

Buchave, P., George, W. K., Jr. and Lumley, J. L., 1979, "The Measurement of Turbulence With the Laser-Doppler Anemometer," *Ann. Rev. Fluid Mech.*, Vol. 11, pp. 443-503.

Chevrin, P. A., 1988, *The Structure of the Reynolds Stress In the Near Wall Region of a Turbulent Pipe Flow*, Ph.D. Thesis, The Pennsylvania State University.

Clark, J. A. and Marklan, E., 1971, "Flow Visualization in Turbulent Boundary Layers," *J. Hydr. Div.*, ASCE, vol. HY-10, pp. 1653-1663.

Coleman, H. W. and Steele, W. G., 1989, *Experimentation and Uncertainty Analysis for Engineers*, Published by J. Wiley and Sons, Inc.

Comte-Bellot, G., Sabot, J. and Saleh, I., 1978, "Detection of Intermittent Events Maintaining Reynolds Stress," In *Proc. Dynamic Flow Conf.- Dynamic Measurements in Unsteady Flows*, Marseille, France, pp. 213-231.

Corino, C. R. and Brodkey, R. S., 1969, "A Visual Investigation of the Wall Region In Turbulent Flow," *J. Fluid Mech.*, Vol. 37-1, pp.1-30.

Devenport, W. J. and Simpson, R. L., 1990, "Time-Dependent and Time Averaged Turbulence Structure Near the Nose of a Wing-Body Junction," *J. Fluid Mech.*, Vol. 210, pp. 23-55.

Edwards, R. V., 1987, "Report of the Special Panel On Statistical Particle Bias Problems in Laser Anemometry," *J. Fluids Eng.*, Vol. 109, pp. 89-93.

Edwards, R. V. and Jensen A. S., 1983, "Particle Sampling Statistics In Laser Anemometers: Sample and Hold Systems and Saturable Systems," *J. Fluid Mech.*, Vol. 133, pp. 397-411.

Fiebig, M., Kallweit, P., Mitra, N. and Tiggelbeck, S., 1991, "Heat Transfer Enhancement and Drag By Longitudinal Vortex Generators In Channel Flow," *Exp. Thermal Fluid Sci.*, Vol. 4, pp. 103-114.

Fontaine, A. A., Petrie, H. L. and Brungart, T. A., 1992, "Turbulent Velocity Profile Statistics In With Modification Due to Drag Reducing Polymers," *J. Fluid Mech.*, Vol. 238, pp. 435-466.

Fontaine, A. A. and Deutsch, S., 1992, "The Influence of the Type of Gas On the Reduction of Skin Friction Drag By Microbubble Injection," *Exp. in Fluids*, Vol. 13, pp. 128-136.

Gad-el-Hak M., 1989, "Flow Control," *Appl. Mech. Rev.*, Vol. 42, No. 10, pp. 261-293.

Guezennec, Y. G., 1989, "Stochastic Estimation of Coherent Structures In Turbulent Boundary Layers," *Phys. Fluids A*, Vol. 1, No. 6, pp. 1054-1060.

Guezennec, Y. G., Gieseke, T. J. and Trigui, N., 1991, "Stochastic Estimation of Coherent Structures and Their Dynamics In Transitional and Turbulent Boundary Layers," AFOSR-89-0434, AFOSR/NA Report AFOSR-TR-91 0511.

Head, M. R. and Bandyopadhyay, P., 1981, "New Aspects of Turbulent Boundary Layer Structure," *J. Fluid Mech.*, Vol. 107, pp. 297-338.

Herzog, S., 1986, *The Large Scale Structure in the Near-Wall Region of a Turbulent Pipe Flow*, Ph.D. Thesis, Cornell University.

Hunt, J. C. R., Abell, C. J., Peterka, J. A., and Woo, H., 1978, "Kinematical Studies of the Flows Around Free or Surface Mounted Obstacles; Applying Topology to Flow Visualization," *J. Fluid Mech.*, Vol. 86-1, pp. 179-200.

Johnson, P. L. and Barlow, R. S., 1989, "Effect of Measuring Volume Length on Two Component Laser Velocimeter Measurements In a Turbulent Boundary Layer," *Exp. Fluids*, Vol. 8, pp. 137-144.

Karlsson, R. I. and Johansson, T. G., 1988, "LDV Measurements of Higher Order Moments of Velocity Fluctuations In a Turbulent Boundary Layer," *Laser Anemometry in Fluid Mechanics*, Published by Ladoan-Instituto Superior Tecnico, 1096 Lisbon Codex, Portugal.

Kasagi, N., Hirata, M. and Nishino, K., 1986, "Streamwise Pseudo-Vortical Structures and Associated Vorticity in the Near Wall Region of a Wall Bounded Turbulent Shear Flow," *Exp. Fluids*, vol. 4, pp. 309-318.

Kim, H. T., Kline, S. J. and Reynolds, W. C., 1971, "The Production of Turbulence Near a Smooth Wall In a Turbulent Boundary Layer," *J. Fluid Mech.*, Vol. 50-1, pp. 133-160.

Kim, J., Moin, M. and Moser, R., 1987, "Turbulence Statistics in Fully Developed Channel Flow at Low Reynolds Number," *J. Fluid Mech.*, vol. 177, pp. 133-166.

Kline, S. J. and Afgan, P. H., 1990, *Near Wall Turbulence*, Proceedings of the Zoran Zaric Memorial Conference, Edited by Kline and Afgan, Published by Hemisphere Publishing Corp.

Kline, S. J., Reynolds, W. C., Schraub, F. A., and Runstadler, P. W., 1967, "The Structure of Turbulent Boundary Layers," *J. Fluid Mech.*, Vol. 30-4, pp. 741-773.

Kline, S. J. and Robinson, S. K., 1989, "Quasi-Coherent Structures in the Turbulent Boundary Layer. Part I: Status Report on a Community-Wide Summary of the Data," Proceedings of the *Zoran P. Zaric Memorial International Seminar on Near-Wall Turbulence*, pp. 200-217.

Koskie, J. E. and Tiederman, W. G., 1992, "Turbulence Structure and Polymer Drag Reduction in Adverse Pressure Gradient Boundary layers," Rep. PME-FM-91-3, Purdue University Technical Report.

Laufer, J., 1954, "The Structure of Turbulence In Fully Developed Pipe Flow," N.B.S. Report, No. 1174.

Lu, S. S. and Willmarth, W. W., 1973, "Measurements of the Structure of the Reynolds Stress in a Turbulent Boundary Layer," *J. Fluid Mech.*, vol. 60, pp. 481-511.

Luchik, T. S. and Tiederman, W. G., 1987, "Timescale and Structure of Ejections and Bursts in Turbulent Channel Flows," *J. Fluid Mech.*, vol. 174, pp. 529-552.

Lumley, J.L., 1988, Personal Communication.

Mansour, N. N., Kim, J. and Moin, P., 1988, "Reynolds-Stress and Dissipation-Rate Budgets in a Turbulent Channel Flow," *J. Fluid Mech.*, vol. 194, pp.15-44.

McComb, W. D. and Rabie, L. H., 1982, "Local Drag Reduction Due to Injection of Polymer Solutions Into Turbulent Flow In a Pipe, Part 1: Dependence On Local Polymer Concentration and Part 2: Laser Doppler Measurement of Turbulence Structure," *A. IChE*, Vol. 28, pp. 547-565.

Merkle, C. L. and Deutsch, S., 1989, Microbubble Drag Reduction, *Frontiers in Exp. Fluid Mech.*, Edited by Gad-el-Hak, (Springer-Verlag, Berlin) pp.291-335.

Moin, P. and Kim, J., 1985, "The Structure of the Vorticity Field in Turbulent Channel Flow. Part 1. Analysis of Instantaneous Fields and Statistical Correlations," *J. Fluid Mech.*, vol. 155, pp. 441-464.

Moin, P., Adrian, R. J. and Kim, J., 1987, "Stochastic Estimation of Conditional Eddies In Turbulent Channel Flow," 6th Symp. Turbulent Shear Flows, Toulouse, France.

Nagib, H. M. and Guezennec, Y. G., 1986, "On the Structure of Turbulent Boundary Layers," Proc. 10th Symp. Turbulence, Rolla Missouri.

Petrie, H. L., Samimy, M. and Addy, A. L., 1988, "Laser Doppler Velocity Bias In Separated Turbulent Boundary Layers," *Exp. Fluids*, Vol. 6, pp. 80-88.

Robinson, S. K., 1991, "The Kinematics of Turbulent Boundary Layer Structure," NASA Tech. Memo., No. 103859, pp. 1-333.

Rundstadler, P. W., Kline, S. J. and Reynolds, W. C., 1963, "An Experimental Investigation of the Flow Structure of the Turbulent Boundary Layer," Report MD-8, Mech. Eng. Dept. Report, Stanford University.

Saxena, V., 1985, "Power Spectrum Estimation From Randomly Sampled Velocity Data," Int. Symp. Laser Anem., ASME WAM, Florida, Editors A. Dybbs and P.A. Pfund.

Schofield, W. H. and Logan E., 1990, "Turbulent Shear Flow Over Surface Mounted Obstacles," *J. Fluids Eng.*, Vol. 112, pp. 376-385.

Shekarriz, A., Fu, T. C., Katz, J., Liu, H. L. and Huang, T. T., 1992, "Study of Junction and Tip Vortices Using Particle Displacement Velocimetry," *AIAA Journal*, vol. 30, no. 1, pp. 145-152.

Sedney, R., 1973, "A Survey of the Effects of Small Protuberances On Boundary Layer Flows," *J. AIAA*, Vol. 11, No. 6, pp. 782-792.

Smith, C. R. and Metzler, S. P., 1983, "The Characteristics of Low Speed Streaks In the Near Wall Region of a Turbulent Boundary Layer," *J. Fluid Mech.*, Vol. 129, pp. 27-54.

Spalart, P. R., 1988, "Direct Numerical Simulation of a Turbulent Boundary Layer Up to $Re_\tau=1410$," *J. Fluid Mech.*, Vol. 187, pp. 61-98.

Spalding, D. B., 1961, "A Single Formula for the Law of the Wall," *J. Appl. Mech.*, vol. 28, pp. 455-457.

Sreenivasan, K. R., 1990, "The Turbulent Boundary Layer," In *Frontiers in Exp. Fluid Mech.*, (ed. M. Gad-el-Hak), pp. 159-209, Springer.

Tennekes, H. and Lumley, J. L., 1972, *A First Course in Turbulence*, MIT Press.

Theodorsen, 1952, "Mechanism of Turbulence," In *Proc. Second Midwestern Conference on Fluid Mech.*, Ohio State University, Columbus Ohio.

Walker, D. T. and Tiederman, W. G., 1990, "Turbulent Structure In a Channel Flow With Polymer Injection At the Wall," *J. Fluid Mech.*, Vol. 218, pp. 377-403.

Wei, T. and Willmarth, W. W., 1989, "Reynolds Number Effects On the Structure of a Turbulent Channel Flow," *J. Fluid Mech.*, Vol. 204, pp. 57-95.

White, F. M., 1974, *VISCOUS FLUID FLOW*, McGraw-Hill Publishers, New York.

Winter, A. R., Graham, L. J. W., and Bremhorst, K., 1991, "Effects of Time Scales On Velocity Bias In LDA Measurements Using Sample and Hold Processing," *Exp. Fluids*, Vol. 11, pp. 147-152.

Appendix A

LDV VELOCITY MEASUREMENT ERROR DUE TO REFRACTION EFFECTS

The slight mis-match in the index of refraction of the glycerin and the acrylic pipe wall produces an increasing error in the radial velocity measurement as the wall is approached. This error is produced by a decrease in the half angle of the radial component laser beams inside the tunnel. It may be shown that estimated velocities are lower than the actual velocities producing the Doppler signal when the decreased half angle is not accounted for in the data reduction of the Doppler frequency.

The Doppler frequency, f_D , produced by a particle traveling with velocity V_a is given by,

$$f_D = \frac{V_a \cdot 2 \cdot \sin(\kappa_p)}{\lambda} \quad A.1$$

The actual half angle in the tunnel is denoted by κ_a and λ is the wavelength of the LDV laser beams. The counter-processors output a signal which is proportional to the measured Doppler Frequency. The measurement of velocity is obtained by converting the acquired Doppler frequency from the counter-processors using equation A.2.

$$V_m = \frac{f_D \lambda}{2 \cdot \sin(\kappa)} \quad A.2$$

In Equation A.2, the half angle κ is the assumed half angle estimated by optical principals.

An equation relating the measured velocity, V_m , to the actual velocity V_a is obtained by substituting Equation A.1 into Equation A.2. The resulting equation is,

$$V_m = V_a \frac{\sin(\kappa_a)}{\sin(\kappa)} \quad \text{A.3}$$

The error in the measured velocity is proportional to the ratio of the sines of the actual half angle in the tunnel to the assumed half angle used to convert the Doppler frequency into a velocity. If κ_a is smaller than κ , the measured velocities will be smaller than the actual velocity in the tunnel. Since κ_a and κ are constants at a given location, the error in the velocity statistics will also be proportional to the ratio of the sines of the half angles. As an example of the magnitude in the error defined by Equation A.3, let the assumed half angle equal 3.0° and the actual half angle equal 2.5° . With these values, the measured velocity would be approximately 17% low.

Appendix B

VELOCITY CORRECTIONS FOR OFF-CENTER MEASUREMENTS

As discussed in Chapter 3, displacement of the LDV probe volumes to off-center positions causes a rotation of the radial and circumferential probe volumes with respect to the pipe coordinate system. The axial component is not effected however. The following correction for rotation can only be applied to single-point radial and spanwise velocity measurements. The amount of rotation can be estimated from the following equation for negative z displacement.

$$\beta = \tan^{-1} \frac{z}{(R \cos(\alpha) - y)} \quad \alpha = \sin^{-1} \frac{z}{R} \quad \text{B.1}$$

With the rotation angle known, the actual radial and spanwise velocities, V_a and W_a , are related to the measured velocities by the following relations,

$$V_a = W_m \sin \beta + V_m \cos \beta \quad \text{B.2a}$$

$$W_a = W_m \cos \beta - V_m \sin \beta. \quad \text{B.2b}$$

While these equations are written for the total velocities, similar equations apply for the mean and fluctuating radial and spanwise velocity components. In the event of coincident velocity measurements, the corrections given by Equations B.2a and B.2b can be directly applied to the measured data.

If the velocity data are not measured simultaneously, the long time averaged statistics can be corrected. Equations B.2a and B.2b are written in terms of the fluctuating velocities. A correction to the radial and spanwise velocity variance is obtained by time averaging the

square of Equations B.2a and B.2b. The resulting equations for the corrections to the radial and spanwise variance are,

$$\overline{v_s^2} = 2 \overline{vw_m} \cos \beta \sin \beta + \overline{w_m^2} \sin^2 \beta + \overline{v_m^2} \cos^2 \beta \quad B.3a$$

$$\overline{w_s^2} = -2 \overline{vw_m} \cos \beta \sin \beta + \overline{v_m^2} \sin^2 \beta + \overline{w_m^2} \cos^2 \beta. \quad B.3b$$

Corrections to the uv and uw Reynolds stress components can be obtained by multiplying Equations B.2a and B.2b by the streamwise velocity fluctuations and time averaging. The vw correlation correction is derived by cross multiplying Equations B.2a and B.2b together and time averaging. The corrections to the Reynolds stress components are,

$$\overline{uv_s} = \overline{uw_m} \sin \beta + \overline{uv_m} \cos \beta \quad B.4a$$

$$\overline{uw_s} = \overline{uw_m} \cos \beta - \overline{uv_m} \sin \beta \quad B.4b$$

$$\overline{vw_s} = (\overline{w_m^2} - \overline{v_m^2}) \cos \beta \sin \beta + \overline{vw_m} (\cos^2 \beta - \sin^2 \beta). \quad B.4c$$

A set of equations to correct the third and fourth order statistics can be developed in a similar manner. These corrections are applied as a post processing procedure on the calculated time averaged statistics.